



**HAL**  
open science

# Design, synthesis and transporting mechanism of hydrophilic artificial water channels

Libo Huang

► **To cite this version:**

Libo Huang. Design, synthesis and transporting mechanism of hydrophilic artificial water channels. Other. Université Montpellier, 2021. English. NNT : 2021MONT081 . tel-03630551

**HAL Id: tel-03630551**

**<https://theses.hal.science/tel-03630551>**

Submitted on 5 Apr 2022

**HAL** is a multi-disciplinary open access archive for the deposit and dissemination of scientific research documents, whether they are published or not. The documents may come from teaching and research institutions in France or abroad, or from public or private research centers.

L'archive ouverte pluridisciplinaire **HAL**, est destinée au dépôt et à la diffusion de documents scientifiques de niveau recherche, publiés ou non, émanant des établissements d'enseignement et de recherche français ou étrangers, des laboratoires publics ou privés.

# THÈSE POUR OBTENIR LE GRADE DE DOCTEUR DE L'UNIVERSITÉ DE MONTPELLIER

En Chimie et Physico-Chimie des Matériaux

École doctorale ED459

Unité de recherche UMR5635

## Design, Synthesis and Transporting Mechanism of Hydrophilic Artificial Water Channels

Présentée par Libo HUANG  
Le 23 Novembre 2021

Sous la direction de Dr. Mihail BARBOIU

Devant le jury composé de

M. Nicolas GIUSEPPONE, Prof, Université de Strasbourg

M. Mihail BARBOIU, DR, CNRS

Mme. Sophie CERNEAUX, MCF, École Nationale Supérieure de Chimie de Montpellier

M. Stéphane VINCENT, Prof, Université de Namur

Mme. Andreea PASC, Prof, Université de Lorraine

M. Narcis AVARVARI, DR, CNRS

M. Sébastien ULRICH, CR, CNRS

Président du jury

Direction de thèse

Co-encadrant de thèse

Rapporteur

Rapporteur

Examineur

Examineur



UNIVERSITÉ  
DE MONTPELLIER



## Acknowledgements

First and foremost, I would like to express my deepest gratitude to my thesis director Prof. Mihail Barboiu for giving me the opportunity to join his group, Nanosystèmes Supramoléculaires Adaptatifs, and for providing me an excellent research environment. He is an admirable mentor with immense enthusiasm and creativity for science which has greatly inspired me. Whenever I was frustrated by setbacks in my research, he was always able to patiently diagnose the problems and guide me with his profound knowledge, giving me renewed hope to re-engage in my experiments. I feel a deep sense of pleasure and accomplishment during the three-year research experience with him.

I am very grateful to my thesis co-director Dr. Sophie Cerneaux for sharing her experience on ceramic membranes and making effort on our laboratory management. I would also like to thank my current and former lab colleagues Dr. Yuhao Li, Dr. Shaoping Zheng, Dr. Maria Di Vincenzo, Mihai Deleanu, Dr. Dmytro Strilets, Dandan Su, Iuliana-Marilena Andrei, Sanaa Daakour, Dr. Omar Samhari, Dr. Romain Dupuis, Dr. Dinesh Mahalingam, Kelvin Nursiah, Maxime Leclère and Sharath Jayakumar for their company and support.

Many thanks to Dr. Arie van der Lee and Dr. Dominique Granier for solving the single-crystal structures, and to Eddy Petit for helping me with NMR and Mass spectrometry. Moreover, I also appreciate the molecular dynamics simulations performed by Prof. Marc Baaden and Arthur Hardiagon from IBPC Paris, and Prof. Guillaume Maurin from ICGM Montpellier.

I would like to acknowledge the *Centre National de la Recherche Scientifique* (CNRS), *Agence Nationale de la Recherche* (ANR) and *China Scholarship Council* (CSC) for funds of this doctoral program. Last but not least, I am also grateful to the members of the jury for attending my thesis defense and, in particular, to Prof. Stéphane Vincent and Prof. Andreea Pasc for accepting to be the reviewers of this work.



# Table of contents

<b>ABBREVIATIONS .....</b>	<b>3</b>
<b>GENERAL INTRODUCTION .....</b>	<b>5</b>
<b>CHAPTER I – BIBLIOGRAPHIC STUDY .....</b>	<b>9</b>
1.1. INTRODUCTION.....	10
1.2. AQUAPORINS AND PORINS.....	11
1.3. ARTIFICIAL WATER CHANNELS: SYNTHETIC AQPs .....	17
1.4. BIOMIMETIC AWC MEMBRANES FOR DESALINATION.....	38
1.5. CONCLUSIONS .....	43
<b>CHAPTER II – HYDROXY CHANNELS.....</b>	<b>49</b>
2.1. INTRODUCTION.....	50
2.2. RESULTS AND DISCUSSION .....	54
2.3. CONCLUSIONS .....	69
2.4. EXPERIMENTAL SECTION .....	71
<b>CHAPTER III – U-SHAPED DIIMIDAZOLE CHANNELS.....</b>	<b>111</b>
3.1. INTRODUCTION.....	112
3.2. RESULTS AND DISCUSSION .....	114
3.3. CONCLUSIONS .....	126
3.4. EXPERIMENTAL SECTION .....	127
<b>CHAPTER IV – BILAYER VERSUS POLYMERIC ARTIFICIAL WATER CHANNEL MEMBRANES</b> <b>.....</b>	<b>143</b>
4.1. INTRODUCTION.....	144
4.2. RESULTS AND DISCUSSION .....	146
4.3. CONCLUSIONS .....	161
4.4. EXPERIMENTAL SECTION .....	162
<b>CONCLUSIONS AND OUTLOOK.....</b>	<b>193</b>

LIST OF PUBLICATIONS.....	199
REFERENCES.....	201

## Abbreviations

AQP – aquaporin

AWC – artificial water channel

BWRO – brackish water reverse osmosis

CF – 5(6)-Carboxyfluorescein

Chl – cholesterol

CNTPs – carbon nanotube porins

DLS – dynamic light scattering

DSC – differential scanning calorimetry

EYPC – egg yolk *L*- $\alpha$ -phosphatidylcholine

HPTS – pyranine, 8-hydroxypyrene-1,3,6-trisulfonic acid trisodium salt

I-quartet – imidazole-quartet

IP – interfacial polymerization

LUV – large unilamellar vesicles

mCLR – compound to lipid molar ratio

MD – molecular dynamics

MPD – *m*-phenylenediamine

*m*-PE – hexa(*m*-phenylene-ethynylene) macrocycles

MOF – metal–organic framework

PA – polyamide

PAH[4] – peptide-appended hybrid[4]arene

PAH[5] – hydrazide-appended pillar[5]arene

PAP[5] – peptide-appended pillar[5]arene

PC – phosphatidylcholine

PEG – polyethylene glycol

POCs – porous organic cages

PS – phosphatidylserine

PVDF – poly(vinylidene fluoride)

RMSD – root mean square displacement



RO – reverse osmosis

SEM – scanning electron microscopy

SF – selectivity filter

SWRO – seawater reverse osmosis

TFC – thin-film composite

TFN – thin-film nanocomposite

TGA – thermogravimetric analysis

wCLR – channel to lipid ratio at weight

## **General Introduction**

Cell membranes are mainly composed of phospholipids enclosing the cell components, while the outer side of the membrane is in contact with the external environment. The cell membranes are the barrier that prevents various metabolites from entering the cell freely from outside the cell. It ensures the relative stability of the intracellular environment and allows various biochemical reactions to operate in an orderly manner. However, cells must exchange information, substances and energy with their surroundings in order to carry out specific biological functions, so they must have transporting systems to obtain the required substances and excrete metabolic waste.

Aquaporins, also known as natural water channels, are channel proteins from a larger family of major intrinsic proteins that form pores in the membranes of biological cells and primarily facilitate the transport of water between cells.<sup>1</sup> Despite their high permselectivity to water molecules, aquaporins, being channel proteins, require a mild biological environment (e.g. stable temperature, pH and osmotic pressure) to function effectively. Several groups around the world incorporated the Aquaporins in synthetic membranes and used them for water desalination. These membranes showed excellent water permeabilities and performances under the mild conditions, while the high pressure and salinity conditions used in sea water desalination are preventing their use under such harsh conditions. The development of artificial water channels as alternatives to aquaporins has thus become a research direction of widespread interest among researchers. In order to develop biomimetic artificial water channels, several groups around the world have constructed synthetic water channels with high selectivity and permeability, relying on the concepts from supramolecular chemistry and inspired by the structure of aquaporins.

Back in 1987, supramolecular chemistry was in the spotlight for the Nobel Prize in Chemistry which was awarded jointly to Donald J. Cram, Jean-Marie Lehn, and Charles J. Pedersen "for their development and application of molecules with structure-specific interactions of high selectivity." Jean-Marie Lehn in his Nobel lecture summarized that: Supramolecular chemistry may be defined as "chemistry beyond the molecule", bearing on the organized entities of higher complexity that result from the association of two or more chemical species held together by intermolecular forces".<sup>2</sup> Molecular chemistry creates a wide range of more complex molecules and materials and has developed a very powerful library of procedures for constructing them from atoms connected by covalent bonds. Beyond molecular chemistry, supramolecular chemistry aims to develop highly complex chemical systems from components that interact through non-covalent intermolecular forces.<sup>3</sup>

Two essential concepts are established in supramolecular chemistry: 1) Molecular recognition is a process involving both binding and selection of substrates by a given molecular receptor, as well as a specific function.<sup>2</sup> Generally it refers to the specific interactions between two or more components through noncovalent bonding such as hydrogen bonding, metal coordination, hydrophobic forces, van der Waals forces,  $\pi$ - $\pi$  interactions, halogen bonding, or resonant interaction effects; 2) Self-assembly and multiple binding with positive synergy are processes of spontaneous molecular organization that also allow for the conception of amplified molecular devices.<sup>2</sup> Although self-assembly usually occurs between weakly interacting species, this organization may be transferred into strongly bound covalent systems.

In particular, supramolecular chemistry is well known for biomimetics of important biological processes through self-assembly of small molecules. To replicate the functions of biological systems, many synthetic supramolecular

constructs are designed and utilized to investigate biological models and activities.

### **Research Objectives**

The research objective of this Ph.D. study aims to understand the structure performance of different artificial water channels - AWCs systems towards water permeation and salt rejection. This can be studied in two ways: fundamental analysis of new artificial water systems using biomimetic lipid bilayer membranes, or system as well as their incorporation into polymer membranes.

The main objective is further divided into the following specific objectives:

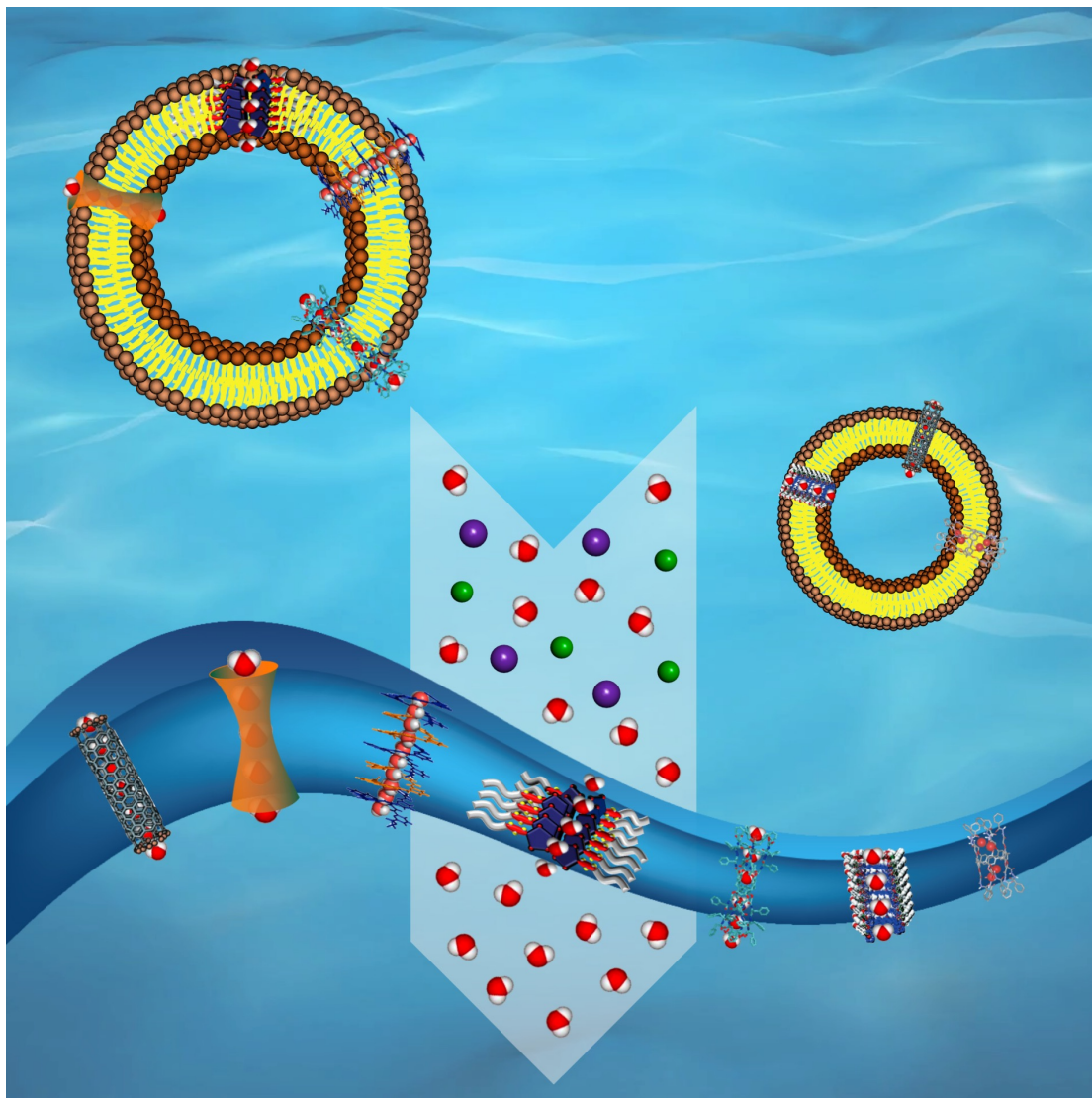
- i) investigating the feasibility of the precursors compounds to self-assemble and to act as water channels;
- ii) to study the structural-functional relationship of AWCs compounds with respect to their ability to function as water channel in bilayer membranes;
- iii) investigating the feasibility of AWCs to be incorporated in polymeric water membranes and other functionalities.

With this in mind, we start with the historical development and significant advancements of current reported artificial water channels, and attempt to reveal important structural insights and supramolecular self-assembly principles governing the selective water transport mechanisms, toward innovative AWC-based biomimetic membranes for desalination (Chapter I). Furthermore, we report octyl-ureido-polyols capable of self-assembly into hydrophilic hydroxy channels which adaptively transport water molecules or clusters depending on their concentration in lipid membranes (Chapter II). Afterwards, to get deeper insight into the differences of water-wires/water-clusters permeation approaches, we bring forward U-shaped diimidazole water channels constructed from pyridine bis(formamide-ethyl-imidazole)

derivatives in which single-crystal structures reveal the two distinct transport behaviors of water (Chapter III). At last, we investigate the structural determinants affecting the performance of I-quartet water channels in bilayer or polymeric membranes, and develop new concepts for desalination through bio-assisted AWC-membranes (Chapter IV).

This Ph.D. project introduces new synthetic water channels, and elaborate on the structure-performance analysis that can be used to rationalize artificial water channels design toward the fabrication highly permselective membranes for desalination.

## Chapter I – Bibliographic Study



This chapter is adapted *with permission from* L.-B. Huang, M. Di Vincenzo, Y. Li, M. Barboiu. Artificial water channels: towards biomimetic membranes for desalination. *Chem. Eur. J.* **2020**, *27*, 2224–2239. Copyright © 2021, Wiley.

## 1.1. Introduction

Water scarcity or lack of the clean/fresh water is a highly important issue taking into account the actual synergistic growth of population and industrial activities.<sup>4, 5</sup> To address the water supply requirements, membrane systems have been extensively explored during the few last years. Although seawater (SWRO) or brackish water (BWRO) reverse osmosis desalination are still expensive processes, their efficiency may be improved in the next years by modifying the technological process or by improving the membrane chemistry and composition leading to innovative structures and morphologies. There is a need for membrane innovation for which selectivity matters more than permeability.<sup>6</sup> Modern desalination technologies are using innovative materials with controlled porosity and morphology. Increasing the porosity of the membrane can easily lead to significant gains in both water and ion permeabilities with a detrimental decrease in selectivity. Specific water channels inserted in membranes can be used to improve the molecular interactions between water and conduits, providing selective water translocation through the membrane. Such a combination of robust polymeric matrix with selective AWCs will break the *permeability/selectivity* trade-off for channel-based scalable membranes (Figure 1).

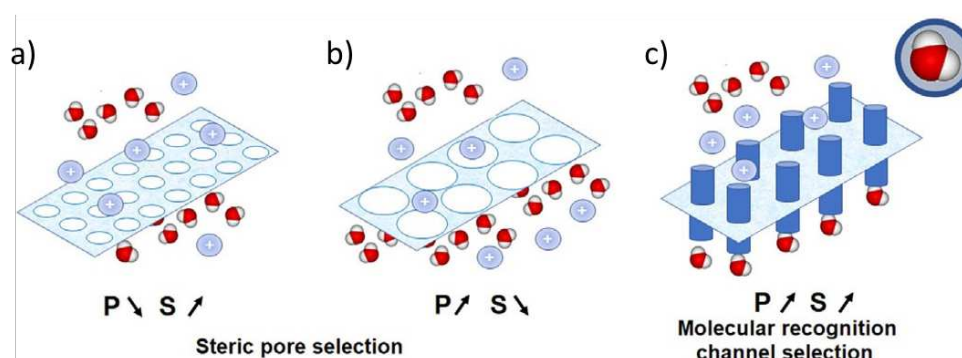


**Figure 1.** Permeability/selectivity trade-off for scalable membranes. Translocation/rejection governed by water–ion interaction through (a and b) porous polymeric networks and (c) selective channel superstructures.

Among such specific channels, AQPs are proteins known to transport water very fast with ion exclusion and are used for the fabrication of *bio-assisted* membranes. AQPs can be bio-mimicked by employing AWCs to assess the basis for biomimetic membranes for desalination processes. The objective of this chapter is to contribute to a better and deeper understanding of the natural and biomimetic water transport functions and to discover new ways to generate advanced selective water desalination systems. To achieve this aim, different families of channels, materials, and membranes that maintain the highly selective water conduction activity, particularly those discovered in the last decade, will be presented. Toward this objective, this bibliographic study will describe AWCs combining a particularly broad range of self-assembly and recognition features through hydrogen-bonding or hydrophobic effects, which play an important role in the ability to finely control the selective water translocation. Densely packed molecular/supramolecular AWCs may lead to an understanding of how such selective channels can be optimized at the nanoscale and incorporated within polymeric matrixes to facilitate ultrafast and highly selective transport of water at the macroscale through innovative membranes.

## **1.2. Aquaporins and Porins**

Natural systems developed over millions of years to evolve complex devices to translocate species across the cell membrane.<sup>7, 8</sup> Biomimicry is a scientific strategy behind mimicking the well-tuned natural processes. Thus, nature should provide answers for efficient desalination.

### **1.2.1. Natural and artificial aquaporins**

The most important natural water channels, the AQPs, are known to transport  $\approx 10^8\text{--}10^9$  H<sub>2</sub>O s<sup>-1</sup> channel<sup>-1</sup> with perfect rejection of ions.<sup>1, 9-16</sup> Structural information encoded within the hourglass-shaped structure of AQPs controls the efficient transport of water (Figure 2 a): i) its selectivity filter (SF) with a



narrowest diameter of 2.8 Å is adapted enough for water translocation, but restrictive to block the hydrated cations  $>3$  Å, which is reinforced through electrostatic repulsion in the aromatic and arginine (ar/R) constriction region;<sup>1, 12-16</sup> ii) a supramolecular water wire self-assembly occurs in the SF, adopting a bipolar orientation in two halves from the centre to the entries of the pore. This creates an inversion central region, breaking the water wire dipoles, which inhibits the proton transport;<sup>12</sup> iii) the positive charges at the entrance of the channel AQPs could further enhance the water transport activity owing to the reduction in the collective hydrogen bonding lifetime of the single water file;<sup>13</sup> iv) water molecules form a “self-protecting” dynamic superstructure toward the exclusion of other species like H<sup>+</sup> or OH<sup>-</sup>. Their inclusion favors disruption of the constitutive hydrogen-bonding network and energetically perturb the water self-assembly.<sup>14</sup>

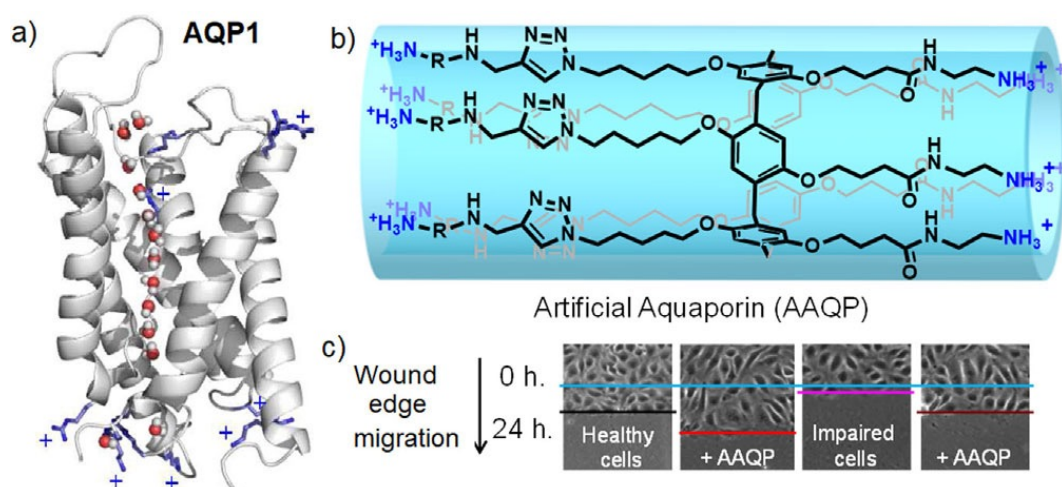


**Figure 2.** Structure of a) natural AQP showing the water wire channels as well as the positive charge at the entry and in the narrowest region of the pore and b) artificial AQP channels AAQP, with positive charges at the entry of the pillararene pore. c) Representative images of wound healing analysis of Chang cell assays showing wound edges (blue line) at 0 h (up) and 24 h (down) in the presence of AAQP (1.0 mm).

AQPs are essential for biological systems for their important function of regulating cellular osmotic pressure. The loss of function of AQPs could lead to some serious diseases, such as congenital cataracts and nephrogenic diabetes

insipidus. Because of the simple passive and non-gating water transport mechanism of AQPs, it was also envisioned that the AWCs might be used to treat the AQP-related diseases by making the channels work as efficiently and selectively as AQPs in cell membranes. This possibility was firstly tested and achieved very recently by Hou and co-workers.<sup>17</sup> They have developed AAQP, an artificial AQP, which can work in cell membranes to allow its water permeability to reach that of AQPs with simultaneous ion and proton exclusion (Figure 2 b,c). The elegant AAQP was constructed from tubular pillararenes, mimicking the key structural features of AQPs, including their positively charged channel entrances, hourglass-like cavity, single water wire file, and small constrictions to generate steric hindrance. It was revealed that the channel is functional in the cell membranes in a unimolecular manner, which is the best way to attain high channel stability. Interestingly, the high-water permeability of AAQP enables the restoration of the water transport of cells containing function-lost AQPs. Remarkably, the artificial AQP-mediated water transport can restore wound healing of the impaired cells that contain function-lost AQPs. This excellent work not only provided a simple model for chemists to investigate the influence of channel structures on the water transport and ion exclusion activities at the Ångstrom scale, but also developed a new strategy for the treatment of AQP-related diseases.

### **1.2.2. Porins**

A significant number of studies have been dedicated to porins, which are a class of protein aquapores that form larger pores to transport ions, water, or small molecular solutes. Their structures show that their large pores are filled with clusters of water molecules in interaction with the walls of the porin pores. The structures of bacterial Omp32 anion selective porin or OmpF porin present wider nanopores with larger diameters of approximately 10–20 Å.<sup>15</sup> Their pores are completely filled with water molecules. Molecular simulations show that

water diffuses more slowly than in bulk, probably owing to the strong structuration of water within the pores, similar to what is observed in carbon nanotubes (CNTs).<sup>16</sup>

### **1.2.3. Bio-assisted protein-based membranes**

During the last two decades, researchers around the world have been trying to capitalize on the unique properties of the AQPs in the design of bio-assisted membranes for desalination.<sup>18-22</sup> The natural proteins embedded in host polymeric membrane matrixes are active components for the selective transport of water. The question of how the AQPs and artificial host matrixes can efficiently work together has been answered.<sup>18-22</sup> Natural or engineered AQPs were first investigated by embedding them in protective amphiphilic polymersomes. They exhibit a productivity of  $167 \mu\text{m s}^{-1} \text{bar}^{-1}$ , that is, approximately two orders of magnitude more than a typical RO membrane with a productivity of  $1 \mu\text{m s}^{-1} \text{bar}^{-1}$ .<sup>22</sup> However, a such improvement in polymersomes permeability at the nanoscale does not have the same impact when translated to the macroscopic membrane films embedding AQPs. Currently, the market of biomimetic membranes is represented by AQP membranes, in which natural AQPZ are embedded with proteo-liposomes and immobilized in the reverse osmosis (RO) polyamide matrix by interfacial polymerization (Figure 3 a).<sup>23-29</sup> For these membranes, the major drawbacks are the protein stability and the vesicles rupture under the harsh conditions of SWRO ( $\geq 35000$  ppm NaCl, 70 bar), which ultimately result in lower salt rejection values compared with marketed state-of-the-art RO membranes.<sup>23-28</sup> Most importantly, today no readily usable AQP-based membrane exists for SWRO desalination.

Overall, the challenges to use AQPs as the selective elements in bio-assisted membranes incorporating AQPs relate to their:

- i) Long-term stability when embedded in vesicle-polyamide (PA) thin layers, which was demonstrated;<sup>27, 28</sup>
- ii) Bio-related processing and low resistance to SWRO (65 bars and high salinity 35 000 ppm NaCl) or BWRO (15–20 bars and salinity 3000 ppm NaCl) unconventional requirements; low pressure 5–10 bars RO applications are usually reported for these membranes. Under SWRO conditions an AQP embedded membrane shows a water flux of around 20 L m<sup>-2</sup> h<sup>-1</sup>, at least half of that observed for a SWRO membrane under the same conditions ( $\approx 1\text{--}2 \text{ L m}^{-2} \text{ h}^{-1} \text{ bar}^{-1}$ )<sup>20</sup> and 98.5 % NaCl rejection at 55 bar when using 32 000 mg L<sup>-1</sup>, meaning a 91% increase of the water flux is seen compared with the reference thin-film composite (TFC) membrane without AQPs.<sup>24</sup>
- iii) Production—membrane proteins are challenging to mass produce; however, production of 45 g AQP/100 L fermentation has been reported;<sup>23-28</sup>
- iv) The area of AQPs (9.0 nm<sup>2</sup>) is very large in relation to the size of its Å-scale active water channel;<sup>1, 12-16</sup>
- v) AQPs present a significant flux per channel, but not an acceptable permeability per active area, with a 25%<sup>25</sup> to 83.6%<sup>26</sup> to 166%<sup>27</sup> increase in permeability for low-pressure (LP)RO or BWRO planar or hollow fiber AQP membranes, compared with the reference traditional TFC membrane without AQPs. Unfortunately, the NaCl rejection reached 97–98.5%, which remains a critical problem and defects created at the interfaces between vesicles and PA still have the leading performances of these RO membrane for desalination.

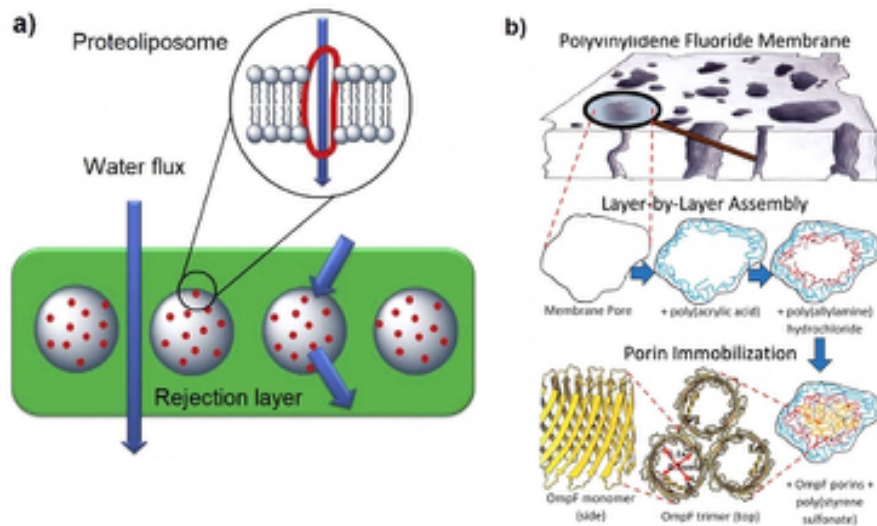


**Figure 3.** a) AQP-based biomimetic membranes, showing the AQP incorporation within proteoliposomes dispersed in a polyamide membrane.<sup>25</sup> b) Layer-by-layer organization of polyelectrolytes into a PVDF membrane and stable immobilization of OmpF.<sup>29</sup>

Other “porins” with larger pores of 7–11 Å, that is, OmpF protein trimeric channels from *Escherichia coli*, have been immobilized within poly(vinylidene fluoride) (PVDF) microfiltration membranes by polyelectrolyte layer-by-layer (LBL) self-assembly (Figure 3 b).<sup>29</sup> The OmpF-selective membranes reject 84% of 0.4–1.0 kDa neutral organics over ionic solutes, which are transported two times faster than through traditional nanofiltration membranes. Different to AQPs membranes, the OmpF membranes are exceptionally stable, with constant high permeability and recovery for more than 160 h of filtration. This approach has been extended for larger proteins as building blocks with well-defined channel sizes that control the separation performances:  $\approx 300\text{--}1000 \text{ L h}^{-1} \text{ m}^{-2}$  at 1 atm and low solute concentrations  $\approx 20 \text{ mg L}^{-1}$ , with organic solute rejection similar to commercial nanofiltration (NF) membranes.<sup>30</sup>

On this basis, the scalability of the biomimetic membranes for future applications in desalination will need careful consideration to improve water/salt selectivity and to make use of the high permeance values of these

membranes under BWRO industrial conditions, that is, using at least 15 bars and salt concentrations  $> 2 \text{ g L}^{-1}$ .<sup>31</sup> The OmpF membranes with higher porosity than AQP membranes allow an impressive increase of water permeability with sharp and clear cut-offs at the nanometric level, but they are failing in terms of the water/ion selectivity required for desalination. The optimization of both water permeability and selectivity remains important and is still a challenge when specific industrial operating conditions with concentration polarization challenges are employed.

### **1.3. Artificial Water Channels: Synthetic AQPs**

As an alternative, chemists have attempted to replicate natural systems by using synthetically accessible and low-cost materials with an elegant combination of simplicity and utility. Indeed, biomimicking the biostructures of proteins at the molecular level is an important challenge. A possible alternative to AQPs are the synthetic biomimetic AWCs. A similar impact of water conduction activity obtained with natural AQPs can be obtained by using simpler artificial compounds displaying selective and high water transport functions like the natural ones.

The first biomimetic I-quartet channel was discovered in 2011<sup>32</sup> whereas the term “Artificial Water Channels” was first proposed in 2012 independently by Barboiu and Hou.<sup>33, 34</sup> Amazingly, there was little or no systematic progress in the area of AWCs before this period. Within this context, biomimicking AQPs by using AWCs is an important endeavour from a) a fundamental science perspective, related to the deeper understanding of the relationship between the structural organization of water and its dynamic translocation under confined conditions through the channels and from b) an applied science perspective, as AWCs might have a huge impact on improving water filtration

performances by using natural strategies to implement new paradigms for desalination.

Highly permeable AWCs may provide a route to producing efficient biomimetic membranes at laboratory and industrial levels, particularly for desalination. AWCs offer an effective and economic alternative to natural water channels.<sup>32-</sup>

37

AWCs are synthetic ion-rejecting channels mainly consisting of unimolecular or self-assembled columnar structures, presenting a central hydrophilic or hydrophobic pore, to ensure the directional translocation of water, and an outer hydrophobic exterior matching the lipid bilayer or polymeric membrane environment.<sup>33, 34</sup> AWCs offer the unique opportunity to set up high-performance systems with both high water permeability and completely selective rejection of ions. Recent results have made possible the production of AWCs, which feature efficient permeability of water, but their selectivity issues remain, in most cases, still unsolved. Having an artificial nature, the AWCs present the following important advantages:

- i) their structural design is simple and they are easily tunable to be optimized for higher water recognition;
- ii) they can be synthesized in large amounts and at lower cost than biological counterparts;
- iii) their engineering scale-up becomes simpler and more reproducible without bio-related processing steps, they should be easy to include in membranes without the use of specific additives;
- iv) they are robust and stable when incorporated into membranes. We know that the active cross-section area of the AWCs is less important than that of AQPs, which increases their permeability per membrane surface area compared with AQPs membranes.

Most of the studies in the last decade on AWCs describe their synthesis, molecular modelling, and transport performances through lipid bilayers. Naturally, the inherent comparison of AWCs performances with those of AQPs appear to be restricted to specific research during that period. The water permeability of AWCs is from 2–3 orders of magnitude lower than that of AQPs, to similar or even better permeability for some AWCs; however, a major drawback is their low ion selectivity. Meeting the standard natural performances, discrete AWCs that are more stable for easy processing,<sup>38</sup> although their incorporation into large-scale membranes strongly depends on material design considerations and fabrication methods.<sup>29</sup> Among the promising material design approaches, Langmuir–Blodgett, vesicle rupture, pore-spanning, layer-by-layer techniques or interfacial polymerization have been used to form biomimetic membranes.<sup>39</sup> All these methods employ reconstituted channels in lipid bilayers or block copolymers as a strategy to preserve their integrity and functionality in the host membrane, which poorly rejects hydrophobic solutes. However, the formation of defects along with the functional modifications of the channels suggest that direct introduction approaches must be explored to better control the interactions and the compatibility between functional water channels and the surrounding membrane matrices.<sup>40, 41</sup>

The specific structural design of selective channels is highly related to how we are able to construct such structural behaviors, to be able to selectively pump water like AQPs.<sup>32-34</sup> Therefore, there are incentives to further include these specific selective filter sites, which will increase the chances to attain improved selectivity for water through selective recognition and not by size restriction, rejecting ions and neutral molecules.

The two main challenging future endeavors for AWCs are:



- i) to design perfect highly selective channels rejecting salts, allowing the preferential translocation of water;
- ii) the scale-up of the AWCs from the molecular level to that of macroscopic materials and meter-scale membranes.

Although this has been already proved by using AQPs,<sup>23-28</sup> no result has been reported yet on using the AWCs within active layers for industrial membranes. To compete with RO technology, the current industrial standard for water desalination, water flux and salt rejection for AWC membranes need to be as high as that of natural AQPs. Higher flux values do not have an economic impact on desalination performances; however, it may improve the quality of the produced water by removing pretreatment processes. Preparing adaptive polymeric membranes able to host active AWCs are crucial for the future of the next generation of membranes for desalination. The performances of lipidic or amphiphilic polymeric membranes as well as the classical RO polyamide materials can be diminished by organic molecules or surfactants present in water.<sup>40, 41</sup> For the AWCs, the use of amphiphilic additives is not a necessary option. However, the study of AWCs in bilayer membranes is particularly important, as their performances need to be referenced to those of AQPs. Industrial application will certainly require polymers with a good mechanical robustness better than the lipid bilayers. It is important to know that the self-assembly and dynamics of channels may strongly depend on the nature of the hosting matrix and certainly their performances would depend on their interactions with external matrices. The structural self-organization of the channels within the polymeric matrix and that induced by external stimuli leads to variable materials with interesting adaptive behaviors, which cannot be totally predicted. In such scenarios, the predictive self-assembly of the channels in different matrixes cannot be described by specific chemical engineering equations. Chemistry would better mediate on a molecular level the dynamic self-assembly of addressable low-size domains of aggregated channels adapting

their structure to external matrix environments, toward the construction of macroscopic films in which domains of percolated channels might exist.

### **1.3.1. AWCs with hydrophilic pores**

According to the central pore structural features, AWCs can be mainly classified into two categories: AWCs with hydrophilic or hydrophobic pores. In this section, we review the hydrophilic AWCs, referring to the bottom-up supramolecular approach towards transmembrane biomimetic AQPs architectures.<sup>42</sup> Back in 2011, our group discovered the Imidazole-quartet (I-quartet) channels, resulting from the self-assembly of alkylureido-imidazoles **HC6H** or **HC6-8**, mutually stabilized by the scaffolding urea and imidazole-water hydrogen-bonding (Figure 4 a-f).<sup>32</sup> I-quartet water channels with 2.6 Å pores are dimensionally similar to AQPs channels. They form oriented dipolar water wires inside the tubular I-quartet architectures.<sup>36</sup> The inner water wires form through hydrogen-bonding with the channel wall and with vicinal water molecules, reminiscent of the encapsulated water molecules in AQPs. It is important to note that I-quartets are easily crystallized from ethanolic aqueous solutions, by selectively encapsulating only water molecules, even in the presence of salt solutes of other water mimics like sugars or glycerol. Based on these specific recognition effects, the I-quartets entirely exclude the incorporation of hydrated ions, favoring the transport of water and H<sup>+</sup>.

Water/proton transport activities of I-quartets through bilayer membranes decrease substantially with the decreasing length of the grafted alkyl chain: **HC8** >> **HC6** > **HC4** (Figure 4 g, h).<sup>36</sup> Indeed, the tail length of octyl chains seems to be optimal. The increased permeability of the I-quartets is the result of their hydrophobic stabilization, based on the optimal interaction of the hydrophobic tails with the bilayer membrane.

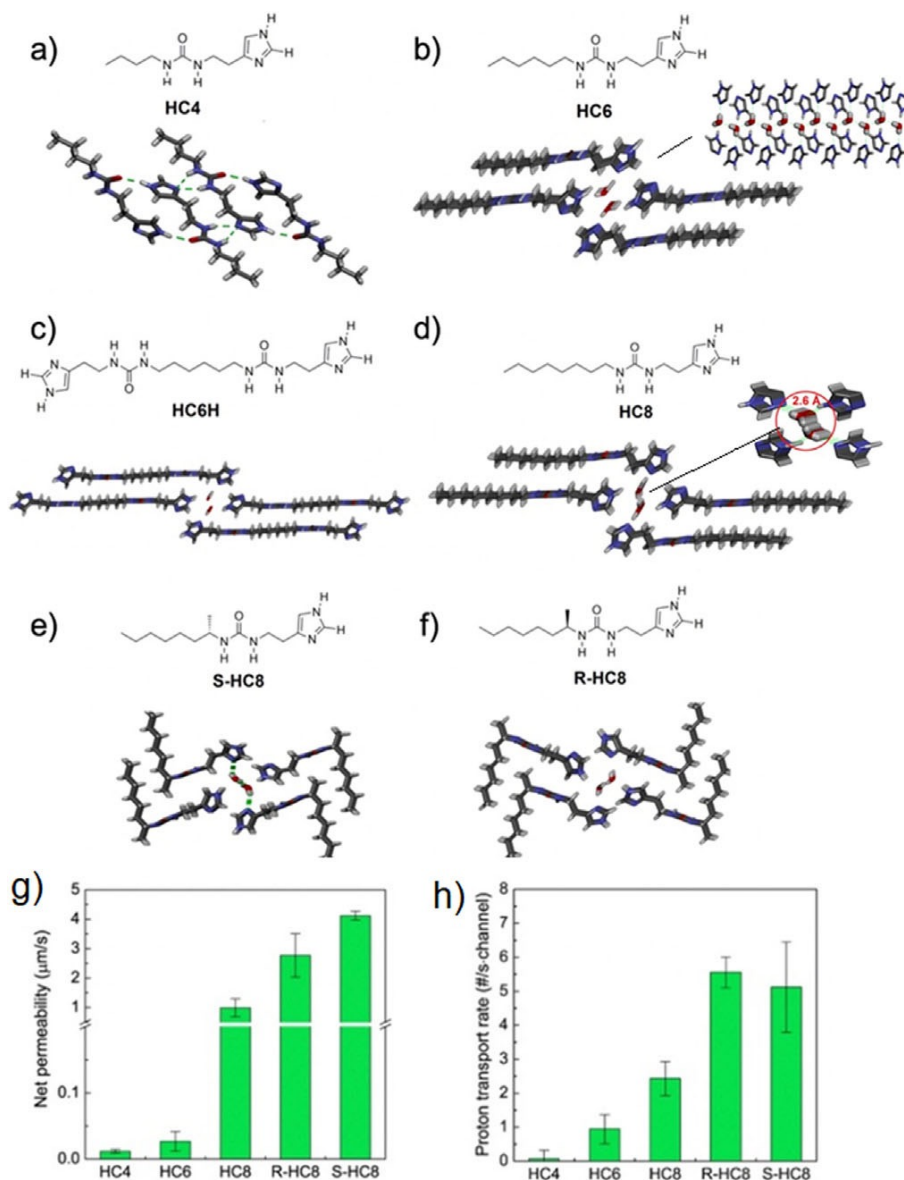


**Figure 4.** Top views of the I-quartet channels observed in their X-ray single-crystal structures of a) **HC4**, b) **HC6** (detail of the side view of the channel), c) **HC6 H**, d) **HC8** (detail of the top-view of the channel), e) **S-HC8**, and f) **R-HC8**. g) Water permeabilities and h) proton conducting rates of I-quartet channels.<sup>36</sup>

Molecular modelling studies show that permeation of water by I-quartet-by-I-quartet jumps is not linear in time, with intermediate steady states, between dynamic translational states on the timescale of ns (Figure 5 a).<sup>43</sup>

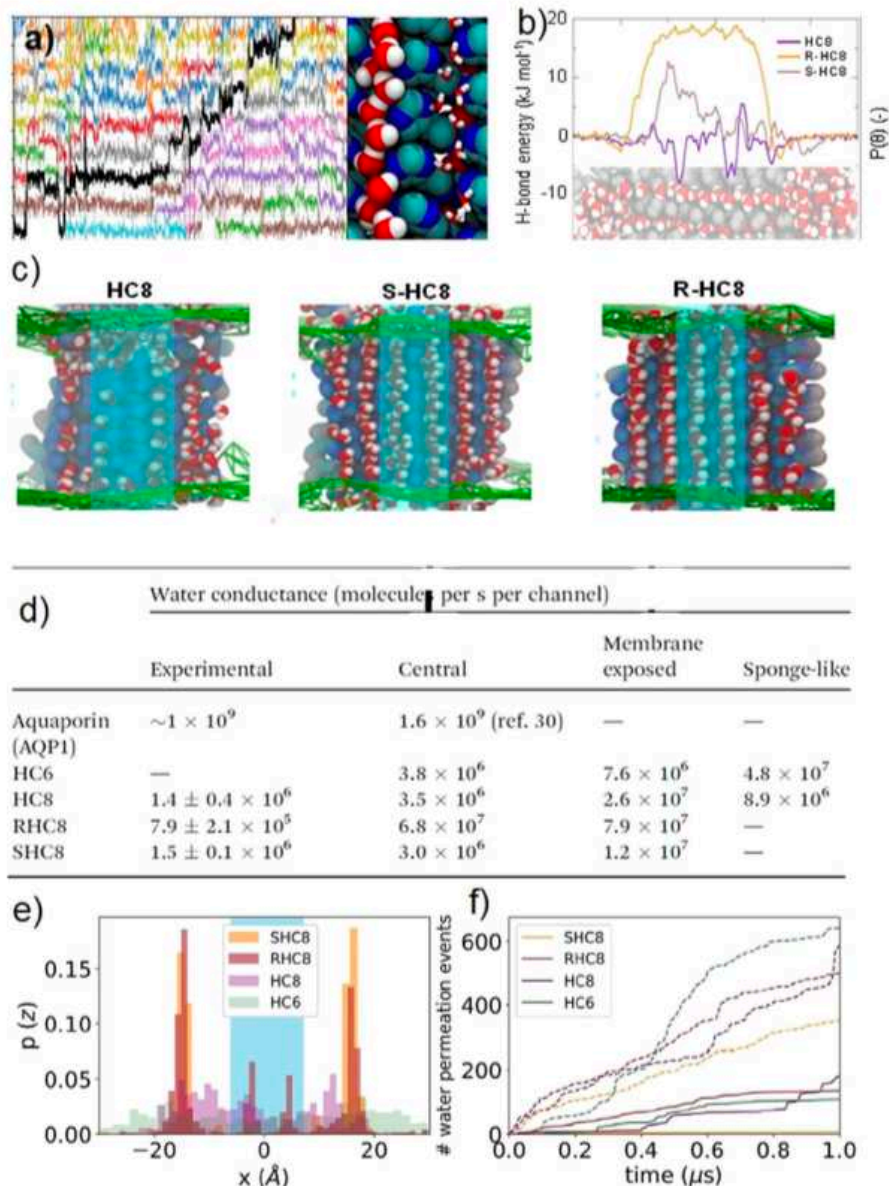


**Figure 5.** a) Dynamics of single water wires within I-quartet **R-HC8**. The  $z$  axis position of water molecules versus time are displayed with different colors in individual channels.<sup>43</sup> b) Hydrogen-bond energy depicting the stabilization of water molecules within the two central water channels relative to bulk water.<sup>44, 45</sup> c) MD simulations emphasizing the well-structured water wires in central channels and less structured sponge-like clusters of lateral membrane exposed channels. d) Experimental and simulated water conductance of central water wire channels or of lateral sponge-like channels. e) Water permeation in the crystal patch: the cyan region emphasizes the central water channels, protected from the lipids, whereas the white background displays membrane exposed lateral channels. f) Total transport of water molecules in both central pores shown as plain lines and lateral channel indicated as dashed lines, outward and inward directions across the membrane.<sup>43</sup>

The computed patterns for chiral **R-HC8** and **S-HC8** channels have similar hydrogen-bonding patterns with 1.4–1.6 water–water hydrogen bonds and 1.6–1.8 hydrogen bonds linking water molecules to the imidazoles. With only 0.9 hydrogen bonds, the water–water cohesion is lower for **HC8**. The total number of hydrogen bonds for the water molecules reaches up to 3.2–3.4 hydrogen-bonds, very similar to a value of 3.2 hydrogen-bonds observed for bulk water.

The hydrogen bonds in I-quartets exhibit a strong and constant stabilization of the water molecules of almost 20 kJ mol<sup>-1</sup> for **S-HC8** or 13 kJ mol<sup>-1</sup> for **R-HC8**. (Figure 5 b).<sup>44, 45</sup> As a consequence, the water–water and water–channel interactions are both important to stabilize self-protecting selective water superstructures within the channels. The friction related to hydrogen bonding events is not much stronger than that observed for bulk liquid water and, once stabilized within the channel, these structures do not need supplementary energy to translocate through the whole length of the channels. Ion transport through the bilayers incorporating the I-quartets was assessed by using HPTS (8-hydroxy-1,3,6-pyrene trisulfonate) fluorescence assays. No response versus the control experiment in the absence of the channels and no variation of the transport activity with variable concentration of I-quartets was observed. The reflection coefficient for NaCl, calculated as the ratio of the permeabilities in the presence of NaCl to that of sucrose osmolytes, (113 ± 15 %, n = 4) indicates that the I-quartet channel achieve almost total salt rejection in a bilayer membrane.<sup>36</sup>

The I-quartets show an experimental water permeation rate of  $1.4 \times 10^6 \text{ H}_2\text{O s}^{-1} \text{ channel}^{-1}$ , determined in bilayer membranes with a hydrophobic thickness of 3.5 nm and using 200 mM NaCl (8.3 bar) as the draw solution. From the single-crystal structures,<sup>36</sup> the density of I-quartet channels is  $3.3 \times 10^{17} \text{ channels m}^{-2}$ , which multiplied with  $1.4 \times 10^6 \text{ H}_2\text{O s}^{-1} \text{ channel}^{-1} = 4.6 \times 10^{23} \text{ H}_2\text{O s}^{-1} \text{ m}^{-2} = 49.2 \text{ L m}^{-2} \text{ h}^{-1}$ . Given an osmotic pressure of 8.3 bar (200 mM NaCl), the permeability

of water through a 3.5 nm bilayer membrane is  $P = 5.92 \text{ L m}^{-2} \text{ h}^{-1} \text{ bar}^{-1}$ . Molecular modelling simulations have been performed on four I-quartet channels embedded within a bilayer membrane for water permeation (Figure 5 c). The inspection of the I-quartets at the end of the MS shows that lateral channels tend to form a sponge-like, slightly disordered hydrogen-bonded water network, whereas the central channels remain very close to the water wires organization initially observed in the single-crystal structure. Water permeation prominently occurs at the most exposed membrane lateral positions, corresponding to slightly disorganized sponge-like structures. Compared with experimental single-channel permeances (Figure 5 d–f), MS values have the same magnitude for central channels ( $3 \times 10^6 \text{ H}_2\text{O s}^{-1} \text{ channel}^{-1}$ ) with the exception of **R-HC8** ( $6.8 \times 10^7 \text{ H}_2\text{O s}^{-1} \text{ channel}^{-1}$ ), which features a one order of magnitude higher permeation rate.<sup>43</sup> The sponge-like membrane exposed lateral channels that display higher conductance ( $2.6\text{--}7.9 \times 10^7 \text{ H}_2\text{O s}^{-1} \text{ channel}^{-1}$ ). Following the previous calculation, the sponge-like structures will allow a permeability of  $P = 334 \text{ L m}^{-2} \text{ h}^{-1} \text{ bar}^{-1}$  through a 3.5 nm bilayer membrane for an osmotic pressure of 8.3 bar (200 mM NaCl), which is almost two orders of magnitude higher than the permeability of crystal water wires superstructures ( $P = 5.92 \text{ L m}^{-2} \text{ h}^{-1} \text{ bar}^{-1}$ ). These values are superior to those observed for BWRO membranes ( $2\text{--}8 \text{ L m}^{-2} \text{ h}^{-1} \text{ bar}^{-1}$ ),<sup>20</sup> which are usually operated at slightly higher pressure (15–18 bars) and higher saline concentrations.

These experimental and theoretical studies are of tremendous importance as they show the adaptive behavior of water inside the channels depending on the environmental conditions, for which the structures of supramolecular self-assembled water are well defined. This reveals the stable selective water translocation pathways on the microsecond timescale; they can form water wires and sponges, which are still ion selective and more permeable. This

discovery opens up new avenues in AWCs research, towards the construction of selective membranes for desalination.<sup>46</sup>

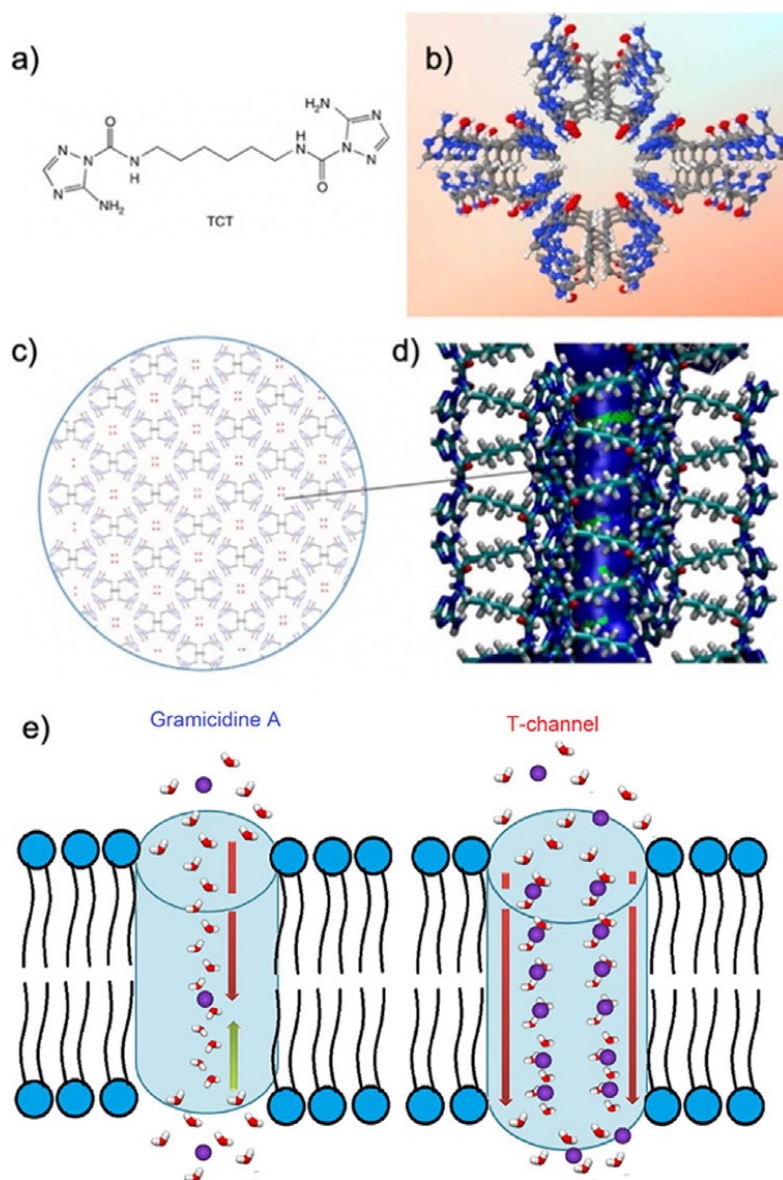


**Figure 6.** a) Chemical formula of bola-amphiphilic triazole **TCT**. b) Crystal structures of the T-channel. c) Top and d) side view in ball and stick representations of the T-channel. e) Single channel or multi-channel water/ion translocation through Gramicidin A and T-channels, respectively.

Although these I-quartet channels may be considered as highly water-permeable in bilayer membranes, they might behave differently when embedded in glassy polymeric membranes. Although single-crystal structures

and MS simulations provide interesting information about their bilayer organization,<sup>36, 43-45</sup> a detailed investigation must be reserved for further experimental work to construct highly selective polymeric membranes for desalination.

In 2014, our group reported a simple artificial T-channel, formed by self-assembly of bola-amphiphilic triazoles, mimicking the natural Gramicidin-A (gA) functions (Figure 6).<sup>37</sup> Water/proton permeability with large open channel conductance states and cation versus anion selectivity of the T-channel were revealed by molecular simulations and conduction assays. The water transport rate obtained for the T-channel ( $k = 6.0 \times 10^{-4} \text{ min}^{-1}$ ) is fifty times greater than the blank experiment ( $k = 1.3 \times 10^{-5} \text{ min}^{-1}$ ). Similar to gA, the cation transport activity sequence of the T-channel is  $\text{Li}^+ < \text{Na}^+ < \text{K}^+ < \text{Rb}^+ \ll \text{Cs}^+$ , and the  $\text{Na}^+$  transport activity ( $k = 2.7 \times 10^{-3} \text{ min}^{-1}$ ) is two orders of magnitude higher than that of the  $\text{Cl}^-$  transport rate. Different from the cation-water single wire within the gA channel, the conductance of ions along the T-channel is surrounded by double file dipolar water wires, which might also inspire novel strategies for ion conducting processes.

Aquafoldamers are hydrogen bonding induced, helically folded aromatic molecules, which possess a channel interior containing pyridine N- and amide N—H-atoms, as hydrogen bond acceptors and donors for water recognition. The helically folded aquapentamer (Figure 7 a) accommodates solvent or water molecules in a tubular architecture with the size of approximately 2.8 Å, similar to the narrowest pore of AQPs. In 2012, Zeng et al. introduced the “sticky ends” strategy to electrostatically connect the helical two ends of short oligomers, which complementarily pile up and overlap to form one-dimensional helices embedding  $\text{H}_2\text{O}$ ,  $\text{MeOH}$ , and  $\text{CH}_2\text{Cl}_2$  (Figure 7 b).<sup>47</sup> Importantly, oriented water wires self-assemble within the pores of the helical stacks, which are first found



to effectively transport protons with an efficiency comparable to that of Gramicidin A (Figure 7 c).<sup>48</sup> These results highlight the important role played by proton gradients, producing dynamic osmotic gradients, acting to synergistically facilitate the transport of confined water wires through the membrane. A series of crystallographic structures of aquafoldamers demonstrated a preferential recognition of the water versus methanol with a selectivity of about 17.7.<sup>49</sup> Importantly, the approximately 20% enlargement in Å-scale pore volume results in the formation of dynamic, more fluidic pores, which induce a 15-fold enhancement of water transport. This sheds light on the fastest AWC to date, which is able to translocate water at a rate of  $\sim 3 \times 10^9 \text{ H}_2\text{O s}^{-1} \text{ channel}^{-1}$  with a high rejection of NaCl and KCl.<sup>50</sup>

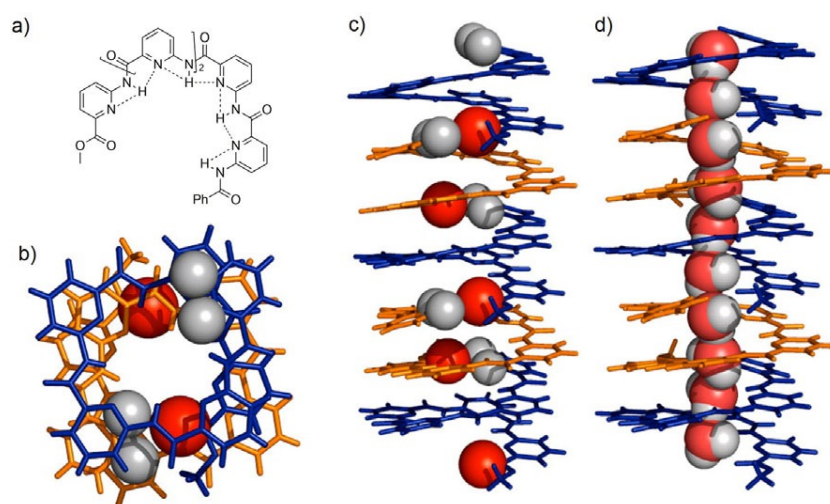


**Figure 7.** a) Chemical formula of aquafoldamer. b) Top view and c) side view of chiral helical stacks of the same handedness and d) adapted aquapores with high water permselectivity.

As for sponge-like I-quartet channels, a relaxed structure of the aquafoldamers, preserves the continual structure of water and induces higher and controlled diffusion of water inside the pore. The optimal deviation from the thermodynamically stable single-crystal structures is one of the most important features of synthetic water channels, synergistically improving water permeability and selectivity. The tedious synthetic route and relatively low

general synthetic yield of the aquafoldamers limit their large-scale production. Their cylindrical shape would cause the functional channels to be oriented within the membrane scaffold, which would not constitute an insurmountable problem.

### 1.3.2. AWCs with hydrophobic pores

Inspired by the structure of the AQPs, hydrophobic NPA motifs allowing rapid permeation of water in the form of hydrogen-bonded single-file chains of water have been developed.<sup>51</sup> We present in the following part a few examples of biomimetic hydrophobic AWCs that serve the purpose of fast water conduction.

#### Carbon nanotube porins

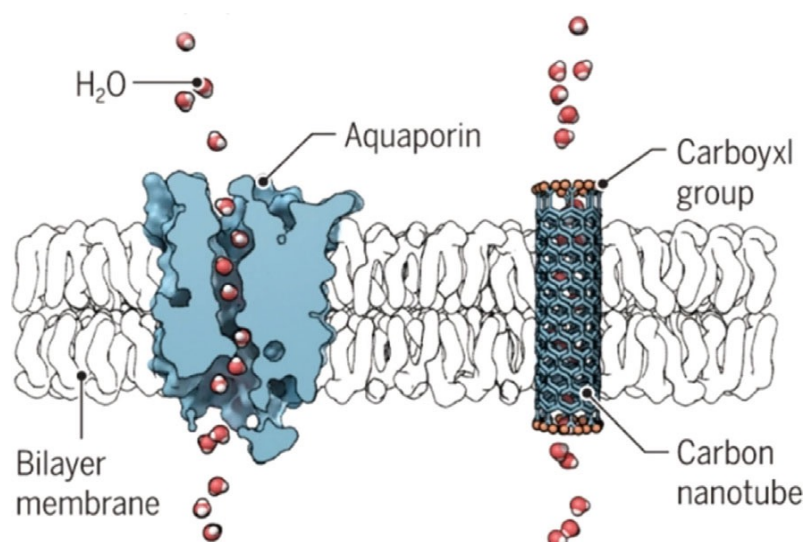


**Figure 8.** Schematic analogy between AQP and CNTs in lipid bilayers for the fast transport of water.<sup>52</sup>

Faster water transport through hydrophobic carbon nanotubes (CNTs) seems to be counter-intuitive at first when compared with the structure of natural AQPs (Figure 8). Over the past 20 years, extensive investigations have confirmed that water fills the CNTs interiors,<sup>53-55</sup> and ultrafast flow of water has been reported,<sup>56-59</sup> following the predictions from simulations.<sup>60</sup> Water weakly interacts with the hydrophobic walls, which contributes to its nearly frictionless

transport, whereas the selectivity may be sterically controlled.<sup>61</sup> Ultrashort carbon nanotube porins (CNTPs)<sup>62</sup> have been successfully embedded in lipid bilayers by Noy et al. and they demonstrated ultrafast proton permeability under nanoconfinement in CNTPs.<sup>63</sup> Later, the same group reported that narrow nCNTPs (6.8 Å diameter) transport  $2.3 \times 10^{10}$  H<sub>2</sub>O s<sup>-1</sup> channel<sup>-1</sup> ( $6.8 \times 10^{-13}$  cm<sup>3</sup> s<sup>-1</sup>), whereas wide wCNTPs (13.5 Å diameter) had a single channel water permeability of  $1.9 \times 10^9$  H<sub>2</sub>O s<sup>-1</sup> channel<sup>-1</sup> ( $5.9 \times 10^{-14}$  cm<sup>3</sup> s<sup>-1</sup>).<sup>64</sup> This is the first and a unique example of AWCs exceeding the water permeability of AQPs with osmotic pressure. Unfortunately, this incredible water transport rate, unlike AQPs, is not supported by their efficiency, as CNTPs were still able to transport ions. Reverse potential measurements revealed that the nCNTPs had a  $P_{K^+} = P_{Cl^-}$  selectivity of 184 at seawater salinity level, indicative of possible desalination applications. Later, Freger estimated the water salt permselectivity of nCNTPs to be  $10^4$ , one order of magnitude lower than the target set for the desalination membranes.<sup>65</sup>

### Dendritic dipeptides

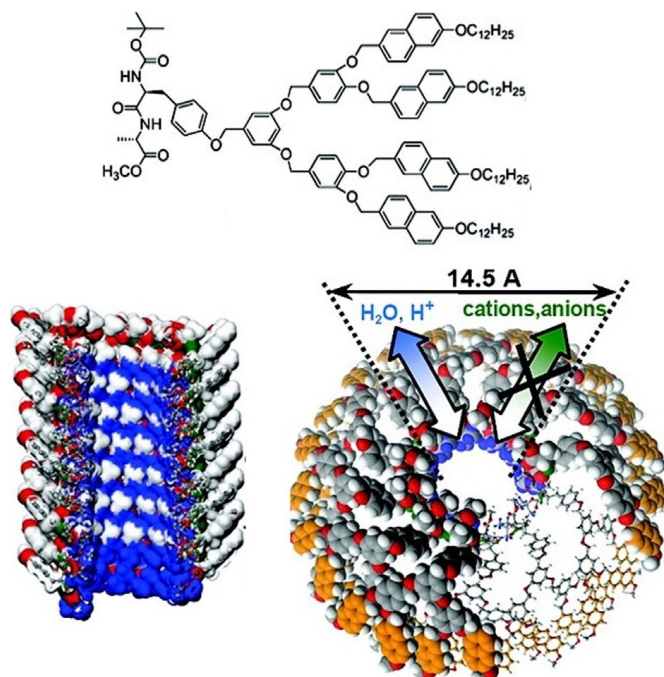


**Figure 9.** Chemical structure of dendritic dipeptide and the side and top views of their self-assembled helical tubular porins.<sup>66</sup>

Percec et al. reported synthetic dendritic dipeptides that are able to self-assemble through multivalent hydrogen bonding into helical porins with an inner pore of  $12.8 \pm 1.2 \text{ \AA}$ .<sup>67</sup> Their conformation is controlled by the solvent and the dendrons were found to be able to assemble as hydrophobic pores for proton translocation through a Grotthuss mechanism, for which water must mediate the proton migration.<sup>68</sup> Three years later, water transport driven by osmotic pressure through more stable pores assembled from modified dendrons was directly observed by the same group, making this the first example of AWCS in bilayer membranes (Figure 9).<sup>66</sup> Additionally, multinuclear NMR studies showed no transport of monovalent ions  $\text{Li}^+$ ,  $\text{Na}^+$ , and  $\text{Cl}^-$ . However, there is no elucidation of the mechanism for the selective exclusion of these monovalent ions by the  $14 \text{ \AA}$  pores.

### Shape-persistent macrocyclic channels

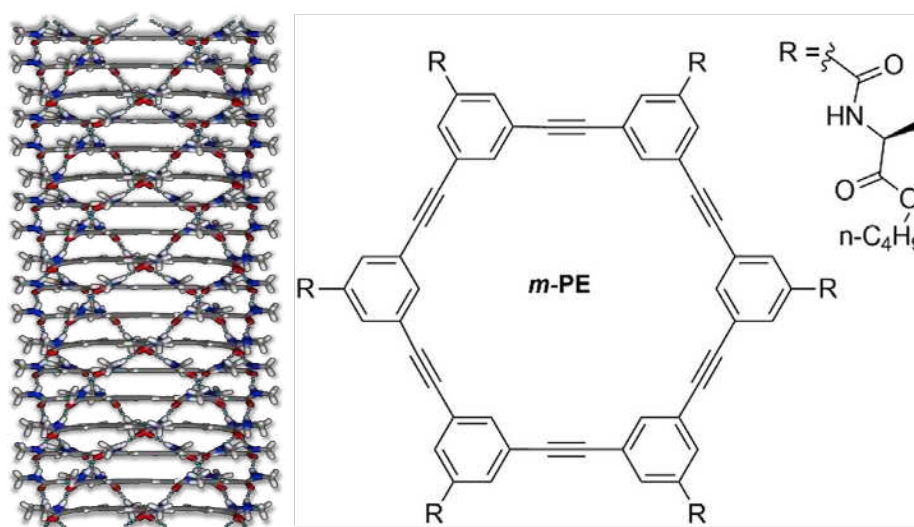


**Figure 10.** Molecular structure of *m*-oligophenylethynyl *m*-PE macrocycles and the helical stack of the macrocycles demonstrated from the simulation.<sup>69</sup>

A series of hexa(*m*-phenylene-ethynylene) ***m*-PE** macrocycles were synthesized by Gong et al.<sup>69</sup> with the aim of developing well-defined synthetic self-assembled nanopores, thanks to the multiple hydrogen bonding and  $\pi$ - $\pi$  stacking interactions between the side chains (Figure 10).

The helical stacked macrocycle has a defined pore with an internal van der Waals diameter of 6.4 Å. Direct measurement of water transport by stopped-flow assays demonstrated faster net flow of water across the lipid bilayer under osmotic stress, with an estimated water permeability of  $4.9 \times 10^7 \text{ H}_2\text{O s}^{-1} \text{ channel}^{-1}$ , representing about 20% that of AQP1. Besides that, the single-channel conductance exhibited a remarkable  $P_{\text{H}^+}/P_{\text{Cl}^-}$  selectivity of over 3000. A significant lower permeability for  $\text{K}^+$  compared with  $\text{H}^+$  is also inferred. These self-assembled synthetically accessible, robust nanostructures are good alternatives to hydrophobic pores such as CNTs and pillar[5]arenes.<sup>70</sup>

### Hydrazide-appended pillar[5]arene

First introduced in 2008, by Ogoshi et al.,<sup>71</sup> pillararenes represent an interesting class of symmetrical synthetic hosts with electron-rich interiors, variable size, and versatile functionality of their cavity.<sup>72</sup>

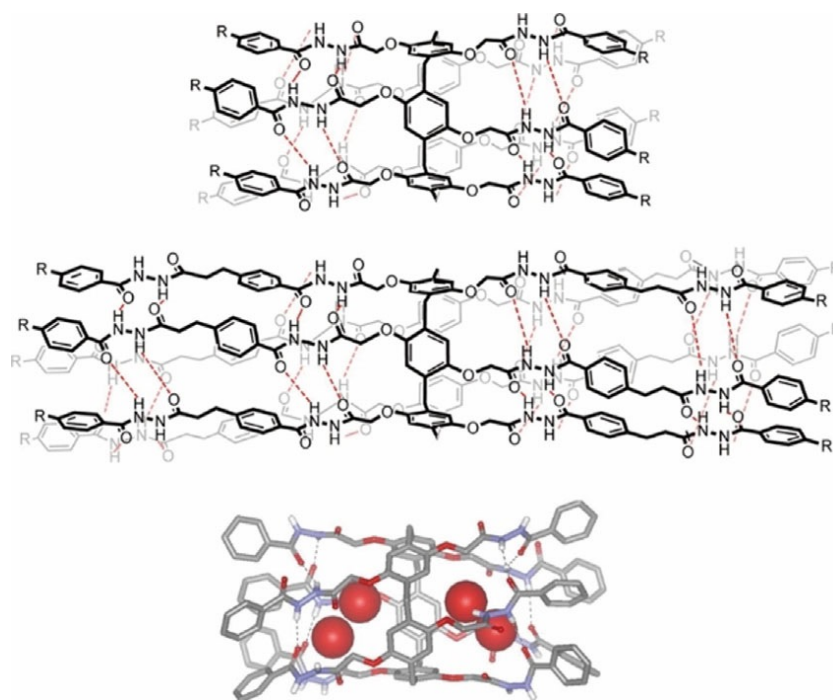


**Figure 11.** Chemical structures of hydrazide-attached pillar[5]arene mono-molecular channels, and single-crystal structure of the shorter pillar[5]arene counterpart.<sup>34</sup>

The formation of single-crystal nanotubes of pillar[5]arene (PA[5]) under the template effect of water wires<sup>73</sup> inspired the pioneering work by Hou and his group in which several AWCs based on PA[5] were developed.<sup>74</sup> By connecting two PA[5] with a suitable aliphatic arm, they created a H<sup>+</sup> channel with higher permeability than the original monomers (Figure 11).<sup>34</sup> The isotopic effect shows that the proton transport proceeded through the Grotthuss mechanism.<sup>68</sup> Functional hydrazide PAH[5] derivatives were then synthesized. Their tubular structures form through intramolecular hydrogen-bonding of the hydrazide subunits. The single-crystal structure of the shortest PAH[5] derivative revealed that the water was absent in the hydrophobic region, resulting in encapsulated water dimers within the hydrazide side chain rather than water wires.<sup>34</sup> Their permeability was estimated to be  $8.6 \times 10^{-10} \text{ cm s}^{-1}$  or  $40 \text{ H}_2\text{O s}^{-1} \text{ channel}^{-1}$ . The PAH[5] showed no proton transport, yet clear hydroxide transport was monitored by HPTS assay, corroborating the presence of truncated water wires in the crystal structures. Together with I-quartet channels, the hydrazide PAH[5] channels are the first examples of synthetic molecules mimicking the water transport function of AQP, while rejecting all ions/no proton (I-quartet) or only proton/no ion (PAH[5]). No other channel before these systems has been considered as artificial AQPs. They are pioneering in the field and despite their lower permeability, they still represent unique examples with interesting selectivity compared with the other novel, more permeable, but non-selective AWCs more recently developed.

### **Peptide-appended pillar[5]arene**

Hou et al.<sup>75</sup> later developed a second-generation pillararene PAP[5] with unimolecular channels, first used for the selective transmembrane transport of chiral amino acids. Instead of hydrazide, the authors appended hydrophobic phenylalanine side chains to improve their insertion rate (Figure 12 a). The change resulted in a distinct boost in performance within two orders of magnitude to the permeability of AQP1, as the water permeability reaches  $1.0 \times$

$10^{-14} \text{ cm s}^{-1}$  ( $3.5 \times 10^8 \text{ H}_2\text{O s}^{-1}$ ) as determined by stopped-flow light-scattering measurements in cooperation with Kumar group. Interestingly, hexagonal supramolecular arrays of PAP[5] can be easily packed in lipid bilayers on samples of 100 nm scale. Molecular simulations show that partial (80%) permeation events can be detected through water-filled PAP[5] channels, whereas the remaining 20% of them were devoid of water or were blocked by lateral phenylalanine chains, present within the pillararene core. Moreover, the PAP[5] (4.7 Å) cannot reject ions and showed the cation selectivity follows the trend:  $\text{NH}_4^+ > \text{Cs}^+ > \text{Rb}^+ > \text{K}^+ > \text{Na}^+ > \text{Li}^+ > \text{Cl}^-$ . The molecular cutoff of 420 Da of the PAP[5] channel is not suitable for selective removal of salts and other small molecules required by desalination.

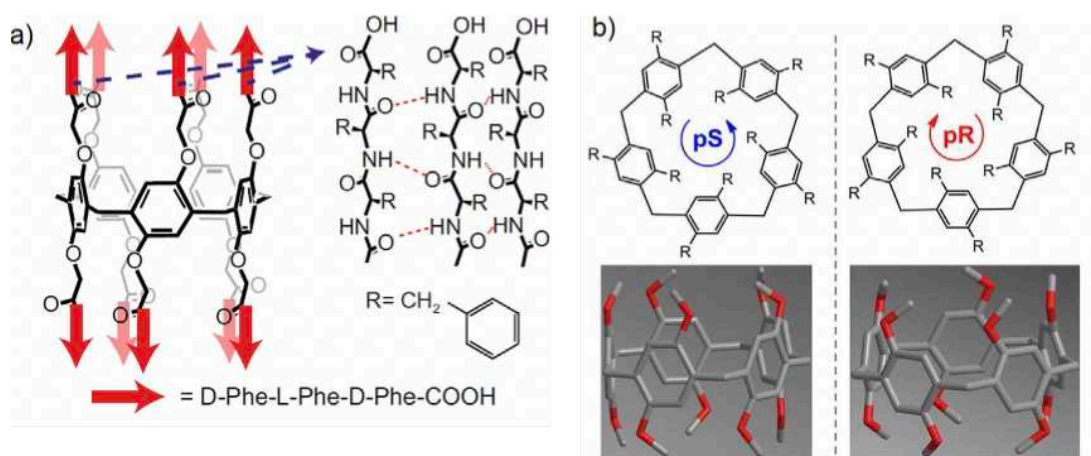


**Figure 12.** a) Chemical structure and molecular modeling representation of the Phe<sub>3</sub>-pillar[5]arene PAP[5] channel.<sup>76</sup> b) The chiral pS and pR-isomers of PAP[5] pillar[5]arene.<sup>77</sup>

A subsequent study by Kumar et al.<sup>78, 79</sup> demonstrated the successful PAP[5] incorporation into block-copolymer membranes with a substantial increase of pore (channel) packing density of approximately  $4.2 \times 10^5 \mu\text{m}^{-2}$  (determined again at nm scale films), which are a few orders of magnitude higher than CNTs packing or than polymeric iso-porous membranes. Micrometric PAP[5]/polybutadiene-polyethylene-oxide 2D sheets have been prepared and stacked by polyelectrolyte PEI insertion. The bioinspired composite

membranes displayed an over 10-fold permeability ( $\approx 65 \text{ L m}^{-2} \text{ h}^{-1} \text{ bar}^{-1}$ ) enhancement over other commercial membranes ( $4\text{--}7 \text{ L m}^{-2} \text{ h}^{-1} \text{ bar}^{-1}$ ) and a sharp, selective molecular weight cutoff of  $\approx 500 \text{ Da}$ . Although PAP[5] channels showed a ion selectivity  $\text{K}^+/\text{Cl}^-$  ratio of 10, and a permselectivity of 0.83, similar to CNTs channels,<sup>64</sup> high NaCl rejection cannot be observed at the macroscopic level of membranes during hydraulic pressure assisted filtration tests. This difference is indicative of the very difficult challenges in translating the molecular transport properties of single channels to macroscopic materials with a similar filtration performance. A better nano-distribution of channels and physical and chemical mismatch with the material matrix may allow the perfect membrane homogeneity to be reached.

Wang and co-workers<sup>77</sup> prepared a structurally similar PAP[5], and isolated two diastereoisomers, namely pS and pR-PH (Figure 12 b). Although pR-PH had a single-channel water permeability of  $3.9 \times 10^{-14} \text{ cm}^3 \text{ s}^{-1}$ , its isomer displayed no water transport activity. Molecular simulations show that the PheAla side chain of pS-PH blocks the channel in contrast to a well-maintained open channel state for pR-PH, through which water permeates in single-file fashion. In addition, the authors prepared a supported lipid membrane with the incorporation of the pR-PH channels, which had improved LPRO performance in terms of both water nanofiltration flux ( $\approx 30 \text{ L m}^{-2} \text{ h}^{-1} \text{ bar}^{-1}$  compared with  $\approx 17 \text{ L m}^{-2} \text{ h}^{-1} \text{ bar}^{-1}$  of the control membrane) with a low salt rejection of  $\approx 88 \%$   $\text{Na}_2\text{SO}_4$ , although NaCl rejection is not reported.

### **Peptide-appended hybrid[4]arene**

To optimize the water/salt selectivity of the AWCs, novel synthetic channels with pore sizes smaller than PAP[5] ( $\approx 4.7 \text{ \AA}$ ) have been developed. Hou and Kumar<sup>80</sup> have reported a new four-membered pillararene PAH[4] by grafting eight D-L-D-PheAla tripeptides to construct a pore of  $\approx 3 \text{ \AA}$ , an optimal pore size for selective water permeation (Figure 13). Quantitative measurements have



shown that  $3.7 \times 10^9$  water molecules pass through PAH[4] every second (or  $1.1 \times 10^{-13} \text{ cm}^3 \text{ s}^{-1} \text{ channel}^{-1}$ ) at  $25^\circ\text{C}$ , which is comparable to the value of AQP1. The exceptionally high water permeability becomes apparent especially when the density of the channel reaches the threshold between 20 to 45 channels per vesicle. Indeed, molecular dynamics (MD) simulations reveal that PAH[4] assembles into the lipid membrane, but, unlike PAP[5], it does not provide a straightforward inner pathway for water molecules. The cooperative water-permeating pathways were formed between the PAH[4] molecules, giving insights into the water permeation through cluster-forming AWCs. An energy barrier as low as  $3.6 \text{ kcal mol}^{-1}$  for the water permeation was observed for PAH[4] when using PEG osmolyte, indicative of single-file water transport. This impressive result confirms that enhanced water permeability can be observed and is confirmed when water cluster-forming organic nano-architectures self-assemble in lipid membranes. I-quartet sponge channels<sup>43, 46</sup> or porous organic cages (POCs)<sup>81</sup> have been previously described in 2018 and 2019, which feature the rather unique enhanced permeability of water clustering conduction systems.

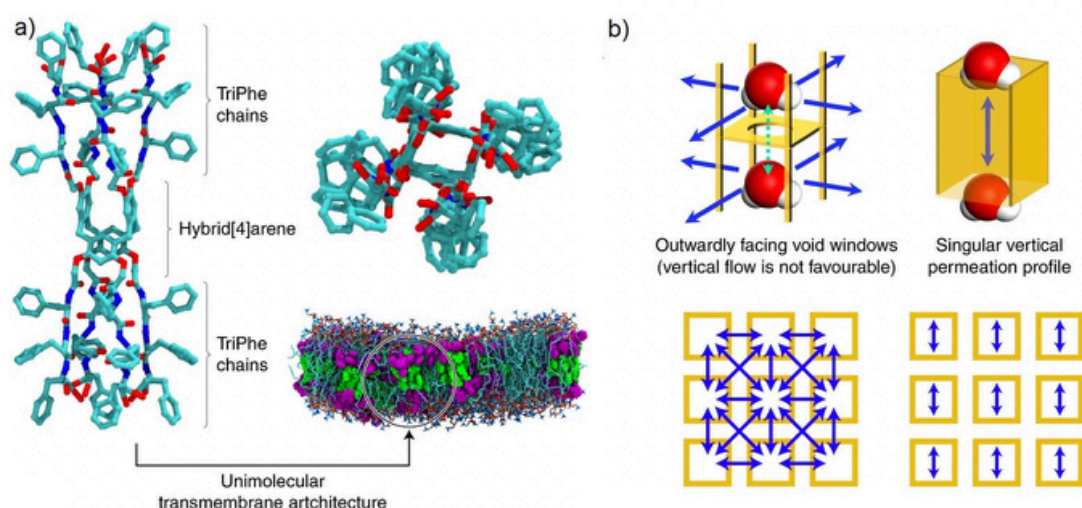


**Figure 13.** a) Molecular model of the peptide-pillar[4]arene, PAH[4]. b) Proposed water permeation conduits (blue arrows) between PAH[4] (left) and traditional AWC (right) configuration.<sup>80</sup>

A significantly low  $\text{Cl}^-$  permeability of  $9.5 \times 10^{-23} \text{ cm}^3 \text{ s}^{-1}$  was determined by using a low concentration salt osmolyte, which helps PAH[4] to achieve a  $\approx 10^9$  water/salt selectivity in bilayer membranes, far beyond the requirements for desalination membranes by at least four orders of magnitude.

However, it is worth mentioning that a few obstacles need to be overcome first to realize the projected performance of PAH[4] in bilayer membranes toward macroscopic membranes for RO desalination at high pressure. Nevertheless, the concept of engineering transient cluster/sponge membrane water channels is clearly evolving, as it considerably expands the range of possibilities for the specific design of macroscopic RO membrane materials embedding AWCs.<sup>46, 82</sup>

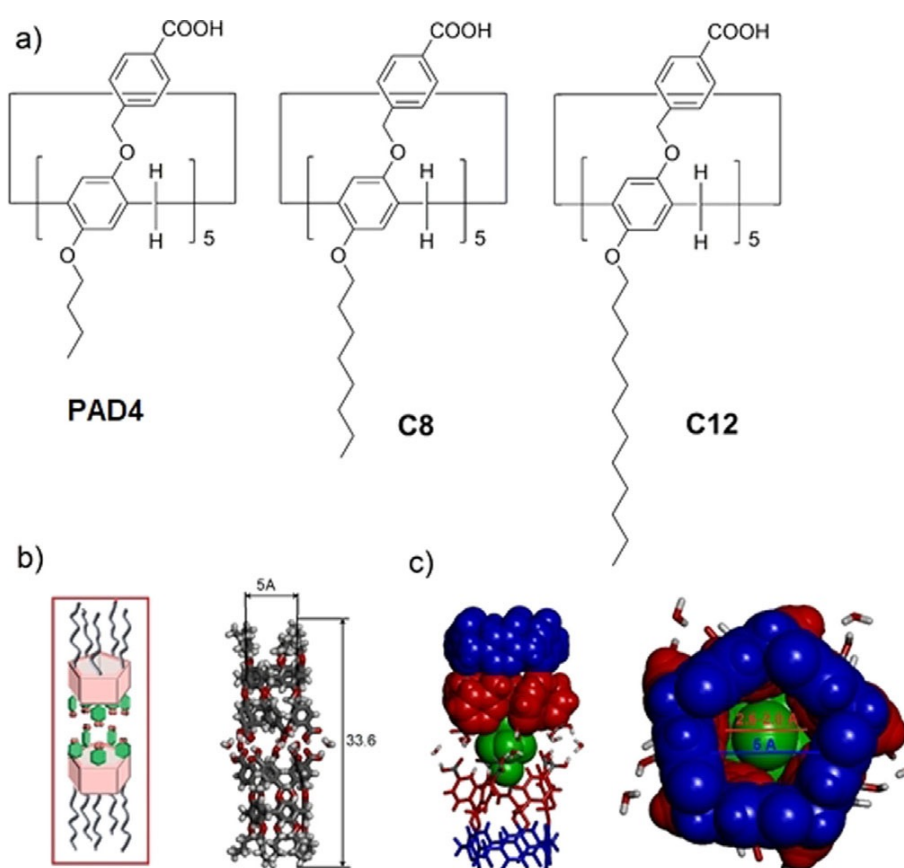


**Figure 14.** a) Structures of peralkylcarboxylate-pillar[5]arenes PAD4, PAD8, and PAD12. b) Crystalline solid-state structure showing the dimeric channel structure of 34 Å length and c) a variable pore geometry composed of pillar[5]arene (blue) of 5 Å diameter and of the narrowest twisted carboxy-phenyl pore of 2.8 Å diameter (red).

Our group very recently discovered that modification of the rims of pillar[5]arene (5 Å diameter) may lead to the narrowest constriction pores of 2.6–2.8 Å diameter within the same structure (Figure 14),<sup>83</sup> similar to the selective hourglass structure of AQPs.<sup>1</sup> This affords control of the translocation by size restriction along the resulting PAD channels at the selectivity filter level. The water permeability of  $\approx 10^7$  water molecules  $s^{-1}$  channel<sup>-1</sup> is only one order of magnitude lower than that of AQPs and importantly they reject alkali cations. Different from I-quartets where, during their translocation, the water molecules interact along the whole structure of the channel, for the PAD channels, whose interactions are mainly related to the narrowest pore structure, are large enough for the water molecules to pass, being restrictive enough to block the passage of hydrated Na<sup>+</sup> or K<sup>+</sup> cations.

#### **1.4. Biomimetic AWC membranes for desalination**

The AWCs optimized in terms of high permeability and ion rejection in bilayer membranes would be naturally used as active components for the preparation of biomimetic membranes for desalination. The next important steps are related to maintain the channel activity observed at the single-channel level in bilayer membranes and to obtain a high channel density on the surface of the membrane support. The major challenge relates to the strategy used for scaling-up functional high-density membranes of meter-scale filtration surface areas.

Several ideal designs may be proposed for producing membranes, including AWCs physically included in thin-layer polymers or the chemical synthesis of polymers from AWC monomers suspended as thin layers over planar or hollow fiber supports (Figure 15 a). An interesting alternative is to generate polymeric cross-linked networks from AWC monomers, further cast on support membranes (Figure 15 b).

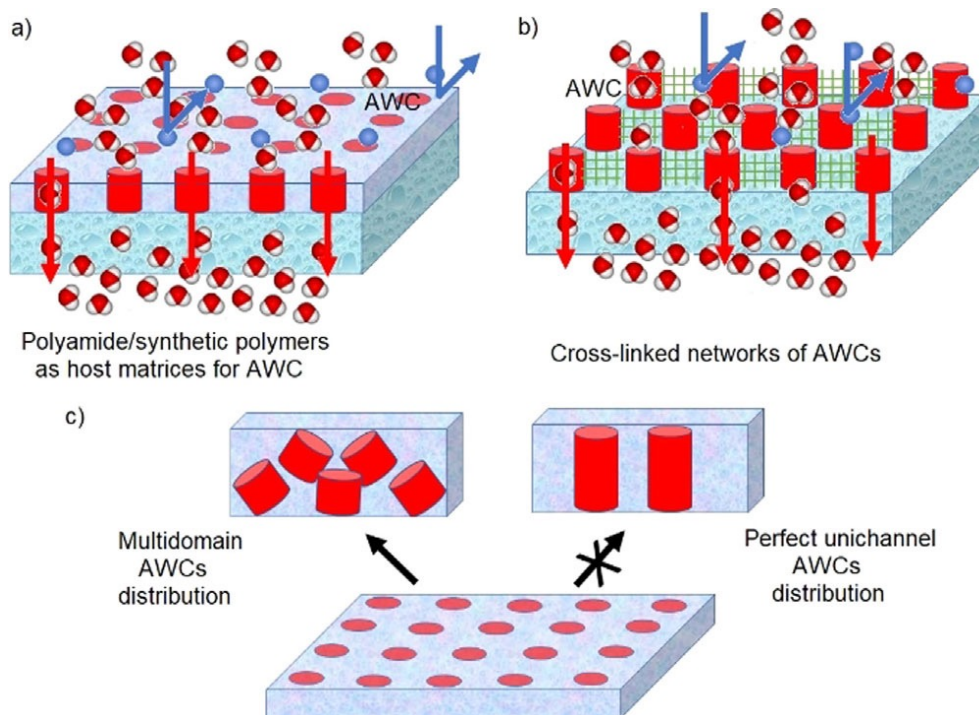


**Figure 15.** Direct inclusion of AWCs in biomimetic membrane supported thin layers. a) Polyamide or polymeric host matrices for AWCs or cross-linked networks of AWCs for scalable membranes. b) Translocation/high salt ejection governed by water–ion interactions within selective AWC superstructures. c) Multi-domain versus uni-channel distribution of AWCs at the nanometric scale within macroscopic thin-layer membrane materials.

One clear advantage is that the AWCs may be more readily stabilized than AQP in the membrane structures. In other words, one might expect the use of AWCs to lead to the formation of highly permeable layers with excellent salt rejection.

We already have the experience for upscaling the supramolecular channels to macroscopic membranes.<sup>84-88</sup> Accordingly, several synthetic routes have been reported and it is impossible to achieve a perfect channel alignment from one side to the other side of the active layer without using a directional scaffolding matrix (Figure 15 c). Multi-domain AWCs distributed with different orientations can be “frozen” in a macroscopic matrix at the nanometric level by compacting directional columnar self-assembled channels, as a straightforward

upscaling approach to high-performance, next-generation, thin-layer membranes for desalination.<sup>89, 90</sup>

The desalination performances of AWCs are mostly related to important challenges in translating the transport properties of the molecular self-assembled channels to performant meter-scale membrane materials and filtration modules needed for desalination. We postulated that one of the creative strategies for addressing the scale-up challenges is to combine the thin-film composite TFC polyamide membrane, known for its scalability by integration within a typical roll-to-roll processing system with the highly permeable and selective AWCs. An easy strategy is to directly incorporate dense networks of AWCs while forming the selective layer of the membrane. Polyamide layers already used for RO filtration are highly desired as the mechanically stable matrix to support the AWCs.

Thin-film composite membranes (TFCs) are currently implemented in the water desalination industry and around 90% of used membranes are based on RO/NF technologies.<sup>56-59</sup> In the early steps, interfacial polymerization (IP) was used to form a TFC thin layer on the support, but this method was not used in industrial fabrication until Cadotte<sup>91</sup> proposed polyamide (PA) composite membranes with an interestingly high flux, which could be prepared by interfacial polymerization of amines and acylchlorides and with varying performances that can be easily reproduced on the laboratory and industrial scales.

With the development of nanomaterials, thin-film nanocomposites (TFNs) have been prepared by the physical inclusion of solid nanocrystals into the polyamide layer of a TFC membrane. Several types of zeolites, metal–organic frameworks (MOFs) or cellulose nanocrystals have been used to obtain TFNs.<sup>56-59</sup> By using a modified strategy, distinct nanocrystalline sponge I-quartet AWCs

have been incorporated into the polyamide layer (Figure 16 a). A typical AWCs incorporation experiment to obtain nanocrystals uniformly disposed in a PA layer includes the injection of a colloidal solution of the I-quartets in a water-miscible solvent on the top of the membrane. The diffusion of organic solvent into the water causes the AWCs to crystallize and to be incorporated within the PA network during the IP process as shown by SEM images of the reference (Figure 16 b) and hybrid (Figure 16 c and d) membranes. To optimize the incorporation, the defect control has been achieved by varying the nature and the concentration of the PA monomers to ensure readiness for the membrane fabrication process. Such uniform distributed nanocrystals of AWCs have been in situ generated from a soft colloidal solution, which forms solid particles during the IP process. This induces a gentle adaptive generation of densely packed AWCs homogeneously integrated within a PA matrix, which allowed us to identify new membranes that remarkably outperform the control TFC polyamide RO membranes in the treatment of saline feed SWRO streams. The AWC-RO biomimetic membrane of 70 cm<sup>2</sup> provides 99.5–99.8 % rejection of NaCl with a water flux of 75 L m<sup>-2</sup> h<sup>-1</sup> (LMH) or 2.8 LMH bar<sup>-1</sup> (+ 200 % larger than a commercial TFC membrane) at 65 bar applied pressure with 35 000 ppm feed solution for seawater desalination. This is more than 75% higher than the flux with equivalent solute rejection and a noteworthy 12% reduction of the required energy compared with the application of current approaches of commercial membranes for desalination.<sup>92</sup>

These initial studies on the inclusion of AWCs within the PA structure led to a greater fundamental understanding of how selective pores can be optimized at the nanoscale to facilitate ultrafast and highly selective transport of water, mainly occurring through selective channels, and to minimize the translocation of ions and molecules bypassing the membrane. The selective highly permeable AWCs will play the role of active and selective relays for which the water transport occurs at the nanometric level with higher permeability up to 300

LMH bar<sup>-1</sup> (see above) compared with the self-supportive PA membrane for which the permeability is 1 LMH bar<sup>-1</sup> (Figure 16 e). The overall permeability of the hybrid AWC-PA membrane will be composed from slow (PA) and very fast (AWC) permeating regions, contributing to a higher overall permeation through nano-dispersed AWC-PA membranes.

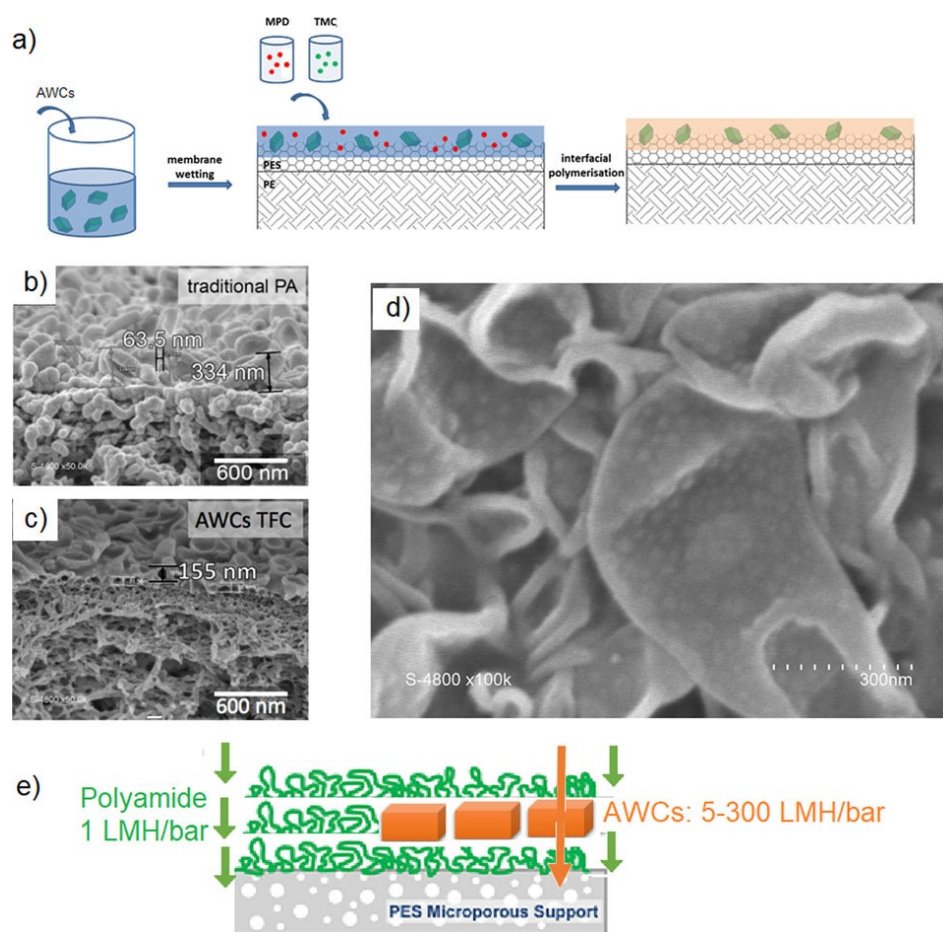


**Figure 16.** a) AWC-PA membrane fabrication with incorporated AWC nano-particles of I-quartets in PA thin-layer membranes. Representative scanning electron microscopy (SEM) micrographs of b) the top view of the surface of a traditional TFC membrane, c) TFC polyamide with AWCs, and d) cross-sectional view of the uppermost active layer including distributed AWCs—as the white dots of 30–40 nm, uniformly included in the PA layer. e) Composite PA-AWC layers with slow (PA) and very fast (AWC) permeating regions contributing to a higher permeation observed through hybrid AWC-PA membranes.<sup>92</sup>

## 1.5. Conclusions

The first identification of AWCs by our group in 2011<sup>32</sup> opened the door to new fundamental and applicative research on AWCs similar to natural ones.<sup>6, 35, 42</sup> We speculated at this time that biomimetic AWCs might have important influences to increase the driving force of the transport by using natural paradigms and improve the water desalination performances. All these assumptions have been confirmed during the last decade.

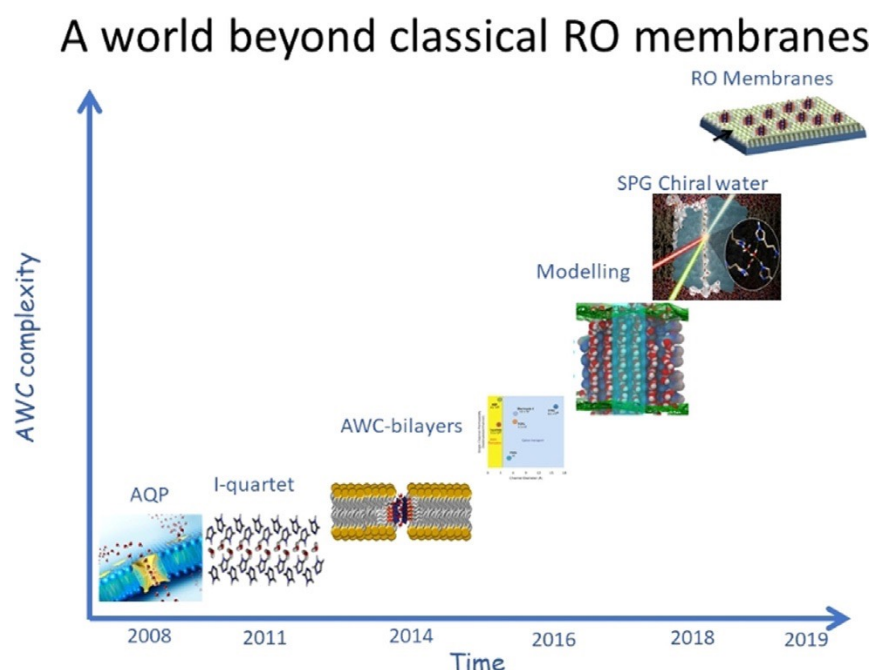


**Figure 17.** AWC development with time towards highly competitive RO membranes for desalination.

AWCs present robust and functional structures (2011), which selectively conduct water through bilayer membranes (2014) and could support better scale-up and mechanical requirements (2016), which seem to not impair the restructuring of AQP biomimetic membranes (2018, Figure 17). Learning from the complex structures of biological channel proteins is an important endeavor (2018). Different scientific advances including novel experimental and modeling experiments complement each other for a more complete



understanding of water structuration and mechanisms to translocate water in biological pathways (2018).

Straightforward easy preparation of AWCs—artificial AQPs—give rise to novel strategies towards the design of highly selective membranes that transport water with unprecedented fluxes (2019). The next step is related to up-scaling membrane and related filtration processes.

Owing to the notable simplest structural features of AWCs, for instance, most of them are low-cost and synthetically accessible with chemical robustness, they have been identified as promising alternatives to AQPs. Over the past decade, the increase of relevant publications in this field clearly indicates that the design and functionalization of various AWCs offers flexible avenues toward mimicking natural AQPs in bilayer membranes (Table 1).<sup>45</sup>

Again, efforts to achieve both high selectivity and reasonable permeability is an important challenge for AWC channels. High permeability has been mostly achieved by designing tubular structures with inner hydrophobic pores for water translocation. During the last decade, the permeation through such frictionless inner pores was increased by 2–4 orders of magnitude, reaching that of natural AQPs. The water-over-ions selectivity of such hydrophobic AWC systems can be achieved only with dimensionally limited pores ( $d < 0.6$  nm). For larger AWCs porins, the rearrangements at the entry of the pore control the hydrogen bonding of water patterns that further self-assemble with variable density in the available inner space of the porin.<sup>64</sup>

**Table 1.** Overview of the features of current reported water channels.<sup>45</sup>

Channel	Type of pore	Pore size	Water permeability/selectivity
AQPs <sup>1</sup>		2.8 Å	$4 \times 10^9$ H <sub>2</sub> O s <sup>-1</sup> channel <sup>-1</sup> , high selectivity for water, rejects all ions and H <sup>+</sup>
I-quartet <sup>32, 33, 36</sup>		2.6 Å	$1.5 \times 10^6$ H <sub>2</sub> O s <sup>-1</sup> channel <sup>-1</sup> , high selectivity for water, rejects all ions except H <sup>+</sup>
T-channel <sup>37</sup>	hydrophilic	$\approx 2.5-4$ Å	No water permeability reported, enhanced conduction states for alkali cations and protons
Aquafoldamer <sup>93</sup>		$\approx 2.8$ Å	$3 \times 10^9$ H <sub>2</sub> O s <sup>-1</sup> channel <sup>-1</sup> , rejects all ions except protons
nCNTPs <sup>64</sup>		6.8 Å	$2.3 \times 10^{10}$ H <sub>2</sub> O s <sup>-1</sup> channel <sup>-1</sup> , rejection of ions only in dilute solutions
wCNTPs <sup>64</sup>		13.5 Å	$1.9 \times 10^9$ H <sub>2</sub> O s <sup>-1</sup> channel <sup>-1</sup> , no selectivity for water
dendritic dipeptide <sup>66, 67</sup>		$12.8 \pm 1.2$ Å	No reported permeability, rejects ions except H <sup>+</sup> , attributed to hydrophobic entrance effects
<i>m</i> -PE <sup>69</sup>	hydrophobic	6.4 Å	$4.9 \times 10^7$ H <sub>2</sub> O s <sup>-1</sup> channel <sup>-1</sup> , no water selectivity, a remarkable $P_{H^+}/P_{Cl^-}$ selectivity over 3000, and a significantly lower conduction for K <sup>+</sup> compared with protons
PAH[5] <sup>34</sup>		4.7 Å	40 H <sub>2</sub> O s <sup>-1</sup> channel <sup>-1</sup> , no selectivity for water, transports alkali cations but no conduction for protons
PAP[5] <sup>76</sup>		4.7 Å	Swelling: $3.5 \times 10^8$ H <sub>2</sub> O s <sup>-1</sup> channel <sup>-1</sup> ; shrinking: $3.7 \times 10^6$ H <sub>2</sub> O s <sup>-1</sup> channel <sup>-1</sup> , no selectivity for water, good activity for alkali cations
PAH[4] <sup>80</sup>		$\approx 3 \text{ Å} \times 5 \text{ Å}$	$3.7 \times 10^9$ H <sub>2</sub> O s <sup>-1</sup> channel <sup>-1</sup> , $\approx 10^9$ water/salt selectivity

Note: I-quartet: imidazole-quartet; nCNTPs: narrow carbon nanotube porins; wCNTPs: wide carbon nanotube porins; *m*-PE: hexa(*m*-phenylene ethynylene); PAH[5]: hydrazide-appended pillar[5]arene; PAP[5]: peptide-appended pillar[5]arene; PAH[4]: peptide-appended hybrid[4]arene.

There is only the steric confinement that controls the supramolecular water recognition, whereas water self-clustering cannot totally avoid the ion permeation through AWCs, impeding their permselectivity. Several AWCs demonstrated a preferential recognition of water over ions or small molecules through specific hydrogen-bonding of water with a high selectivity factor near to perfect rejection.<sup>33, 34, 47-50</sup> The optimal binding of water in interaction with the recognition groups on the inner surface of the channel is an important prerequisite for its selection. Importantly, the deviation from the thermodynamically stable, hydrogen-bonded, strongly confined structures observed within the single-crystal structures toward more relaxed molecules of supramolecular aggregates, which generate more relaxed and highly permeable water clusters, is one of the most important discoveries that can be considered for the simultaneous improvement of both water permeability and selectivity. Relaxed I-quartet sponges,<sup>43, 46</sup> aquafoldamers,<sup>50</sup> or porous organic cages (POCs)<sup>94</sup> as well as confined pillararene networks are representative examples that have been independently reported during the last three years (2018–2021).

The key structural features that enable efficient translocation of water are high permeation through hydrophobic channels for fast water translocation, whereas molecular recognition selectivity filters (SF) are the prerequisite for high selectivity. The AWCs reported to date use water binding sequences along the entire pore length, rather than only in a very specific selectivity filter region like natural porins for which the selection occurs only in the very short SF region.

Thus, AWCs, which are fundamental in nature, will allow us to develop new knowledge on the natural principles of selective water translocation and gain a greater understanding of the fabrication of highly competitive biomimetic membranes for desalination. The thin-layer polyamide membranes, used for water desalination since 1972, have improved dramatically over the last 60

years. However, their low-resolution structure and the transport mechanism are still poorly understood. The ultimate performance of a membrane is usually determined by an increased flux (or permeance) owing to the introduction of defects in the membrane structure lowering the selectivity, which is always decreasing.

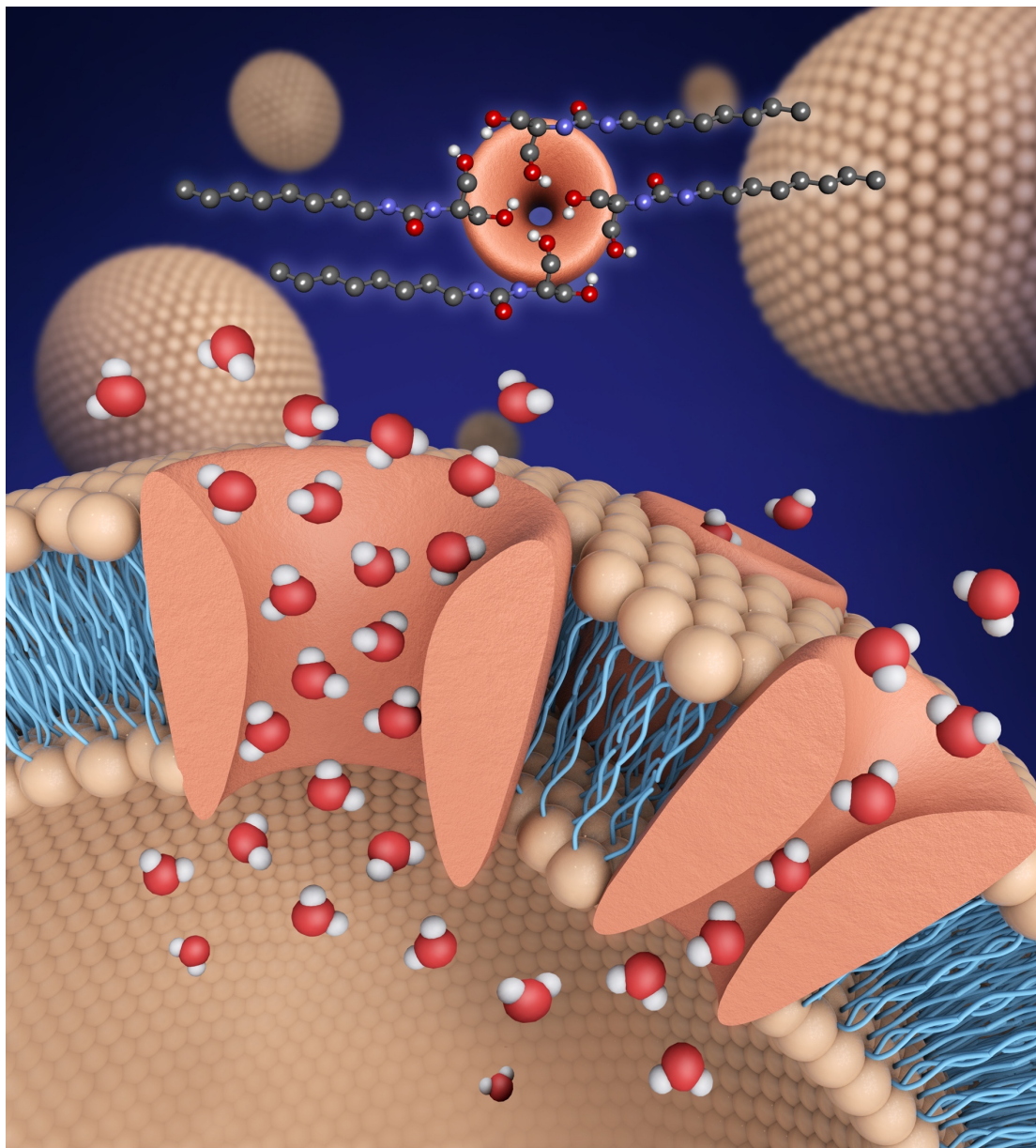
The result of the fast and selective transport of water through the AWCs has enormous benefits for several practical applications: advanced desalination, production of ultrapure water for biomedical or electronic applications, purification of highly diluted solutions. We believe that AWCs have enormous potential to become an integral part of breakthrough water desalination and purification technologies. They will promote the fabrication of channel-based membranes for enhanced low-energy desalination, blue energy harvesting, production of ultrapure water for medicine and electronics, and purification of residual water.

We believe that AWCs will provide the right information at the right time by changing a 60-year-old desalination paradigm only a decade after they were discovered.



## Chapter II – Hydroxy Channels

### – Adaptive Pathways for Selective Water Cluster Permeation



This chapter is adapted *with permission from* L.-B. Huang, A. Hardiagon, I. Kocsis, C.-A. Jegu, M. Deleanu, A. Gilles, A. van der Lee, F. Sterpone, M. Baaden, M. Barboiu, Hydroxy channels—adaptive pathways for selective water cluster permeation. *J. Am. Chem. Soc.* **2021**, *143*, 4224–4233. Copyright © 2021, American Chemical Society.

## 2.1. Introduction

One of the most ambitious goals in separation science today is to accomplish the reconstruction of natural carriers or channels through synthetic design. Proteins have evolved for millennia to adopt their current functional structures. Although they are remarkable in functional efficacy, their structural complexity and environmental sensitivity undermine their reproducibility and further applications for “out of the membrane cell” use.<sup>6</sup>

A key step in achieving this goal is the replacement of natural transporters with simpler synthetic analogues. Synthetic biomimetic approaches offer us the possibility to build artificial unimolecular or supramolecular constructs that can mimic biological functionality, while featuring procedural and structural simplicity.<sup>45</sup> The functions of carriers, ion channels and porins have been successfully replicated using small building blocks. There are several advantages for using artificial mimics; the most notable are the possible lower costs, tunability, improved stability, and compatibility with the membrane host matrices.

A decade after their discovery,<sup>32-34, 42</sup> artificial water channels (AWCs) have come very close to the performance of their natural counterparts, the aquaporins. Carbon nanotube porins (CNTPs) (Figure 18 a and b),<sup>64, 95</sup> pillar[5]arene (PAP5) (Figure 18 c)<sup>75, 76</sup> pillar[4]arene (PAH[4]) clusters (Figure 18d),<sup>80</sup> aquafoldamers (Figure 18 e),<sup>50</sup> porous organic cages (POCs) (Figure 18 f),<sup>94</sup> pillar[5]arene hydrazones (PAH5) (Figure 18 g),<sup>34</sup> and pillar[5]arene-AQPs (Figure 18 h)<sup>17</sup> are able to perform close to or even better than AQPs, when it comes to water permeability and/or selectivity.<sup>6</sup> In all artificial setups, transport of water occurs either through a single water file, as seen in the case of AQPs, or through the water cluster structures inside or outside the cavity of the channels.<sup>96</sup>

Increasing water–salt permselectivity or improving the salt rejection is the actual challenge to boost the efficiency of AWCs.<sup>96</sup> Most artificial channels lack the complex mechanism involved in selective water transport, including wetting–dewetting events and intermolecular water–water or channel–water H-bonding; these translate to water translocation through the channels. Only a few synthetic channels (I-quartet, PAH[4], POC, aquafoldamers, pillar[5]arene-AQPs) are capable of the selective rejection of ions. In these examples, the water transport takes places via water wires or clusters.<sup>6, 96</sup>

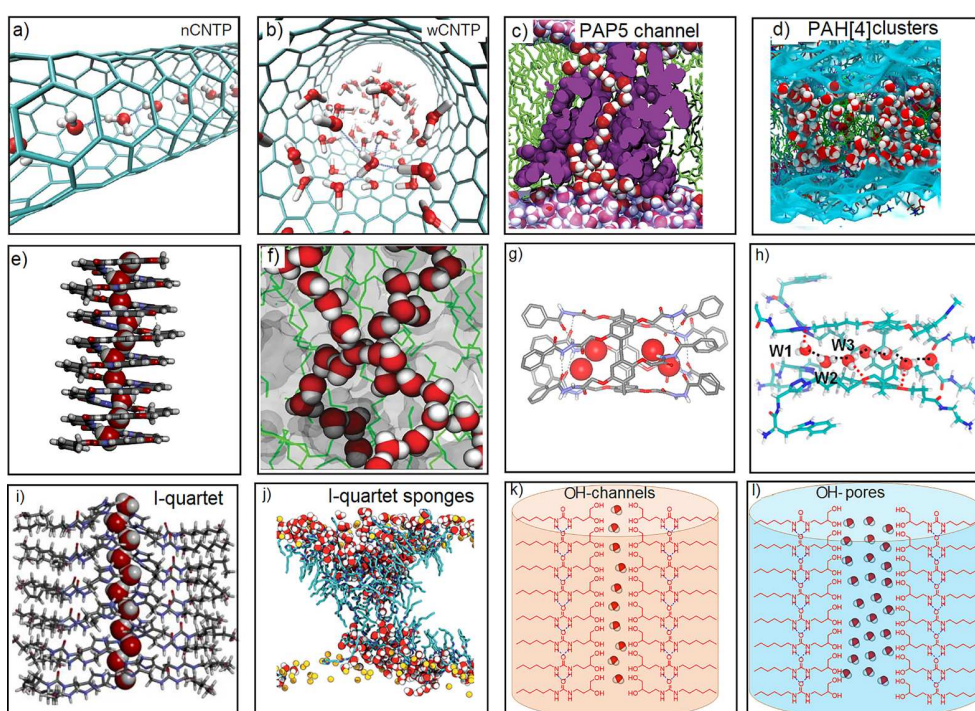


**Figure 18.** Artificial water channels: (a) narrow nCNTPs and (b) wider wCNTPs (carbon nanotube porins) encapsulating single water wires and water clusters;<sup>64</sup> (c) pillar[5]arene (PAP5) channels for water-wire transport;<sup>76</sup> (d) water permeation through PAH[4] clusters in a bilayer membrane;<sup>80</sup> (e) single water-wire permeation through highly selective aquafoldamers;<sup>50</sup> (f) water chains/clusters within POC nanoaggregates embedded in a bilayer membrane;<sup>94</sup> (g) encapsulated water dimers within pillar[5]arene hydrazones (PAH5);<sup>34</sup> (h) molecular structure of pillar[5]arene-AQPs<sup>17</sup> and their interaction with a single water wires; (i) I-quartet water channels and their interaction with single water wires;<sup>36</sup> (j) water clusters within I-quartet sponges embedded in bilayer membranes;<sup>43</sup> adaptive (k) adaptive narrow OH channels and (l) wider OH pores described in this work, presenting hydroxyl decorated pathways for water wires and water cluster translocation, through directional OH channels or OH pores in bilayer membranes.



Structural issues with channels, dimensionally adapting the formation of wires or clusters, depending on their interior pore diameter, can enhance/reduce the water permeability that can significantly impede/exceed the channel selectivity. Weak interactions of water molecules with the hydrophobic walls of channels contribute to their nearly frictionless transport, while the selectivity is sterically controlled. The structural design represents a formidable challenge in the synthetic chemistry of AWCs. Within this context our pioneering work on I-quartet<sup>32, 36</sup> (Figure 18 i) or I-quartet sponges<sup>43</sup> (Figure 18 j) highlights the tremendous importance of controlling the water superstructures via channel–water H-bonding events between communicating water molecules in the channel cavity, exerting the prohibition of ion insertion/translocation events. Obtaining absolute water selectivity resides in designing a channel, at least in its selectivity filter/region, with an environment that is favorable for the selective recognition/self-assembly of water via synergetic donor–acceptor H-bonding.

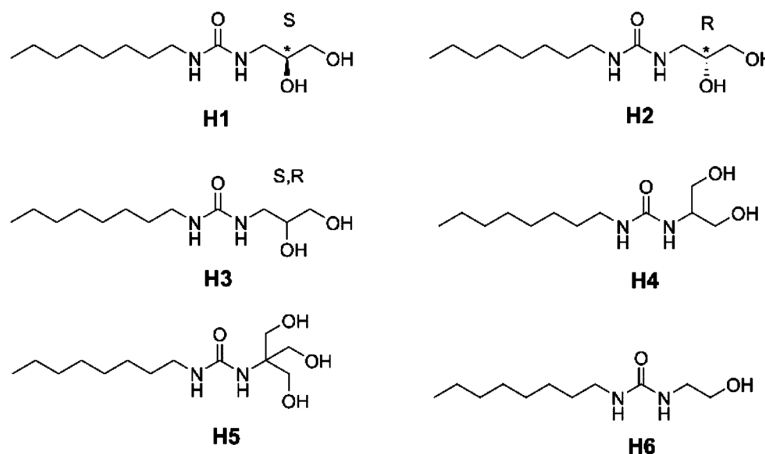
Basically, one molecule of water is able to form four hydrogen bonds, simultaneously acting as a donor and an acceptor through two bonds for each. We previously observed near-perfect single water-wire formation within I-quartet channels,<sup>32, 36</sup> where the inner walls of the channels interact with a water molecule through one donor and one acceptor hydrogen bond, leaving the two other H-bonds to be used to interconnect the water wires throughout the channel. Using the same principles, highly specific unimolecular water channels have been achieved using aquafoldamers<sup>50</sup> or pillar[5]arene-AQPs,<sup>17</sup> in which water wires are stabilized *via* channel donor–acceptor H-bonding.<sup>42,</sup>

45

Increasing the water–water H-bonding results in the formation of clusters, which become highly selective in interactions with other species that are mostly rejected, as they perturb the stability of water superstructures. Within this

context, the concept of engineering cluster/sponge-type AWCs is clearly evolving,<sup>43</sup> as it considerably expands the range of possibilities for the design of macroscopic biomimetic membrane materials embedding AWCs for reverse osmosis desalination.<sup>92</sup>

In combination with our previous experience in constructing self-assembled AWCs,<sup>36, 43</sup> herein we report a new class of AWCs based on octyl-ureido-polyols **H1–H6** (Scheme 1) bearing hydrophilic hydroxyl groups, which form adaptive hydroxy OH channels in lipid bilayers. Accommodating single water wires or water clusters, the OH channels are able to selectively transport water across a lipid membrane. We argue that water transport substantially occurs through donor–acceptor H-bonding interactions, influencing the permselectivity: (a) water–channel with hydroxyl groups at the surface of the channel or (b) water–water intrapore interactions.



**Scheme 1.** Compounds **H1–H6**, as components for self-assembled hydroxy OH channels

The scheme 1 underlines the functional versatility of the artificial OH channels, containing polar hydroxyl heads reminiscent of ceramide phospholipids that have now been well-known for more than 40 years to be involved in cell regulation (apoptosis of cancer cells, differentiation, ...).<sup>97, 98</sup> In addition to their cell regulation properties, ceramides are also known, when they are mixed with

phospholipids, to generate two main effects: they increase the molecular order and they give rise to lateral phase and domain formation. Indeed, an increase in the membrane permeability has been studied by Colombini et al., who have demonstrated the formation of pores.<sup>99</sup> To the best of our knowledge, ceramides are the only class of nonproteogenic natural compounds able to form supramolecular assemblies that span the membrane bilayer, to generate pores for facilitated translocation.

## **2.2. Results and Discussion**

### **2.2.1. Design strategy**

Herein, we focused on using the simple octyl-ureido-polyols building blocks **H1–H6** (Scheme 1) that would be capable of combining alkyl ureido groups of the I-quartet and polyhydroxyl heads of natural ceramide channels. Therefore, we synthesized a series of compounds containing water/ion hydroxylic interacting heads and bearing an octyl chain in order to introduce the optimal lipophilicity.<sup>36</sup> The connection between these two elements is one urea group, known to form directional ribbon-type superstructures.<sup>43</sup> Hydroxyl, as the simplest organic group to form both donor and acceptor hydrogen bonds, has a natural affinity with water molecules. Ethanol, propanediol, and trimethanol were employed as the hydrophilic binding motif for obtaining selective AWCs. Similar to the imidazole groups in I-quartets<sup>36, 43</sup> the “amphoteric” hydroxyl groups can selectively bind the water molecules through the donor–acceptor H-bonds.

Six compounds were synthesized for the studies presented here (Scheme 1). They were obtained through a one-step reaction between octyl isocyanate and different amino-alkyl-polyols in a mixture of solvents. The <sup>1</sup>H, <sup>13</sup>C NMR and ESI-MS spectra agree with the proposed formulas (Figures 24–35). The

potential to form OH channel superstructures was assessed initially by the crystallization of compounds **H1–H6**. X-ray single-crystal structures give a good indication of the self-assembly preferences of the compounds in solution and their possible self-organization in bilayer membranes. However, these assumptions may be treated with caution, as the solid-state single-crystal structures are representing only snapshots of possible arrangements of functional channels or pore-forming aggregates in the bilayer membrane.

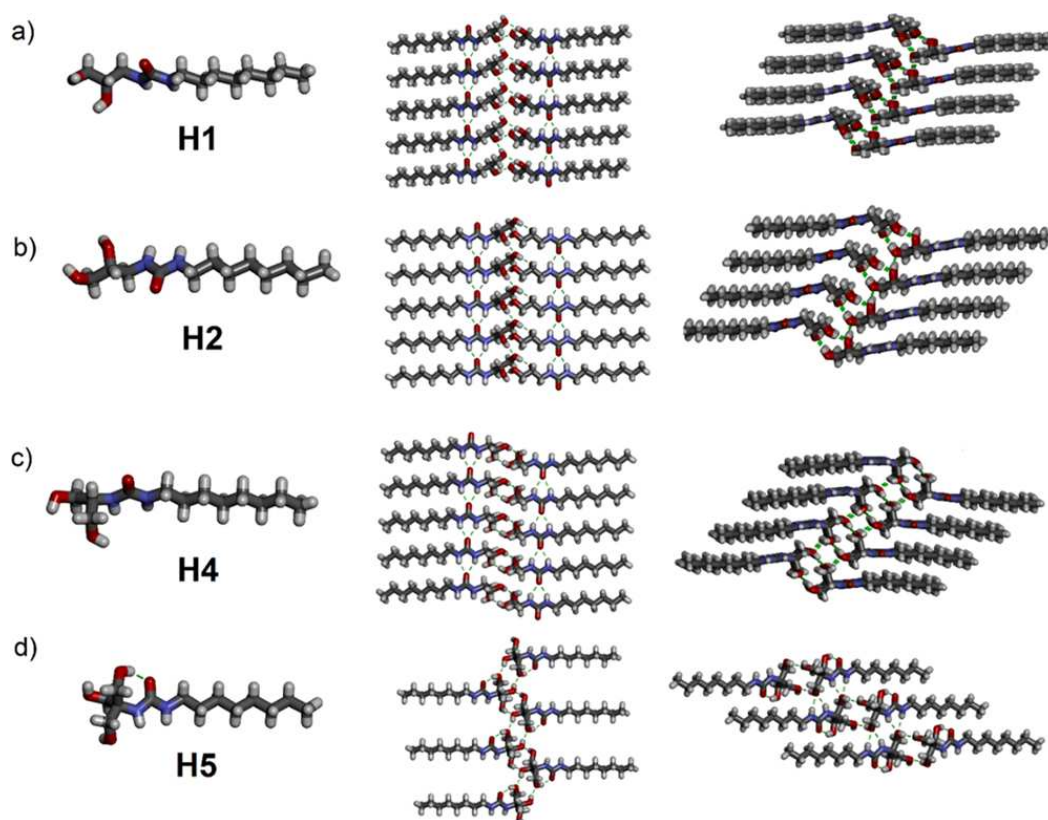


**Figure 19.** Crystal structures in stick representations of (a) **H1**, (b) **H2**, (c) **H4**, and (d) **H5** (N, blue; C, gray; O, red; H, white) showing (left) the monomeric molecules together with the lateral packing of H-bonded hydroxyl tetrads (middle) and their perpendicular packing *via* urea–urea and urea–hydroxyl H-bonding ribbons (right).

Single crystals of good quality for X-ray structure determination were obtained for the 1,2-diols **H1** and **H2**, 1,3-diol **H4**, and 1,3,5-triol **H5** (Table 3). Their solid-state structures reveal the formation of networks of  $(\text{OH}-\text{O})_4$  H-bonding OH-quartets, with the participation of two (**H1**, **H2**, and **H5**) and four (**H4**)

different molecules each involving two or one hydroxyl arm, respectively. They form almost perfect rectangular assemblies with sides of  $\sim 2.7$  Å. This OH tetrameric motif then repeats both perpendicularly, as quartet component molecules are stacking through the urea moiety in crystal structures of **H1**, **H2**, and **H4**, and laterally, the second arm of the compounds participating in the formation of another adjacent OH quartet. The distance between laterally repeating units is  $\sim 3.5$  Å (Figure 19 a–c). We note that no water molecule is included in the former crystalline structures. Further MD simulations show that OH quartets are key motifs for the strong stabilization of the low-impermeability water channels and they are not important for water translocation, as only lateral water diffusion at the interface with the membrane is occurring. Changing the structural crystallinity of the channels in the membranes led to water inclusion within spongelike channels, which is an essential step to produce larger, highly permeable channels, as previously observed with I-quartet sponges.<sup>43</sup> The double H-bonding between the third OH group and adjacent HNCONH urea groups disrupts the formation of urea ribbons but preserves a strong perpendicular H-bonding between interconnected OH quartets in the crystal structure of **H5** (Figure 19 d). Figures 36–39 in the experimental section present structural details, and CCDC 2015548–2015551 contain supplementary crystallographic data for this paper.

### **2.2.2. Bilayer membrane transport experiments**

In order to determine the transport permeability and selectivity, the OH channels **H1–H6** were tested for water and ion transport experiments. Water transport was quantified through a scattering modulation method of a vesicle suspension using a stopped-flow setup,<sup>36</sup> registering the shrinkage rate of vesicles under osmotic pressure to determine the induced osmotic water permeability of the OH channels, in the presence of D(+)-sucrose or NaCl, as competitive osmolytes. To determine if the compounds are also inducing ion

transport, we conducted pH-sensitive HPTS fluorometric experiments for different cations ( $\text{Li}^+$ ,  $\text{Na}^+$ ,  $\text{K}^+$ ,  $\text{Rb}^+$ , and  $\text{Cs}^+$ ) and anions ( $\text{Br}^-$ ,  $\text{I}^-$ ,  $\text{HCO}_3^-$ ,  $\text{CO}_3^{2-}$ ,  $\text{NO}_3^-$ , and  $\text{SO}_4^{2-}$ ) and followed the flow of species through the OH channels. By using the control FCCP and valinomycin as an assisting  $\text{H}^+$  and  $\text{K}^+$  carrier, respectively, we were able to check the specificity of the OH channels to transport ions and to determine the intrinsic selectivity of the channels, on the basis of deconvoluted transport rates for cations and anions separately, rather focusing on their proton transport behaviors that could kinetically influence the translocation process. The transmembrane experiments offered all the prerequisites to assume that compounds **H1–H6** assemble into functional and selective water-permeable OH channels in liposomes.

**Water-transport experiments.** The OH channels were reconstituted into phosphatidylcholine (PC)/phosphatidylserine (PS)/cholesterol (Chl) (PC/PS/Chl) mixture with a molar ratio of 4/1/5 lipid vesicles (100 nm in diameter). The channel-forming compounds were added by simple addition of the dimethyl sulfoxide (DMSO) solutions of **H1–H6** to the preformed vesicle suspensions using different compound to lipid molar ratios (mCLRs) (see the experimental section for details). Then, the vesicles were exposed to an outward directed osmotic pressure gradient. Under hypertonic conditions driven by an outward 10 mM PBS buffer solution (pH 6.4) of 57.5 or 100 mM NaCl or 100 mM D(+)-sucrose osmolytes (Figure 20, Figures 40 and 41), the shrinkage of the liposomes increased the light-scattering signal (Figure 20 a).

The water transport rates are strongly dependent on the concentration of the hydroxy channels, which increase the overall water permeability relative to the background lipid permeability in the bilayer membrane. The net permeabilities show a continual increase when mCLRs increase. A large range of permeabilities from 9.36 to 19.63  $\mu\text{m/s}$  can be obtained at  $\text{mCLR} < 1.48$  for **H1–H6**. Interestingly, for **H2–H4** we observe an abrupt 10-fold increase in

water permeability values (160 to 560  $\mu\text{m/s}$ ) for  $\text{mCLR} > 1.48$  (Figures 40 and 41), reminiscent of the formation of larger channels/pores within the membrane. This unique adaptive behavior is probably related to an important concentration-dependent morphology change of more permeable channels presenting different self-assembly behaviors within the membrane.

To confirm this hypothesis, the water transport measurements (Figure 20) were performed under different hypertonic solutions containing the competitive osmolytes D(+)-sucrose (Figure 40) and NaCl (Figure 41) covering low and high channel concentration domains. It can be noticed that with 100 mM D(+)-sucrose or 57.5 mM NaCl ( $\Delta_{\text{osm}} = 106 \text{ mOsm/kg}$ ) the net channel permeabilities remain on the same level of magnitude for all channels and all concentrations and show a tendency of decreasing for **H5** and **H6** with NaCl osmolarity in comparison with D(+)-sucrose osmolarity (Figure 41). Increasing the osmotic pressure to  $\Delta_{\text{osm}} = 186 \text{ mOsm/kg}$  (100 mM NaCl), the net permeability increases, showing high water permselectivity with an increase in salt concentration increase. In comparison with D(+)-sucrose osmolarity the permeability strongly increases for the high-selectivity channels **H2** and **H4**, while it decreases for low-selectivity **H3**, **H5**, and **H6** for high concentrations (Figure 42). The channel selection of D(+)-sucrose *via* size exclusion might enable water to selectively flux through the for **H3**, **H5**, and **H6** channels, while the presence of an NaCl osmolyte as a competitive salt transport agent might hinder the hydrophilic hydroxyl groups to remain accessible to water. The situation is completely opposite for **H2** and **H4**, showing higher water to salt selectivity at high concentration.

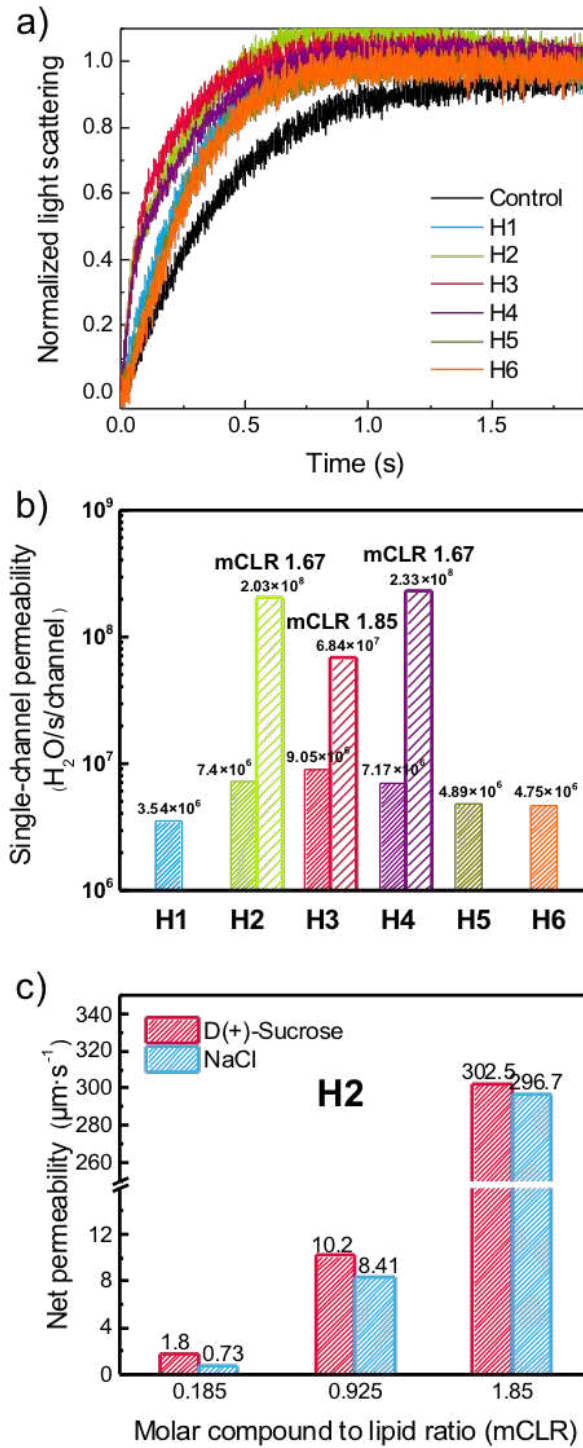


**Figure 20.** Measurements of water permeability through OH channels: (a) stopped-flow light scattering traces of liposomes containing channels at mCLR = 1.85, 1.67, 1.85, 1.67, 1.85, and 1.67, respectively; (b) single-channel permeability calculated from the light scattering traces at different concentration in the membrane; (c) comparison of net permeability values for channels of **H2**, determined by stopped-flow light scattering experiments with 100 mM D(+)- sucrose (pink) and 57.5 mM NaCl (blue) as osmolytes ( $\Delta_{\text{osm}} = 106 \text{ mOsmol/kg}$ ).



We then performed carboxyfluorescein (CF) leakage experiments<sup>100</sup> to monitor the channel formation at low and high concentrations of **H1–H6** (Figure 43). The magnitudes of CF release are very similar for all samples with a magnitude of less than 20% for **H1**, **H4**, and **H6** and practically no activity for **H2**, **H3**, and **H5**, while incipient abrupt activity can be observed for **H3** and **H4**. According to these CF leakage experiments, incipient formation of large pores can be observed at a high concentration, which allows a huge efflux of CF, while no important activity was monitored for the next period when the stabilization is observed for all channels. Following these results, we decided to perform the water/ion experiments after a period of 30 min incubation time after the addition of the channels in the bilayers. Colombini et al.<sup>99</sup> observed the same behavior, showing that the average channel size increased with an increase of ceramide content in the membrane.

**Table 2.** Single-channel permeability,  $P_s$ , of **H1–H6** Channels

OH channel	$P_s$ , (H <sub>2</sub> O/s/channel)
<b>H1</b>	$3.54 \times 10^6$
<b>H2</b>	$2.03 \times 10^8$
<b>H3</b>	$6.84 \times 10^7$
<b>H4</b>	$2.33 \times 10^8$
<b>H5</b>	$4.89 \times 10^6$
<b>H6</b>	$4.75 \times 10^6$

We further estimated the single-channel permeability,  $P_s$ , of **H1–H6**, on the basis of the OH channel insertion, lipid concentration, and channel configuration in the lipids (Table 2).<sup>43</sup> In order to determine the single-channel permeabilities, we used two rational assumptions. (i) First, that there was spontaneous total insertion of the compounds into the lipid bilayer. The total

partitioning coefficients of **H1–H6** in the bilayer membrane are confirmed at a maximum concentration of 80 mM solutions and are perfectly clear in the presence of lipid vesicles, while precipitate turbidity is formed when the compounds are added to aqueous solutions, reminiscent of almost total partition of **H1–H6** in the bilayer membrane (please note that lower partition coefficients would lead to higher single-channel permeabilities in comparison to those considered for total partition). (ii) Second, the number of molecules needed to form a channel that spans the bilayer is equal to the number of molecules found in the single-crystal structure, which corresponds to 8 stacks of **H1–H6** and 64 molecules per assembly within a transmembrane length of 5 nm. Accordingly, the single-channel permeability values obviously varied, covering the range of  $3.5 \times 10^6$  to  $2.4 \times 10^8$  H<sub>2</sub>O/s/channel at mCLR 0.026, which are only two orders of magnitude lower or similar than those of AQPs ( $\sim 10^8$ – $10^9$  H<sub>2</sub>O/s/channel<sup>6, 45</sup>) (Figure 20 and Table 2).

Water transport activities increase substantially at higher concentrations of **H2–H4**, implying the formation of highly permeable channels. Indeed, the hydrophilic diol heads seemed to be more optimized for permeation in comparison to monol and triol heads, leading to higher water permeation when they are mixed with lipids. The tendency for an increase in net and single-channel permeability at high concentration can be explained by progressive higher cluster-type aggregation of OH channels, promoting the increased water transport *via* sponge like structures as we previously observed for I-quartet channels.<sup>43</sup> Differently, a low concentration of OH channels prevents the aggregation and allows only the reduction of water-wire translocation.

**Cation and Anion Transport Experiments.** Cation (M<sup>+</sup> = Li<sup>+</sup>, Na<sup>+</sup>, K<sup>+</sup>, Rb<sup>+</sup>, and Cs<sup>+</sup>) transport activities across the bilayer membranes incorporating **H1–H6** OH channels, reconstituted into phosphatidylcholine (PC) lipid vesicles (100 nm), at the same mCLRs used for the water transport, were

assessed using standard HPTS fluorescence assays (Figures 44 and 45).<sup>101, 102</sup> Indeed, when they were tested with MCl on external buffer, the **H1–H6** channels do not present a dose–response-type activity, showing constant nearly zero activity behaviors, independently of a low (10 mM, Figure 44) or high (80 mM, Figure 45) concentration of active channels in the membrane. It is very clear that  $M^+/H^+$  antiport conductance states of the assembled channels are not observed for any of the studied concentrations.

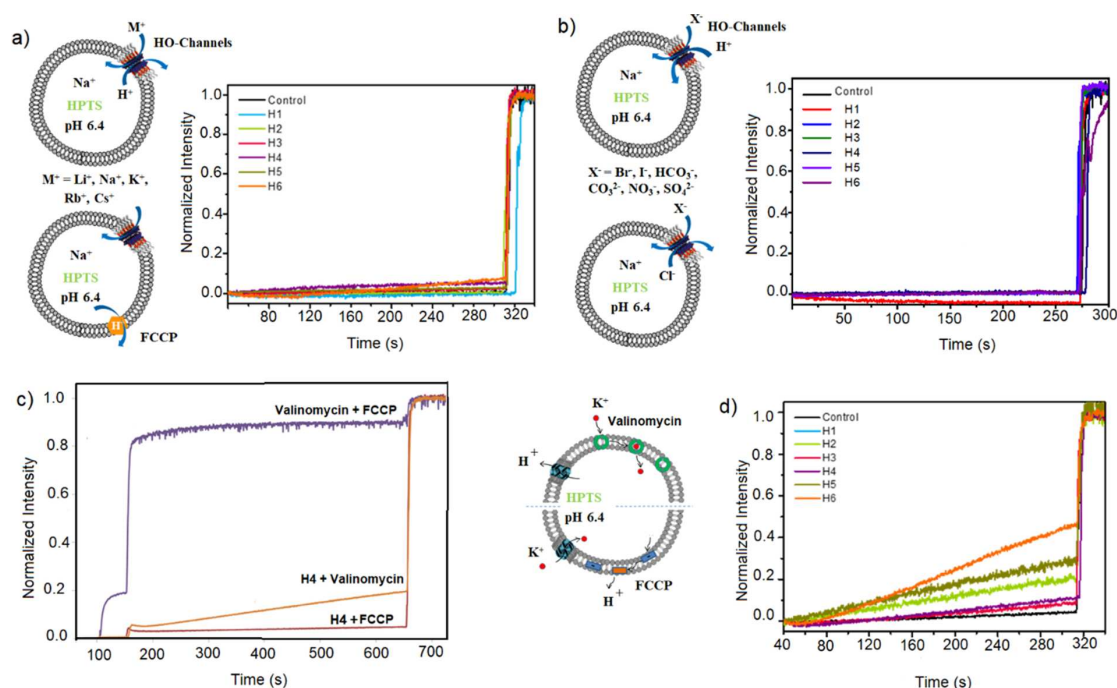


**Figure 21.** (a) Comparison of  $Na^+$  transport activity expressed as normalized fluorescence intensity of 10 mM channels in the extravesicular media containing 100 mM NaCl (in the absence of FCCP) together with a schematic representation of antiport  $M^+/H^+$  mechanisms in the absence or the presence of FCCP as a  $H^+$  carrier. (b) Comparison of  $Br^-$  transport activity expressed as normalized fluorescence intensity of 10 mM **H1–H6** channels in the extravesicular media containing 100 mM NaBr, together with schematic representations of anion/ $H^+$  symport and  $Cl^-/X^-$  antiport mechanisms. (c) Transport experiments coupling **H4** channels with valinomycin and FCCCP as  $K^+$  and  $H^+$  carriers. (d) Coupled transport between the valinomycin  $K^+$  carrier (50  $\mu$ M) and **H1–H6** channels (80 mM) with 100 mM  $K_2SO_4$  in the extravesicular media.

We were then interested in supplementary evidence on the anion translocation mechanisms through the H-bonded hydroxylic networks, already used as

channel recognition motifs for anion/proton cotransport.<sup>103, 104</sup> In order to check the anion transport activity resulting from anion/chloride antiport or anion/H<sup>+</sup> cotransport, we conducted HPTS assays.

Different sodium salts (Br<sup>-</sup>, I<sup>-</sup>, HCO<sub>3</sub><sup>-</sup>, CO<sub>3</sub><sup>2-</sup>, NO<sub>3</sub><sup>-</sup>, and SO<sub>4</sub><sup>2-</sup>) were used to determine the anion transport activity of **H1–H6** OH channels. On this basis, the resulting transport profiles showed rather weak near to zero transport rates for the different NaX salts in the presence of 10 mM (Figure 46) and 80 mM (Figure 47) **H1–H6**, indicating that the transport of the hydrated anions is not governed by the solvation free energy of the anions (Figure 47). Compounds **H1** and **H6**, with low water transport activities, present very low (< 5%) anion transport activity, most probably related to a Cl<sup>-</sup>/X<sup>-</sup> (X<sup>-</sup> = Br<sup>-</sup>, I<sup>-</sup>, NO<sub>3</sub><sup>-</sup>, SO<sub>4</sub><sup>2-</sup>) antiport.

In order to verify if the H<sup>+</sup> transport is the rate-limiting step for M<sup>+</sup>/H<sup>+</sup> antiport activity, we conducted HPTS assays with compounds **H1–H6** in the presence of carbonyl cyanide 4-(trifluoromethoxy)phenylhydrazone (FCCP) as a H<sup>+</sup> carrier (Figure 45).<sup>102</sup> These experiments did not show a difference from the previous results. All tested OH channels have very low to total inactivity for cation transport in the presence or the absence of a FCCP proton carrier.

Moreover, we were interested in further testing the compound specificity by testing **H1–H6** for proton transport. We thus used a classical HPTS assay and control valinomycin (K<sup>+</sup> cations) and FCCP (proton) transporters, known to generate a strong K<sup>+</sup>/H<sup>+</sup> electrogenic antiport (Figure 4 c and d). Potential proton transport acceleration is unlikely, given the case of coupling of valinomycin with **H1–H6**. Electrogenic membrane polarization *via* Val-K<sup>+</sup> transport generates a variable medium ( $I = 0.45$ , **H6**) to low ( $I = 0.2–0.25$ , **H2**, **H5**) or very low ( $I < 0.1–0.25$ , **H1**, **H3**, **H4**) proton antiport rates through OH channels.

### 2.2.3. Molecular dynamics simulations of H1 aggregates in a fully hydrated lipid bilayer environment

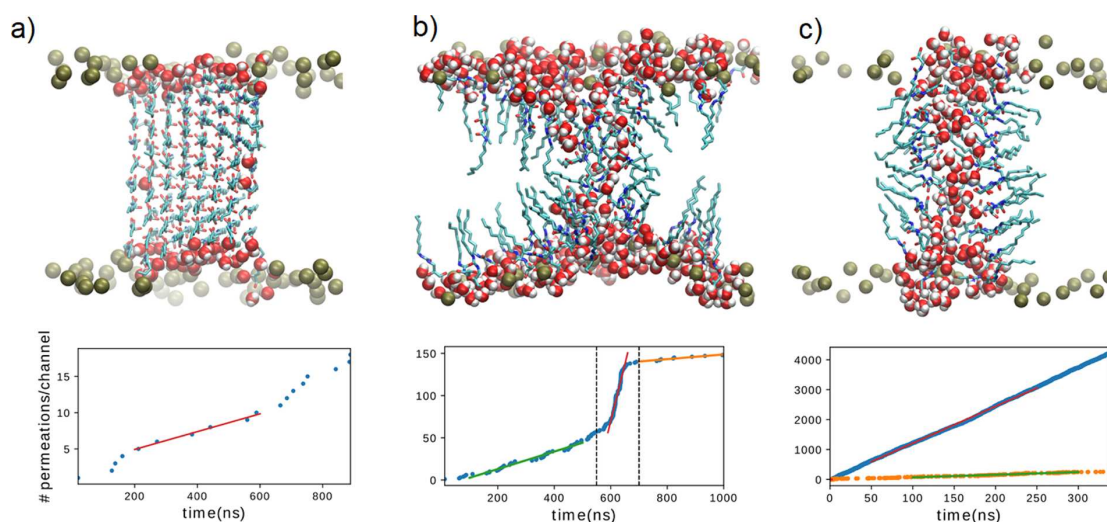


**Figure 22.** Molecular dynamics simulation results for **H1** hydroxy channels in a fully hydrated lipid bilayer environment. The top row shows snapshots for three transport regimes that were observed: (a) a crystal-like patch arrangement after  $t = 475$  ns; (b) spongelike structure after  $t = 635$  ns; (c) cylinder-like single membrane-spanning channel in an artificially restrained simulation with a constant force of 1000 kJ/mol (blue, simulation harm1000) and 10 kJ/mol (orange, simulation harm10) at  $t = 337$  ns. Channel molecules are drawn in licorice representation. For clarity, lipid and water molecules in the bulk have been omitted. Water molecules within the lipid bilayer or close to the head groups in contact with **H1** are shown in a Van der Waals representation.

Molecular dynamics simulations carried out in a membrane environment allowed us to observe a range of permeation scenarios, ranging from an almost completely sealed membrane with only minimal transport at the compound/lipid boundaries, through a previously described sponge-resembling regime,<sup>43</sup> in attempts to build putative permeant channels to water-filled channel transport when ceramide-pore-inspired hypothetical constructs were stabilized through a biasing potential (Figure 22).

First, we tested crystal patches in the membrane. Depending on the simulation setup, we observed either dissolution of the crystal structure aggregate to the lipid–water interface or an impenetrable stable membrane-inserted assembly.

The strong intermolecular hydrogen bonding pattern observed in the crystal structure precluded the formation of any water wires or water clusters within the structure, suggesting that a significant rearrangement of the compounds is required to enable water permeation. Only residual water leakage at the boundary between the crystal patch and the lipids was observed. The crystal structure is stable and displays low permeability, as shown in the plot on the bottom of Figure 22. Fitting a line (Figure 22 a, red line) to the central part of the curve leads to an estimated permeability of  $4 \times 10^6$  H<sub>2</sub>O/s/channel (see the experimental section for details on the simulation `crys_gaff`).

Next, we attempted the activation of the crystal patch using extensive enhanced sampling simulations to favor internal rearrangements. None of these simulations gave rise to water transport. In addition to these membrane simulations, we attempted to soak crystal patches in aqueous solution in order to assess how they might accommodate water. Despite an initial separation of the **H1** layers by ca. 2 Å, the crystal patches resisted any significant water penetration.

Further molecular simulations allowed us to assess whether the water-free crystal superstructures may adaptively reassemble within the membrane to accommodate any water translocation. These simulation results taken together suggest that the permeant membrane-embedded channel structures substantially differ from the crystal arrangement. At some stage the compounds may rearrange into a spongelike form, possibly a stable channel-like form, to give rise to a steady water flow. Three permeation regimes can be distinguished by fitting green, red, and orange lines (Figure 22 b), with respectively  $3 \times 10^7$ ,  $8 \times 10^8$ , and  $1 \times 10^7$  H<sub>2</sub>O/s/channel permeability (see the experimental section for details on simulation `crys_cgen`). These regimes account for the crystal-like, the spongelike, and the dissolved forms of the channels, which are probably most present at low concentration of channels in the membrane.

These observations may likely echo the experimental measurements, indicating a first occurrence of water permeation at low concentrations, a minimal transport regime, originating in the perturbation of the membrane arrangement induced by the presence of the OH channels in the lipid membrane. It is important to note that the dynamics of different channel-like forms vary significantly, as our hypothetical constructs require artificial stabilization to remain intact within the membrane.

Finally, we constructed a cylindrical pore of **H1** OH channels resembling the ceramides.<sup>99</sup> Our tentative cylindrical channel pore was artificially stabilized in the simulations using harmonic restraints. The corresponding geometry is described in the experimental section. With such a stabilized cylindrical channel, water transport is indeed observed and can be tuned by increasing the bias from  $4 \times 10^8$  H<sub>2</sub>O/s/channel (weaker force shown in orange in Figure 22 c) up to ca.  $6 \times 10^9$  H<sub>2</sub>O/s/channel (strong force shown in blue in Figure 22 c). These observations point to the very subtle balance of interactions that needs to be achieved between the inter-compound and compound–lipid/compound–water interactions to generate highly permeable channels as observed at high concentrations of **H1–H6** in the bilayer membrane.

This ensemble of molecular dynamics simulations was further used to check for ion permeation events. Interestingly, in none of the simulations in a bilayer environment we observed ion permeation during the average 500 ns duration. The limiting case of a simulation with a channel that is forced to stay wide open through strong biasing forces of 1000 kJ/mol leads to some ion permeation. As soon as this restraint force was lowered and the structure gained flexibility, ion permeation stopped.

From a structural point of view, to better understand the membrane modifications operated by this series of compounds, complementary computer simulations are required. These calculations should aim to extend our initial tests with cylindrical pores. The goal is to design and test new constructs of the OH-channel compounds with the challenge of rendering their architectures sufficiently stable in the membrane environment competing for interactions.

So far, we were able to test some artificially stabilized constructs of cylindrical shape, which did feature permeation. However, by release of the stabilizing bias, they were torn apart by the favorable lipid interactions in the membrane environment. Our working hypothesis for future tests is to start from the ureic core to assemble the OH-channel compounds, in a fashion similar to that observed for ceramide-like aggregates of cylindrical shapes.<sup>99</sup>

#### **2.2.4. Discussion**

We showed that the systematic design of the octyl-ureido-polyols led to highly effective and selective artificial water channels. Simple use of the variable number and sterically different hydroxyl binding sites led to unexpected increased water-transport activities at a high concentration of the channels within the membranes. The formation of OH-decorated channels/pores are probably the only common structural behaviors with ceramides that form hydrophilic pores with variable geometries. They are related to adaptive changes in the structure of the channels, reminiscent of the formation of larger pores for translocation, showing a 10-fold increase, as observed for natural ceramide transporters.

From a mechanistic point of view, the H-bonding network offered by the hydroxyl OH networks can act itself as a recognition-based barrier within highly selective channels for water translocation. The energy penalty for



binding either cations or anions would be too high, as either one of the ions can bind either the O or the H in one instance. On the other hand, however, a H-bonding water molecule can intervene with both donor and acceptor H-bonds, satisfying the full number of hydrogen bonds within the networks, making possible its facilitated translocation through the gate. The hydroxyl-rich cavity of the channels can offer complete amphoteric donor–acceptor hydrogen bonding for the water, while the molecules retain a bulk-like bonding environment under confined conditions of the channels where the water conductance is occurring within pores for which the sizes are distributed between 0 and a maximum value in the central part of the channel: 3.0, 3.2, and 3.6 Å (Figure 55). The distribution of pore sizes reflects a porous structure and the transient appearance of water clusters inside the channel. For such narrow pores, the entrance of hydrated ions into the channels may be restricted by the dehydration energy penalty arising from the preference of ions to be surrounded by water molecules, rather than incomplete hydration within OH channels. The OH-channel preference to form interconnected channel OH–O<sub>2</sub>H networks is the major factor determining the OH-channel water/ion permselectivity. In contrast to cation/anion diffusion, proton translocation through such clusters is more a structural diffusion than a carrier diffusion of ions and in OH channels case is strongly dependent on the self-assembly features of the OH channels in bilayer membranes, as protons can translocate principally via directional H-bonds of water clusters stabilized by the OH channels.<sup>105</sup>

The OH-channel architectures are very intriguing systems. It is very tempting to equate that impermeable crystalline phases, medium-permeability sponge like, or high-permeability cylindrical constructs are stabilized in the bilayer membrane. The unifying assumption is that dynamic H-bonding and hydrophobic interactions would lead to the dominant structures in a membrane environment depending on the concentration of the channels and providing

pathways for water translocation through the transient water clusters. The water cluster stabilization *via* H-bonding to hydroxyls confer to these channels self-adaptive behaviors, which make the intrinsic features of water sponges or clusters, particularly self-protective against ions. Having all H-bonds saturated via the formation of water wires or water clusters, the cation/anion insertion will impede and interrupt the communication between adjacent water and OH channels/pores, explaining the very low ion permeation events. As was observed for I-quartet single water wires<sup>36</sup> or sponge channels,<sup>43</sup> PAH[4] channel<sup>80</sup> or porous organic cage (POC)<sup>94</sup>, OH channels feature this rather unique enhanced permeability of water cluster conduction systems stabilized within membranes. This strategy recently described by us<sup>43</sup> predicts almost 2 orders of magnitude higher permeability of water clusters than of water-wire channels.

### **2.3. Conclusions**

We have demonstrated here that self-assembled adaptive OH channels can be obtained from simple octyl-ureido-polyol building blocks that present enhanced selective water permeability with almost total ion rejection across a lipid bilayer. Slight modifications to the number and disposition of hydroxyl (-OH) functional groups surrounding the hydrophilic cavity of the channels or an increase in the concentration of the compounds in the membrane can drastically change the water permeability. Even with the highest margins of errors, these channels are capable of transporting water at a rate that is 1 order of magnitude below that of the natural AQP. More importantly, salt rejection and the extremely low proton permeability of the OH channels offer the closest functional mimic of the natural AQP through a synthetic scaffold (Figure 23).

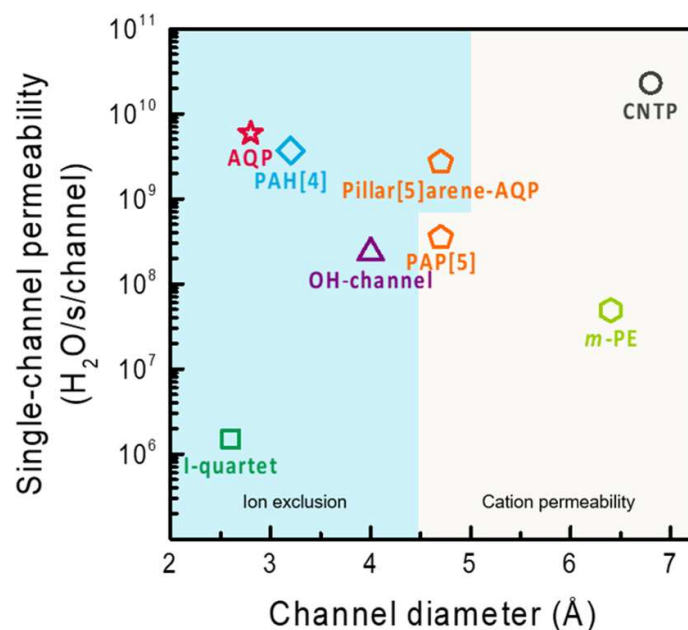


**Figure 23.** Comparison of single-channel permeabilities vs diameter of AQPs, CNTPs, artificial water channels (OH channels) (represented as mean value  $4 \pm 2.5$  Å), I-quartet, pillar[5]arene-AQP, PAH[4], PAP5, and *m*-PE.

The present studies are of tremendous importance, showing adaptive behaviors of water molecules inside the channels depending on the dimension of channels determining the water-conduction behaviors as a function of concentration of OH channels within membranes.

It is very well known that binding energies define the flux of solutes through an artificial channel. Multiple interactions of molecules with the walls of a channel will impede permeation and result in a reduced flow rate. It was demonstrated that the high water permeability values of CNTPs, PAP5s, PAH[4]s, and POCs can be attributed to the no-slip translocation mechanism, which is in direct correlation with the weakness of interactions between the water molecules and the walls of the nanotubes

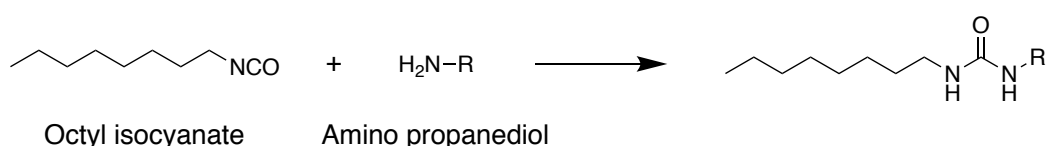
This phenomenon gives hydrophobic channels an increase in performance from the point of view of mass transfer. On the other hand, the advantage of hydrophilic channels comes from the very interactional nature of the channel cavity. Due to a variety of binding moieties to interact with the transported

water, specific binding motifs can be designed. This feature can be exploited, making it possible to design permselectivity filters or tailor the transport mechanism of the channels. They can adapt transient water wires and sponges that are ion selective and water permeable. Within this context, this discovery of OH channels reported here opens up new directions and perspectives in AWC research<sup>96</sup> toward the construction of selective membranes for desalination channels,<sup>92</sup> biomimicking the function of natural channels.<sup>6</sup>

## 2.4. Experimental Section

### 2.4.1. Materials and characterization

**Chemical synthesis.** All of the compounds have been synthesized following the general scheme shown above. The amino propanediol (10 mmol) was mixed with the corresponding equimolar amount of octyl isocyanate, with sonication. The mixture was dissolved in 10 mL of THF (tetrahydrofuran), 5 mL of ethyl acetate and 5 mL of acetonitrile. The reaction system was heated to 80°C for two hours. The resulting solution was dried with conventional rotary evaporation under vacuum to obtain white powder. The products were washed with methanol and hexane, then were separated by rotary centrifuge. The residual solvent was removed by vacuum desiccator.

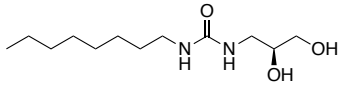
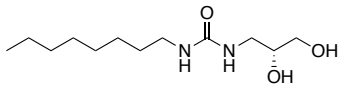
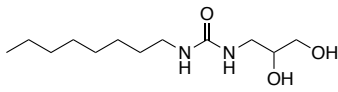
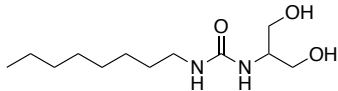
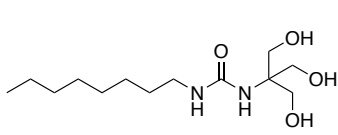
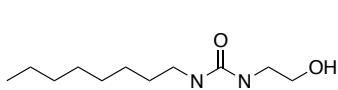


**Scheme 2.** Synthesis of alkylureido-isopropyl derivatives **H1–H6**.

**Structural characterization.** All reagents were purchased from commercial suppliers and used without further purification. <sup>1</sup>H NMR spectrum were recorded on Bruker Avance III 400 MHz NMR spectrometer in DMSO-*d*<sub>6</sub>, with the use of the residual solvent peak ( $\delta = 2.50$  ppm) as reference. Mass

spectrometric analyses were performed in the positive ion mode using a quadrupole mass spectrometer (Micromass, Platform II).

**Table 3.** Chemical parameters of alkylureido-isopropyl derivatives **H1–H6**.

	Chemical structure	Name	Formula	MS Cal.
<b>H1</b>		( <i>S</i> )-1-(2,3-dihydroxypropyl)-3-octylurea	C <sub>12</sub> H <sub>26</sub> N <sub>2</sub> O <sub>3</sub>	246.4
<b>H2</b>		( <i>R</i> )-1-(2,3-dihydroxypropyl)-3-octylurea	C <sub>12</sub> H <sub>26</sub> N <sub>2</sub> O <sub>3</sub>	246.4
<b>H3</b>		( <i>R,S</i> )-1-(2,3-dihydroxypropyl)-3-octylurea	C <sub>12</sub> H <sub>26</sub> N <sub>2</sub> O <sub>3</sub>	246.4
<b>H4</b>		1-(1,3-dihydroxypropan-2-yl)-3-octylurea	C <sub>12</sub> H <sub>26</sub> N <sub>2</sub> O <sub>3</sub>	246.4
<b>H5</b>		1-(1,3-dihydroxy-2-(hydroxymethyl)propan-2-yl)-3-octylurea	C <sub>13</sub> H <sub>28</sub> N <sub>2</sub> O <sub>4</sub>	276.4
<b>H6</b>		1-(2-hydroxyethyl)-3-octylurea	C <sub>11</sub> H <sub>24</sub> N <sub>2</sub> O <sub>2</sub>	216.3

**(S)-1-(2,3-dihydroxypropyl)-3-octylurea, H1:** <sup>1</sup>H NMR (DMSO-*d*<sub>6</sub>, 400 MHz) δ (ppm) = 0.86 (t, *J* = 6 Hz, 3H, CH<sub>3</sub>CH<sub>2</sub>), 1.21 – 1.37 (m, 12H, CH<sub>3</sub>(CH<sub>2</sub>)<sub>6</sub>CH<sub>2</sub>), 2.87 – 2.98 (m, 3H, CH<sub>2</sub>CH<sub>2</sub>NH, CHCH<sub>2</sub>NH), 3.11 – 3.30 (m, 3H, CHCH<sub>2</sub>NH, CHCH<sub>2</sub>OH), 3.37 – 3.44 (m, 1H, CH<sub>2</sub>CHCH<sub>2</sub>OH), 4.54 (t, *J* = 5.9 Hz, 1H, CH<sub>2</sub>OH), 4.77 (d, *J* = 4.7 Hz, 1H, CHOH), 5.80 (t, *J* = 5.7 Hz, 1H, CH<sub>2</sub>NH), 5.98 (t, *J* = 5.6 Hz, 1H, CH<sub>2</sub>NH); <sup>13</sup>C NMR (DMSO-*d*<sub>6</sub>, 100 MHz) δ (ppm) = 14.45 (CH<sub>3</sub>), 22.57, 26.85, 29.19, 29.24, 30.46, 31.72 (6xCH<sub>2</sub>), 39.68 (CH<sub>2</sub>NH) 43.08 (CH<sub>2</sub>NH), 63.93 (CH<sub>2</sub>OH), 71.61 (CHOH), 159.16 (CO); MS Cal. = 246.4, ESI-MS found [M + H]<sup>+</sup> = 247.5.

**(R)-1-(2,3-dihydroxypropyl)-3-octylurea, H2:**  $^1\text{H NMR}$  (DMSO- $d_6$ , 400 MHz)  $\delta$  (ppm) = 0.86 (t,  $J = 6$  Hz, 3H,  $\text{CH}_3\text{CH}_2$ ), 1.17 – 1.38 (m, 12H,  $\text{CH}_3(\text{CH}_2)_6\text{CH}_2$ ), 2.87 – 2.98 (m, 3H,  $\text{CH}_2\text{CH}_2\text{NH}$ ,  $\text{CHCH}_2\text{NH}$ ), 3.10 – 3.30 (m, 3H,  $\text{CHCH}_2\text{NH}$ ,  $\text{CHCH}_2\text{OH}$ ), 3.37 – 3.44 (m, 1H,  $\text{CH}_2\text{CHCH}_2\text{OH}$ ), 4.55 (t,  $J = 5.9$  Hz, 1H,  $\text{CH}_2\text{OH}$ ), 4.78 (d,  $J = 4.7$  Hz, 1H,  $\text{CHOH}$ ), 5.89 (dt,  $J = 72.4, 5.7$  Hz, 2H,  $\text{NHCONH}$ );  $^{13}\text{C NMR}$  (DMSO- $d_6$ , 100 MHz)  $\delta$  (ppm) = 14.45 ( $\text{CH}_3$ ), 22.57, 26.85, 29.19, 29.24, 30.46, 31.72 (6x $\text{CH}_2$ ), 39.68 ( $\text{CH}_2\text{NH}$ ) 43.08 ( $\text{CH}_2\text{NH}$ ), 63.93 ( $\text{CH}_2\text{OH}$ ), 71.60 ( $\text{CHOH}$ ), 159.16 (CO); MS Cal. = 246.4, ESI-MS found  $[\text{M} + \text{H}^+]^+ = 247.2$ .

**(R,S)-1-(2,3-dihydroxypropyl)-3-octylurea, H3:**  $^1\text{H NMR}$  (DMSO- $d_6$ , 400 MHz)  $\delta$  (ppm) = 0.86 (t,  $J = 6$  Hz, 3H,  $\text{CH}_3\text{CH}_2$ ), 1.20 – 1.37 (m, 12H,  $\text{CH}_3(\text{CH}_2)_6\text{CH}_2$ ), 2.88 – 2.98 (m, 3H,  $\text{CH}_2\text{CH}_2\text{NH}$ ,  $\text{CHCH}_2\text{NH}$ ), 3.11 – 3.28 (m, 3H,  $\text{CHCH}_2\text{NH}$ ,  $\text{CHCH}_2\text{OH}$ ), 3.37 – 3.44 (m, 1H,  $\text{CH}_2\text{CHCH}_2\text{OH}$ ), 4.55 (t,  $J = 5.9$  Hz, 1H,  $\text{CH}_2\text{OH}$ ), 4.78 (d,  $J = 4.7$  Hz, 1H,  $\text{CHOH}$ ), 5.80 (t,  $J = 5.8$  Hz, 1H,  $\text{CH}_2\text{NH}$ ), 5.98 (t,  $J = 5.6$  Hz, 1H,  $\text{CH}_2\text{NH}$ );  $^{13}\text{C NMR}$  (DMSO- $d_6$ , 100 MHz)  $\delta$  (ppm) = 14.45 ( $\text{CH}_3$ ), 22.57, 26.85, 29.19, 29.24, 30.46, 31.72 (6x $\text{CH}_2$ ), 39.68 ( $\text{CH}_2\text{NH}$ ) 43.08 ( $\text{CH}_2\text{NH}$ ), 63.93 ( $\text{CH}_2\text{OH}$ ), 71.60 ( $\text{CHOH}$ ), 159.17 (CO); MS Cal. = 246.4, ESI-MS found  $[\text{M} + \text{H}^+]^+ = 247.6$ .

**1-(1,3-dihydroxypropan-2-yl)-3-octylurea, H4:**  $^1\text{H NMR}$  (DMSO- $d_6$ , 400 MHz)  $\delta$  (ppm) = 0.86 (t,  $J = 6$  Hz, 3H,  $\text{CH}_3\text{CH}_2$ ), 1.21 – 1.35 (m, 12H,  $\text{CH}_3(\text{CH}_2)_6\text{CH}_2$ ), 2.94 (q,  $J = 6.7$  Hz, 2H,  $\text{CH}_2\text{CH}_2\text{NH}$ ), 3.38-3.43 (m, 2H,  $\text{CH}(\text{CH}_2\text{OH})_2$ ), 3.45 – 3.53 (m, 1H,  $\text{CH}_2\text{CHNH}$ ), 4.62 (t,  $J = 5.3$  Hz, 2H,  $\text{CH}(\text{CH}_2\text{OH})_2$ ), 5.62 (d,  $J = 7.8$  Hz, 1H,  $\text{CH}_2\text{NH}$ ), 5.98 (t,  $J = 5.6$  Hz, 1H,  $\text{CHNH}$ );  $^{13}\text{C NMR}$  (DMSO- $d_6$ , 100 MHz)  $\delta$  (ppm) = 14.44 ( $\text{CH}_3$ ), 22.57, 26.88, 29.19, 29.24, 30.46, 31.72 (6x $\text{CH}_2$ ), 39.60 ( $\text{CH}_2\text{NH}$ ), 53.09 ( $\text{CHNH}$ ), 60.90 ( $\text{CH}_2\text{OH}$ ), 159.45 (CO); MS Cal. = 246.4, ESI-MS found  $[\text{M} + \text{H}^+]^+ = 247.4$ .

**1-(1,3-dihydroxy-2-(hydroxymethyl)propan-2-yl)-3-octylurea, H5:**  $^1\text{H NMR (DMSO-}d_6, 400 \text{ MHz)}$   $\delta$  (ppm) = 0.86 (t,  $J = 8 \text{ Hz}$ , 3H,  $\text{CH}_3\text{CH}_2$ ), 1.21 – 1.36 (m, 12H,  $\text{CH}_3(\text{CH}_2)_6\text{CH}_2$ ), 2.94 (q,  $J = 6.7 \text{ Hz}$ , 2H,  $\text{CH}_2\text{CH}_2\text{NH}$ ), 3.41 (d,  $J = 5.6 \text{ Hz}$ , 6H,  $\text{C}(\text{CH}_2\text{OH})_3$ ), 5.06 (t,  $J = 5.6 \text{ Hz}$ , 3H,  $\text{C}(\text{CH}_2\text{OH})_3$ ), 5.69 (s, 1H,  $\text{CH}_2\text{NH}$ ), 6.44 (t,  $J = 5.5 \text{ Hz}$ , 1H,  $\text{CNH}$ );  $^{13}\text{C NMR (DMSO-}d_6, 100 \text{ MHz)}$   $\delta$  (ppm) = 14.44 ( $\text{CH}_3$ ), 22.57, 26.86, 29.18, 29.21, 30.19, 31.71 (6x $\text{CH}_2$ ), 57.15 ( $\text{CH}_2\text{NH}$ ), 60.93, 61.78 ( $\text{CH}_2\text{OH}$ ), 63.83 ( $\text{CNH}$ ), 159.45 (CO); MS Cal. = 276.4, ESI-MS found  $[\text{M} + \text{H}^+]^+ = 277.5$ .

**1-(2-hydroxyethyl)-3-octylurea, H6:**  $^1\text{H NMR (DMSO-}d_6, 400 \text{ MHz)}$   $\delta$  (ppm) = 0.86 (t,  $J = 6 \text{ Hz}$ , 3H,  $\text{CH}_3\text{CH}_2$ ), 1.20 – 1.37 (m, 12H,  $\text{CH}_3(\text{CH}_2)_6\text{CH}_2$ ), 2.94 (q,  $J = 6.8 \text{ Hz}$ , 2H,  $\text{CH}_2\text{CH}_2\text{NH}$ ), 3.03 (q,  $J = 5.8 \text{ Hz}$ , 2H,  $\text{CH}_2\text{CH}_2\text{NH}$ ), 3.33 – 3.38 (m, 2H,  $\text{CH}_2\text{CH}_2\text{OH}$ ), 4.64 (t,  $J = 5.2 \text{ Hz}$ , 1H,  $\text{CH}_2\text{OH}$ ), 5.84 (dt,  $J = 41.9, 5.6 \text{ Hz}$ , 2H,  $\text{NHCONH}$ );  $^{13}\text{C NMR (DMSO-}d_6, 100 \text{ MHz)}$   $\delta$  (ppm) = 14.44 ( $\text{CH}_3$ ), 22.57, 26.87, 29.19, 29.25, 30.48, 31.72 (6x $\text{CH}_2$ ), 39.68 ( $\text{CH}_2\text{NH}$ ), 42.49 ( $\text{NHCH}_2\text{CH}_2\text{OH}$ ), 61.30 ( $\text{CH}_2\text{OH}$ ), 158.72 (CO); MS Cal. = 216.3, ESI-MS found  $[\text{M} + \text{H}^+]^+ = 217.5$ .

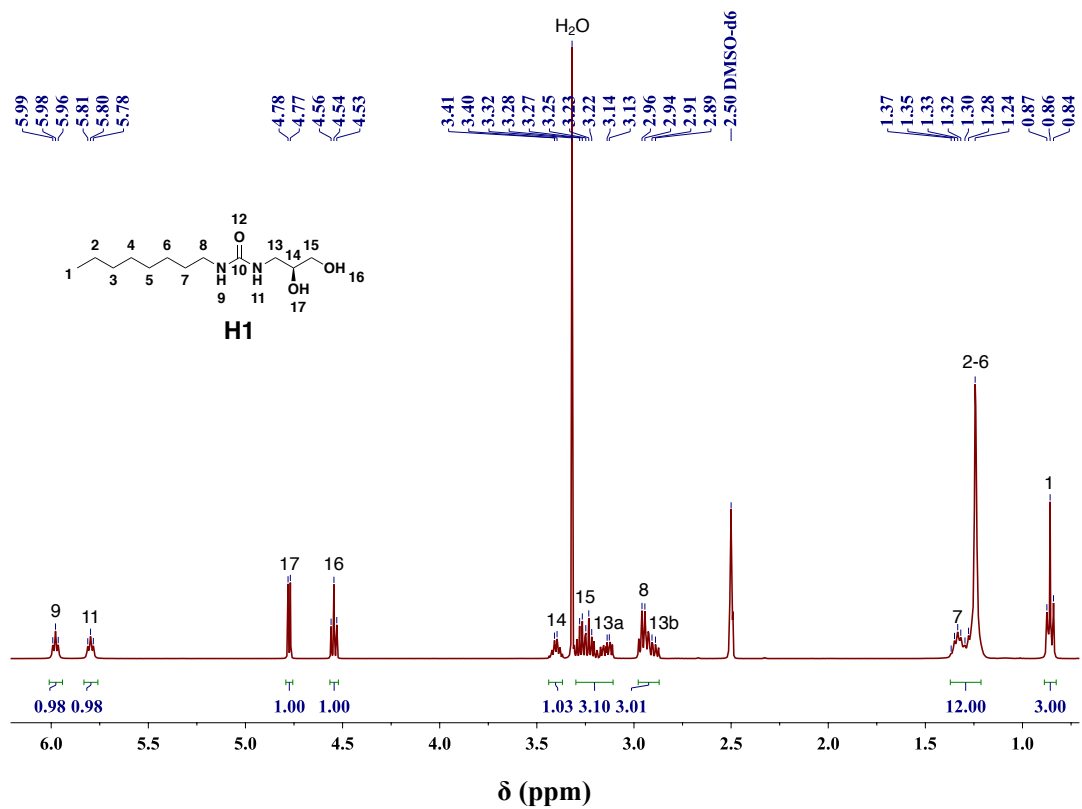


**Figure 24.**  $^1\text{H}$  NMR spectrum of H1.

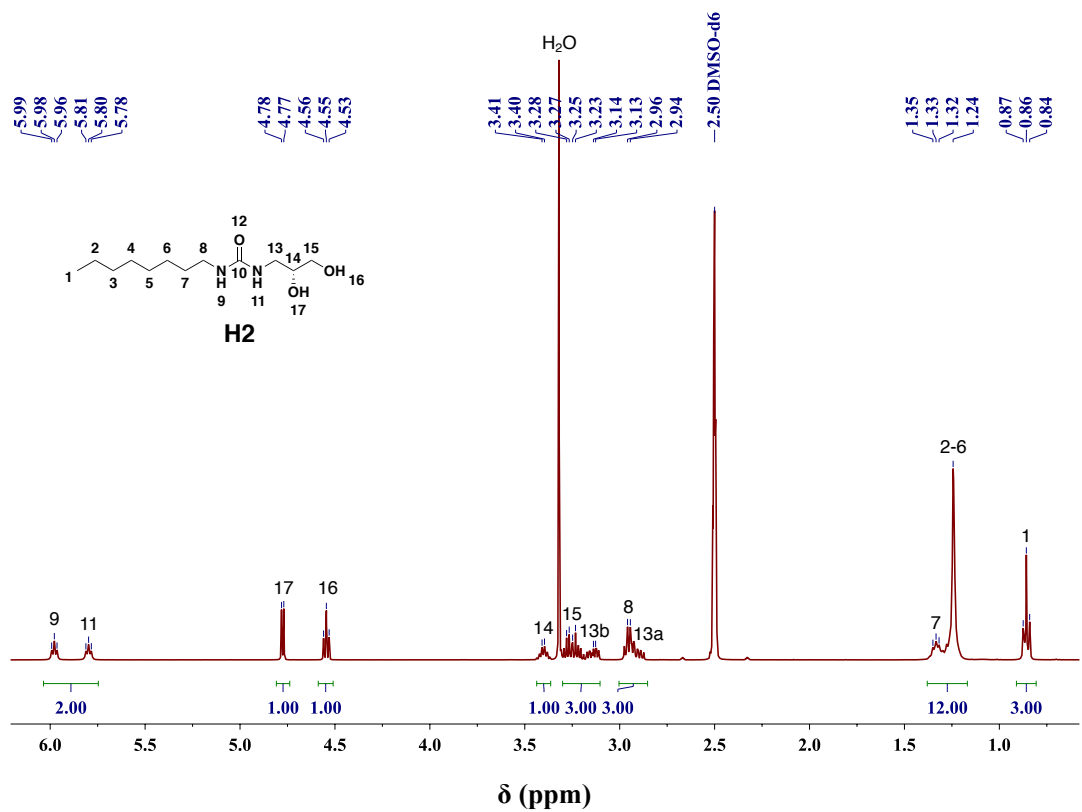


**Figure 25.**  $^1\text{H}$  NMR spectrum of H2.



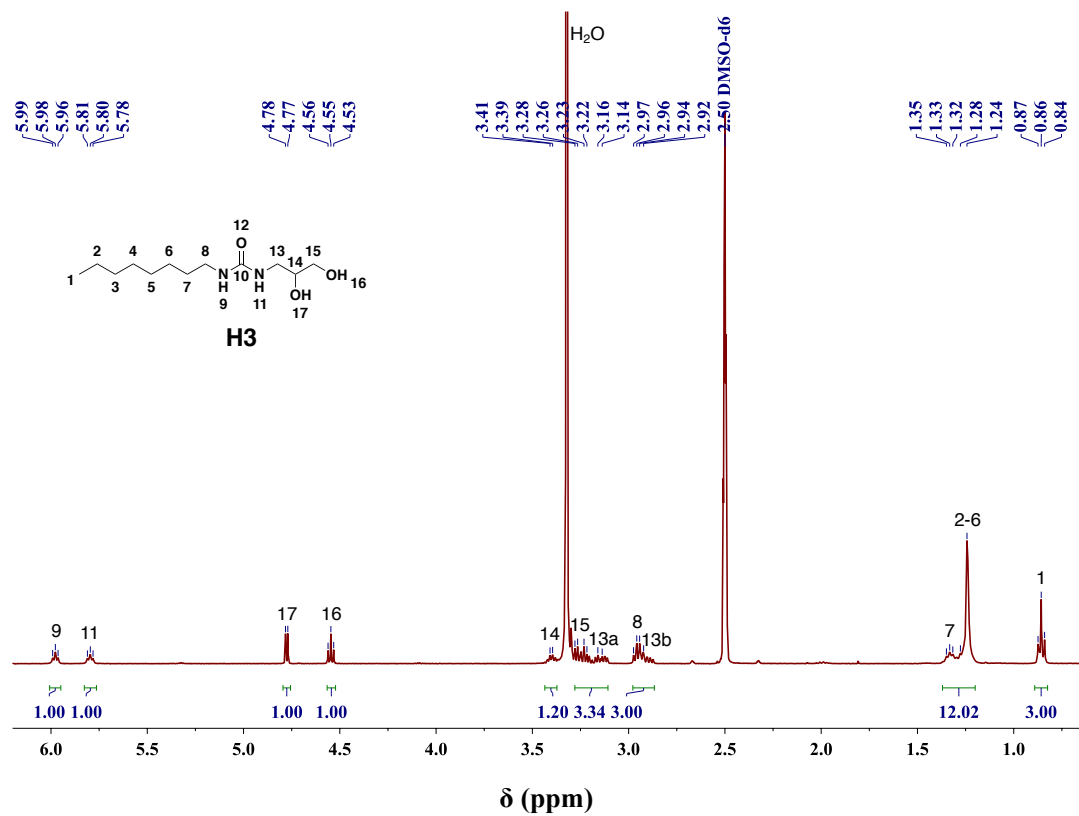


**Figure 26.** <sup>1</sup>H NMR spectrum of H<sub>3</sub>.

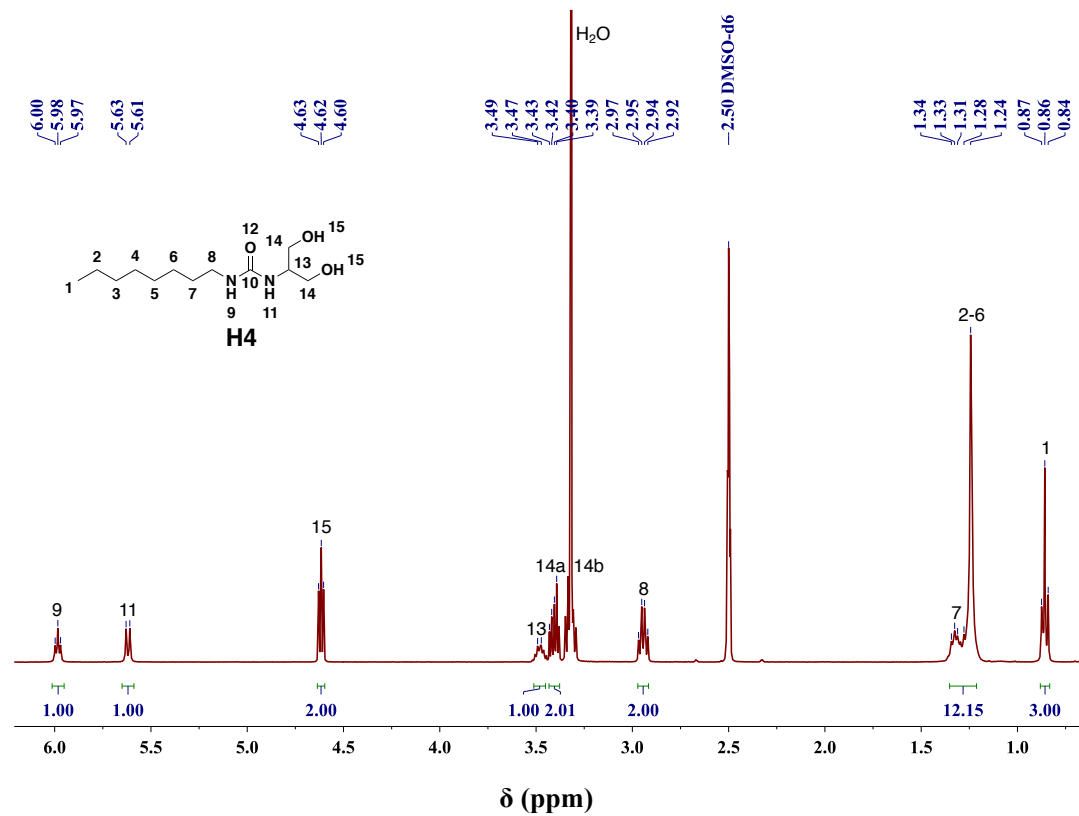


**Figure 27.** <sup>1</sup>H NMR spectrum of H<sub>4</sub>.

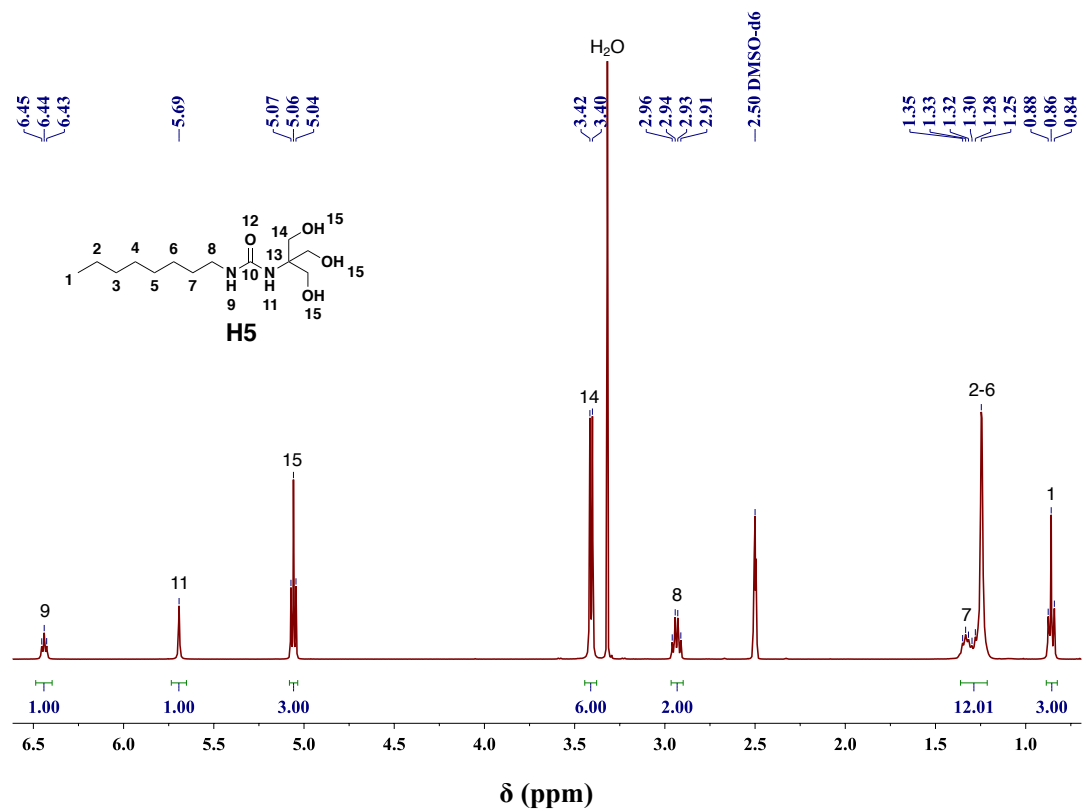


**Figure 28.**  $^1\text{H}$  NMR spectrum of **H5**.

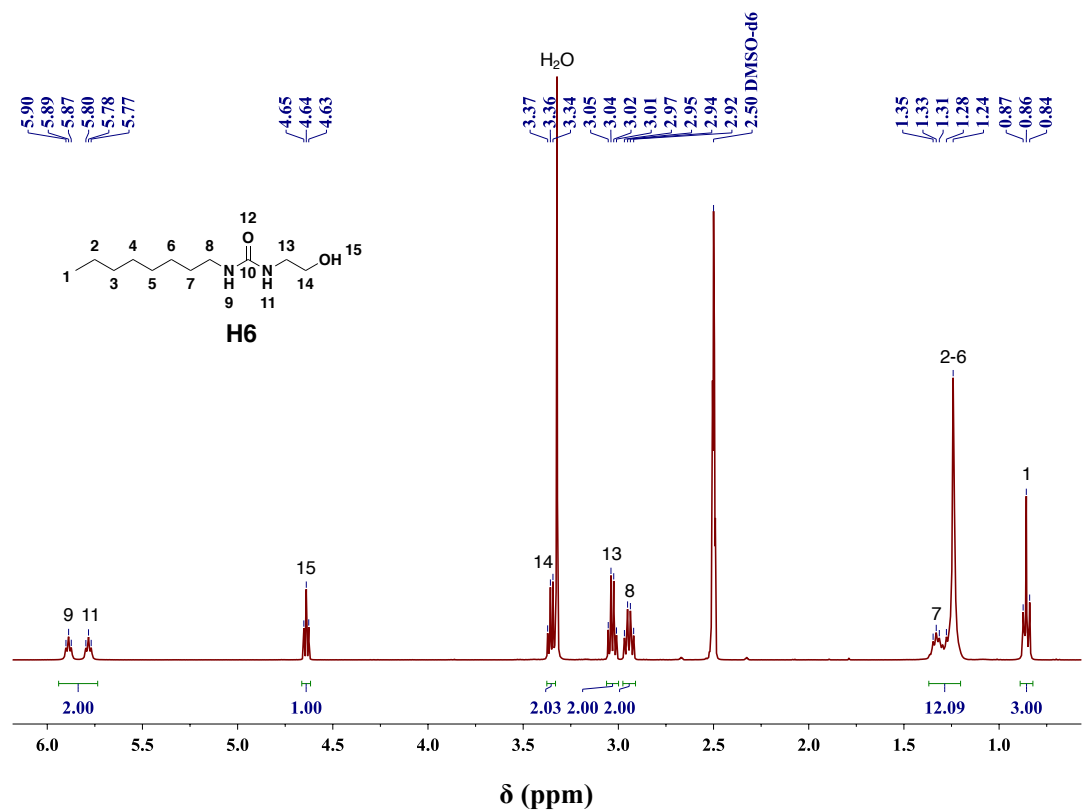


**Figure 29.**  $^1\text{H}$  NMR spectrum of **H6**.

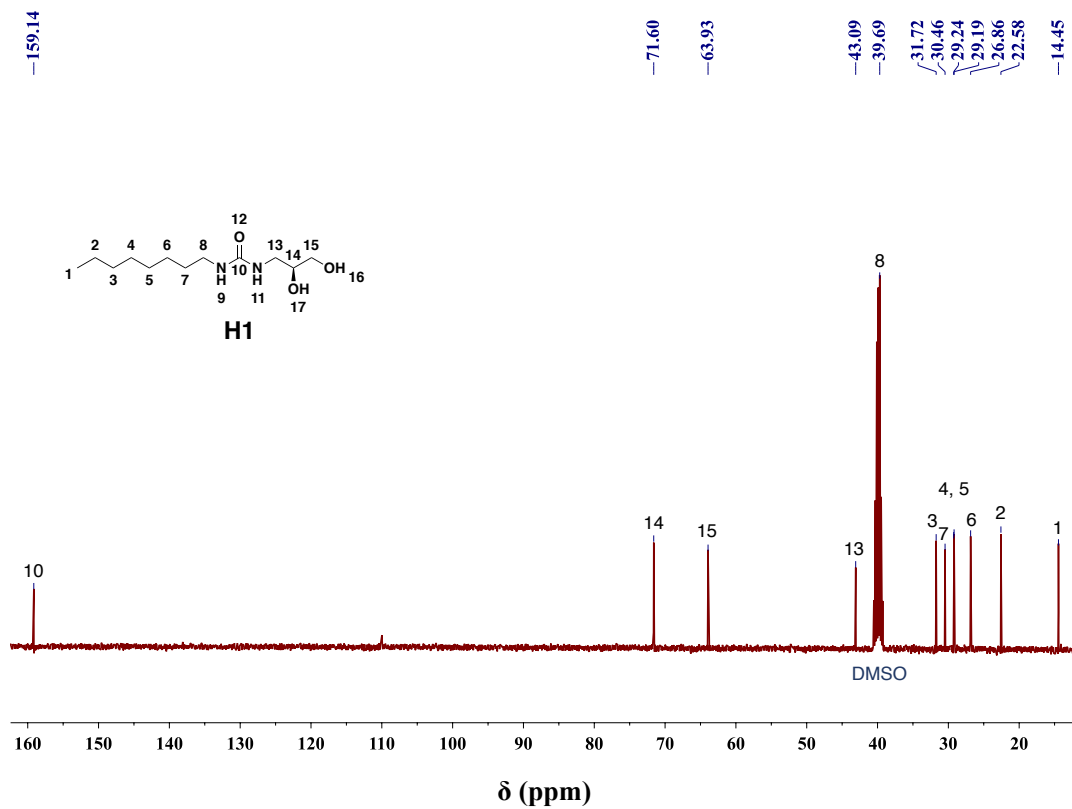


**Figure 30.**  $^{13}\text{C}$  NMR spectrum of **H1**.

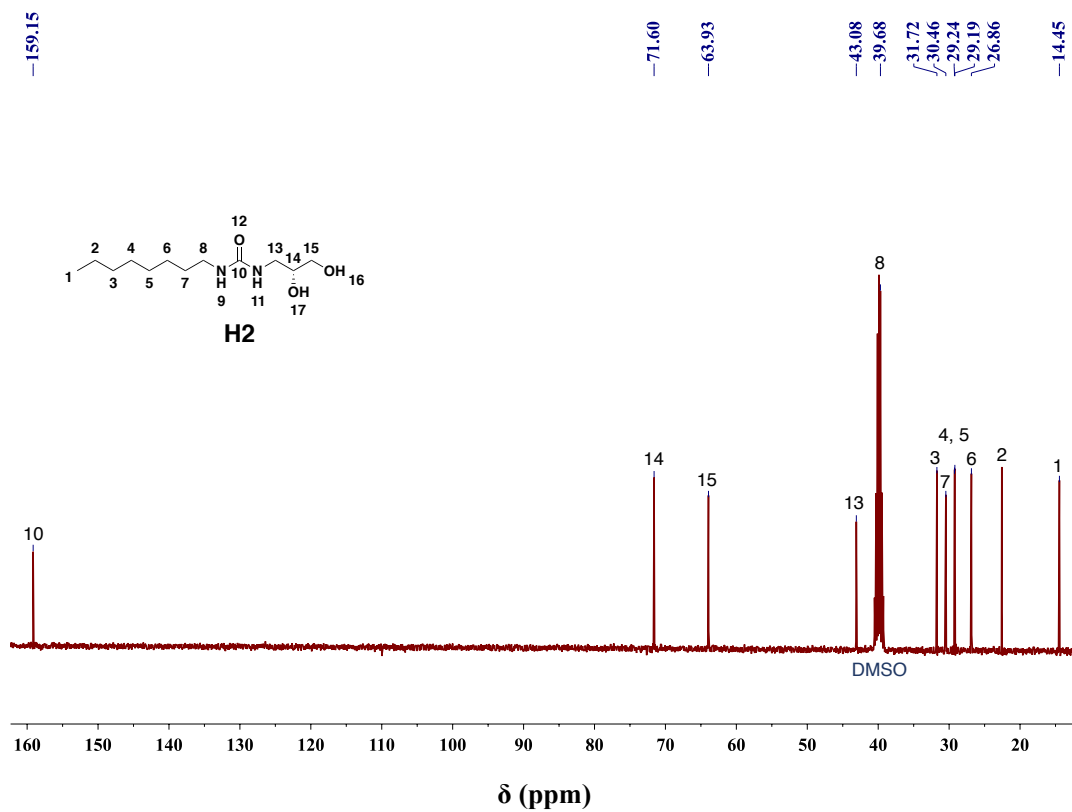


**Figure 31.**  $^{13}\text{C}$  NMR spectrum of **H2**.

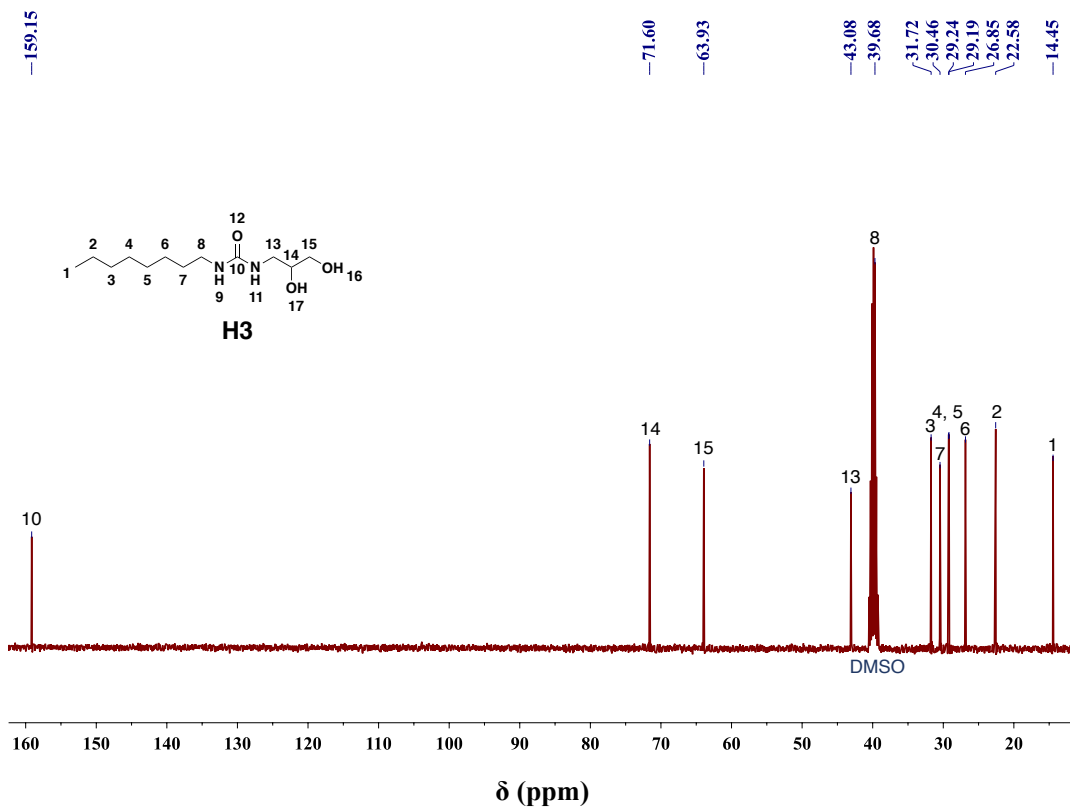


Figure 32. <sup>13</sup>C NMR spectrum of H3.

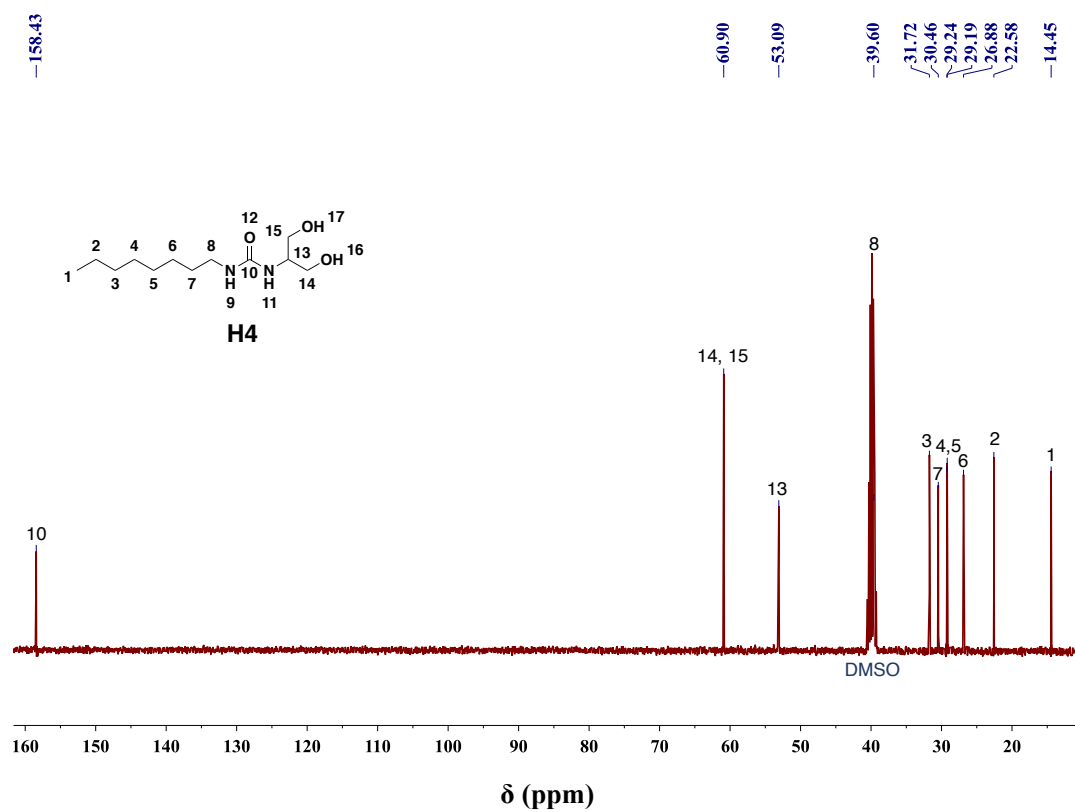
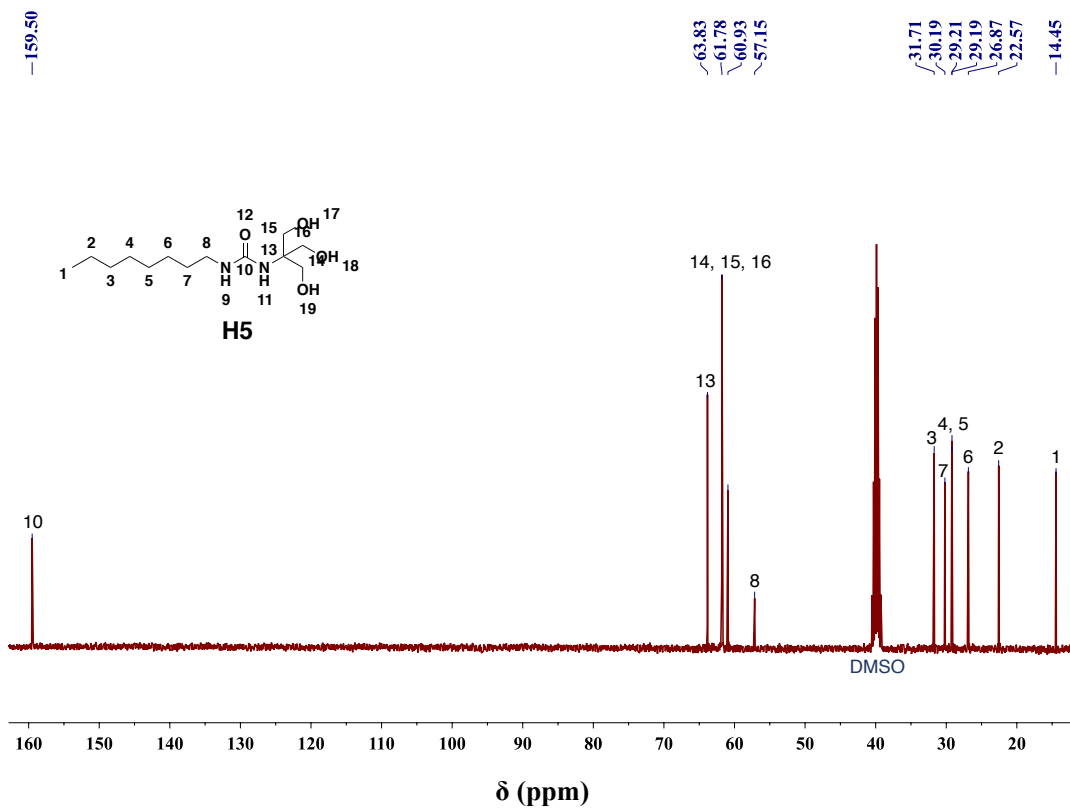
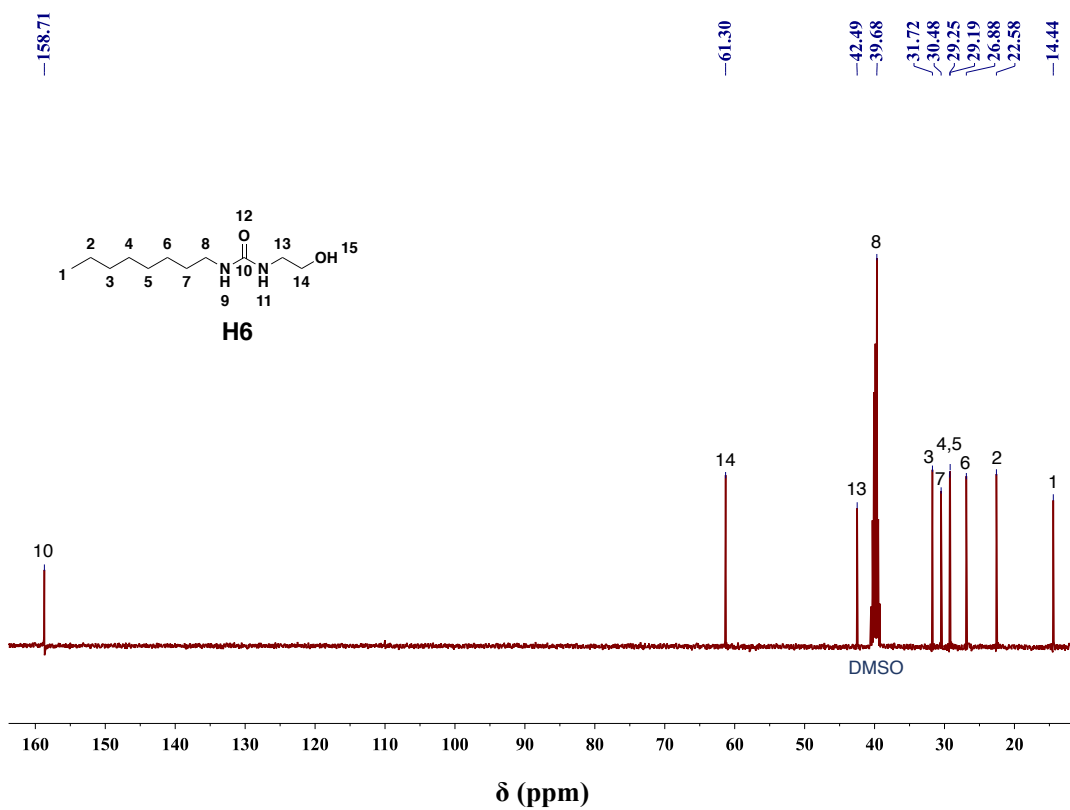


Figure 33. <sup>13</sup>C NMR spectrum of H4.



**Figure 34.**  $^{13}\text{C}$  NMR spectrum of **H5**.



**Figure 35.**  $^{13}\text{C}$  NMR spectrum of **H6**.

### 2.4.2. X-ray crystallography

The four structures **H1**, **H2**, **H4**, and **H5** were measured at four different instruments. The crystals of two of them, **H1** and **H5**, were of sufficient quality for a high-quality data collection on laboratory diffractometers, but after many attempts to grow crystals of **H2** and **H4** of sufficient quality to be measured at the laboratory diffractometers, it was decided to rely on synchrotron radiation for their structure determination and even using the data collected at the synchrotrons it proved to be difficult to solve and refine these crystal structures.

Crystal evaluation and data collection of **H1** were performed at 173 K on a Bruker Venture diffractometer with a Cu-K $\alpha$  microsource and equipped with a Photon-II detector.

The structure of **H2** was determined using data measured at the CRISTAL beam line of the Soleil synchrotron in St-Aubin, France. The beamline energy was calibrated with a fast data acquisition performed on the NIST ruby crystal (SRM 1990). The wavelength used for this experiment was 0.6722 Å and an Atlas detector from Rigaku Oxford Diffraction was used to record the data at 118 K. All crystals tested appeared to be twinned. The data of one crystal with twin matrix (1 0 0 1 0 0 -0.16 0.24 1) were used to solve the structure using intensity data from non-overlapping reflections (*hklf*<sub>4</sub>). The crystal structure was refined with both *hklf*<sub>4</sub> data as overlapping *hklf*<sub>5</sub> reflection data. Since the refinement with the *hklf*<sub>4</sub> data performed much better than that with the *hklf*<sub>5</sub> data, the first reflection set was taken for the final refinement. Despite the high flux at the synchrotron source, the quality of the final structure is relatively low.

The structure of **H4** was measured at the XRD1 beamline of the Elettra synchrotron at a wavelength of 0.7000 Å and a Pilatus-2M (Dectris) detector at 100 K. The structure appeared to be a  $Z=9$  structure, so it was checked whether

it was not actually commensurately or incommensurately modulated. An approximate repetition of the same motif can be observed along the  $\mathbf{b}+\mathbf{c}$  direction, so it is well possible that there is a modulation in this direction. Attempts to describe the modulation using the superspace group formalism have not been attempted in the context of this study. Instead, the supercell has been used to describe the structure.

The data for the structure of **H5** were collected with Mo- $K\alpha$  radiation on a Rigaku-Oxford Gemini diffractometer equipped with a Sapphire-3 detector at 175 K.

The APEX3 program was used for data collection and SAINT, XPREP and SADABS for the integration of the **H1** data using default parameters, for the empirical absorption correction using spherical harmonics employing symmetry-equivalent and redundant data, and the correction for Lorentz and polarization effects (Bruker, 2016). The CRYSTALIS-program (Rigaku Oxford Diffraction, 2012) was used for **H2** and **H5** to collect data and for frame integration using default parameters, for the empirical absorption correction using spherical harmonics employing symmetry-equivalent and redundant data, and for the correction for Lorentz and polarization effects. The XDS program (Kabsch, 2010) was used for data integration and applying correction for the **H4** data. All crystal structures were solved using the *ab-initio* iterative charge flipping method with parameters described by Van der Lee (2013) using the *Superflip* program (Palatinus & Chapuis, 2007) and they were refined using full-matrix least-squares procedures as implemented in CRYSTALS (Betteridge *et al.*, 2003) on all reflections with  $I > 2s(I)$ . The H atoms were in general all located in a difference map, but repositioned geometrically. They were initially refined with soft restraints on the bond lengths and angles to regularize their geometry (C–H in the range 0.93–0.98 Å) and  $U_{\text{iso}}(\text{H})$  (in the range 1.2–1.5

times  $U_{\text{eq}}$  of the parent atom), after which the positions were refined with riding constraints (Cooper *et al.*, 2010).

**Table 4.** Crystal structure data.

	<b>H1</b>	<b>H2</b>	<b>H4</b>	<b>H5</b>
formula	C <sub>12</sub> H <sub>26</sub> N <sub>2</sub> O <sub>3</sub>	C <sub>12</sub> H <sub>26</sub> N <sub>2</sub> O <sub>3</sub>	C <sub>12</sub> H <sub>26</sub> N <sub>2</sub> O <sub>3</sub>	C <sub>13</sub> H <sub>28</sub> N <sub>2</sub> O <sub>4</sub>
moiety	C <sub>12</sub> H <sub>26</sub> N <sub>2</sub> O <sub>3</sub>	C <sub>12</sub> H <sub>26</sub> N <sub>2</sub> O <sub>3</sub>	C <sub>12</sub> H <sub>26</sub> N <sub>2</sub> O <sub>3</sub>	C <sub>13</sub> H <sub>28</sub> N <sub>2</sub> O <sub>4</sub>
$T$ (K)	173	118	100	175
spacegroup	$P1$	$P1$	$P-1$	$P-1$
crystal system	triclinic	triclinic	triclinic	triclinic
$a$ (Å)	4.61530(10)	4.882300(14)	4.6450(9)	8.2083(6)
$b$ (Å)	4.89630(10)	4.605000(14)	34.300(7)	8.2927(6)
$c$ (Å)	31.1476(8)	31.09920(4)	38.669(8)	12.0733(11)
$\alpha$ (°)	89.0121(15)	91.916(4)	90.37(3)	74.553(7)
$\beta$ (°)	88.0335(15)	88.607(4)	90.54(3)	79.407(7)
$\gamma$ (°)	75.7539(14)	104.139(4)	91.09(3)	85.918(6)
$V$ (Å <sup>3</sup> )	681.795(18)	677.548(11)	6159(2)	778.42(11)
$Z$	2	2	18	2
$\rho$ (gcm <sup>-3</sup> )	1.200	1.207	1.195	1.179
$M_r$ (gmol <sup>-1</sup> )	246.35	246.35	246.35	276.37
$\mu$ (mm <sup>-1</sup> )	0.690	0.075	0.081	0.086
$R_{\text{int}}$	0.032	0.226	0.089	0.046
$\theta_{\text{max}}$ (°)	59.202	30.822	27.692	29.143
$N_{\text{tot}}$ (measured)	10713	14017	86925	6048
$N_{\text{ref}}$ (unique)	3872	4220	27352	3507
$N_{\text{ref}}$ ( $I > 2\sigma(I)$ )	3705	2537	10918	2175
$N_{\text{ref}}$ (least-squares)	3705	2537	10918	2175
$N_{\text{par}}$	331	307	1378	192
$\langle \sigma(I)/I \rangle$	0.0212	0.111	0.119	0.076
$R_1$ ( $I > 2\sigma(I)$ )	0.0322	0.1266	0.1162	0.0688
$wR_2$ ( $I > 2\sigma(I)$ )	0.0350	0.1832	0.1575	0.0676
$R_1$ (all)	0.0345	0.1266	0.1162	0.0688
$wR_2$ (all)	0.0350	0.0417	0.1832	0.1832
GOF	1.0258	1.2448	1.4677	1.0071
$\Delta\rho$ (eÅ <sup>-3</sup> )	-0.18/0.14	-0.64/0.79	-0.68/0.40	-0.44/0.44
crystal size (mm <sup>3</sup> )	0.05x0.10x0.13	0.05x0.10x0.12	0.02x0.05x0.07	0.05x0.07x0.12



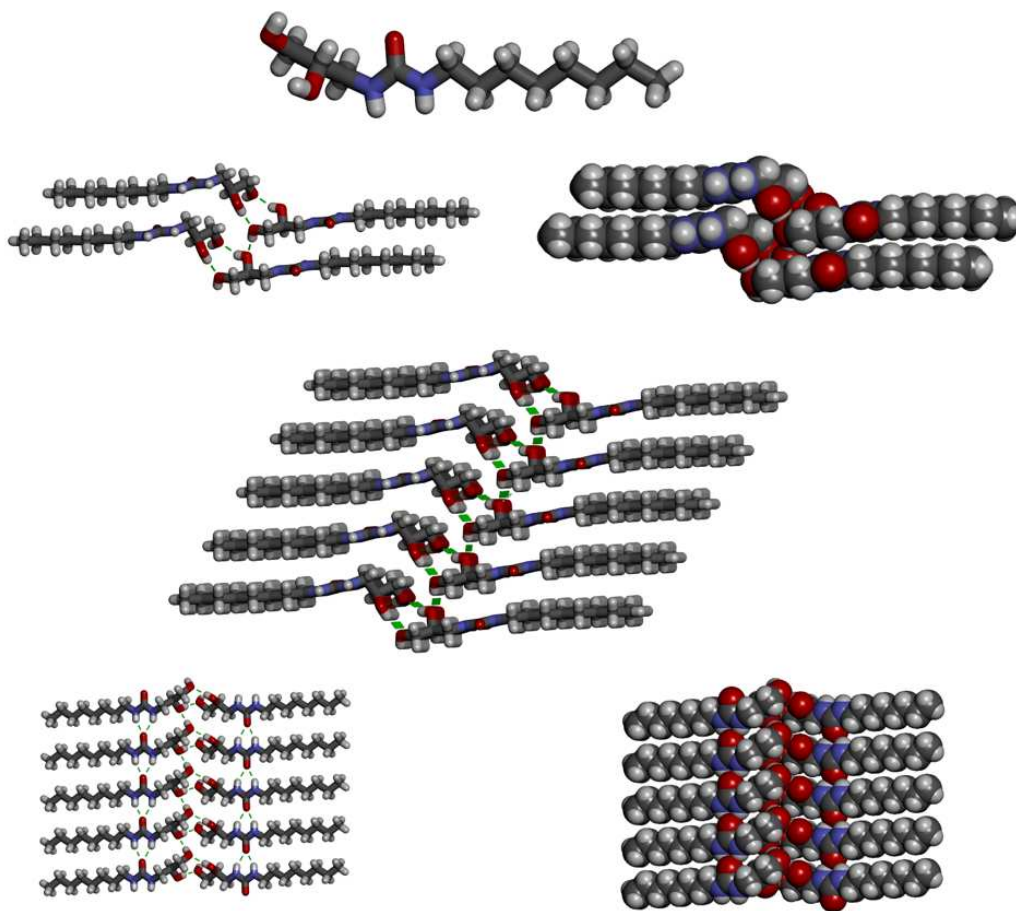


**Figure 36.** Solid state crystal structure of **H1** (N, blue; C, gray; O, red; H, white) with crystal packing.

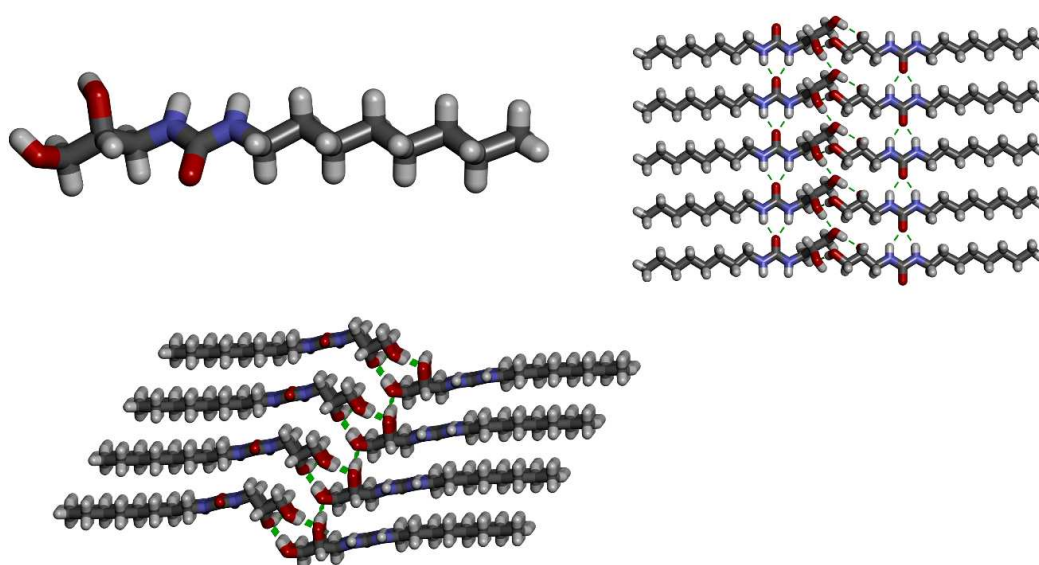


**Figure 37.** Solid state crystal structure of **H2** (N, blue; C, gray; O, red; H, white) with crystal packing.

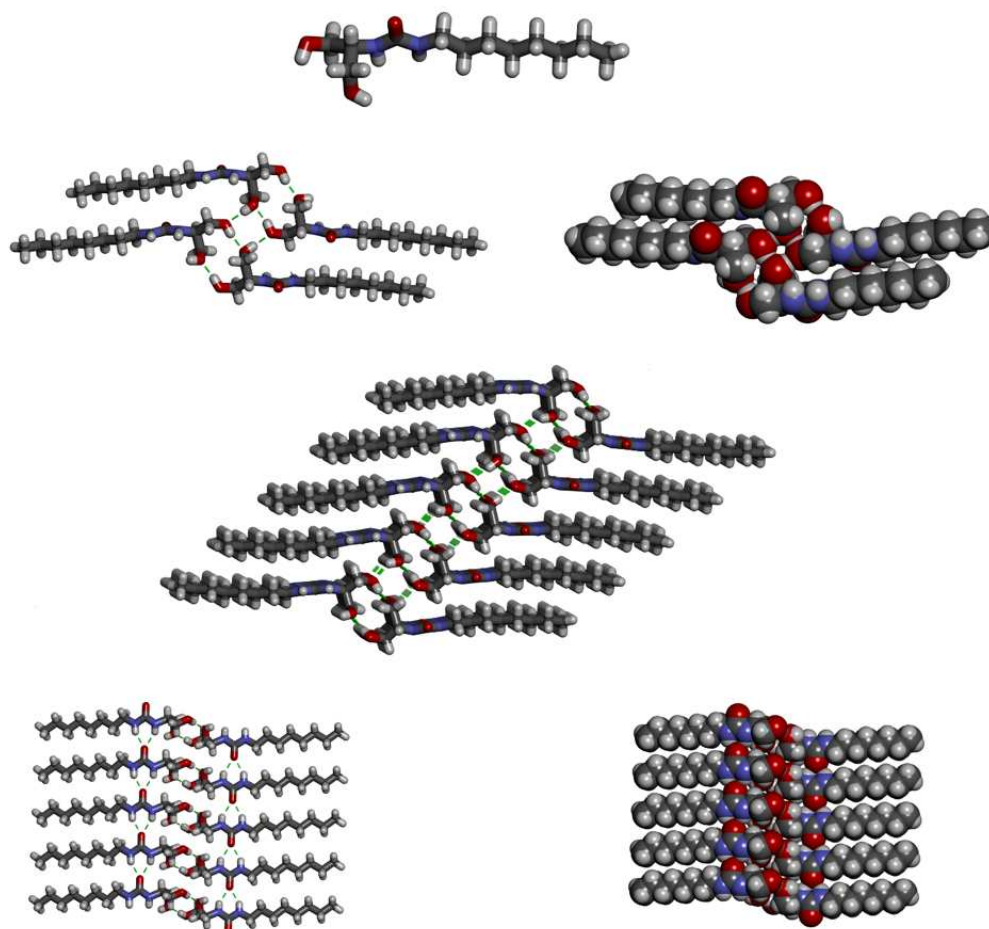


**Figure 38.** Solid state crystal structure of **H4** (N, blue; C, gray; O, red; H, white) with crystal packing.

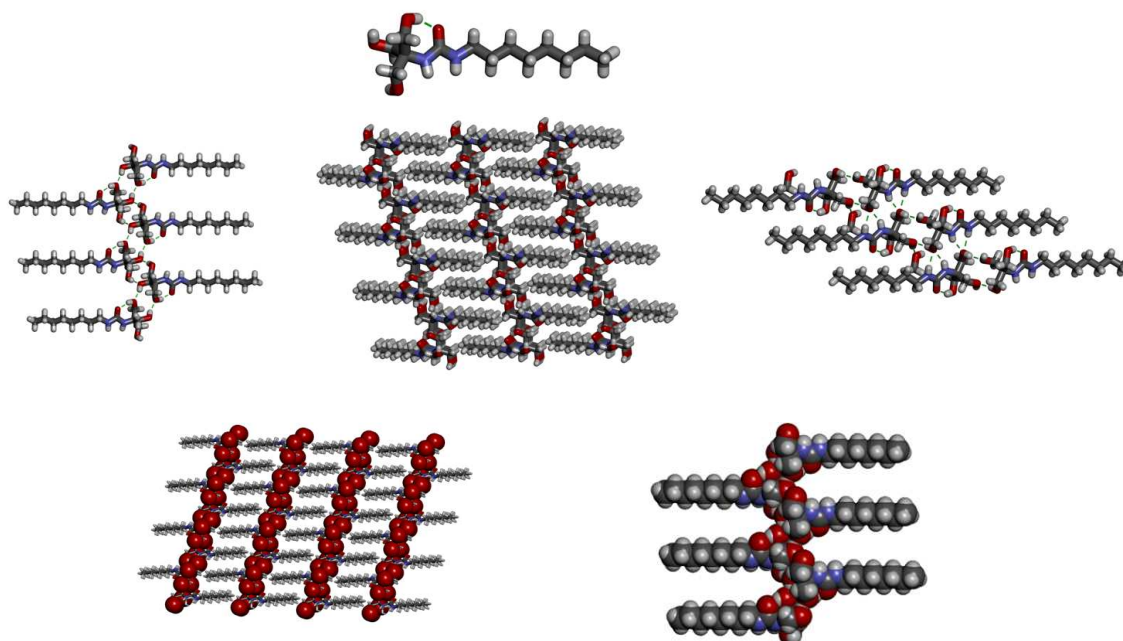


**Figure 39.** Solid state crystal structure of **H5** (N, blue; C, gray; O, red; H, white) with crystal packing.

### 2.4.3. Transmembrane transport experiments

**Sample preparation.** We set the concentration gradients (8 mM, 16 mM, 24 mM, 32 mM, 40 mM, 48 mM, 56 mM, 64 mM, 72 mM and 80 mM) of **H1**, **H2**, **H3**, **H4**, **H5** and **H6** solutions in DMSO for water transport experiments. In the ion transport experiments, 10 mM of each compound solutions in DMSO were submitted.

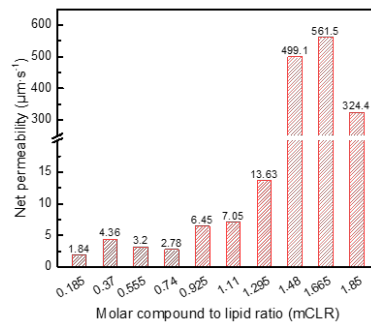
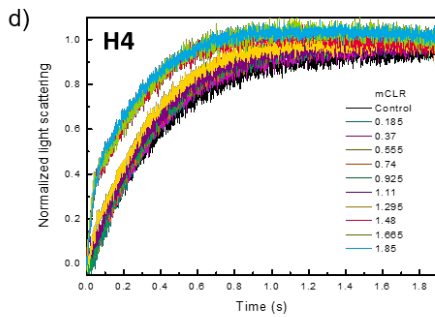
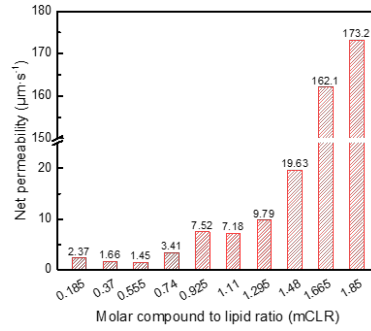
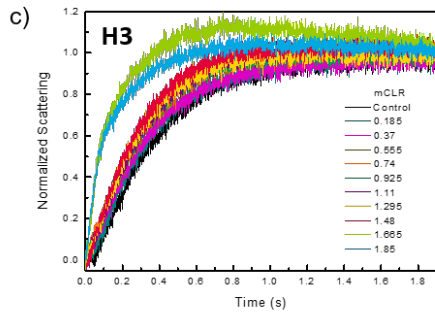
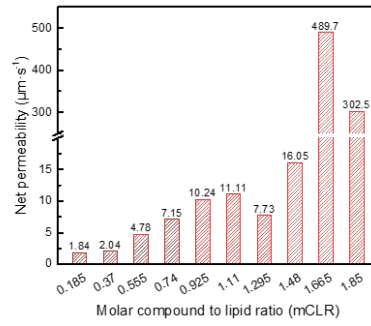
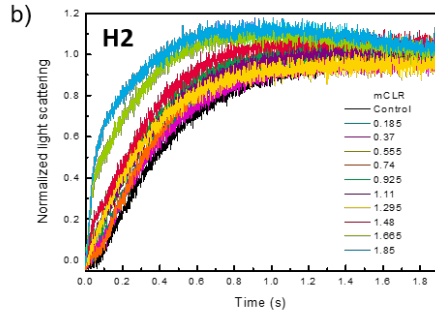
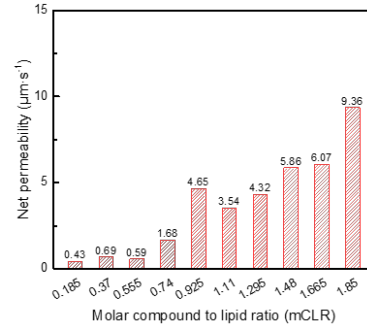
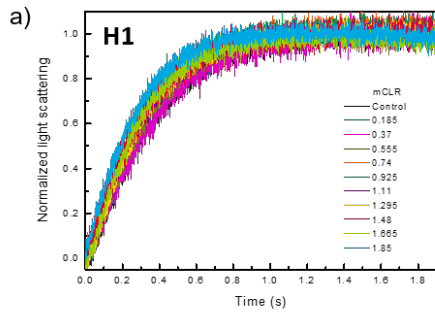
**Water transport by using D(+)-sucrose as osmolyte.** Liposomes were prepared using the film rehydration method. A PC/PS/Chl mixture with a molar ratio of 4/1/5 was dissolved in chloroform/methanol mixture (CHCl<sub>3</sub>/MeOH, v/v: 1/1). The solution was dried on a rotary evaporator and subsequently in a vacuum desiccator to remove residual solvent. After rehydration with 1 mL buffer containing 200 mM D(+)-sucrose and 10 mM PBS (pH = 6.4), the suspension was extruded through 100 nm track-etched filters for 21 times (Whatman, UK) to obtain monodisperse unilamellar vesicles, the size of which was characterized by dynamic light scattering (Zetasizer Nano, Malvern Instruments Ltd., UK). The aliquot of the compounds dissolved in DMSO have been added to the liposomes. The water permeability tests were conducted on a stopped-flow instrument (SFM3000 + MOS450, Bio-Logic SAS, Claix, France). Exposure of vesicles to hypertonic osmolyte (300 mM sucrose) in the same buffer resulted in the shrinkage of the vesicles due to an outwardly directed osmotic gradient. The changes of light scattering were recorded at a wavelength of 345 nm.

The abrupt change of the vesicle size lead to variation in the light scattering at 90° according to the Rayleigh-Gans theory applied to this system and could be fitted in the form of the sum of two exponential function. The osmotic permeability ( $P_f$ ) was calculated as following:

$$P_f = \frac{k}{\frac{S}{V_0} \times V_w \times \Delta_{osm}}$$

where  $k$  is the exponential coefficient of the change in the light scattering;  $S$  and  $V_0$  are the initial surface area and volume of the vesicles, respectively;  $V_w$  is the molar volume of water, and  $\Delta_{osm}$  is the osmolarity difference.

In an average experiment, 100  $\mu$ L stock lipid solution containing 0.524 mg of lipids was diluted with 1880  $\mu$ L of 200 mM sucrose in 10 mM PBS buffer solution. The compounds were injected in 20  $\mu$ L aliquots in DMSO. The solution mix was thermostatted at 20 °C for 30 minutes before exposure to the 300 mM sucrose solution. Experiments have been conducted at different concentrations of the injected compounds, in which the concentrations of hydroxy channels solutions in DMSO were 8 mM, 16 mM, 24 mM, 32 mM, 40 mM, 48 mM, 56 mM, 64 mM, 72 mM and 80 mM corresponding to the molar compound to lipid ratio (mCLR) = 0.185, 0.37, 0.555, 0.74, 0.925, 1.11, 1.295, 1.48, 1.665 and 1.85 respectively. Average permeability was calculated by using the permeability values obtained from at least three different batches of vesicles.



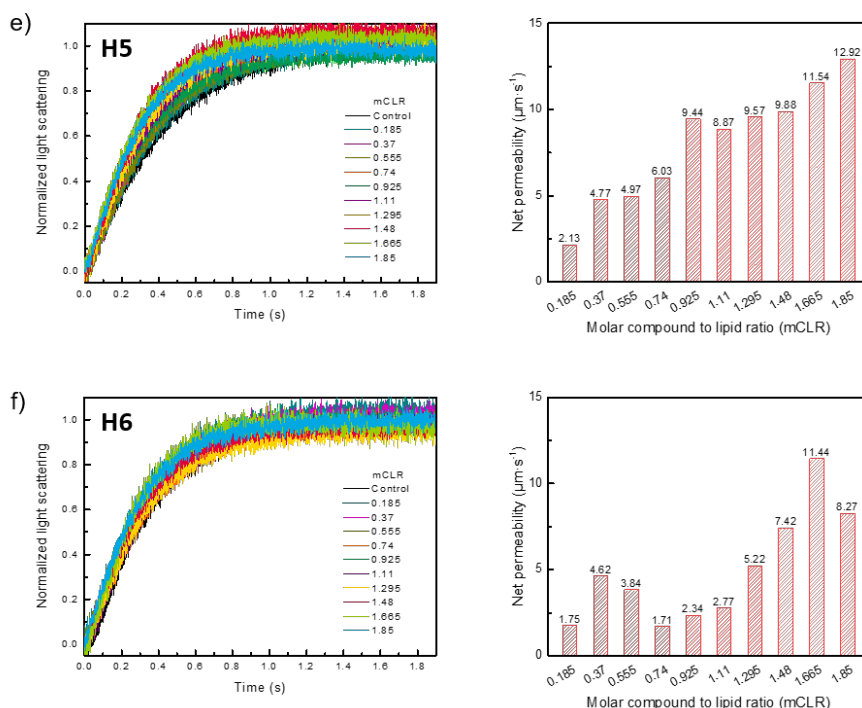
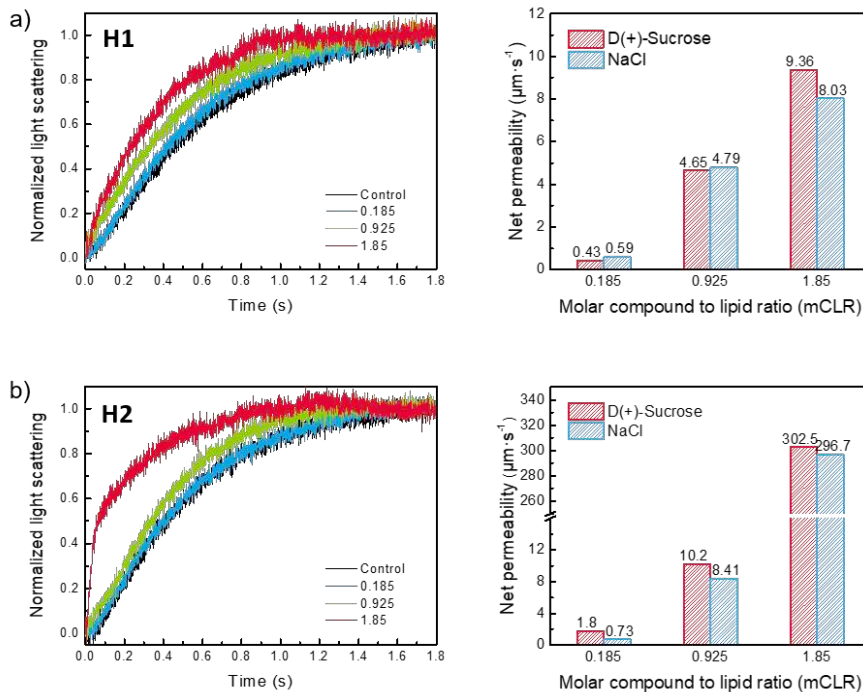


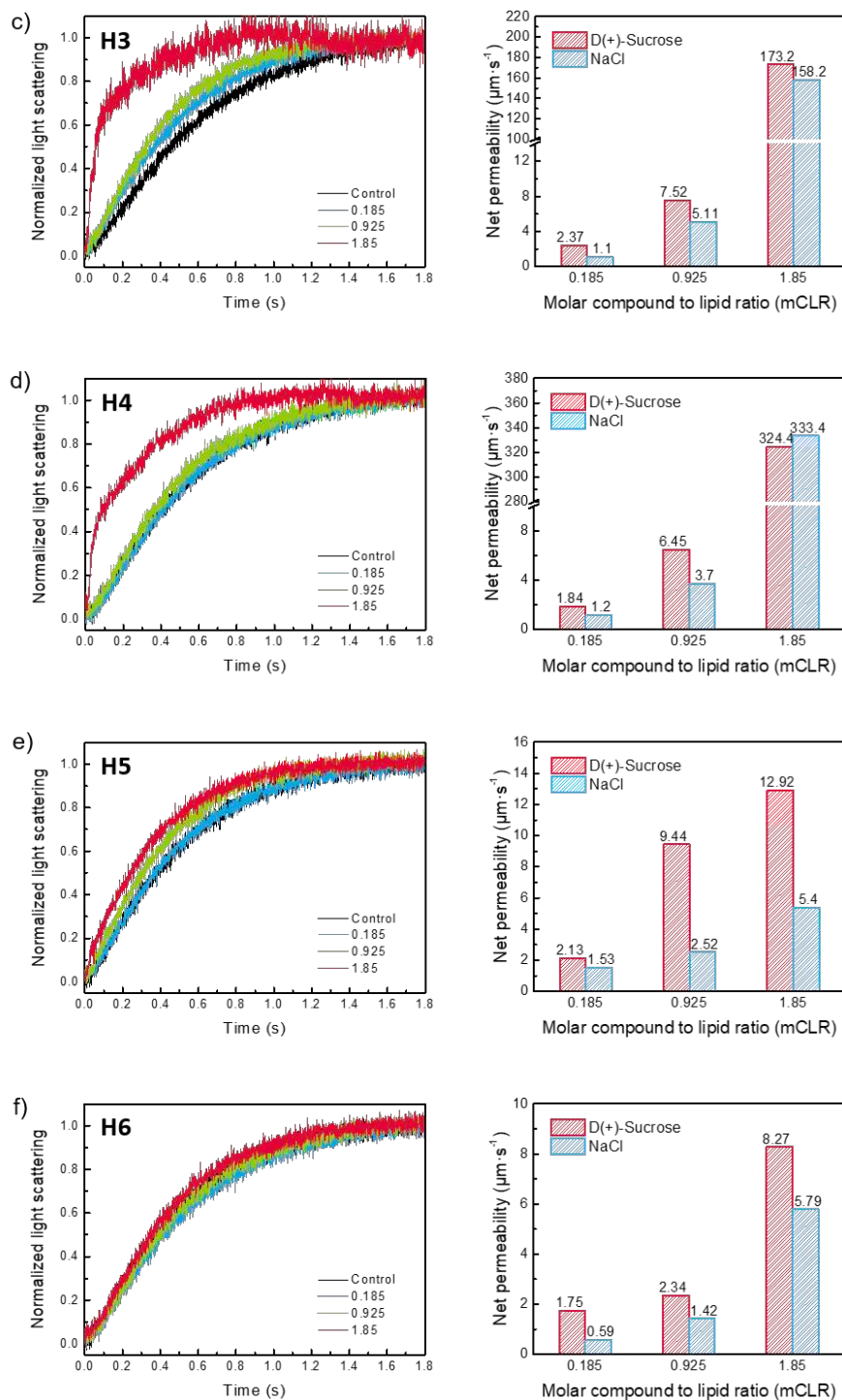
**Figure 40.** The water permeabilities expressed as normalized light scattering of the channels assembled by (a) **H1**, (b) **H2**, (c) **H3**, (d) **H4**, (e) **H5** and (f) **H6** were determined by stopped-flow light scattering experiments with 100 mM D(+)-sucrose as osmolyte. The stopped-flow traces of liposomes containing different concentrations of hydroxy channels (left). The net permeabilities of different channel to lipid ratios of hydroxy channels (right).

**Single-channel permeability calculation.** 8 stacks of **H1-H6** OH-quartets and 64 molecules are needed to form a channel within a transmembrane length of 5 nm. Taking the sample of **H4** at mCLR = 1.665 as an example, the molar channel to lipid ratio is 0.026. The average radius of the liposome was 72.5 nm determined by DLS experiments. Hence, the sum of outer and inner surface areas was  $4\pi \times R^2 + 4\pi \times (R - 5)^2 = 123,308 \text{ nm}^2$ . The average cross-sectional area of a lipid in average was  $0.287 \text{ nm}^2$  (PC/PS/Chl lipids with a molar ratio of 4/1/5: the cross-sectional areas of PC and PS were  $\sim 0.35 \text{ nm}^2$  and that of cholesterol was  $0.223 \text{ nm}^2$ ), and that of the **H4** OH-channel (not including the alkyl chain) was estimated as  $1.37 \text{ nm}^2$ . So, the insertion number of the channel was  $\sim 4,968$  per vesicle. If the overall net permeability by channels in liposomes was  $561.54 \mu\text{m/s}$ , the single-channel permeability was  $6.97 \times 10^{-15} \text{ cm}^3/\text{s}$  and  $2.33 \times 10^8$  water molecules/s.

According to the same algorithm, the highest single-channel permeabilities for **H1**, **H2**, **H3**, **H4**, **H5** and **H6** hydroxy channels were  $3.54 \times 10^6$ ,  $2.03 \times 10^8$ ,  $6.84 \times 10^7$ ,  $2.33 \times 10^8$ ,  $4.89 \times 10^6$  and  $4.75 \times 10^6$  water molecules/s, respectively. (Figure 20 b, Table 2) The single channel permeability values varied obviously, covering the range of  $3.5 \times 10^6$ - $2.4 \times 10^8$  H<sub>2</sub>O/s/channel, which are only one order of magnitude lower than that of AQPs ( $\sim 10^8$ - $10^9$  water /s/channel).

**Water transport by using NaCl as osmolyte.** The preparation of liposomes and the stopped-flow assays were the same as the previous method for water transport in sucrose solution. To implement the same osmotic pressure (106 mOsmol/kg), the osmolyte was replaced from 100 mM sucrose to 57.5 mM NaCl solution.

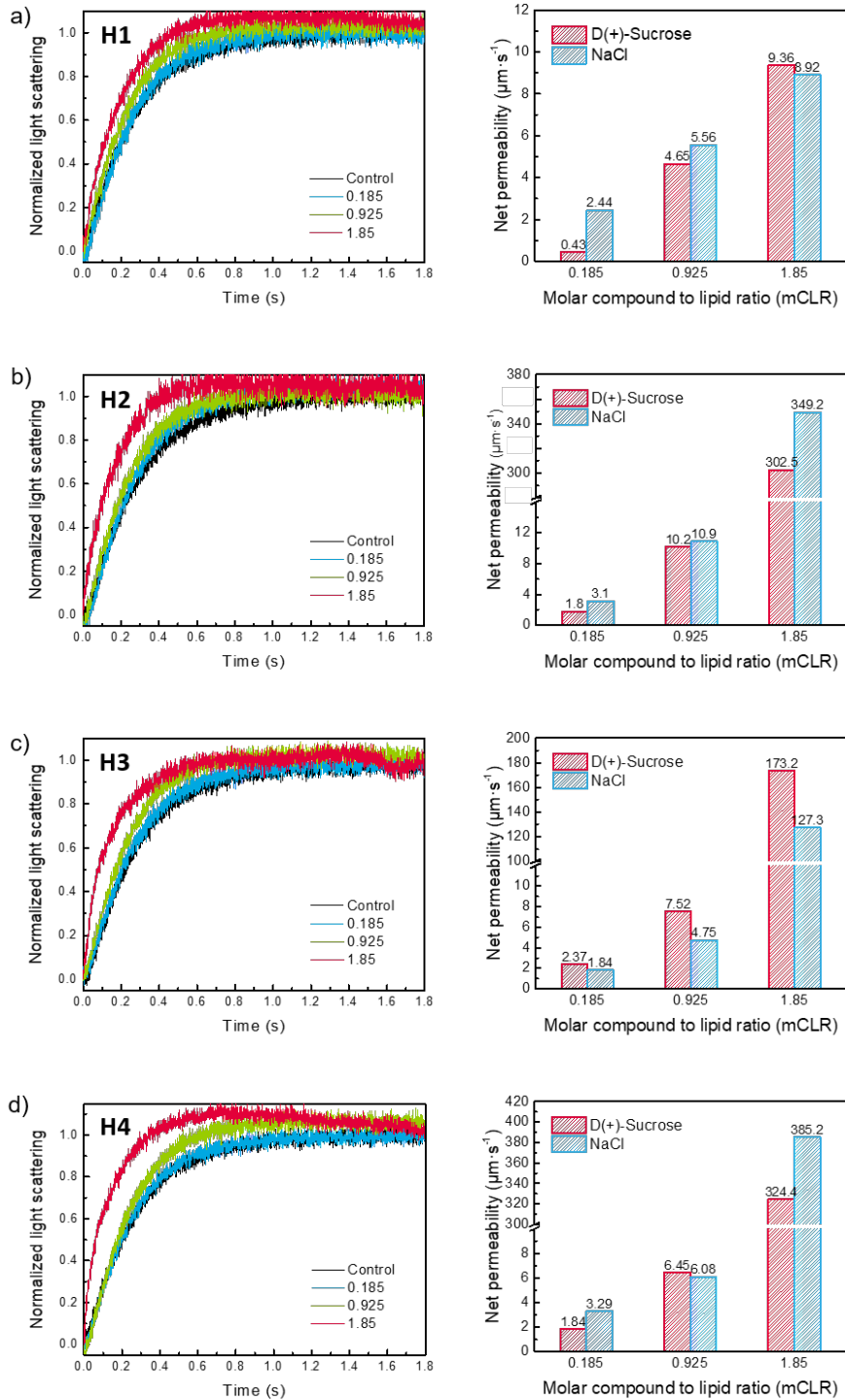




**Figure 41.** The water permeabilities expressed as normalized light scattering of the channels assembled by (a) H1, (b) H2, (c) H3, (d) H4, (e) H5 and (f) H6 were determined by stopped-flow light scattering experiments with 57.5 mM NaCl as osmolyte. The stopped-flow traces of liposomes containing different concentrations of hydroxy channels (left). The comparison of net permeability values for hydroxy channels (right).



The water transport was comparatively performed also for 100 mM sucrose ( $\Delta_{\text{osm}} = 106 \text{ mOsmol/kg}$ ) to 100 mM NaCl ( $\Delta_{\text{osm}} = 186 \text{ mOsmol/kg}$ ) osmolytes (Figure 42)



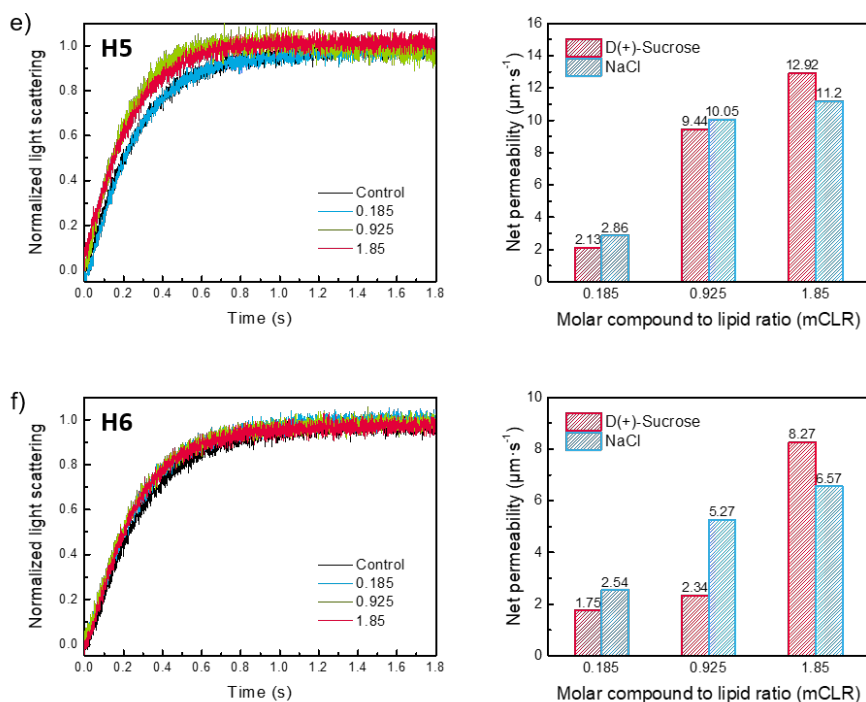


**Figure 42.** The water permeabilities expressed as normalized light scattering of the channels assembled by (a) **H1**, (b) **H2**, (c) **H3**, (d) **H4**, (e) **H5** and (f) **H6** were determined by stopped-flow light scattering experiments with 100 mM NaCl as osmolyte. The stopped-flow traces of liposomes containing different concentrations of hydroxy channels (left). The comparison of net permeability values for hydroxy channels (right).

**CF Leakage experiments:** The preparation of LUVs for leakage experiment is similar as for entrapped HPTS LUVs. The difference is the salt solution contains 70 mM of 5(6)-Carboxyfluorescein (CF) instead of HPTS: the right amount of CF was introduced in a PBS (pH 7.0) and NaCl (100mM) solution in order to obtain a 70 mM concentration of CF. Then the pH was adjusted to 7.0 by addition of 5M NaOH, CF being completely solubilized at this time. The next steps are the same as previously described for HPTS LUVs preparation. The stock solution of CF entrapped LUVs has to be first diluted 20 times (giving a lipid concentration of about 500 µM).

We used direct fluorescence measurement. 100 µL of the diluted stock vesicle solution was suspended in 1.88 mL of the corresponding buffer (10 mM PBS pH 7.0 containing 100 mM NaCl) and placed into a quartz fluorimetric cell

(lipid concentration become ca. 25  $\mu\text{M}$ ). The fluorescence of CF was monitored at a 492 nm excitation and 517 nm emission wavelengths. After 40 sec from the beginning of the experiment, 20  $\mu\text{L}$  of compound solution in DMSO was added. After 320 sec, the vesicles are lysed with detergent (40  $\mu\text{L}$  of 5% aqueous Triton X-100), in order to equilibrate obtain the maximal fluorescence value, corresponding to a 100% efflux of CF.

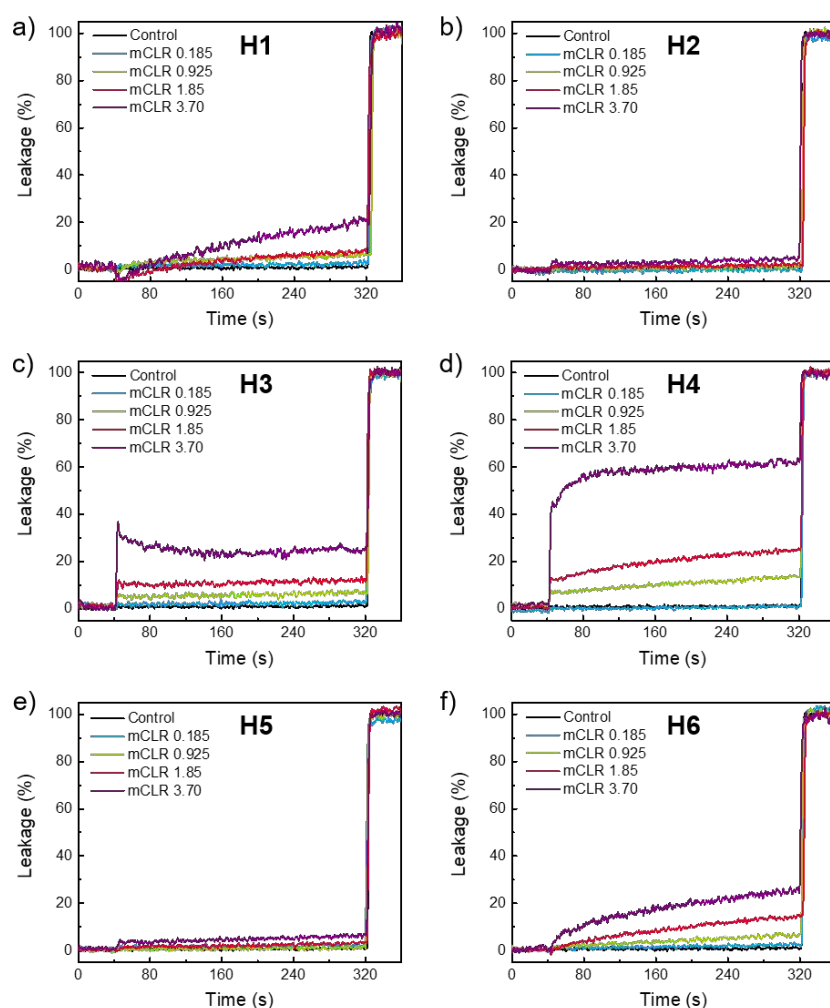


**Figure 43.** Comparison of leakage rate expressed as normalized fluorescence intensity of LUVs containing a) **H1**, b) **H2**, c) **H3**, d) **H4**, e) **H5** and f) **H6** channels.

### Ion transport HPTS assays

**LUV preparation.** Egg yolk *L*- $\alpha$ -phosphatidylcholine (EYPC chloroform solution, 800  $\mu\text{L}$ , 26 mmol) was dissolved in a  $\text{CHCl}_3/\text{MeOH}$  mixture, the

solution was evaporated under reduced pressure and the resulting thin film was dried in a vacuum desiccator for 2 h. The lipid film was hydrated in 400  $\mu\text{L}$  phosphate buffer (10 mM sodium phosphate, pH = 6.4, 100 mM NaCl) containing 10  $\mu\text{M}$  HPTS (pyranine, 8-hydroxypyrene-1,3,6-trisulfonic acid trisodium salt) for 40 min. During hydration, the suspension was submitted to at least 7 freeze-thaw cycles (bathed in liquid nitrogen and water at room temperature, respectively). The large multilamellar liposome suspension (1 mL) was submitted to high-pressure extrusion at room temperature (21 extrusions through a 100 nm polycarbonate membrane afforded a suspension of LUVs with an average diameter of  $\sim 100$  nm). The LUV suspension was separated from extravesicular dye by size exclusion chromatography (SEC) (stationary phase: Sephadex G-50, mobile phase: phosphate buffer) and diluted to 2.8 mL with the same PBS buffer to give a stock solution with a lipid concentration of 9.3 mM (assuming 100% of lipid was incorporated into liposomes).

**Cation transport.** 100  $\mu\text{L}$  HPTS-loaded vesicles (stock solution) was suspended in 1.86 mL sodium phosphate, pH = 6.4 with 100 mM MCl (M =  $\text{Li}^+$ ,  $\text{Na}^+$ ,  $\text{K}^+$ ,  $\text{Rb}^+$  or  $\text{Cs}^+$ ) and placed into a quartz fluorimetric cuvette. The emission of HPTS at 510 nm was monitored with excitation wavelengths at 403 and 460 nm simultaneously, using a Perkin Elmer LS-55 fluorescence spectrometer. During the experiment, 20  $\mu\text{L}$  of a 10 mM hydroxy channel solution in DMSO was added at  $t = 20$  s. At  $t = 40$  s, 29  $\mu\text{L}$  of 0.5 M aqueous NaOH was injected, resulting in the pH value increasing to around 7 in the extravesicular media. For the reference proton transport experiment, 20  $\mu\text{L}$  of 25  $\mu\text{M}$  carbonyl cyanide-4-(trifluoromethoxy)phenylhydrazone (FCCP) solution in DMSO was added at  $t = 30$  s. Maximal possible changes in dye emission were obtained at  $t = 320$  s by lysis of the liposomes with detergent (40  $\mu\text{L}$  of 5 % aqueous Triton X100). We expressed normalized intensity (the value of  $I_{460}/I_{403}$ ) as a function of time from  $t = 40$  s to 360 s.

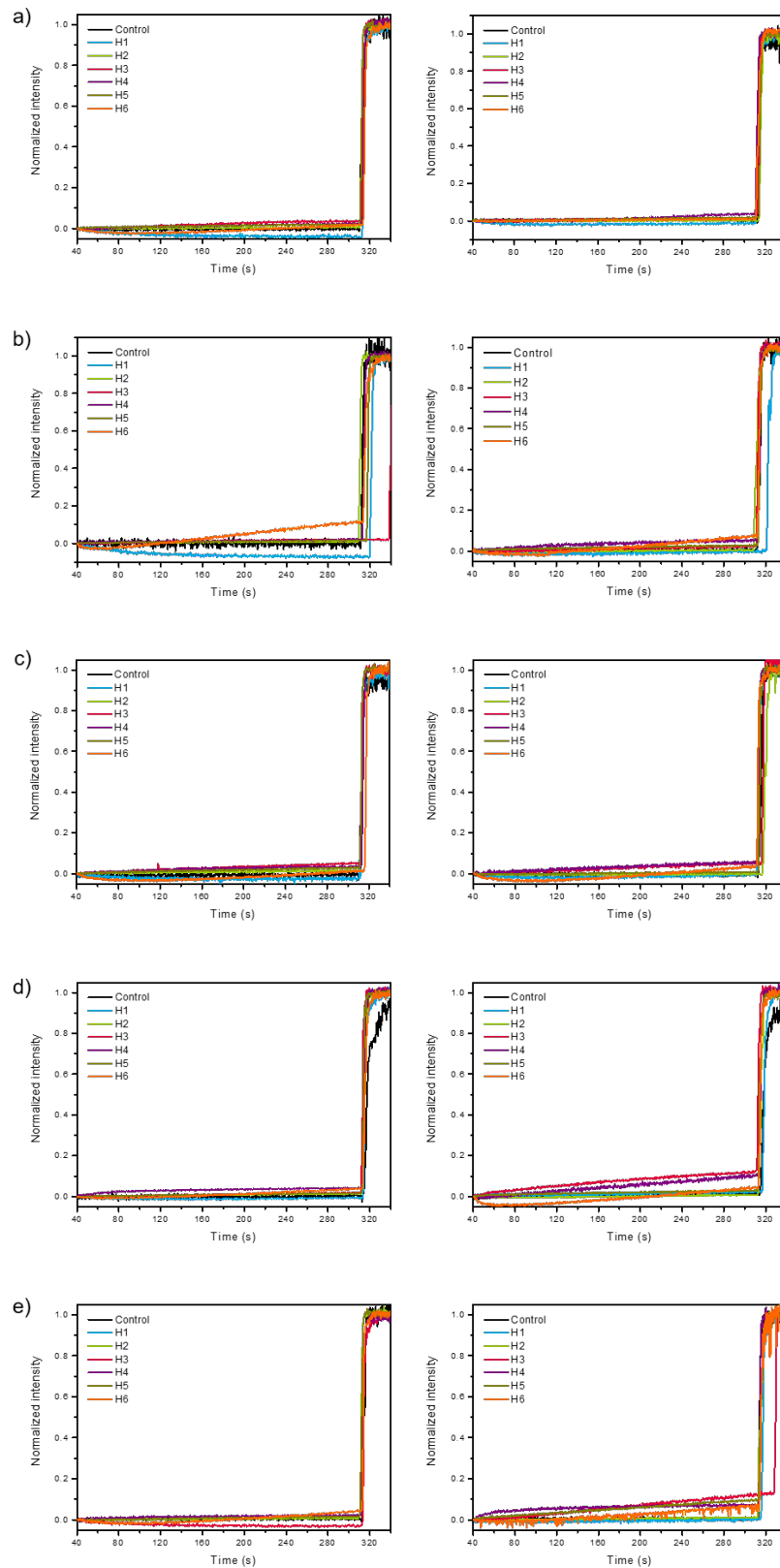


**Figure 44.** Comparison of cation transport activity expressed as normalized fluorescence intensity of 10 mM hydroxy channels in the extravesicular media containing 100 mM (a) LiCl, (b) NaCl, (c) KCl, (d) RbCl and (e) CsCl without FCCP (left) or with the presence of 25  $\mu$ M FCCP (right) as proton carrier.

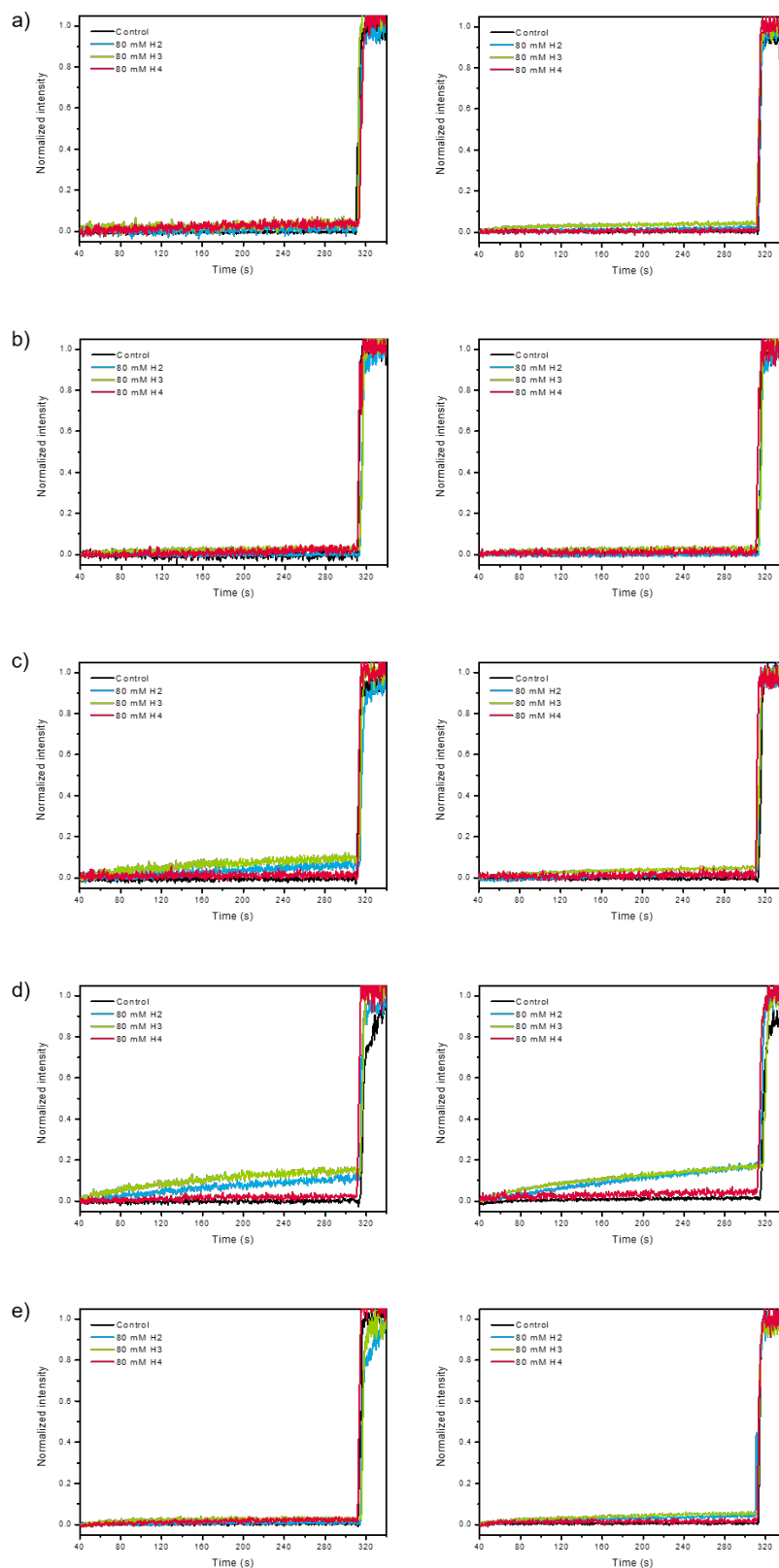


**Figure 45.** Comparison of cation transport activity expressed as normalized fluorescence intensity of 80 mM hydroxy channels in the extravesicular media containing 100 mM (a) LiCl, (b) NaCl, (c) KCl, (d) RbCl and (e) CsCl without FCCP (left) or with the presence of 25  $\mu$ M FCCP (right) as proton carrier.

**Anion transport.** 100  $\mu\text{L}$  HPTS-loaded vesicles (stock solution) was suspended in 1.86 ml sodium phosphate, pH = 6.4 with 100 mM NaX (X = Br<sup>-</sup>, I<sup>-</sup>, HCO<sub>3</sub><sup>-</sup>, CO<sub>3</sub><sup>2-</sup>, NO<sub>3</sub><sup>-</sup> or SO<sub>4</sub><sup>2-</sup>) and placed into a quartz fluorimetric cuvette. The emission of HPTS at 510 nm was monitored with excitation wavelengths at 403 and 460 nm simultaneously, using a Perkin Elmer LS-55 fluorescence spectrometer. During the experiment, 20  $\mu\text{L}$  of a 10 mM hydroxy channel solution in DMSO was added at t = 20 s. At t = 40 s, 29  $\mu\text{L}$  of 0.5 M aqueous NaOH was injected, resulting in the pH value increasing to around 7.4 in the extravesicular media. Maximal possible changes in dye emission were obtained at t = 320 s by lysis of the liposomes with detergent (40  $\mu\text{L}$  of 5 % aqueous Triton X100). We expressed normalized intensity (the value of  $I_{460}/I_{403}$ ) as a function of time from t = 40 s to 360 s.

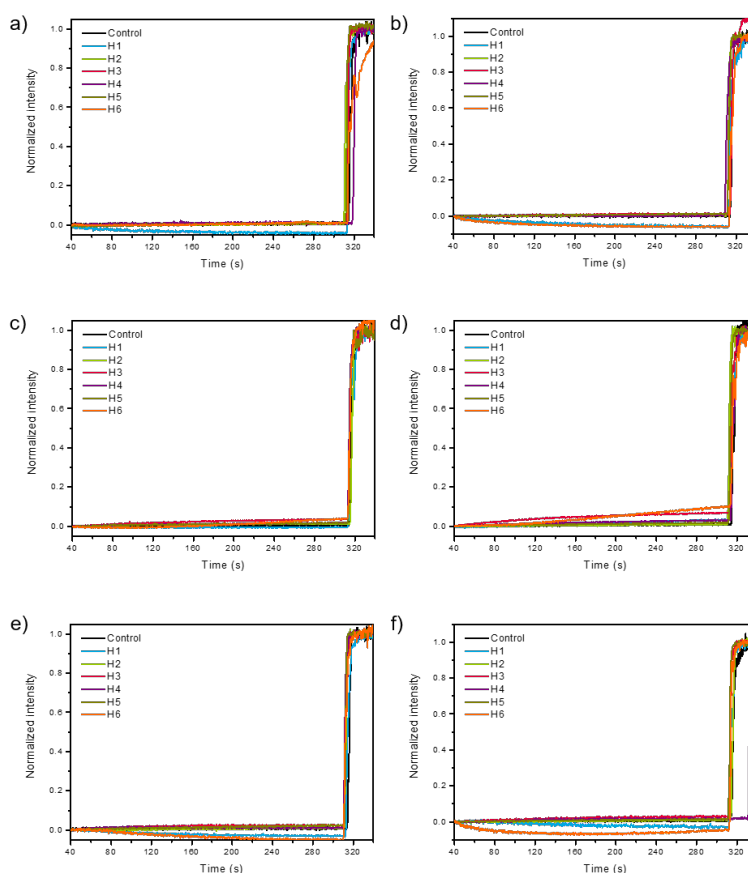


**Figure 46.** Anion transport activity expressed as normalized fluorescence intensity of 10 mM hydroxy channels in the extravesicular media containing 100 mM (a) NaBr, (b) NaI, (c) NaHCO<sub>3</sub>, (d) Na<sub>2</sub>CO<sub>3</sub>, (e) NaNO<sub>3</sub> and (f) Na<sub>2</sub>SO<sub>4</sub>.

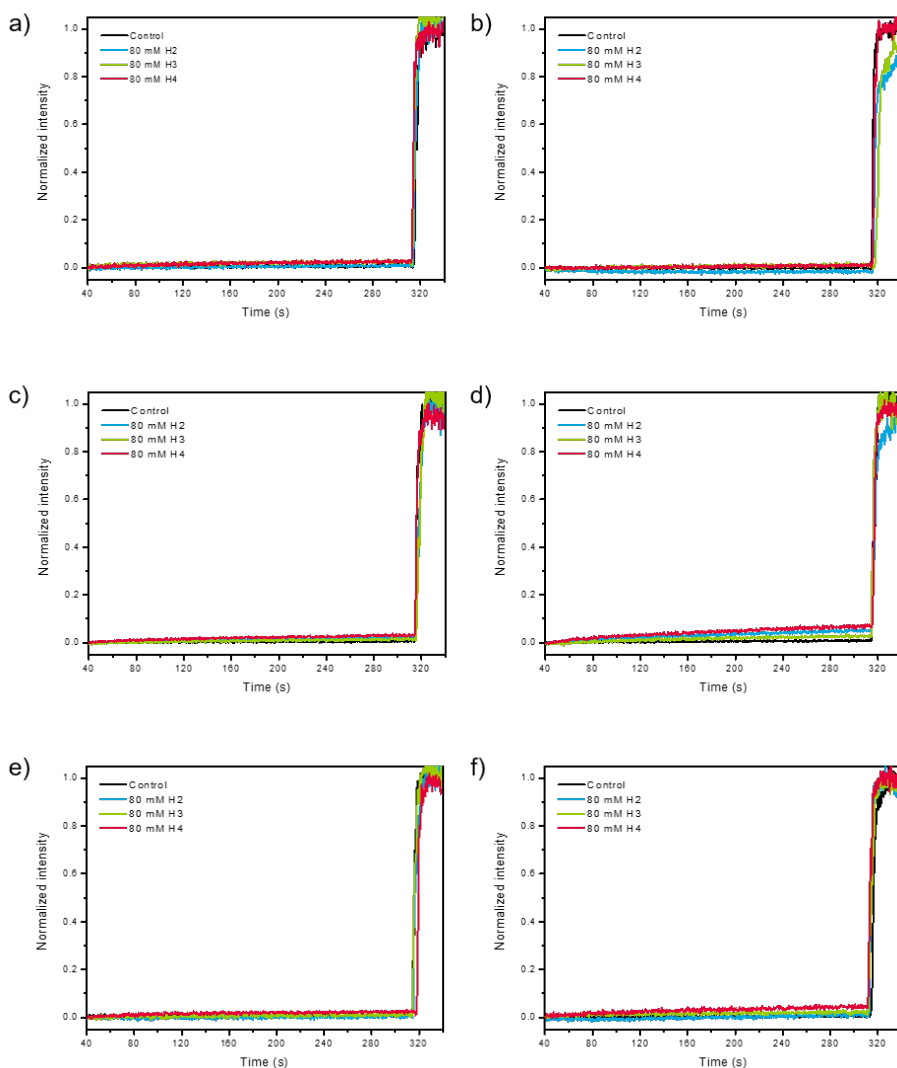


**Figure 47.** Anion transport activity expressed as normalized fluorescence intensity of 80 mM hydroxy channels in the extravesicular media containing 100 mM (a) NaBr, (b) NaI, (c) NaHCO<sub>3</sub>, (d) Na<sub>2</sub>CO<sub>3</sub>, (e) NaNO<sub>3</sub> and (f) Na<sub>2</sub>SO<sub>4</sub>.

#### 2.4.4. Simultaneous thermal analysis (TGA/DSC)

The thermogravimetric analysis (TGA) and differential scanning calorimetry (DSC) unveiled good thermal stability for hydroxy channels (Figure 48-53), of which TGA curves indicated thermal decomposition of the compounds were at ~200 °C. Several phase-transition events can be detected around ~100 °C and ~125 °C reminiscent with progressive H-bonding rupture in the highly cross-linked crystalline matrices.



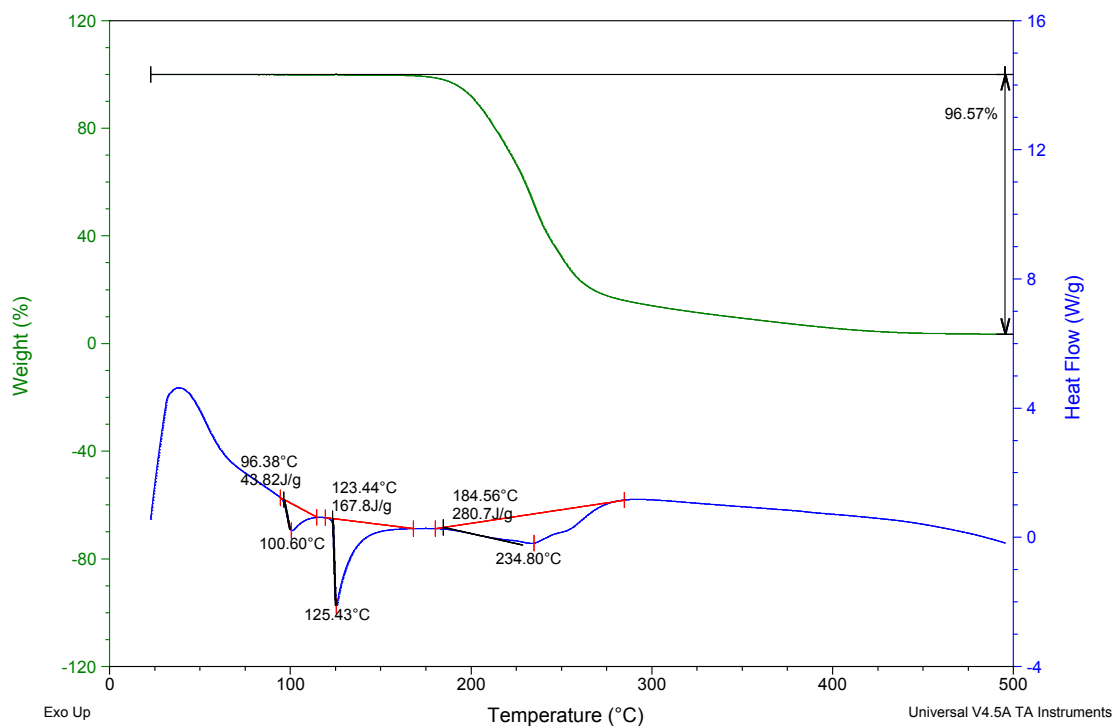


**Figure 48.** Thermogravimetric analysis TGA (green) and differential scanning calorimetry DSC (blue) curves for **H1**.

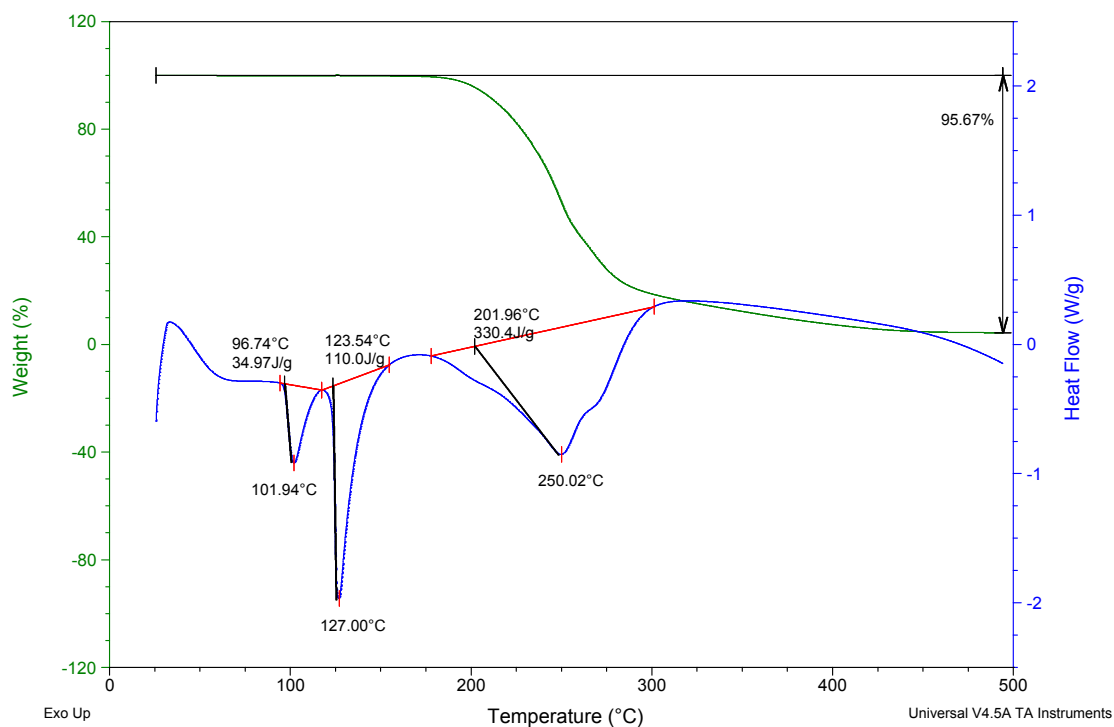


**Figure 49.** Thermogravimetric analysis TGA (green) and differential scanning calorimetry DSC (blue) curves for **H2**.

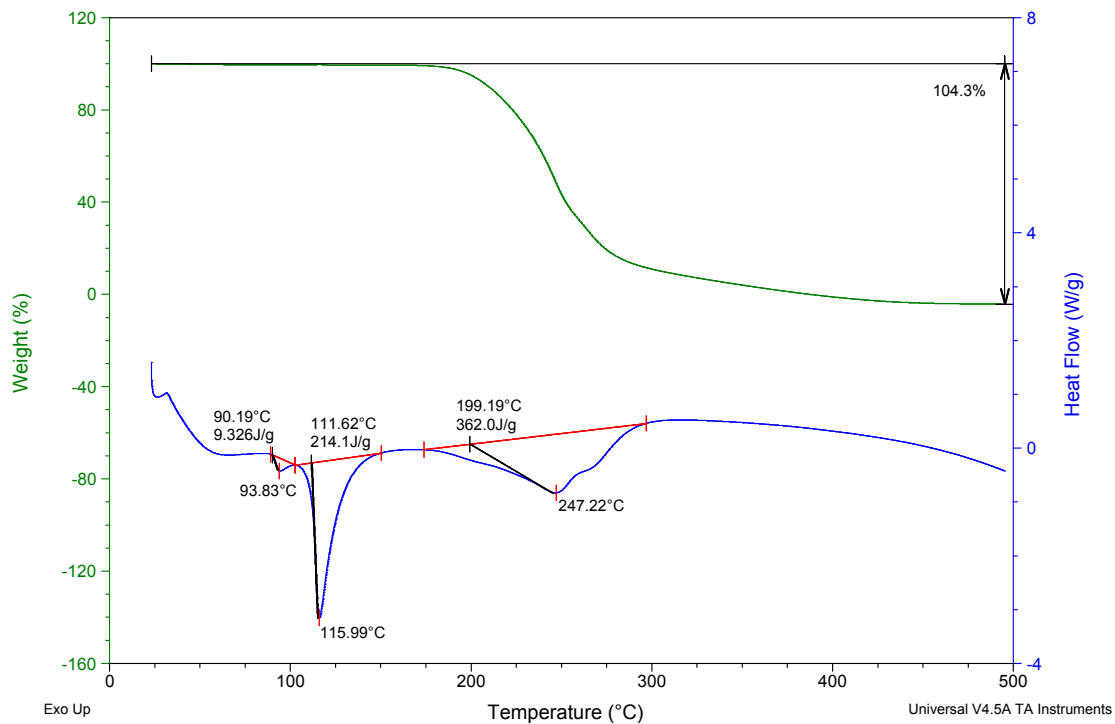


**Figure 50.** Thermogravimetric analysis TGA (green) and differential scanning calorimetry DSC (blue) curves for **H3**.

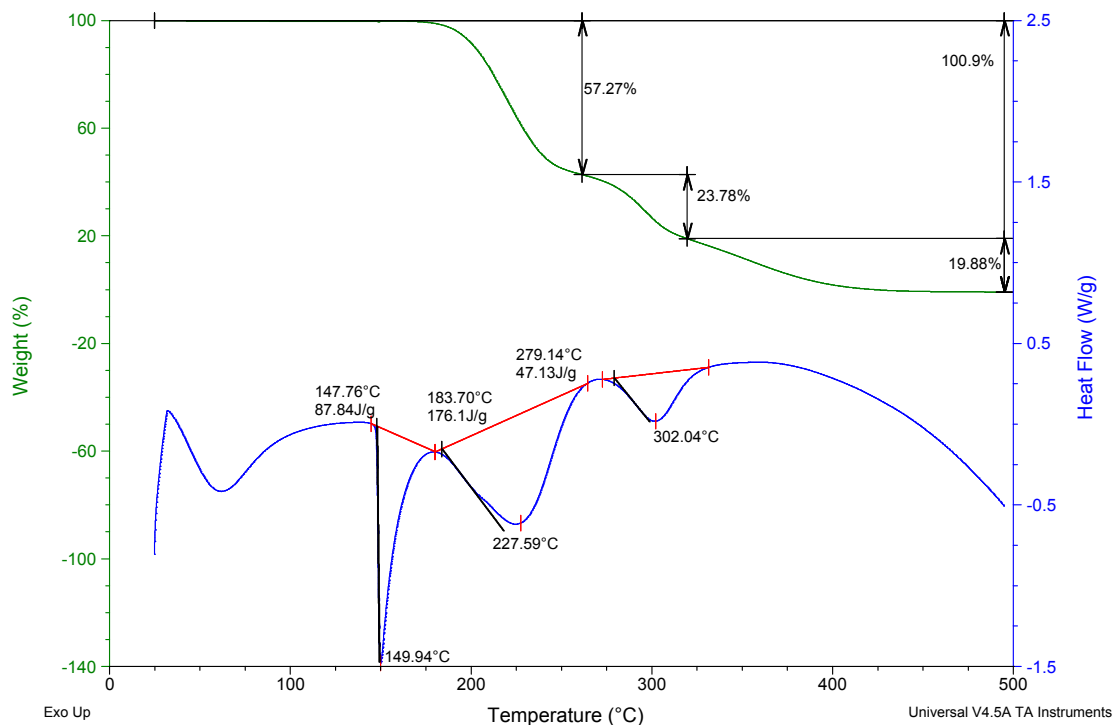


**Figure 51.** Thermogravimetric analysis TGA (green) and differential scanning calorimetry DSC (blue) curves for **H4**.

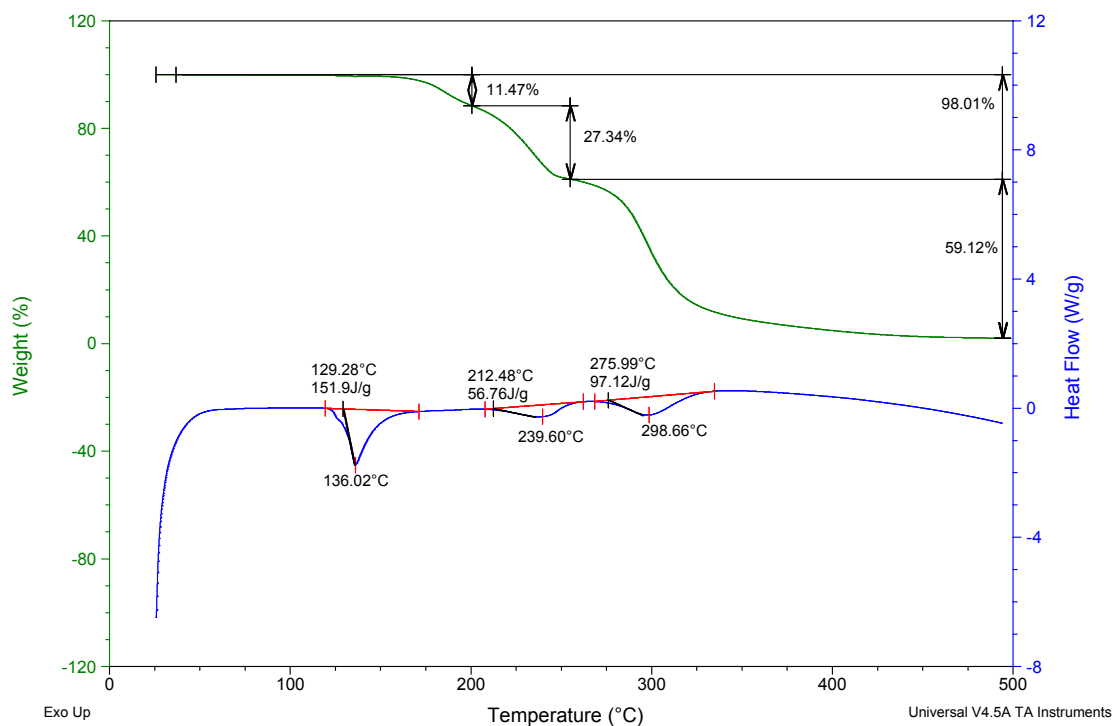


**Figure 52.** Thermogravimetric analysis TGA (green) and differential scanning calorimetry DSC (blue) curves for **H5**.

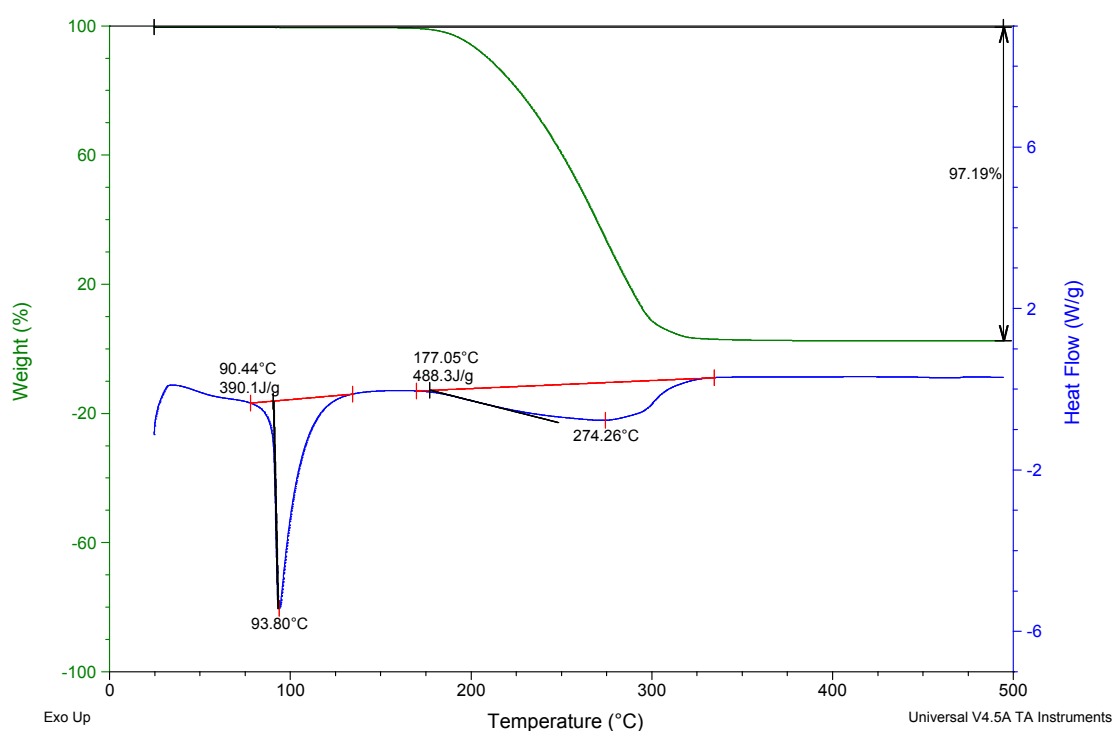


**Figure 53.** Thermogravimetric analysis TGA (green) and differential scanning calorimetry DSC (blue) curves for **H6**.

### 2.4.5. Molecular dynamics simulations

We performed four sets of simulations in order to gain some insights into the stability of the **H1** compound within the lipid membrane. In particular, the water and ion permeation activity of the membrane-embedded **H1**-hydroxychannels was to be explored. The first set of simulations (referred to with the acronyms *crys\**) is related to the hypothesis that self-assemblies may remain close to the experimentally resolved crystal structure. The second set (*solv\**) was aimed to investigate the wetting and in particular the possible presence of water clusters, inside the crystal packing framework and was performed by soaking a modified crystal patch in a pure water solvent without lipids. The third set (*cyl1\**) is motivated by the plausible analogy of hydroxyl-channels with respect to natural toroidal ceramide channels because of their similarity in chemical structure. In the fourth set of simulations (*harm\**), we adopted a reverse methodology where we hypothesize the structure of the channels and tune the level of fluctuations to measure the water flow response of the sponge-like hydroxy channel structure.

All molecular dynamics simulations (*crys\**, *solv\**, *cyl1\** and *harm\**), were performed under periodic boundary conditions with constant pressure. The CHARMM-36 force field<sup>[1]</sup> was used for lipid molecules and the TIP3P force field was chosen<sup>[2]</sup> for water. To represent **H1** molecules and generate their topologies, we used the CHARMM General Force Field (CgenFF)<sup>[3]</sup> together with the ParamChem web service<sup>[4]</sup> or alternatively the General Amber Force Field (GAFF) together with the antechamber program<sup>[5,6]</sup>. The comparison of the two force fields allowed us to assess the role of relative stability and packing on permeation events. The GROMACS 2018.7 and 2019.2 software packages were used to run the simulations with all atoms, with an integration time step of 2fs. Hydrogen bonds were constrained using the LINear Constraint Solver (LINCS) algorithm. Particle mesh Ewald electrostatics was used with a 12 Å

cutoff with the Verlet buffer scheme for nonbonded interactions; the neighbor list was updated every 20 steps.

Three baths (hydroxyl channels, lipids, and water plus ions) were coupled to a temperature of 310 K. In the case of all unrestrained simulations, we used a Nosé-Hoover thermostat with a time constant  $t = 1$  ps and a chain length of 4. Pressure in the x/y dimensions was scaled isotropically with a Parrinello-Rahman barostat at 1 bar, and the z dimension was coupled independently to a reference pressure of 1 bar, with  $t = 5.0$  ps, and compressibility of  $4.5 \cdot 10^{-5} \text{ bar}^{-1}$ . In the restrained simulations, we used a Berendsen thermostat and Berendsen barostat with the same reference values.

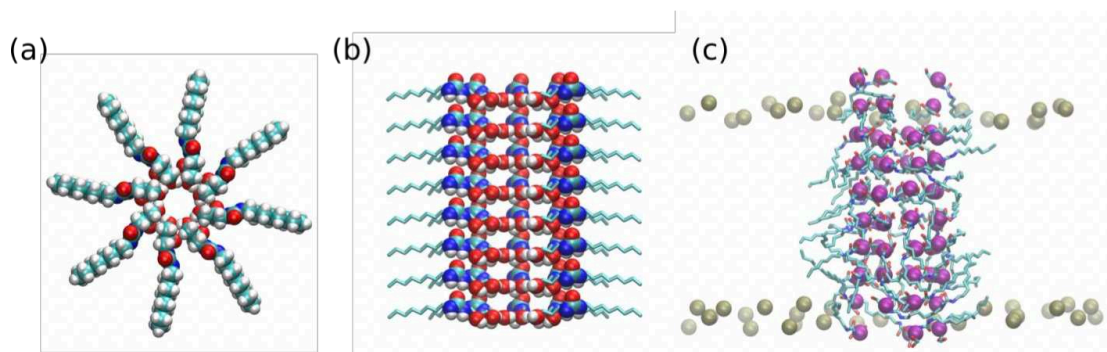


**Figure 54.** Design of a cylinder-like channel structure. (a) top view of the initial construct; (b) lateral view of the initial construct, ureic core and hydroxyl groups are highlighted in van der Waals representation; (c) Reference structure for restrained simulations. Only positions of C13 atoms (purple) are harmonically restrained during the production step.

In the case of *crys\**, *solv\** and *Rest2* simulations<sup>[7,8]</sup>, initial configurations of the channels were based on the X-ray data. The crystal patch was shaped with rectangular geometry with 8 slices along the z-axis to be inserted in a lipid membrane of  $\sim 5\text{nm}$  thickness with 7 pairs of molecules, each pair interacting through hydrogen bonds. The systems result in a crystal patch formed by 112 molecules. In the case of the *cyl\** and *harm\** simulations, we assembled the monomers in such a way as to create a cylindrical channel to mimic the natural

ceramide channels. Using custom scripts, we built a circular slice of 8 **H1** molecules with hydrophilic heads pointing towards the z-axis of the membrane and with ureic cores that form hydrogen bonds with adjacent slices along the z-axis (see Figure 54). We multiplied the structure in the z direction in order to fit with the lipid bilayer thickness. After inserting water molecules in the inner part of the cylinder, minimization and equilibration were performed in vacuum using periodic boundary conditions to maintain water inside the cylinder. The final system consisted of 64 molecules embedded in the lipid membrane (Figure 54). All membrane systems were assembled and solvated using the CHARMM-GUI web interface<sup>[9]</sup> with the addition of a concentration of roughly 50 mM NaCl to the solvent, as well as an excess of Na<sup>+</sup> ions to neutralize the system charge induced by the negatively charged PS lipids.

The composition of lipids follows the one used experimentally with a respective molar ratio 5:4:1 for Chl:PC:PS. The molar ratio between compounds and lipids (mCLR) have been set similar to experimental values. A few simulations with larger molar ratio (mCLR = 1 or 2) using a few rows of cylinders have been tested and showed similar results than in the *cyl1\** set with a unique cylinder-like channel. For this reason, we assume that unbalanced interactions between hydrophilic heads lead to a quick disaggregation of the self-assembly in the membrane. This imbalance has shown to be persistent in larger systems with higher mCLR.

All systems were minimized for 5000 steps with a steepest descent algorithm and equilibrated for 2 ns, using decreasing position restraints of 1000, 400, 200, 100, 40 kJ mol<sup>-1</sup> nm<sup>-2</sup> on heavy atoms, with the crystal structure as a reference or the cylinder-like construct. In the case of restrained simulations, harmonic restraints were applied during both the equilibration and production phases, and acted on a single atom per molecule (C13, located between the ureic core

and the hydrophilic part of **H1**, see Figure 54). In all other simulations, in the production phase, no restraints were maintained.

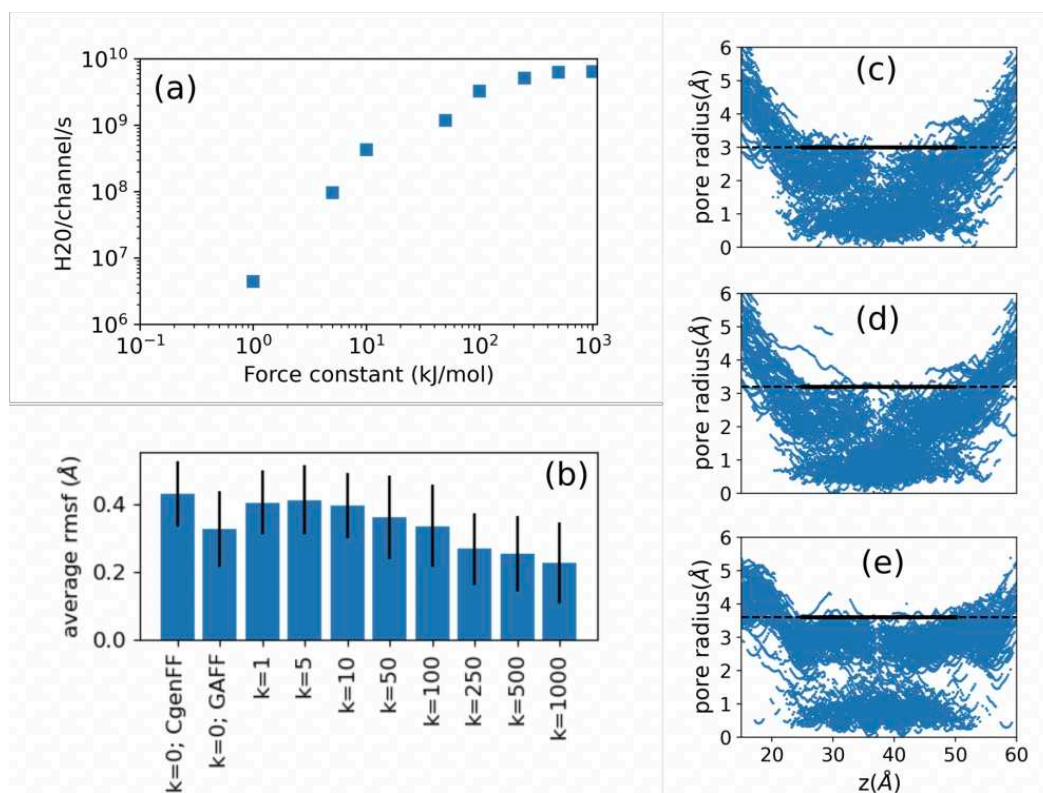


**Figure 55.** (a) Water conductance of one cylinder/sponge channel with respect to the constant force of harmonic potential applied on the C13 atom of **H1** molecules. (b) Average of Root Mean Square Fluctuations over all atoms of the channels on a 20 ns time window. (c, d, e) Cumulated pore profile data points during the last 200 ns of simulations *harm10*, *harm100* and *harm1000*, respectively. Pore sizes are distributed between 0 and a maximal value in the central part of the channel (black line) which corresponds to respectively 3.0 Å, 3.2 Å and 3.6 Å. The large distribution of pore sizes reflects the porous material and the transient appearance of water clusters inside the channel.

Enhanced sampling simulations using REST2 (solute tempering<sup>[7,8]</sup>) methods have been used to investigate and favor conformational changes away from the crystal form. We use 30 replicas and the Hamiltonian terms for **H1** molecules were scaled resulting in an effective temperature ranging from 310K to 430K<sup>[8]</sup>. The exchange frequencies between replicas were set to 1 ps. Exchange probabilities are around 50% between almost all adjacent replicas.

The molecular dynamics trajectories were visually inspected and analyzed using the VMD software<sup>[10]</sup>. Analysis of the trajectories for RMSD and permeation calculations were performed using customized scripts for the MD Analysis library<sup>[11,12]</sup>. Varying the sampling time allowed us to assess the accuracy of the analysis. Fast computation maintaining an acceptable accuracy was achieved using 0.1 ns as sampling time for the analysis of water permeations. The analysis of pore radius was performed using the HOLE software<sup>[13]</sup>.

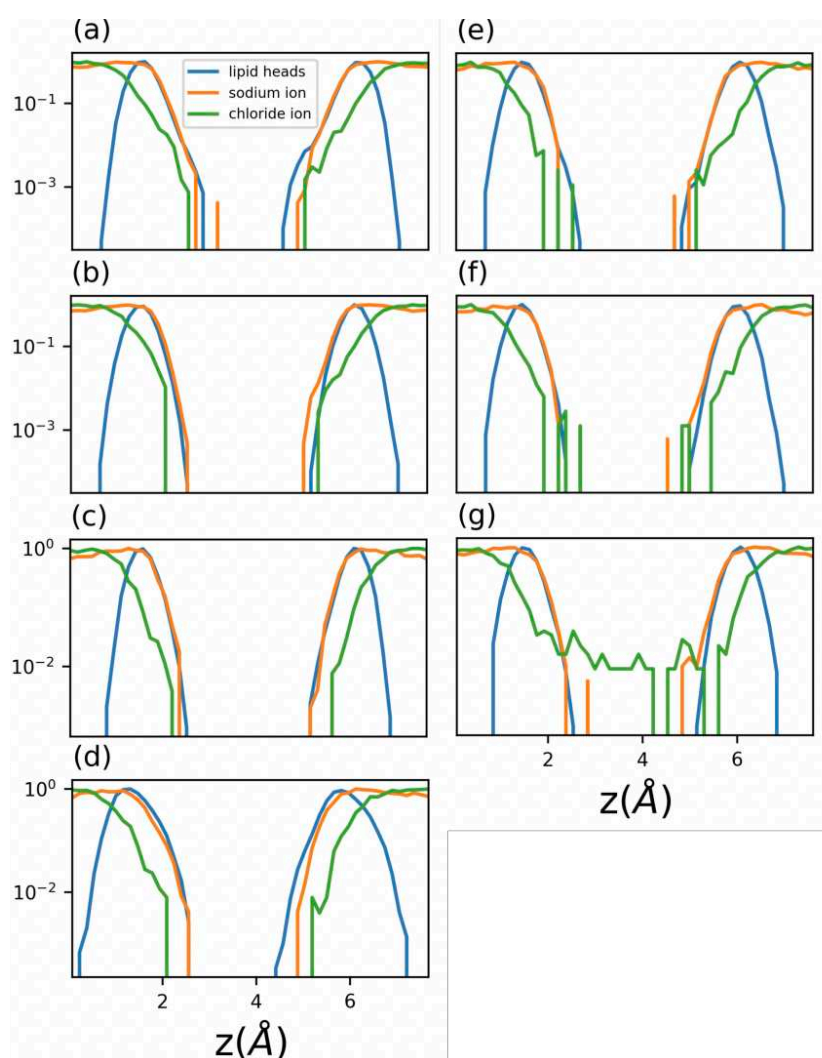


**Figure 56.** Normalized density of phosphorus atoms from lipid heads (blue), sodium ions (orange) and chloride ions (green) along an axis perpendicular to the membrane plane in all MD simulations. (a) *crys\_cgen* (b) *crys\_gaff* (c) *cyl1\_cgen* (d) *cyl1\_gaff* (e) *harm10* (f) *harm100* (g) *harm1000*.



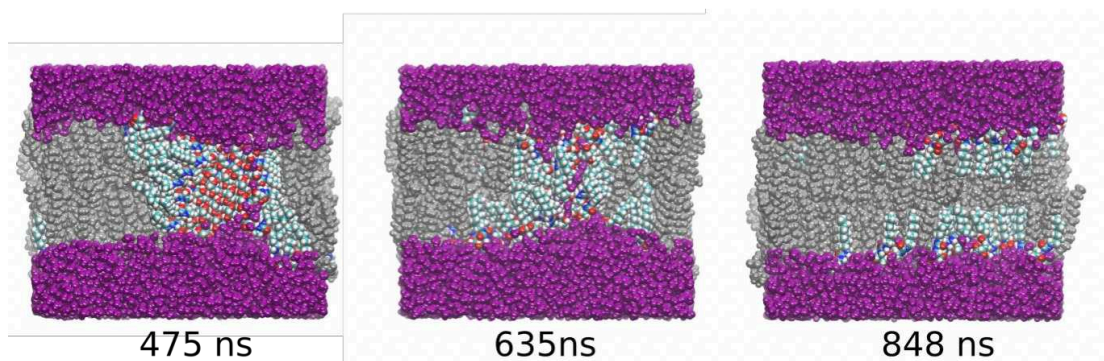


**Figure 57.** Snapshot of the simulation *crys\_cgen* at three times during the simulation. An atom-type coloured representation was kept for **H1** molecules, whereas unique coloring was applied for water molecules (purple) and lipids (silver).

Indeed, applying an electric field across the membrane can be used to probe to what extent ion permeation can be forced. Several methods exist to apply electric fields in molecular dynamics simulations, each with specific advantages and problems. Such simulations are quite delicate. We have in the past obtained the most satisfying results by using a method where two compartments are created in a simulation box, with two explicit membrane bilayers<sup>[14]</sup>. In the present case this means duplicating the size of the simulation system. We conducted six exploratory simulations on the timescale of hundreds of nanoseconds along these lines, yet a full and detailed study is clearly beyond the scope of the present work. The six simulations use a charge imbalance of 4, 4, 4, 8 and 12 electrons, covering a range of channel structures to account for possible scenarii of water permeation. All these setups correspond to potential differences larger than 500mV across the membrane.<sup>[15]</sup> Please note that this value is more than 5 times higher than physiological cross-membrane potential differences, rather between 40 and 90 mV. In order to probe the situation with a 4e difference more thoroughly, we used different forcefields in these simulations. Unsurprisingly, when the applied electric field is strong enough, ions are able to pass the membrane barrier. Interestingly, chloride ions are the first to permeate, whereas sodium permeation only starts with the highest applied voltage. At the lowest 4e charge imbalance, however, for both

forcefields, no ion permeation was observed - other than at the very beginning, when switching on the field, confirming an intrinsically significantly higher activation barrier than for water permeation. Future works could use methodologies such as the Computational Electrophysiology approach by Kutzner et al.<sup>[16]</sup>, maintaining a constant ion imbalance, thereby enabling a more quantitative measure of ion flux and selectivity or the use of an external electric field<sup>[17]</sup>.

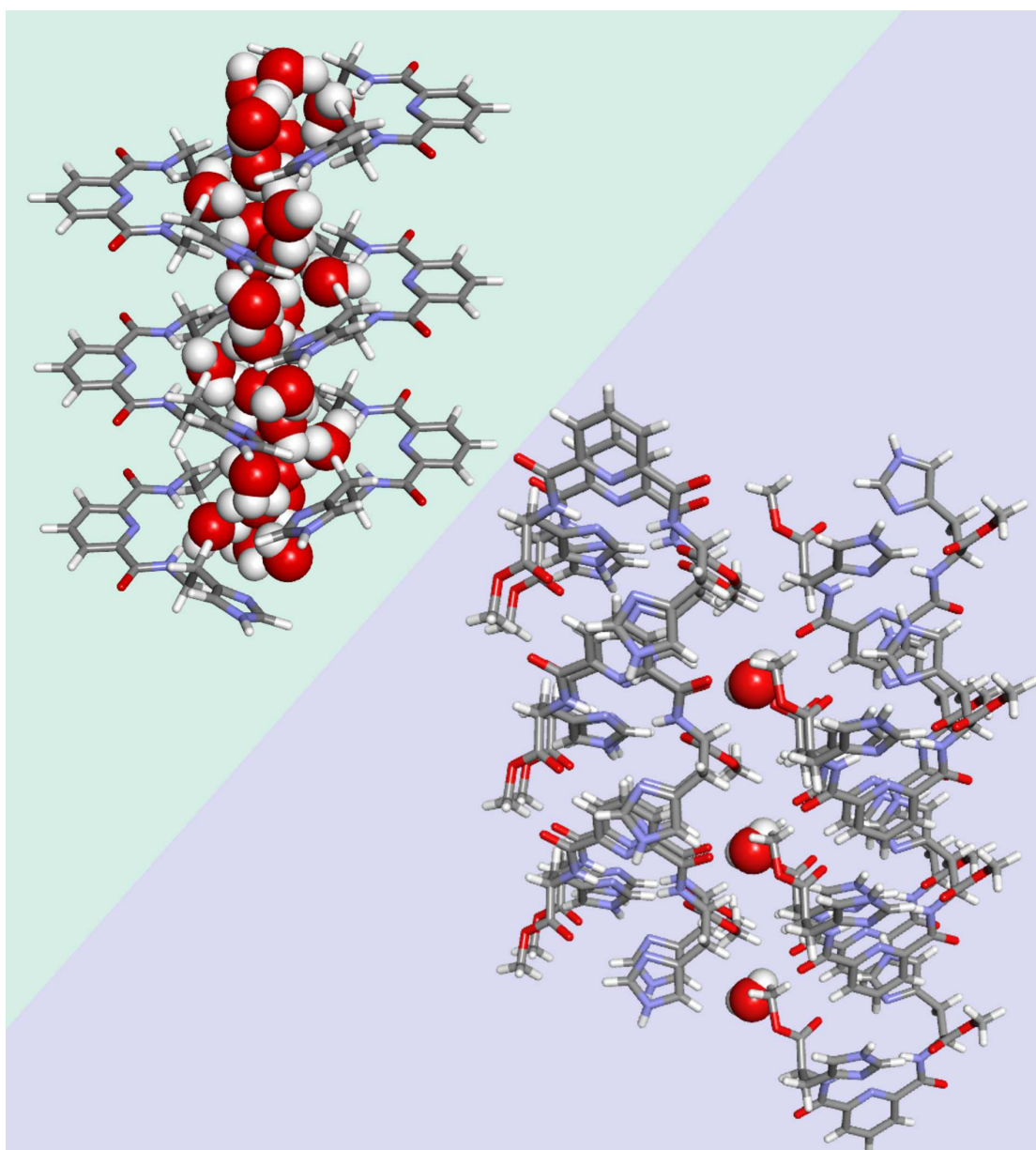
## References

- [1] Klauda, J. B.; Venable, R. M.; Freites, J. A.; O'Connor, J. W.; Tobias, D. J.; Mondragon-Ramirez, C.; Vorobyov, I.; MacKerell, A. D.; Pastor, R. W. *J. Phys. Chem. B* **2010**, *114*, 7830–7843.
- [2] Jorgensen, W. L.; Chandrasekhar, J.; Madura, J. D.; Impey, R. W.; Klein, M. L. *J. Chem. Phys.* **1983**, *79*, 926–935.
- [3] Vanommeslaeghe, K.; MacKerell, A. D. *J. Chem. Inf. Model.* **2012**, *52*, 3144–3154.
- [4] Vanommeslaeghe, K.; Raman, E. P.; MacKerell, A. D. *J. Chem. Inf. Model.* **2012**, *52*, 3155–3168.
- [5] Wang, J.; Wolf, R. M.; Caldwell, J. W.; Kollman, P. A.; Case, D. A. *J. Comput. Chem.* **2004**, *25*, 1157–1174.
- [6] Wang, J.; Wang, W.; Kollman, P. A.; Case, D. A. *J. Mol. Graph. Modell.* **2005**, *25*, 247–260.
- [7] Wang, L.; Friesner, R. A.; Berne, B. J. *J. Phys. Chem. B* **2011**, *115*, 9431–9438.
- [8] Stirnemann, G.; Sterpone, F. *J. Chem. Theory Comput.* **2015**, *11*, 5573–5577.
- [9] Jo, S.; Kim, T.; Iyer, V. G.; Im, W. *J. Comput. Chem.* **2008**, *29*, 1859–1865.
- [10] Humphrey, W.; Dalke, A.; Schulten, K. *J. Mol. Graph.* **1996**, *14*, 33–38.
- [11] Michaud-Agrawal, N.; Denning, E. J.; Woolf, T. B.; Beckstein, O. *J. Comput. Chem.* **2011**, *32*, 2319–2327.
- [12] Gowers, R. J.; Linke, M.; Barnoud, J.; Reddy, T. J. E.; Melo, M. N.; Seyler, S. L.; Domański, J.; Dotson, D. L.; Buchoux, S.; Kenney, I. M.; Beckstein, O. *Proc. 15th Python Sci. Conf.* **2016**, 98–105.

- [13] Smart, O. S.; Neduveilil, J. G.; Wang, X.; Wallace, B. A.; Sansom, M. S. P. *J. Mol. Graph.* **1996**, *14*, 354–360.
- [14] Laurent, B., Murail, S., Da Silva, F., Corringer, P. J., & Baaden, M. *Pure Appl. Chem.* **2012**, *85(1)*, 1-13.
- [15] Gurtovenko, A. A.; Vattulainen, I. J. *Chem. Phys.* **2009**, *130 (21)*, 215107.
- [16] Kutzner, C.; Grubmüller, H.; de Groot, B. L.; Zachariae, U. *Computational Electrophysiology: Biophys J.* **2011**, *101 (4)*, 809–817.
- [17] Gumbart, J.; Khalili-Araghi, F.; Sotomayor, M.; Roux, B. *Biochimica et Biophysica Acta (BBA) - Biomembranes* **2012**, *1818 (2)*, 294–302.

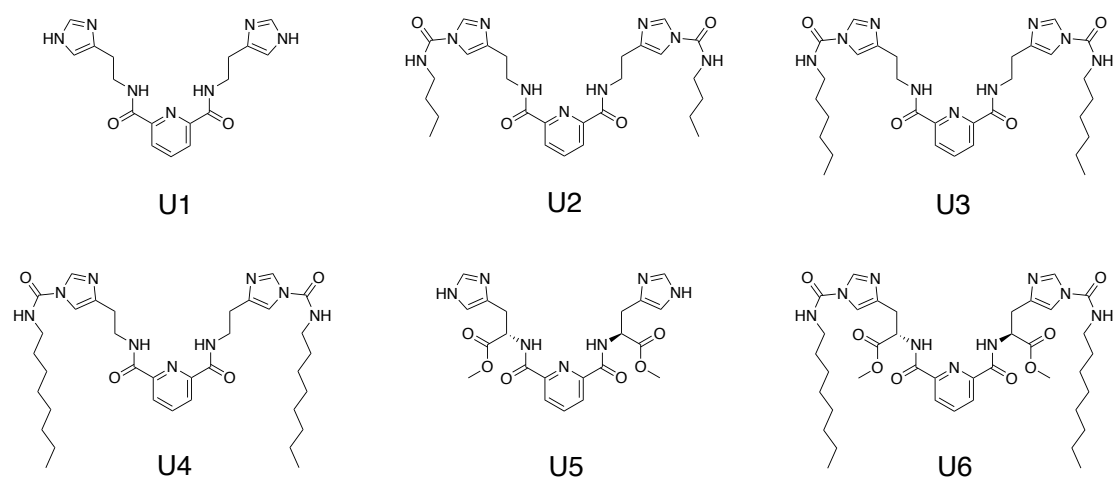
## Chapter III – U-shaped Diimidazole Channels

- Dual Approaches for Selective Water-Wire/Water-Cluster Permeation



### 3.1. Introduction

With approximately two-thirds of the global population (4 billion people) living in severe water scarcity for at least one month per year,<sup>5</sup> sustainably meeting the growing human demand for freshwater is one of the most important and ambitious goals of this century<sup>4, 106</sup>. Aquaporins (AQPs), as naturally occurring proteins, are able to facilitate the transport of water across cell membranes with high permeability and exceptional selectivity.<sup>1, 13, 14</sup> They allow the passive transport of water molecules across the lipid bilayers while rejecting ions and protons.<sup>1</sup> Their selective permeability to water is achieved through the spatial domain-limiting effect of the hourglass-like central structure, the rejection of ions by the positively charged entrance, and the specific interaction of dipole water molecules with the inner wall.<sup>107</sup> In living organisms, impairment of AQPs may lead to several serious diseases such as congenital cataracts and nephrogenic diabetes insipidus.<sup>108, 109</sup> However, the structural complexity and poor stability of aquaporins have prompted researchers to mimic aquaporins and develop artificial water channels (AWCs) combining high permeability and selectivity with chemical stability.



**Scheme 3.** Compounds **U1–U6**, as components for self-assembled diimidazole U-channels.

A rich diversity of artificial water channels (AWCs) has been designed and developed in the last decade<sup>17, 32, 34, 36, 50, 76, 80, 94, 95, 110</sup> and have provided novel research strategies for the fabrication of water desalination membranes<sup>92, 96</sup>. We have seen in the previous chapter that hydroxy channels are capable of self-assembly into both narrow water channels to accommodate water-wire at low concentration and large pores to allow water-clusters permeation at high concentration, thus enabling multiple transport approaches in a single type of AWCs.<sup>110</sup> However, such multiple behaviors of water translocation are mainly triggered by the concentration of the channels within the membranes, and the absence of water molecules in the single-crystal structures of hydroxy channels hinders the further analysis of the differences in these two transport behaviors. Although molecular dynamic simulations have been available to exhibit that, depending on the sizes of channels, narrow CNTPs encapsulate water-wires<sup>64</sup>, while water clusters exist in wide CNTPs<sup>64, 111, 112</sup>, these studies fail to give conclusive evidence for the presence of water clusters within AWCs. Moreover, there is no interaction between water molecules and the inner walls of carbon nanotubes, so that water molecules are confined inside the carbon nanotubes for translocation in a nearly frictionless state.

Hence, in order to demonstrate the feasibility of the water-wire versus water-clusters transport behaviors, we report a class of U-shaped diimidazole water channels formed by self-assembly of pyridylbis(formamide-ethylimidazole) derivatives. Inspired by the structure of imidazole-quartet water channels<sup>32, 36</sup>, the N and N-H in the imidazole moiety act as acceptor and donor, respectively, for hydrogen bonds with water molecules, which are hydrophilic motifs. In order to create large-size hydrophilic cavities to accommodate water clusters, we design hydrophilic motifs such as pyridinedicarboxamide connected to two imidazole groups in the U-channel central structure, which provide highly hydrophilic environment for water molecules. Besides, we introduce methyl

formate side chains to shield the hydrophilic motifs of imidazole groups and realize water-wires transport behavior by simple structural modifications.

## 3.2. Results and Discussion

### 3.2.1. Design strategy

Our group previously put forward a series of alkylureido-ethylimidazole monomers HCx capable of self-assembly into artificial imidazole-quartet water channels (Figure 58), mutually stabilized by the consecutive scaffolding alkylurea and imidazole-water hydrogen-bonding.<sup>32, 36</sup> With the strong hydrophilic motifs provided by inner imidazoles, and a similar pore size (2.6 Å) to AQPs, I-quartet water channel exhibits high water permselectivity.

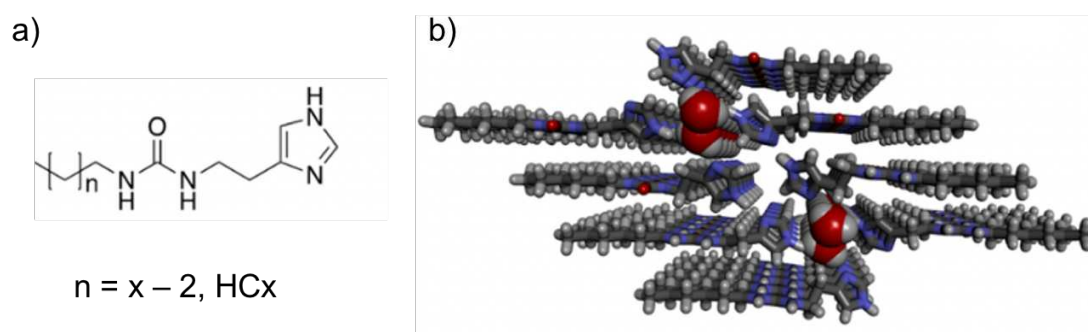
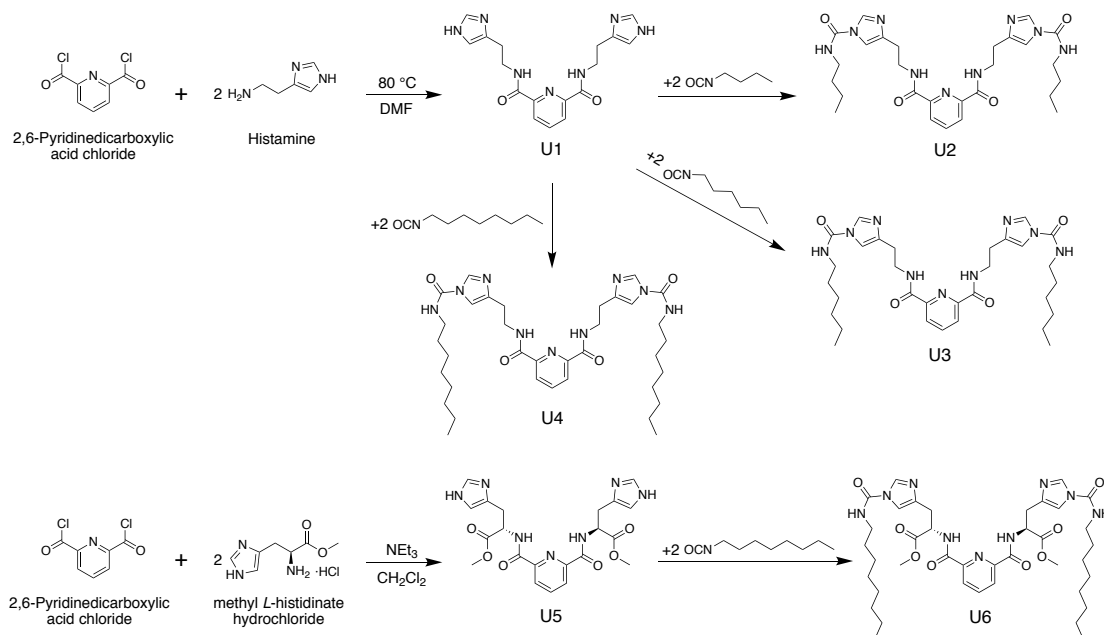


**Figure 58.** a) Chemical structures of alkylureido-ethylimidazole monomers HCx and b) Top view of Imidazole-quartet water channels.

Within this context, and in order to investigate the differences in the transport behaviors and the water permselectivity of water-wires and water clusters, we designed and synthesized a new class of U-shaped diimidazole channel (U-channel) blocks **U1–U6**. As shown in Scheme 3, we adopted the histamine from imidazole-quartet water channels as the two lateral chains for the U-channel compounds, and histamine reacted with 2,6-pyridinedicarbonyl dichloride to generate central hydrophilic cavity. As a result, Nitrogen on pyridine and amino group act as hydrogen bond acceptor and donor, respectively, to interact with

water molecules, which, together with the two imidazole groups on both sides, forms a total of three motifs for binding to water molecules. Based on the structure of **U1**, compounds **U2–U4** were formed by the addition of butylaminocarbonyl, hexylaminocarbonyl or octylaminocarbonyl groups to the imidazoles of **U1**, as hydrophobic chains to insert into lipid bilayers to enhance the stability of U-shaped water channels. And they were set as control groups to investigate the optimal hydrophobicity of U-channels.



**Scheme 4.** Synthetic route of pyridine bis(formamide-ethyl-imidazole) derivatives **U1–U6**.

Our initial concept was to realize water-clusters transport across lipid bilayers by U-channels with large cavities and multiple hydrophilic motifs, and **U1–U4** channels were expected to achieve this objective. Meanwhile, we further designed **U5** and **U6** by introducing methyl formate hydrophobic groups near the imidazole groups to shield the water binding motifs, thus leaving only hydrophilic motif consisting of pyridine and amino groups. Hence, U-channels formed by the self-assembly of compounds **U5** and **U6** potentially adapt to the formation of single water-wire so that both water-wire/clusters transport can



be achieved through the same class of AWCs. By slightly modifying the structure of channel blocks, the variables arising from the differences in chemical composition can be controlled to the maximum extent, achieving the first comparative study of two water transport approaches in individual type of AWCs.

Six compounds were synthesized following the general scheme 4. Compound **U1** was obtained through a one-step reaction between 2,6-pyridinedicarbonyl chloride and histamine, which then reacted with butyl isocyanate, hexyl isocyanate or octyl isocyanate to produce monomers **U2**, **U3** or **U4**, respectively. Similarly, we synthesized compounds **U5** and **U6**, which differ from compounds **U1** and **U4**, in the addition of symmetrical methyl formate groups to the both sides. The <sup>1</sup>H NMR and ESI-MS spectra agree with the proposed formulas (Figures 65–70).

### **3.2.2. Single-crystal structures**

The potential to form U-channel superstructures was initially assessed by the crystallization of monomers **U1** and **U6**. X-ray single-crystal structures give a good indication of the self-assembly preferences of the compounds in solution and their possible self-organization in lipid bilayer membranes. Single crystals **U1** and **U5** of high-quality for X-ray structure determination were obtained. Due to the poor crystallinity and poor stability of lateral chains, the crystallization of compounds **U2**, **U3**, **U4** and **U6** were unsuccessful.

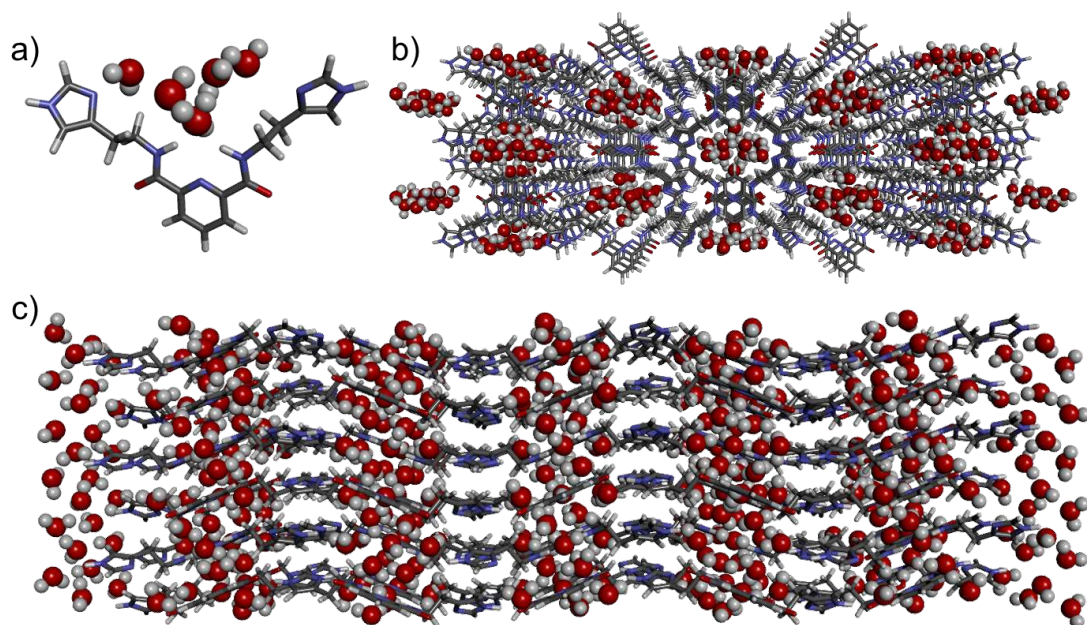


**Figure 59.** X-ray single crystal structures of diimidazole **U1** AWCs: a) Structure of **U1** molecule confining five water molecules. b) Top view and c) Side view of crystal packing for **U1**-channels, confining unoriented water clusters.

Inside **U1**-channel, water clusters were confined within the large-size pores formed by its crystal packing, revealing the potential of transporting water clusters (Figure 59). Unexpectedly, one molecule of **U1** capable of bonding five water molecules, which has only three hydrophilic motifs (Figure 59 a). In addition to the H-bonds with inner hydrophilic motifs, the hydrogen bonding between the water molecules promotes their dense stacking, resulting in the formation of water clusters superstructures. From the top and side views of **U1** water channels, the U-shaped monomers can be self-assembled longitudinally, and two columns of molecules together form one water channel. Among them, the cavity size of **U1**-channel is  $\sim 9 \text{ \AA}$ , which is three times the pore diameter of AQPs, and the distance between the water channel layers is about  $3.6 \text{ \AA}$ . This structure indicates that monomers **U1**–**U4** are able to self-assemble into large-size AWCs, while this type of channel accommodates and potentially transports unoriented water clusters.

Meanwhile, only one water molecule is bound with one molecule of **U5**. Unlike the structure of **U1**-channel, the carbonyl groups on the lateral of **U5**-channel act as a hydrogen-bonding acceptor to the water molecules (Figure 60 a). **U5** molecules self-assemble into water channels in which the water molecules are arranged in an oriented manner to form water wires. From the top and side views of the crystal structure of **U5** water channel (Figure 60), the distance between layers is 4.4 Å, and the pore size of **U5**-channel is ~ 3 Å which is similar to AQPs and one-third of **U1** water channel. In contrast to **U1**-channels, the water molecules in **U5**-channels are oriented in each water-wire.

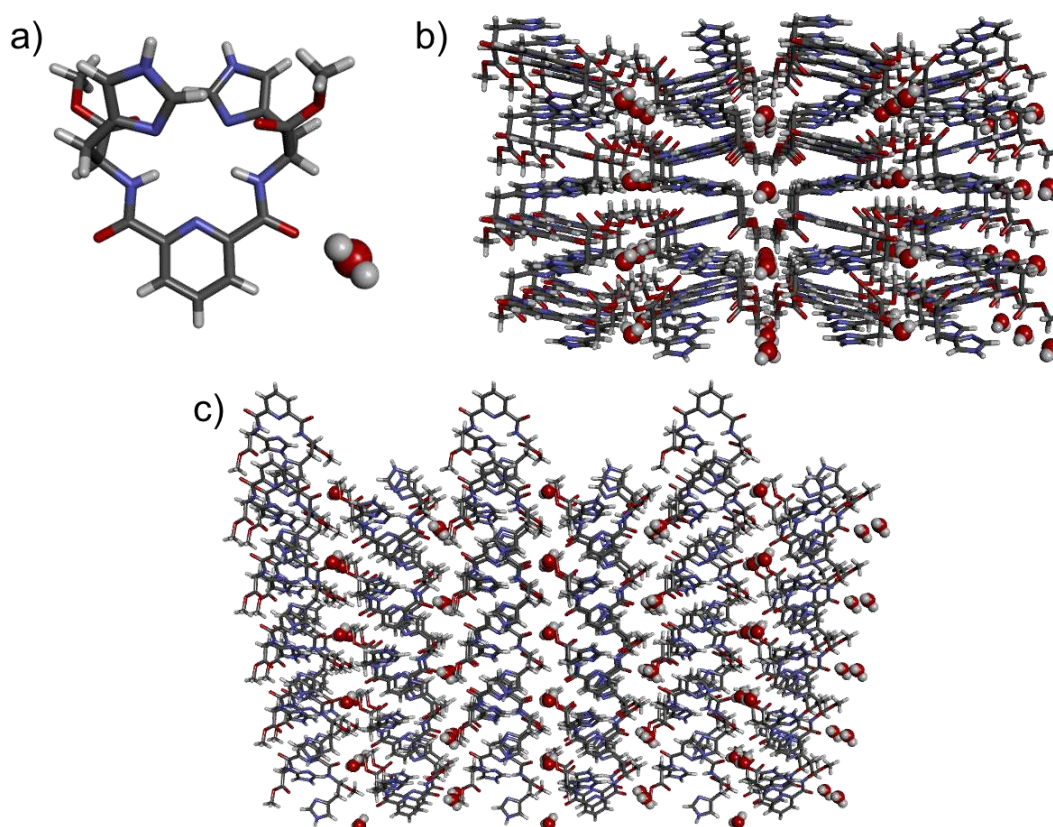


**Figure 60.** X-ray single crystal structures of diimidazole **U5** AWCs: a) structure of **U5** molecule accommodating one water molecule. b) Top view and c) side view of crystal packing for **U5**-channels, accommodating oriented water-wires.

### 3.2.3. Bilayer transmembrane experiments.

**Water transport experiments.** The U-channels were reconstituted into lipid vesicles (100 nm in diameter) consisting of phosphatidylcholine/phosphatidylserine/cholesterol (PC/PS/Chl) mixture with a molar ratio of 4/1/5. The **U1–U6** monomers were solubilized in dimethyl sulfoxide (DMSO) then added to the preformed vesicle suspensions using different channel to lipid ratios at weight (wCLRs). Next, the vesicles were exposed to an outward directed osmotic pressure gradients  $\Delta_{\text{osm}} = 106 \text{ mOsmol/kg}$ . Under hypertonic conditions driven by an outward 10 mM PBS buffer solution (pH 6.4) of 200 mM D(+)-sucrose osmolytes (Figure 61 and Figure 73), the shrinkage of the liposomes resulted in an enhanced light-scattering signal.

The water transport rates are strongly dependent on the concentration of the concentration, and the net permeabilities of each U-channel increase continually with increasing wCLRs. For the **U1–U6** water channels, net permeability values of  $0 \sim 20.06 \mu\text{m s}^{-1}$  can be achieved in the range of  $\text{wCLR} < 1$  (Figure 61).

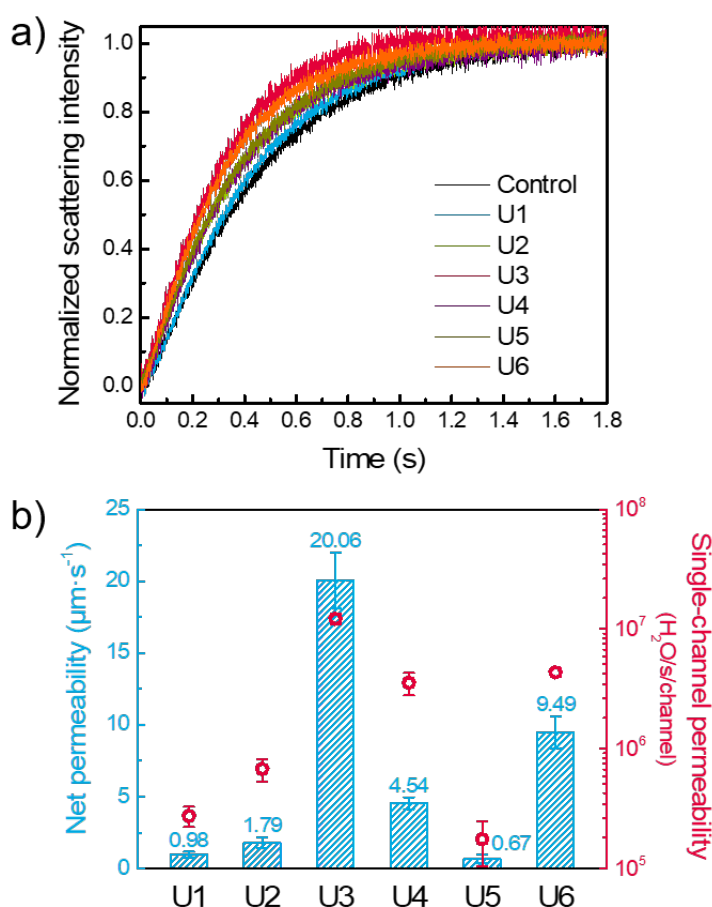


**Figure 61.** Measurements of water permeability through U-channels: (a) stopped-flow light scattering traces of liposomes containing different U-channels; (b) The net permeabilities and single-channel permeabilities calculated from the light scattering traces.

We further estimated the single-channel permeability  $P_s$  of **U1–U6** channels based on the insertion of U-channels, the lipid concentration and the channel configuration in the lipid bilayers (Table 1).<sup>43</sup> To determine their single-channel permeabilities, two rational assumptions were set up: (i) First, all of the injected monomers **U1–U6** spontaneously inserted into the lipid bilayers. The vesicles with a maximum concentration ( $w_{CLR} = 1$ ) of **U1–U6** suspensions were thermostatted at 20°C for 30 minutes, ensuring total partition of the monomers in the bilayer membrane, and it was observed that the solution changed from slightly turbidity to clarity. (ii) Second, the number of molecules required to form a channel that spans the lipid bilayer (thickness of  $\sim 5$  nm) is equal to the number of molecules found in the single-crystal structure, i.e., each **U1–U4**

channel consists of 30 molecules and each **U5** and **U6** channel consists of 24 molecules. Consequently, the single-channel permeability values of U-channel are obviously different, covering the range of  $1.31 \times 10^5$  to  $1.22 \times 10^7$  water molecules  $s^{-1}$  channel $^{-1}$ , in which the highest one is only one order of magnitude lower than that of AQPs ( $\sim 10^8$ – $10^9$  H<sub>2</sub>O/s/channel<sup>6, 45</sup>) (Figure 61 and Table 5).

**Table 5.** Single-channel permeability,  $P_s$ , and the corresponding concentration wCLR values of **U1–U6** Channels.

U-channels	wCLR	Single channel permeability, $P_s$ (H <sub>2</sub> O $s^{-1}$ channel $^{-1}$ )
<b>U1</b>	1.0	$(2.75 \pm 0.53) \times 10^5$
<b>U2</b>	1.0	$(6.87 \pm 1.48) \times 10^5$
<b>U3</b>	0.6	$(1.22 \pm 0.12) \times 10^7$
<b>U4</b>	0.2	$(3.56 \pm 0.75) \times 10^6$
<b>U5</b>	0.8	$(1.31 \pm 0.7) \times 10^5$
<b>U6</b>	0.4	$(4.36 \pm 0.33) \times 10^6$

Due to the lack of alkylaminocarbonyl lateral chains, the **U1** and **U5** water channels cannot be effectively embedded into the lipid membranes, resulting in their net permeability values of less than  $1 \mu m s^{-1}$  and the corresponding single-channel permeability values of less than  $10^6$  H<sub>2</sub>O  $s^{-1}$  channel $^{-1}$ . The single-channel permeability of **U1** water channel ( $2.75 \times 10^5$  H<sub>2</sub>O  $s^{-1}$  channel $^{-1}$ ) is more than twice that of the **U5**-channel ( $1.31 \times 10^5$  H<sub>2</sub>O  $s^{-1}$  channel $^{-1}$ ). Accordingly, the single-channel permeability of the **U3**-channel is  $1.22 \times 10^7$  H<sub>2</sub>O  $s^{-1}$  channel $^{-1}$ , which is also three times higher than that of the **U6**-channel ( $4.36 \times 10^6$  H<sub>2</sub>O  $s^{-1}$  channel $^{-1}$ ), reminiscent of the various transporting rates through water-wire/clusters translocation.

Although **U1–U4** water channels allow water-clusters permeation, their single-channel permeabilities undergo a significant enhancement and then decrease as the hydrophobicity of their lateral chains increases. The **U3**-channel achieves the highest  $P_s$  value ( $1.22 \times 10^7 \text{ H}_2\text{O s}^{-1} \text{ channel}^{-1}$ ), while the **U4**-channel descends more than 70% relative to the former. This suggests that **U3**-channel achieves the best compatibility for U-channels, and the excessively long hydrophobic flexible chains in **U4** disturbs its channel structure, thus impeding the formation of water-clusters. Comparison between **U4** and **U6** water channels with the same octanoylcarbonyl lateral chains directs to a similar conclusion: the  $P_s$  value of the **U6**-channel is even higher than that of the **U4**-channel which allows water-clusters translocation, mainly owes to the water-wires transport behavior is greatly independent of the lateral chains, which is also well demonstrated in I-quartet water channels<sup>36</sup>.

**Ion transport.** We determined the transport activity of **U1–U6** diimidazole water channels at a concentration of 10 mM for cations ( $M^+ = \text{Na}^+, \text{K}^+, \text{or Rb}^+$ ) based on lipid vesicles prepared from egg yolk *L*- $\alpha$ -phosphatidylcholine (EYPC) using standard HPTS fluorescence assays<sup>101, 102</sup> (Figure 62). When tested with an external buffer solution containing MCl, surprisingly, the **U1** and **U5** channels showed almost no cation transport activity. It can be inferred that the presence of hydrophobic lateral chains is a prerequisite for the insertion of U-channels in the lipid bilayers, and the cation transport results further confirm that **U1** and **U5** channels cannot be effectively embedded into the membranes.

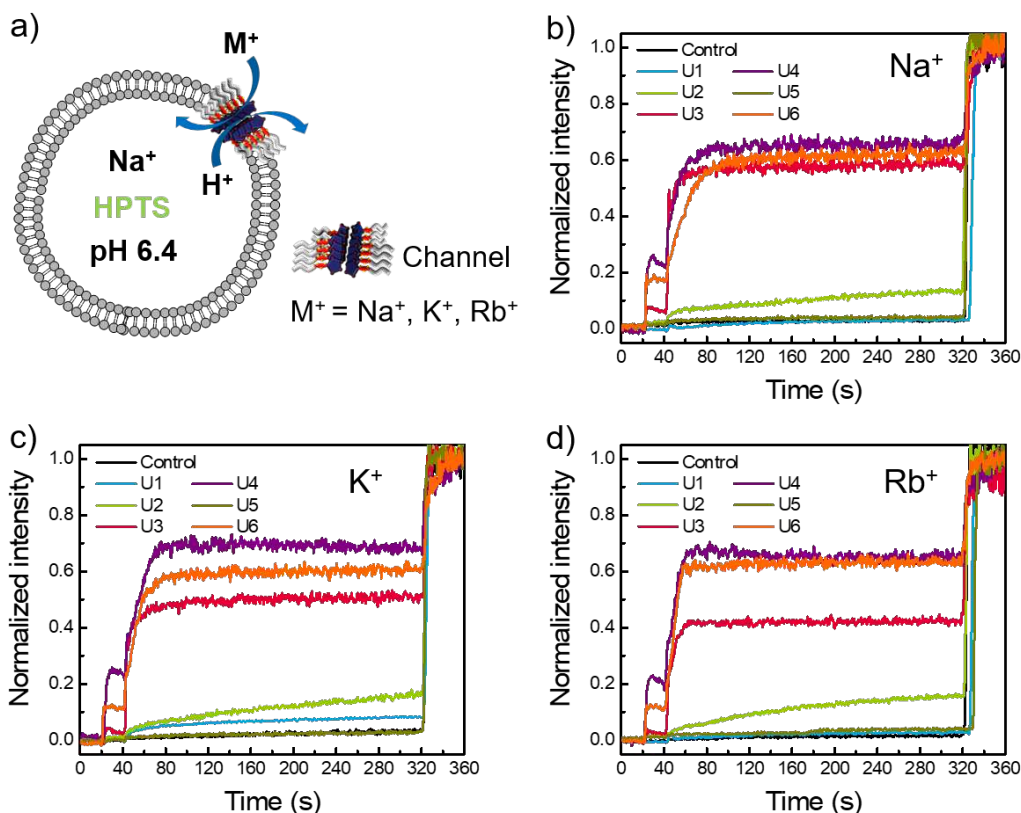


**Figure 62.** (a) Schematic representation of M<sup>+</sup>/H<sup>+</sup> antiport mechanisms together with comparison of cation transport activity expressed as normalized fluorescence intensity of 10 mM U-channels in the extravesicular media containing 100 mM (b) NaCl, (c) KCl and (d) RbCl.

Meanwhile, **U3**, **U4** and **U6** channels all exhibit efficient cation transport activity. **U4** and **U6** channels have the same cation transport activity ( $I = 0.6$ ) due to their identical hydrophobic lateral chains and show no selectivity for the cations. In contrast, the **U3** channel presents decreasing activities ( $I_{Na^+} > I_{K^+} > I_{Rb^+}$ ) for cations of increasing sizes ( $Na^+ < K^+ < Rb^+$ ). The results above suggest that the cation transport activities of U-shaped diimidazole water channels are mainly determined by the nature of the alkylaminocarbonyl lateral chains and are not influenced by the central structures of the channels. The introduction of flexible hydrophobic lateral chains leads to the disorder of U-channel structures that permits the translocation of hydrated cations of certain sizes. In comparison with the hydroxy channels<sup>110</sup>, which also present water-cluster permeation, the disorder of the U-channel cavity also disrupt the



superstructure of the internal water clusters to some extent, drastically reducing its permselectivity to water.

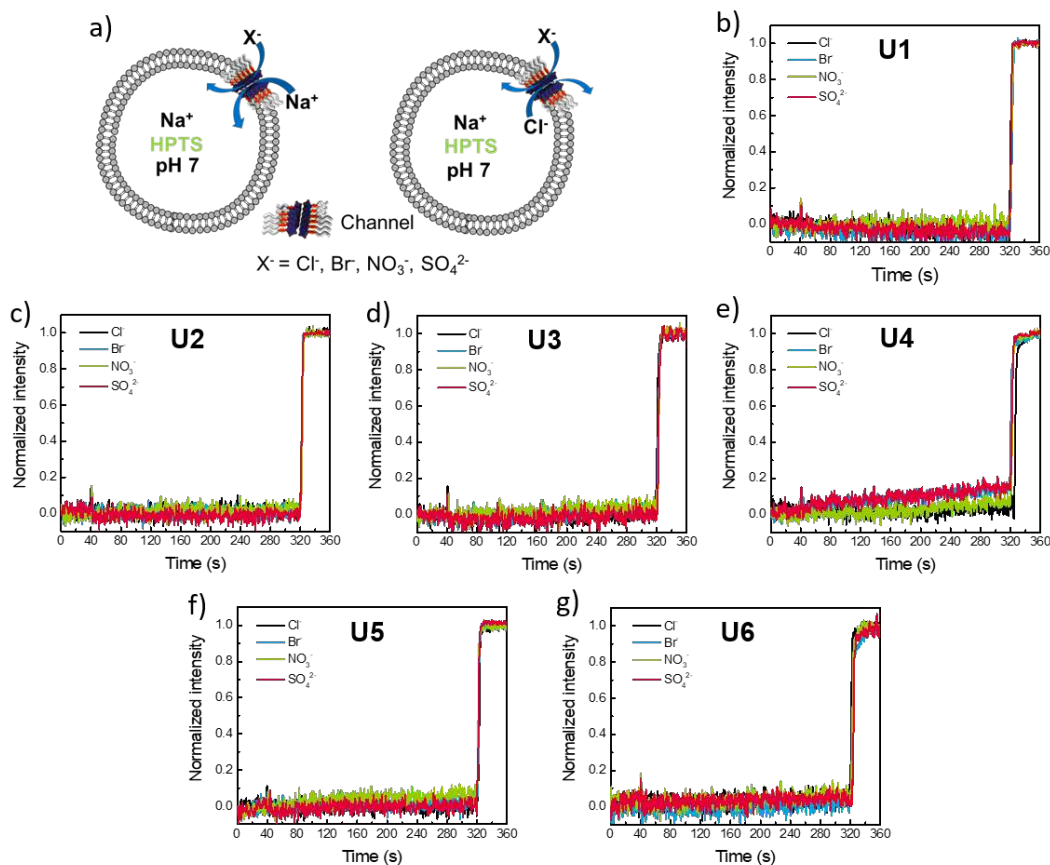


**Figure 63.** (a) Schematic representation of X<sup>-</sup>/Na<sup>+</sup> symport and X<sup>-</sup>/Cl<sup>-</sup> antiport mechanisms together with comparison of anion transport activity expressed as normalized fluorescence intensity of 10 mM (b) U1, (c) U2, (d) U3, (e) U4, (f) U5, and (g) U6 diimidazole U-channels.

To investigate the anion/Na<sup>+</sup> symport and anion/Cl<sup>-</sup> ion antiport mechanisms through U-channels, we conducted anion transport HPTS assays. As shown in Figure 63, all the U-channels exhibit very low (<5%) anion transport activity. Altogether, we confirmed that the U-shaped diimidazole water channels with alkylaminocarbonyl chains present cations and proton transport activity due to the channel structural defects introduced by the lateral chains, but completely reject anions.

**Carboxyfluorescein leakage.** We then performed carboxyfluorescein (CF) leakage experiments<sup>100</sup> to monitor the formation of **U1–U6** channels at different concentrations (Figure 64). Because of the large size of CF and its hydrophilic nature similar to water molecules, its efflux from vesicles is commonly used to determine whether large-size water channels are formed.

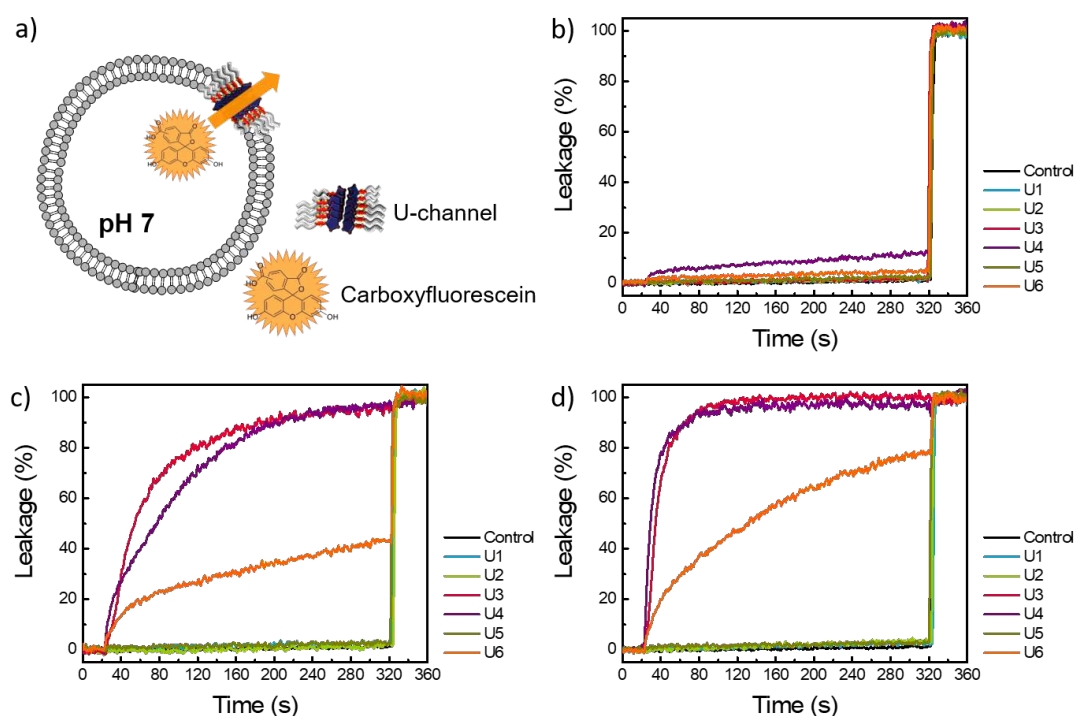


**Figure 64.** Comparison of leakage rate of LUVs containing (a) 0.5 mM, (b) 5 mM and (c) 10 mM of diimidazole U-channels.

With the increase of the added U-channel concentration from 0.5 mM to 10 mM, we observed that the efflux of CF through the **U3**, **U4** and **U6** water channels is substantially increased. According to the variation of CF leakage activity, the U-channels start to form large pores at certain concentrations, and such pores allow the efflux of CF across the lipid membranes. In contrast to the cation transport results, the **U6**-channel achieves only 40% of the CF leakage activity for the **U3** and **U4**-channel. This phenomenon suggests that the channel structural defects introduced by lateral alkylaminocarbonyl chains enhance the leakage of CF from vesicles, but the large-size cavity existing in the **U3** and **U4** channels is the main factor in achieving the high CF efflux rate.

### 3.3. Conclusions

Overall, inspired by the inner hydrophilic center of I-quartet water channels<sup>32, 36</sup>, we designed and synthesized a new class of pyridylbis(formamide-ethylimidazole) derivatives **U1-U6**, which can self-assemble into U-shaped diimidazole water channels. The large size of the **U1-U4** channel cavities together with the presence of multiple hydrophilic motifs, which enable water-clusters transport across lipid membranes. The hydrophilic pores of **U5** and **U6** channels are shielded by the hydrophobic lateral chains, resulting in a tendency for water molecules interacting with the carbonyl groups, thus forming linear water-wires in the channels. Hence, the U-shaped diimidazole water channels achieve a single-channel permeability of  $1.22 \times 10^7$  water molecules/s/channel. Further investigations prove that although all U-channels reject anions, the hydrophobic lateral chains disturb the channel structure, resulting in an increase of cation transport activity with the increasing length of the chains. U-channels can also transport protons, which is consistent with the isotropic arrangement of water molecules in their cavities. Carboxyfluorescein leakage experiments confirm the formation of large pores within **U3** and **U4** channels, while the **U6** channel transports CF attributable to the channel structural defects induced by hydrophobic lateral chains.

In CNTPs, neither water-wires nor water-clusters transport behaviors are able to reject cations and protons.<sup>64</sup> On the contrary, hydroxy channels completely reject ions and protons.<sup>110</sup> In Combination with this work, water-clusters transport exhibits higher water permeability compared to water-wire translocation. However, the selectivity of AWCs for ions and protons is independent of the water-wire/clusters transport behaviors, but depends on the interaction between the water molecules and the inner motifs of the channels. Within this context, both water-wire and clusters permeation approaches are investigated at the single-crystal structural level through U-

channels, and their unique ions/proton selectivity makes them promising for water desalination after slight structural modifications.

### 3.4. Experimental Section

#### 3.4.1. General methods

All reagents were purchased from commercial suppliers (Sigma Aldrich, and VWR) and used without further purification (Purity:  $\geq 95\%$ ). Water utilized in the experiments was referred to milli-Q deionized water. Egg yolk *L*- $\alpha$ -phosphatidylcholine (EYPC) lipid as a solution in chloroform (95%, 25 mg/mL), *L*- $\alpha$ -phosphatidylserine (sodium salt) (PS) as a solution in chloroform (25 mg/mL), polycarbonate membrane (100 nm pore size), and mini-extruders used for vesicle preparation were obtained from Avanti Polar Lipids.  $^1\text{H}$  NMR spectrum were recorded on Bruker Avance III 400 MHz NMR spectrometer in  $\text{DMSO-}d_6$ , with the use of the residual solvent peak ( $\delta = 2.50$  ppm) as reference. Mass spectrometric analyses were performed in the positive ion mode using a quadrupole mass spectrometer (Micromass, Platform II). Fluorescence spectra were recorded in Perkin Elmer LS-55.

#### 3.4.2. Synthesis and characterization

All of the compounds have been synthesized following the general scheme 4. **Synthesis of U1:** 2,6-pyridinedicarbonyl dichloride (1 mmol) was mixed with histamine (2 mmol), and the mixture was dissolved in 10 mL *N,N*-dimethylformamide (DMF) under brief sonication. The reaction system was stirred and heated to 80°C, and refluxed for three hours. After cooling down, we added 10 mL of water to dilute the solution, and added aqueous sodium hydroxide to bring the pH value to 12. Then the pH value was brought back to 7.0 by slowly dropwise adding dilute hydrochloric acid, and white precipitate was observed. The precipitate was collected and dissolved in methanol, then n-

hexane was introduced and pure white powder could gradually be produced under stirring. Solvents were carefully decanted before the products were dried by vacuum desiccator with a yield of 86%.

**Synthesis of U2, U3 and U4:** 1 mmol of compound **U1** was dissolved in 5 mL of tetrahydrofuran (THF), 3 mL of ethyl acetate and 5 mL of acetonitrile under brief sonication. 2 mmol of the corresponding butyl isocyanate, hexyl isocyanate or octyl isocyanate was dropwise added. The solution was stirred and heated to 80°C, and refluxed for three hours. After cooling down, the resulting solution was dried with conventional rotary evaporation under vacuum to obtain white powder. The powder was collected and dissolved in methanol, then n-hexane was introduced and pure white powder could gradually be produced under stirring. Solvents were carefully decanted before the products were dried by vacuum desiccator with a yield of 80%.

**Synthesis of U5:** 6 mmol of *L*-histidine methyl ester dihydrochloride and 3 mL of triethylamine were dissolved in 20 mL of dichloromethane, then the solution was stirred and placed in an ice-water bath. After dropwise adding the dichloromethane solution of 2,6-pyridinedicarbonyl chloride (3 mmol), the solution was withdrawn from the bath and reacted for 24 h at room temperature. 10 mL of aqueous sodium bicarbonate was induced to obtain white precipitate in the aqueous phase. Solvents were removed by filtration before the products were dried by vacuum desiccator with a yield of 53%.

**Synthesis of U6:** 1 mmol of compound **U5** was dissolved in 5 mL of tetrahydrofuran (THF), 3 mL of ethyl acetate and 5 mL of acetonitrile under brief sonication. 2 mmol of octyl isocyanate was dropwise added. The solution was stirred and heated to 80°C, and refluxed for three hours. After cooling down, the resulting solution was dried with conventional rotary evaporation under vacuum to obtain white powder. The powder was collected and dissolved

in methanol, then n-hexane was introduced and pure white powder could gradually be produced under stirring. Solvents were carefully decanted before the products were dried by vacuum desiccator with a yield of 76%.

**Table 6.** Chemical parameters of pyridine bis(formamide-ethyl-imidazole) derivatives **U1-U6**.

	Chemical structure	Name	Formula	MS Cal.
<b>U1</b>		<i>N</i> <sup>2</sup> , <i>N</i> <sup>6</sup> -bis(2-(1 <i>H</i> -imidazol-4-yl)ethyl)pyridine-2,6-dicarboxamide	C <sub>17</sub> H <sub>19</sub> N <sub>7</sub> O <sub>2</sub>	353.16
<b>U2</b>		<i>N</i> <sup>2</sup> , <i>N</i> <sup>6</sup> -bis(2-(1-butylcarbamoyl)-1 <i>H</i> -imidazol-4-yl)ethyl)pyridine-2,6-dicarboxamide	C <sub>27</sub> H <sub>37</sub> N <sub>9</sub> O <sub>4</sub>	551.30
<b>U3</b>		<i>N</i> <sup>2</sup> , <i>N</i> <sup>6</sup> -bis(2-(1-hexylcarbamoyl)-1 <i>H</i> -imidazol-4-yl)ethyl)pyridine-2,6-dicarboxamide	C <sub>31</sub> H <sub>45</sub> N <sub>9</sub> O <sub>4</sub>	607.37
<b>U4</b>		<i>N</i> <sup>2</sup> , <i>N</i> <sup>6</sup> -bis(2-(1-octylcarbamoyl)-1 <i>H</i> -imidazol-4-yl)ethyl)pyridine-2,6-dicarboxamide	C <sub>35</sub> H <sub>53</sub> N <sub>9</sub> O <sub>4</sub>	663.43
<b>U5</b>		Dimethyl 2,2'-((pyridine-2,6-dicarbonyl)bis(azanediyl))(2 <i>S</i> , 2' <i>S</i> )-bis(3-(1 <i>H</i> -imidazol-4-yl)propanoate)	C <sub>21</sub> H <sub>23</sub> N <sub>7</sub> O <sub>6</sub>	469.17
<b>U6</b>		Dimethyl 2,2'-((pyridine-2,6-dicarbonyl)bis(azanediyl))(2 <i>S</i> , 2' <i>S</i> )-bis(3-(1-(octylcarbamoyl)-1 <i>H</i> -imidazol-4-yl)propanoate)	C <sub>39</sub> H <sub>57</sub> N <sub>9</sub> O <sub>8</sub>	779.44

All the samples ready for <sup>1</sup>H NMR were prepared in 0.5 mL of DMSO-*d*<sub>6</sub>. Data for <sup>1</sup>H NMR and ESI-MS spectra are reported as follows:

**U1** (Figure 65):  $^1\text{H NMR}$  (**400 MHz, DMSO-*d*<sub>6</sub>**)  $\delta$  (ppm) = 9.42 (t,  $J = 6.0$  Hz, 2H), 8.21 – 8.14 (m, 3H), 7.55 (d, 2H), 6.86 (d, 2H), 3.62 – 3.57 (m, 4H), 2.85 – 2.80 (m, 4H); MS Cal. = 353.16, ESI-MS found  $[\text{M} + \text{H}^+]^+ = 355.06$ .

**U2** (Figure 66):  $^1\text{H NMR}$  (**400 MHz, DMSO-*d*<sub>6</sub>**)  $\delta$  (ppm) = 9.42 (t,  $J = 6.2$  Hz, 2H), 8.35 (t,  $J = 5.6$  Hz, 2H), 8.24 – 8.12 (m, 5H), 7.52 (dd,  $J = 31.8, 1.2$  Hz, 2H), 3.61 (q,  $J = 6.8$  Hz, 4H), 3.21 (td,  $J = 7.0, 5.5$  Hz, 4H), 2.83 – 2.77 (t, 4H), 1.54 – 1.26 (m, 8H), 0.87 (t,  $J = 11.4, 7.3$  Hz, 6H); MS Cal. = 551.30, ESI-MS found  $[\text{M} + \text{H}^+]^+ = 552.30$ .

**U3** (Figure 67):  $^1\text{H NMR}$  (**400 MHz, DMSO-*d*<sub>6</sub>**)  $\delta$  (ppm) = 9.42 (t,  $J = 6.1$  Hz, 2H), 8.35 (t,  $J = 5.6$  Hz, 2H), 8.22 – 8.15 (m, 5H), 7.48 (s,  $J = 1.3$  Hz, 2H), 3.60 (q,  $J = 7.1$  Hz, 4H), 3.24 – 3.17 (td, 4H), 2.79 (t,  $J = 7.7$  Hz, 4H), 1.50 (m,  $J = 7.1$  Hz, 4H), 1.33 – 1.23 (m, 13H), 0.88 – 0.83 (t, 6H); MS Cal. = 607.37, ESI-MS found  $[\text{M} + \text{H}^+]^+ = 608.37$ .

**U4** (Figure 68):  $^1\text{H NMR}$  (**400 MHz, DMSO-*d*<sub>6</sub>**)  $\delta$  (ppm) = 9.42 (t,  $J = 6.1$  Hz, 2H), 8.35 (t,  $J = 5.5$  Hz, 2H), 8.22 – 8.15 (m, 5H), 7.48 (s,  $J = 1.3$  Hz, 2H), 3.60 (q,  $J = 7.1$  Hz, 4H), 3.20 (td,  $J = 6.7$  Hz, 4H), 2.79 (t,  $J = 7.7$  Hz, 4H), 1.51 (m,  $J = 7.0$  Hz, 4H), 1.25 (m,  $J = 9.7$  Hz, 20H), 0.87 – 0.83 (t, 6H); MS Cal. = 663.43, ESI-MS found  $[\text{M} + \text{H}^+]^+ = 664.43$ .

**U5** (Figure 69):  $^1\text{H NMR}$  (**400 MHz, DMSO-*d*<sub>6</sub>**)  $\delta$  (ppm) = 9.48 (d,  $J = 7.1$  Hz, 2H), 8.19 (d, 3H), 7.55 (d, 2H), 6.90 (d, 2H), 4.73 – 4.67 (m, 2H), 3.66 (s, 6H), 3.17 (t,  $J = 6.5$  Hz, 4H). MS Cal. = 469.17, ESI-MS found  $[\text{M} + \text{H}^+]^+ = 470.15$ .

**U6** (Figure 70):  $^1\text{H NMR}$  (**400 MHz, DMSO-*d*<sub>6</sub>**)  $\delta$  (ppm) = 9.55 – 9.32 (d, 2H), 8.19 (d, 4H), 8.12 (d,  $J = 8.2$  Hz, 1H), 7.62 – 7.47 (d, 2H), 6.92 (s,  $J = 7.3$  Hz, 2H), 4.79 – 4.63 (m, 2H), 3.65 (s, 6H), 3.19 – 3.16 (q, 4H), 3.00 – 2.87 (m,

4H), 1.40 (m,  $J = 60.5, 6.9$  Hz, 4H), 1.23 (m, 20H), 0.85 (t,  $J = 6.4$  Hz, 6H); MS  
 Cal. = 779.44, ESI-MS found  $[M + H]^+ = 780.44$ .

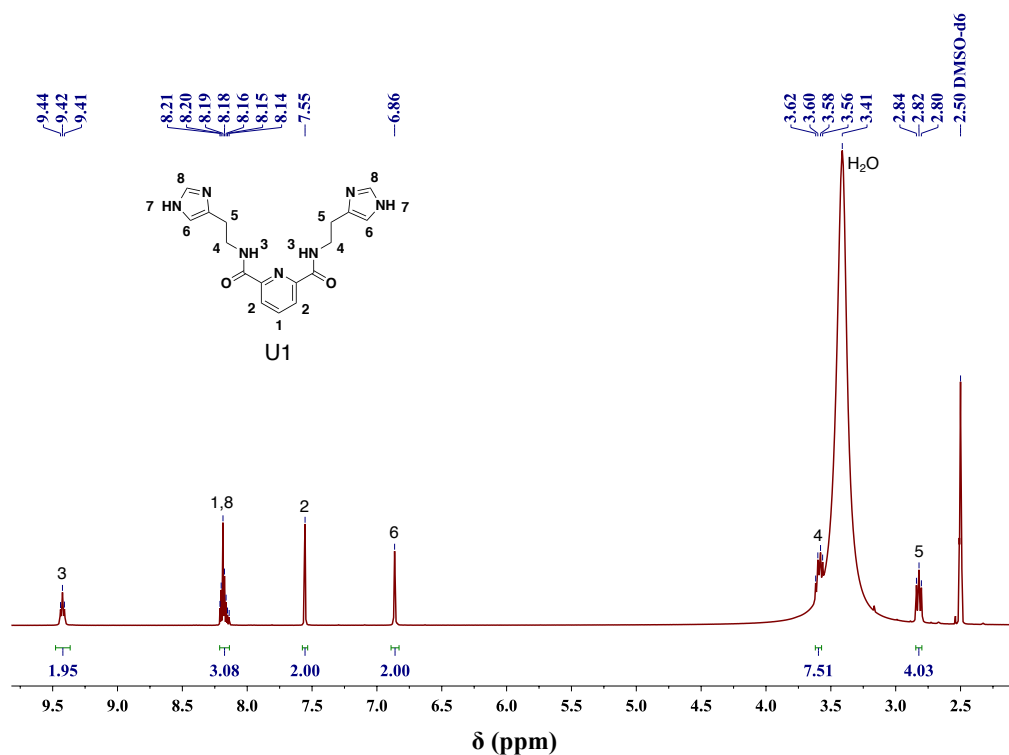


**Figure 65.**  $^1\text{H}$  NMR spectrum of **U1**.

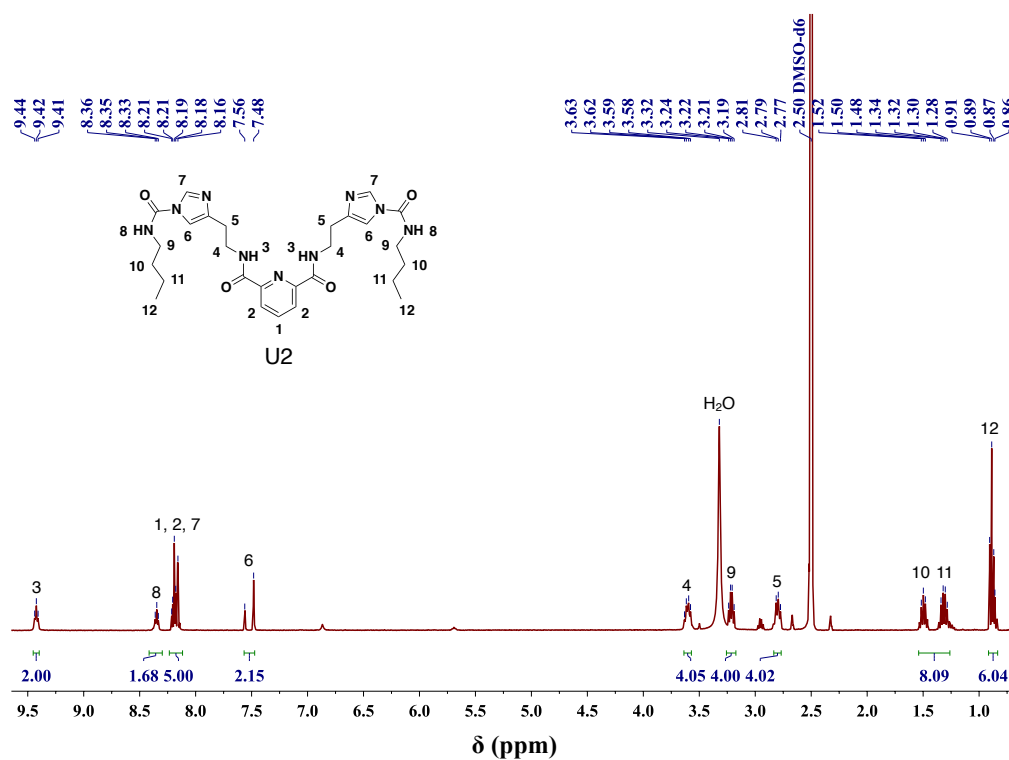


**Figure 66.**  $^1\text{H}$  NMR spectrum of **U2**.



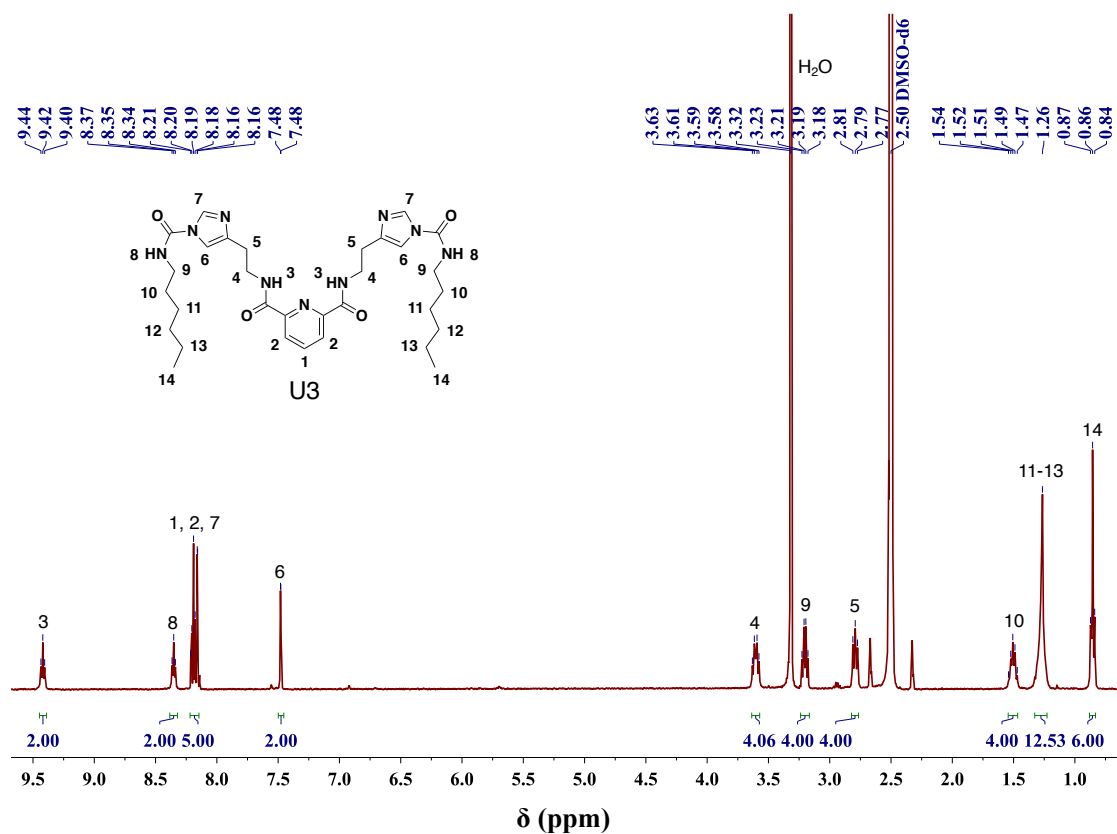


**Figure 67.**  $^1\text{H}$  NMR spectrum of **U3**.

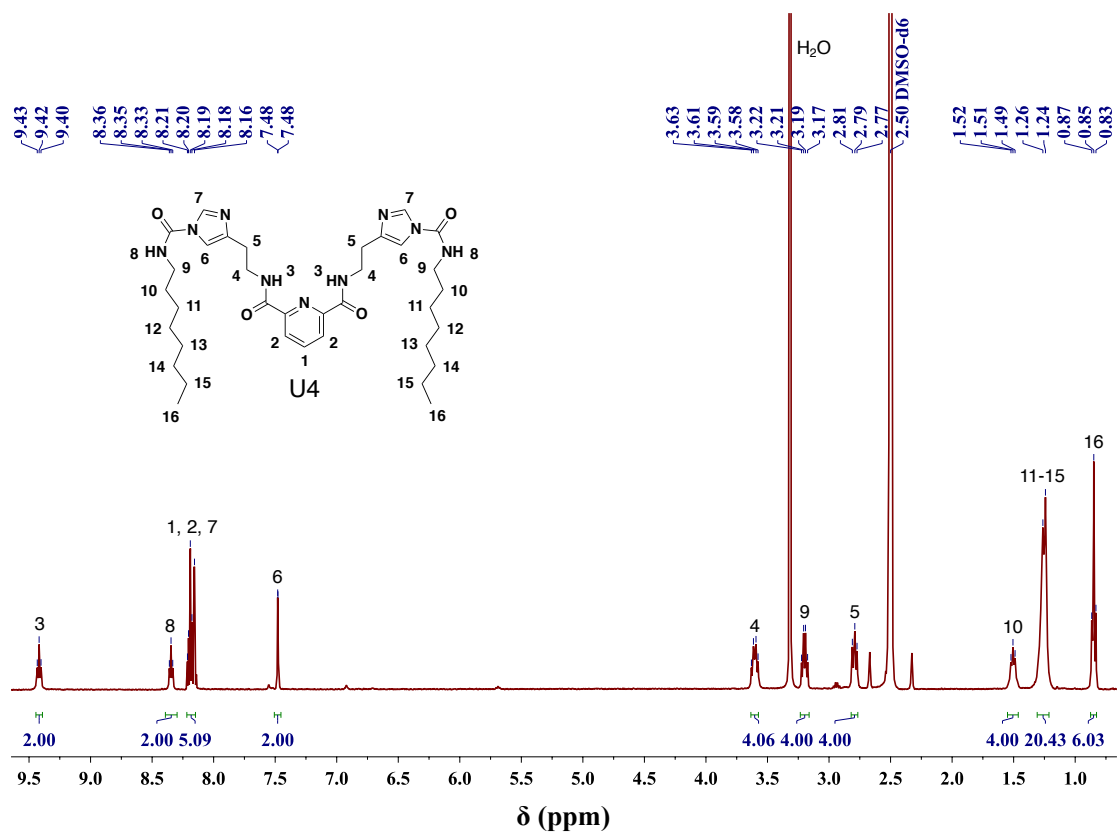


**Figure 68.**  $^1\text{H}$  NMR spectrum of **U4**.

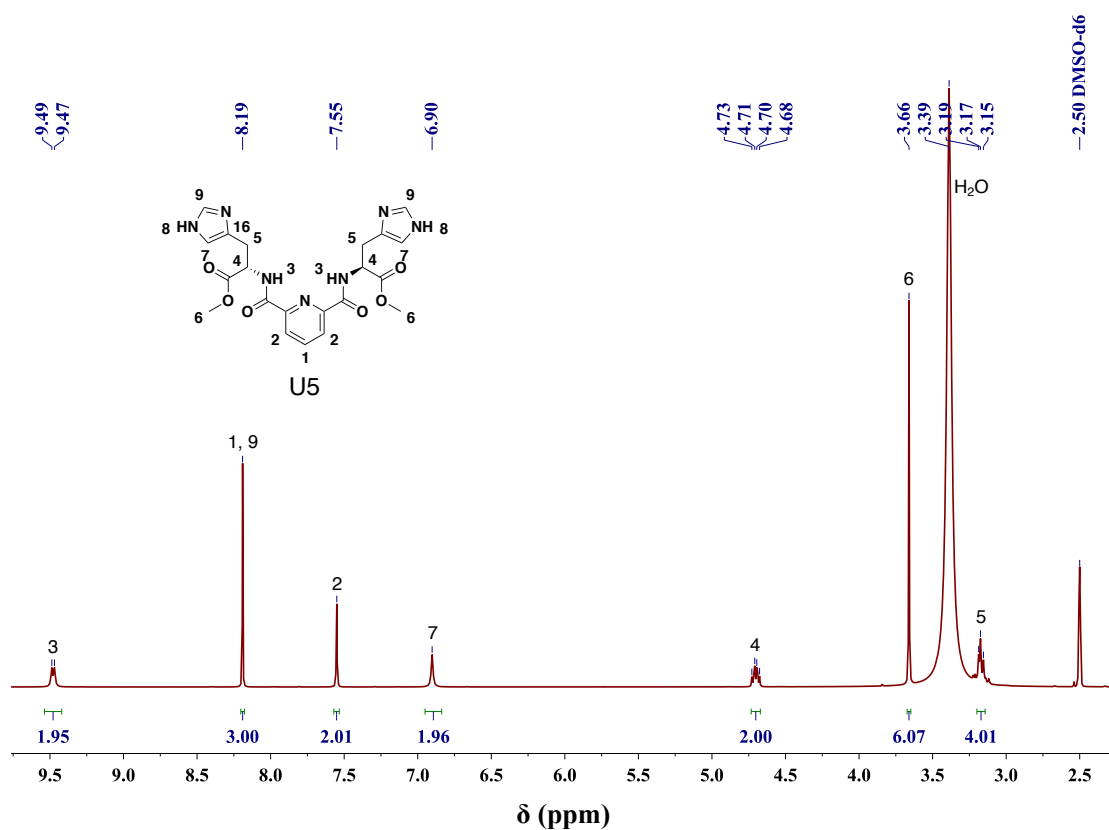


**Figure 69.**  $^1\text{H}$  NMR spectrum of **U5**.

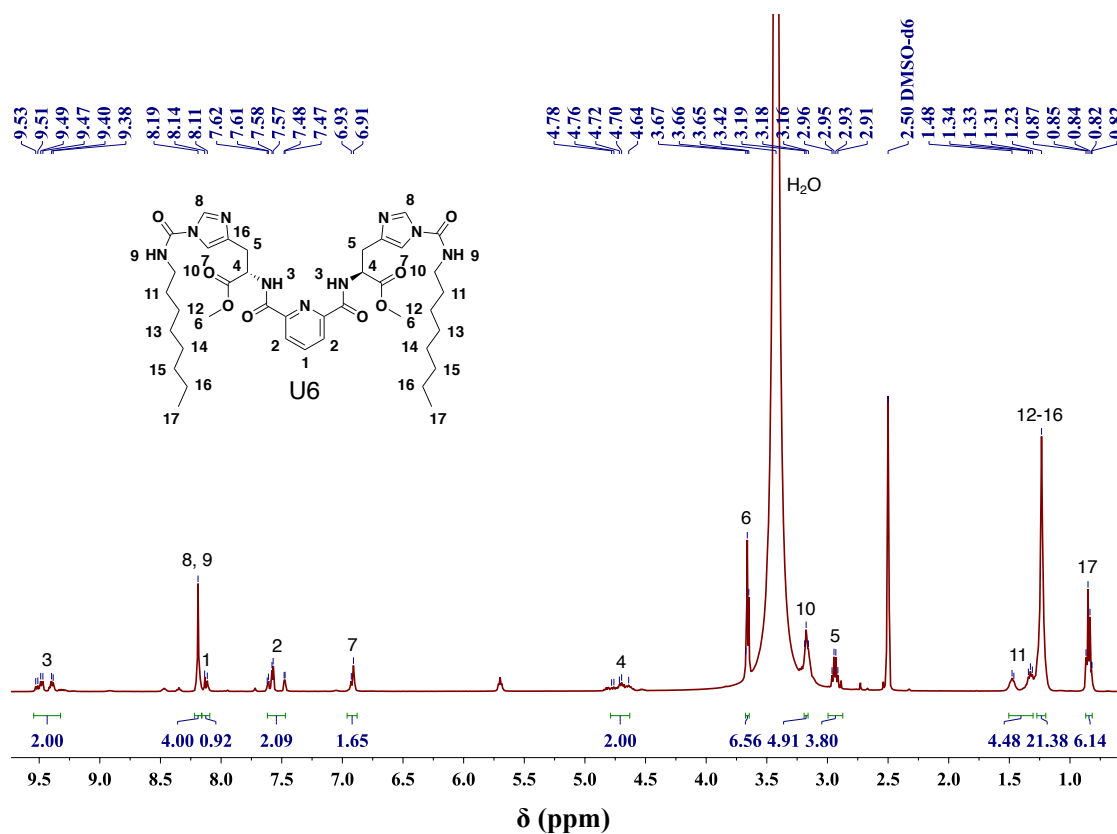


**Figure 70.**  $^1\text{H}$  NMR spectrum of **U6**.

### 3.4.3. X-ray crystallography<sup>[S1-6]</sup>

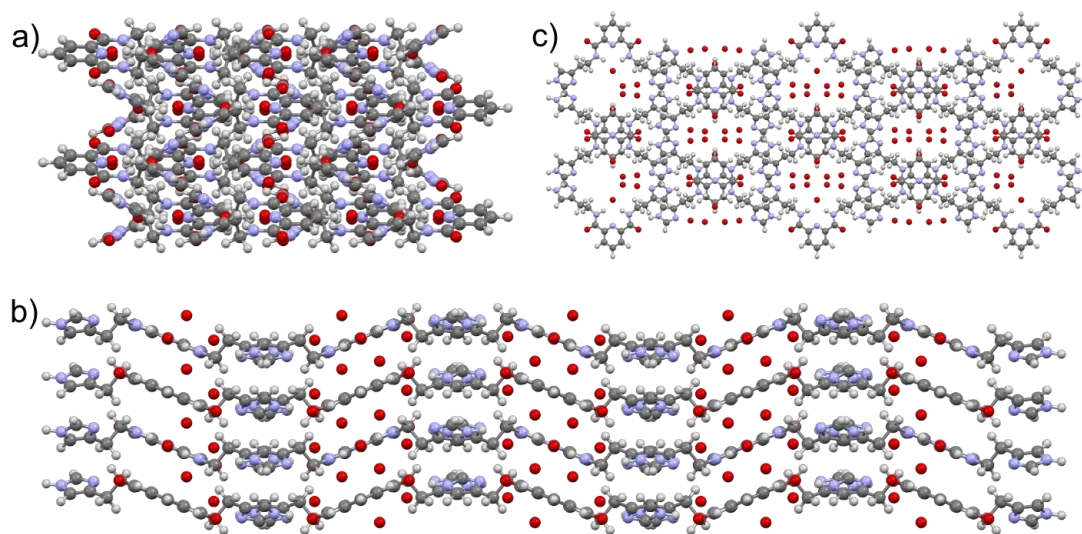


**Figure 71.** Solid state crystal structure of U1 with crystal packing.

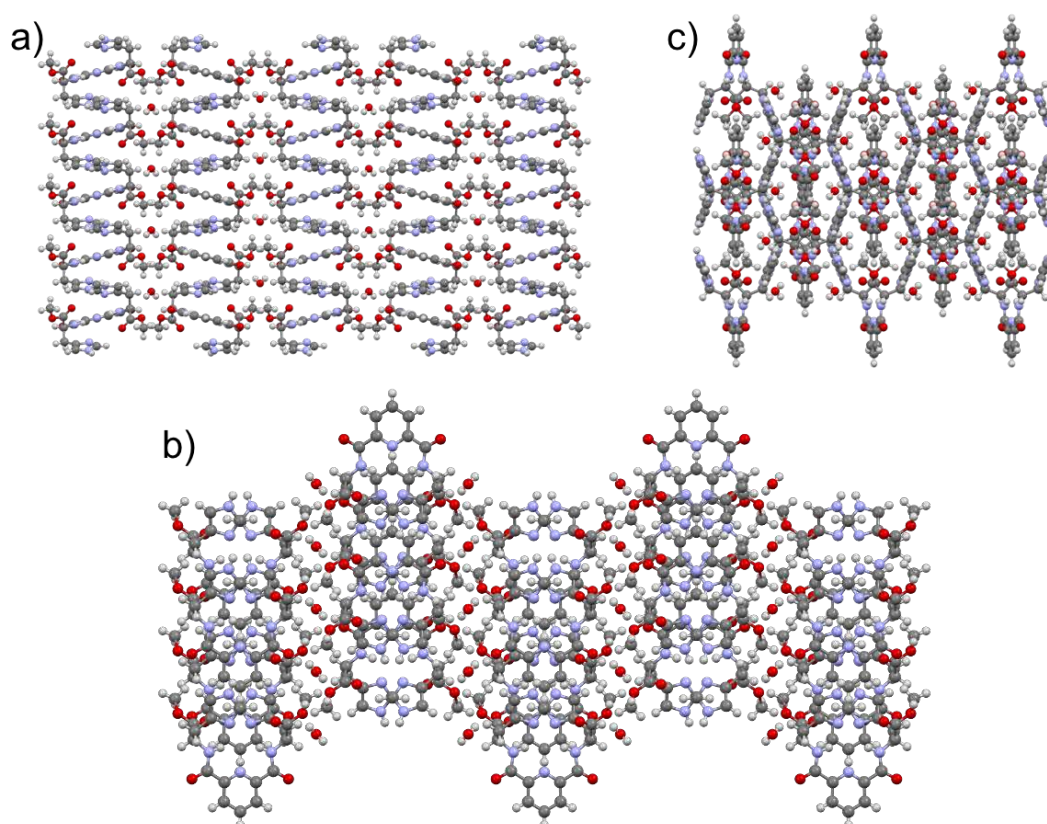


**Figure 72.** Solid state crystal structure of U5 with crystal packing.

### 3.4.4. Transmembrane transport experiments

#### Water transport assays<sup>[S7]</sup>

**Sample preparation.** We set the concentration gradients (5, 10, 15, 20, and 25 mg/mL) of **U1**, **U2**, **U3**, **U4**, **U5**, and **U6** solutions in DMSO for water transport experiments. In the ion transport experiments, 10 mM of each compound solutions in DMSO were submitted.

**LUV preparation.** Liposomes were prepared using the film rehydration method. A PC/PS/Chl mixture with a molar ratio of 4/1/5 was dissolved in chloroform/methanol mixture (CHCl<sub>3</sub>/MeOH, v/v: 1/1). The solution was dried on a rotary evaporator and subsequently in a vacuum desiccator to remove residual solvent for 2 h. After rehydration with 1 mL of phosphate buffer (10 mM sodium phosphate, pH = 6.4) containing 200 mM D(+)-sucrose for 40 min, the suspension was submitted to at least 7 freeze-thaw cycles (bathed in liquid nitrogen and water at room temperature, respectively). The large multilamellar liposome suspension was submitted to high-pressure extrusion at room temperature (21 extrusions through a 100 nm polycarbonate membrane to obtain monodisperse unilamellar vesicles with an average diameter of ~100 nm), and the size of which was characterized by dynamic light scattering (Zetasizer Nano, Malvern Instruments Ltd., UK). The aliquot of the compounds dissolved in DMSO have been added to the liposomes. The water permeability tests were conducted on a stopped-flow instrument (SFM3000 + MOS450, Bio-Logic SAS, Claix, France). Exposure of vesicles to hypertonic osmolyte in the corresponding buffer resulted in the shrinkage of the vesicles due to an outwardly directed osmotic gradient. The changes of light scattering were recorded at a wavelength of 345 nm.

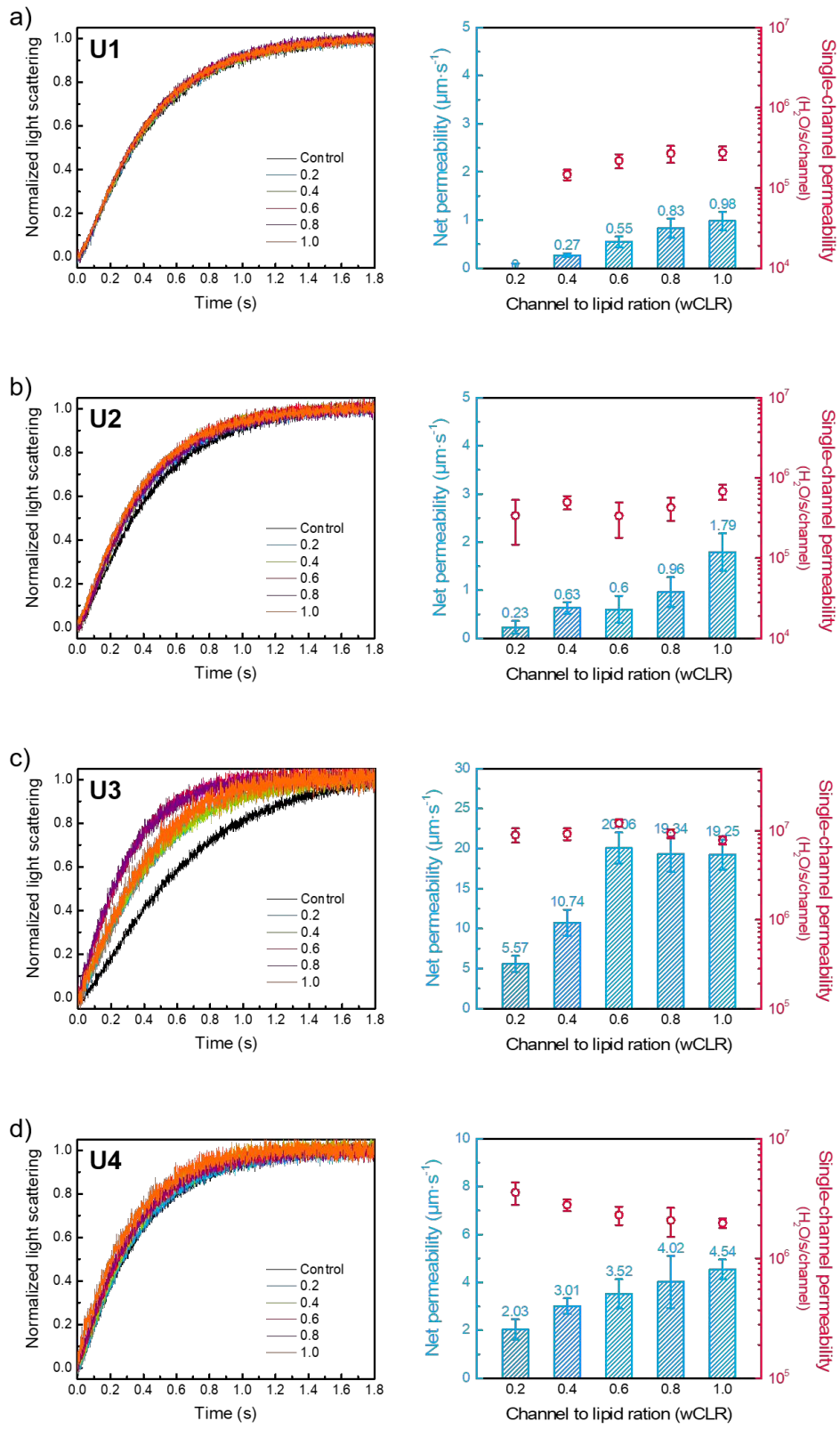
**Water transport.** The abrupt change of the vesicle size led to variation in the light scattering at 90° according to the Rayleigh-Gans theory applied to this

system and could be fitted in the form of the sum of two exponential function. The osmotic permeability ( $P_f$ ) was calculated as following:

$$P_f = \frac{k}{\frac{S}{V_0} \times V_w \times \Delta_{osm}}$$

where  $k$  is the exponential coefficient of the change in the light scattering;  $S$  and  $V_0$  are the initial surface area and volume of the vesicles, respectively;  $V_w$  is the molar volume of water, and  $\Delta_{osm}$  is the osmolarity difference.

In an average experiment, 100  $\mu$ L stock lipid solution containing 0.524 mg of lipids was diluted with 1880  $\mu$ L of 200 mM D(+)-sucrose in 10 mM phosphate buffer solution. The compounds were injected in 20  $\mu$ L aliquots in DMSO. The solution mix was thermostatted at 20 °C for 30 minutes before exposure to the 400 mM D(+)-sucrose solution. Experiments have been conducted at different concentrations of the injected compounds, in which the concentrations of U-channels solutions in DMSO were 5, 10, 15, 20, and 25 mg/mL corresponding to the channel to lipid ratio at weight (wCLR) = 0.2, 0.4, 0.6, 0.8, and 1.0, respectively. Average permeability was calculated by using the permeability values obtained from at least three different batches of vesicles.



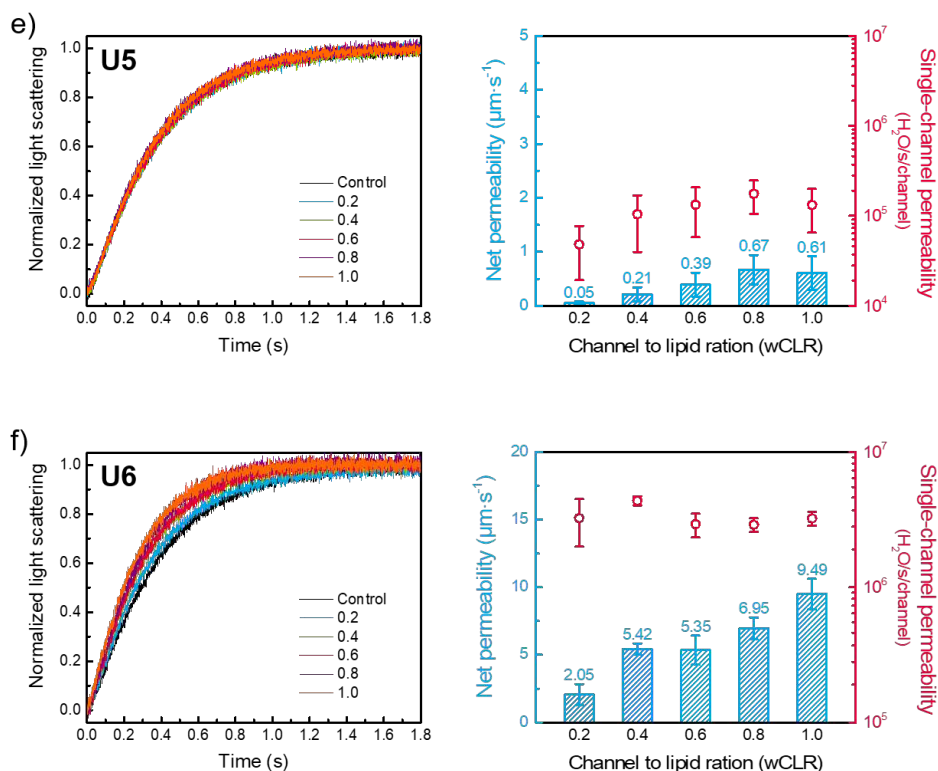


**Figure 73.** The water permeabilities expressed as normalized light scattering of the channels assembled by (a) **U1**, (b) **U2**, (c) **U3**, (d) **U4**, (e) **U5**, and (f) **U6** were determined by stopped-flow light scattering experiments. The stopped-flow traces of liposomes containing different concentrations of U-channels (left). The net permeabilities of different channel to lipid ratios of U-channels (right).

**Single-channel permeability calculation.** 30 molecules of **U1-U4** or 24 molecules of **U5** and **U6** are needed to form a channel within a transmembrane length of 5 nm. Taking the sample of **U3** at wCLR = 0.6 as an example, the molar channel to lipid ratio is 0.019. The average radius of the liposome was 72.5 nm determined by DLS experiments. Hence, the sum of outer and inner surface areas was  $4\pi \times R^2 + 4\pi \times (R - 5)^2 = 123,308 \text{ nm}^2$ . The average cross-sectional area of a lipid in average was  $0.287 \text{ nm}^2$  (PC/PS/Chl lipids with a molar ratio of 4/1/5: the cross-sectional areas of PC and PS were  $\sim 0.35 \text{ nm}^2$  and that of cholesterol was  $0.223 \text{ nm}^2$ ), and that of the **U3** U-channel (not including the alkyl chain) was estimated as  $3.14 \text{ nm}^2$ . So, the insertion number of the channel was  $\sim 3392$  per vesicle. If the overall net permeability by channels in liposomes was  $20.06 \pm 1.95 \text{ μm/s}$ , the single-channel permeability was  $3.65$

$\pm 0.35 \times 10^{-16} \text{ cm}^3/\text{s}$  and  $1.22 \pm 0.12 \times 10^7$  water molecules/s. According to the same algorithm, the highest single-channel permeabilities for **U1**, **U2**, **U3**, **U4**, **U5**, and **U6** channels were  $(2.75 \pm 0.53) \times 10^5$ ,  $(6.87 \pm 1.48) \times 10^5$ ,  $(1.22 \pm 0.12) \times 10^7$ ,  $(3.56 \pm 0.75) \times 10^6$ ,  $(1.31 \pm 0.7) \times 10^5$ , and  $(4.36 \pm 0.33) \times 10^6$  water molecules/s, respectively. (Figure 73, Table 6) The single channel permeability values varied obviously, covering the range of  $1.31 \times 10^5$  to  $1.22 \times 10^7$  H<sub>2</sub>O/s/channel, which are within three orders of magnitude lower than those of AQPs ( $\sim 10^8$ – $10^9$  water /s/channel).

### **Ion transport HPTS assays**

**LUV preparation for cation transport.** Egg yolk *L*- $\alpha$ -phosphatidylcholine (EYPC chloroform solution, 800  $\mu\text{L}$ , 26 mmol) was dissolved in a  $\text{CHCl}_3/\text{MeOH}$  mixture, the solution was evaporated under reduced pressure and the resulting thin film was dried in a vacuum desiccator for 2 h. The lipid film was hydrated in 400  $\mu\text{L}$  of phosphate buffer (10 mM sodium phosphate, 100 mM NaCl, pH = 6.4) containing 10  $\mu\text{M}$  HPTS (pyranine, 8-hydroxypyrene-1,3,6-trisulfonic acid trisodium salt) for 40 min. During hydration, the suspension was submitted to at least 7 freeze-thaw cycles (bathed in liquid nitrogen and water at room temperature, respectively). The large multilamellar liposome suspension (1mL) was submitted to high-pressure extrusion at room temperature (21 extrusions through a 100 nm polycarbonate membrane to obtain monodisperse unilamellar vesicles with an average diameter of  $\sim 100$  nm). The LUV suspension was separated from extravesicular dye by size exclusion chromatography (SEC) (stationary phase: Sephadex G-50, mobile phase: phosphate buffer) and diluted to 2.8 mL with the corresponding phosphate buffer to give a stock solution with a lipid concentration of 9.3 mM (assuming 100% of lipid was incorporated into liposomes).

**Cation transport.** 100  $\mu\text{L}$  HPTS-loaded vesicles (stock solution) was suspended in 1.86 mL of phosphate buffer (10 mM sodium phosphate, pH = 6.4)



containing 100 mM MCl (M = Na<sup>+</sup>, K<sup>+</sup>, or Rb<sup>+</sup>) and placed into a quartz fluorimetric cuvette. The emission of HPTS at 510 nm was monitored with excitation wavelengths at 403 and 460 nm simultaneously, using a Perkin Elmer LS-55 fluorescence spectrometer. During the experiment, 20  $\mu$ L of a 10 mM U-channel solution in DMSO was added at t = 20 sec. At t = 40 sec, 29  $\mu$ L of 0.5 M aqueous NaOH was injected, resulting in the pH value increasing to around 7 in the extravesicular media. Maximal possible changes in dye emission were obtained at t = 320 sec by lysis of the liposomes with detergent (40  $\mu$ L of 5 % aqueous Triton X-100). We expressed normalized intensity (the value of  $I_{460}/I_{403}$ ) as a function of time (Figure 62).

**LUV preparation for anion transport.** Egg yolk *L*- $\alpha$ -phosphatidylcholine (EYPC chloroform solution, 800  $\mu$ L, 26 mmol) was dissolved in a CHCl<sub>3</sub>/MeOH mixture, the solution was evaporated under reduced pressure and the resulting thin film was dried in a vacuum desiccator for 2 h. The lipid film was hydrated in 400  $\mu$ L of HEPES buffer (10 mM HEPES, 100 mM NaCl, pH = 7.0) containing 10  $\mu$ M HPTS (pyranine, 8-hydroxypyrene-1,3,6-trisulfonic acid trisodium salt) for 40 min. During hydration, the suspension was submitted to at least 7 freeze-thaw cycles (bathed in liquid nitrogen and water at room temperature, respectively). The large multilamellar liposome suspension (1mL) was submitted to high-pressure extrusion at room temperature (21 extrusions through a 100 nm polycarbonate membrane to obtain monodisperse unilamellar vesicles with an average diameter of  $\sim$ 100 nm). The LUV suspension was separated from extravesicular dye by size exclusion chromatography (SEC) (stationary phase: Sephadex G-50, mobile phase: phosphate buffer) and diluted to 2.8 mL with the corresponding HEPES buffer to give a stock solution with a lipid concentration of 9.3 mM (assuming 100% of lipid was incorporated into liposomes).

**Anion transport.**<sup>[S8]</sup> 100  $\mu$ L HPTS-loaded vesicles (stock solution) was suspended in 1.86 ml of HEPES buffer (10 mM HEPES, pH = 6.4) containing 100 mM NaX (X = Br<sup>-</sup>, I<sup>-</sup>, NO<sub>3</sub><sup>-</sup>, or SO<sub>4</sub><sup>2-</sup>) and placed into a quartz fluorimetric cuvette. The emission of HPTS at 510 nm was monitored with excitation wavelengths at 403 and 460 nm simultaneously, using a Perkin Elmer LS-55 fluorescence spectrometer. During the experiment, 20  $\mu$ L of a 10 mM U-channel solution in DMSO was added at t = 20 sec. At t = 40 sec, 29  $\mu$ L of 0.5 M aqueous NaOH was injected, resulting in the pH value increasing to around 7.8 in the extravascular media. Maximal possible changes in dye emission were obtained at t = 320 sec by lysis of the liposomes with detergent (40  $\mu$ L of 5 % aqueous Triton X-100). We expressed normalized intensity (the value of  $I_{460}/I_{403}$ ) as a function of time.

### **CF leakage assays**

**LUV preparation.** The preparation of LUVs for leakage experiment is similar as for entrapped HPTS LUVs. The difference is the salt solution contains 70 mM of 5(6)-Carboxyfluorescein (CF) instead of HPTS: the right amount of CF was introduced in a phosphate buffer (10 mM sodium phosphate, 100 mM NaCl, pH = 7.0) in order to obtain a 70 mM concentration of CF. Then the pH was adjusted to 7.0 by addition of 5M NaOH, CF was completely solubilized at this time. The next steps are the same as previously described for HPTS LUVs preparation. The stock solution of CF entrapped LUVs has to be first diluted 20 times (giving a lipid concentration of about 500  $\mu$ M) in case of the maximum fluorescence intensity of CF exceeding the measurement range of the spectrophotometer.

We used direct fluorescence measurement to monitor the efflux of CF. 100  $\mu$ L of the diluted stock vesicle solution was suspended in 1.88 mL of the corresponding buffer (10 mM sodium phosphate, 100 mM NaCl, pH = 7.0) and placed into a quartz fluorimetric cell (lipid concentration became ca. 25  $\mu$ M).

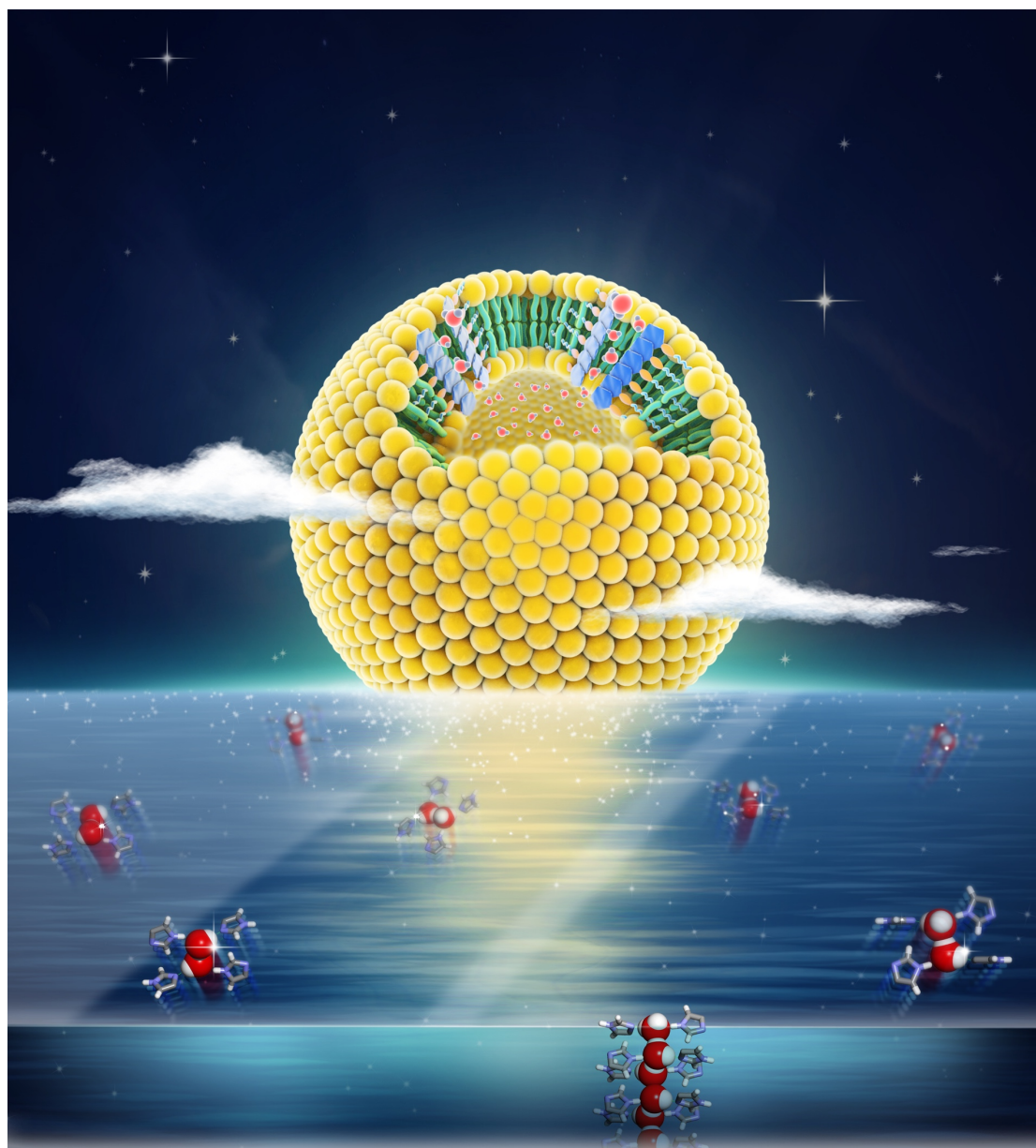
The fluorescence of CF was monitored at a 492 nm excitation and 517 nm emission wavelengths. After 40 sec from the beginning of the experiment, 20  $\mu$ L of U-channel solution in DMSO was added. After 320 sec, the vesicles are lysed with detergent (40  $\mu$ L of 5% aqueous Triton X-100), in order to equilibrate obtain the maximal fluorescence value, corresponding to the 100% efflux of CF.

## References

- [S1] CrysAlisPro, Rigaku Oxford Diffraction, England **2012**.
- [S2] Bruker (2016). APEX3, SAINT, XPREP and SADABS. Bruker AXS Inc., Madison, Wisconsin, USA. van der Lee, A. *J. Appl. Crystallogr.* **2013**, *46*, 1306–1315.
- [S3] Palatinus, L.; Chapuis, G. *J. Appl. Crystallogr.* **2007**, *40*, 786–790.
- [S4] Betteridge, P. W.; Carruthers, J. R.; Cooper, R. I.; Prout, K.; Watkin, D. J. *J. Appl. Crystallogr.* **2003**, *36*, 1487–1487.
- [S5] Cooper, R. I.; Thompson, A. L.; Watkin, D. J. *J. Appl. Crystallogr.* **2010**, *46*, 1100–1109.
- [S6] Kabsch, W. *Acta Cryst. D66*, 125–132 (2010a); Kabsch, W. *Acta Cryst. D66*, 133–144 (2010b).
- [S7] Huang, L.-B.; Hardiagon, A.; Kocsis, I.; Jegu, C.-A.; Deleanu, M.; Gilles, A.; van der Lee, A.; Sterpone, F.; Baaden, M.; Barboiu, M. *J. Am. Chem. Soc.* **2021**, *143*, 11, 4224–4233.
- [S8] Shinde, S. V.; Talukdar, P. *Angew. Chem. Int. Ed.* **2017**, *56*, 4238–4242.

## Chapter IV – Bilayer versus Polymeric Artificial Water Channel Membranes

### – Structural Determinants for Enhanced Filtration Performances



This chapter is adapted *with permission from* L.-B. Huang, M. Di Vincenzo, M. Göktuğ Ahunbay, A. van der Lee, D. Cot, S. Cerneaux, G. Maurin, M. Barboiu, Bilayer versus polymeric artificial water channel membranes - structural determinants for enhanced filtration performances. *J. Am. Chem. Soc.* **2021**, *143*, 14386–14393. Copyright © 2021, American Chemical Society.

## 4.1. Introduction

Water scarcity is an important genuine issue related to the important growth of population and industry, all around the world.<sup>4</sup> To continuously address the water supply needs, innovative membranes have been extensively developed during the last decades for industrial water cleaning and for the production of desalted water.<sup>18</sup>

Cells contain Aquaporins-AQPs to selectively translocate water across their membrane.<sup>12-14</sup> Biomimicking AQPs is an important challenge. Similar water transport performances may be obtained by using synthetic compounds, displaying functions *like* the natural counterparts.<sup>17, 32-34, 73-75, 113</sup> The incipient works in this field showed that “Artificial Water Channels”-AWCs<sup>13</sup> may provide a route to fabricate highly efficient *biomimetic membranes* for desalination. Lipid bilayer<sup>13, 14</sup> and polymeric membranes<sup>92</sup> have been produced particularly for understanding of the relationship between self-assembly of waters and their dynamic translocation within single channels.<sup>96</sup> They have been also proven to have a huge impact on improving the production of pure water *via* desalination with hybrid materials.<sup>92</sup> The filtration performances are highly dependent on how water transport performances translate from the single channel conduits in bilayer membranes to multi-channel m-scale membranes used for industrial desalination.<sup>92, 96</sup>

It is well-known that self-assembly of the monomers to form complex channel architectures, strongly depends on the nature of their host-matrix. In such a scenario, the self-assembled AWCs may adapt their morphologies to external host-environments, toward the construction of single channels in bilayer membranes<sup>32</sup> or to solid percolated multi-channels in macroscopic polymeric membranes.<sup>92</sup> Importantly, the performances observed for the single channels in *soft* bilayer membranes, might not be necessarily translated into multi-

channels configuration in the host-*glassy* layers of polymeric membranes (Figure 74 a). Herein we show that structure-function properties of AWCs should provide answers on how to translate single channel performances observed in bilayer membranes to hybrid polymeric membranes for an efficient desalination.

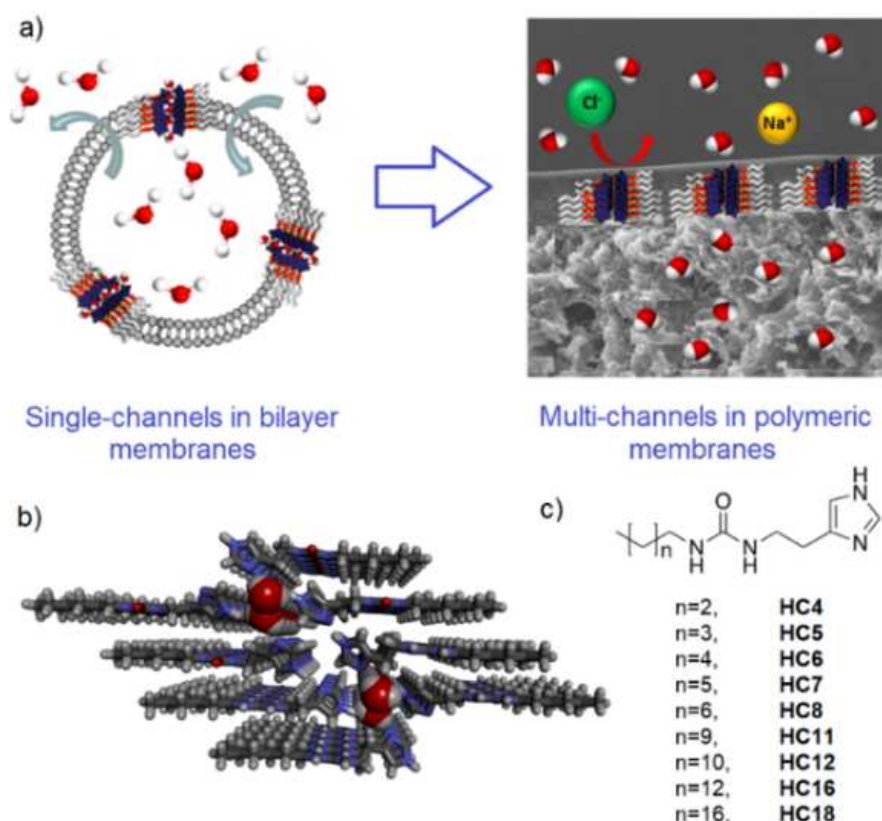


**Figure 74.** (a) Single water channels versus multi-channels architectures stabilized within bilayer and polymeric membranes, respectively. (b) Top view of I-quartet channels and (c) Structure of synthesized alkyl-ureido-ethyl-imidazole compounds **HC4–HC18**.

Back in 2011, our group introduced I-quartet, that form tubular 2.6 Å water channels, mutually stabilized via urea and imidazole-water H-bonding and hydrophobic interactions in bilayer membranes (Figure 74 b).<sup>17, 32, 73-75, 113</sup> They selectively transport water and reject ions.<sup>36, 44</sup> Water permeabilities through bilayer membranes substantially increase when the length of the alkyl tail of I-quartets increases: **HC4** < **HC6** < **HC8**,<sup>36</sup> as a result of enhanced stabilization of central I-quartet conduits, *via* hydrophobic wrapping of alkyl tails as

stabilizers at the interfaces with the lipids of the bilayer membrane. On the other hand, lamellar sponge-like nano-crystals of **HC6** can be obtained from a colloidal solution of the I-quartets *via* simple evaporation.<sup>92</sup> The colloidal aggregates of HC6 can be further incorporated in polyamide-PA dense active layers for the fabrication of reverse-osmosis RO membranes via interfacial polymerization-IP.<sup>92</sup> Defect free layers can be achieved by varying the concentration of the AWCs and PA monomers in the casting solutions.<sup>92</sup> Both single-channel insertion in bilayer membrane and multi-channel nano-dispersion in PA membranes strongly depend on the amphiphilic properties of **HCx**, affecting both the solubility in the bilayer and the kinetic aggregation/crystallization within PA matrix during IP.

The deciphering of the supramolecular self-assembly events under different membrane contentions is of paramount importance for understanding the relationship between the channel stability and its performant water translocation mechanism. Along this line of thought, the properties and features of Å-scale single water channels stabilized in bilayer membranes might behave differently when they are embedded as multichannel within polymeric macroscopic cm<sup>2</sup> to m<sup>2</sup>-scaled membranes (Figure 74 a). This understanding opens up new avenues in AWCs research, towards the construction of selective bioinspired membranes for desalination.<sup>96</sup>

## 4.2. Results and Discussion

With all these in mind, we deliberately examined an extended library of alkyl-ureido-ethyl-imidazoles, **HCx** ( $x = 4-18$ ), with the objective to understand the structural factors leading to the formation and the stabilization of I-quartets in different membrane environments: (a) hydrophobic stabilization of single channels in bilayer membranes and (b) multi-channel crystalline nanoparticles within hybrid polyamide RO-membranes. Nine I-quartet monomers

were prepared for the studies described here: **HC4**, **HC5**, **HC6**, **HC7**, **HC8**, **HC11**, **HC12**, **HC14**, **HC18** (Figure 74 c). **HC4**, **HC6**, **HC8** were previously reported by our group.<sup>36</sup> We treated the corresponding isocyanates with histamine (CH<sub>3</sub>CN/THF/Ethyl acetate, 80°C, 3 h) to crystallize **HC4**, **HC5**, **HC6**, **HC7**, **HC8**, **HC11**, **HC12**, **HC14**, **HC18** as white powders. The <sup>1</sup>H-NMR (Figure 80–88) and ESI-MS spectra agree with the proposed formulas.

We previously discovered that hexylureido-imidazole monomers (**HC6**) when dissolved in an ethanolic aqueous solution, followed by sonication, results in the formation of homogeneous colloidal aggregates.<sup>92</sup> To gain insight into the formation of such aggregates, we monitored by dynamic light scattering (DLS) experiments, the changes of the dimensions of the colloidal particles with increasing concentrations of **HC4**, **HC5**, **HC6**, **HC7**, **HC8**, **HC11**, **HC12**, **HC14**, **HC18** in solution. When water as a non-solvent (i.e. **HCx** are not soluble in pure water) was added to a 1-mL ethanolic solution of soluble 0.5 wt% or 1 wt% **HCx**, the formation of aggregates ( $D_h = 200\text{--}1200$  nm) was observed in mixed solutions (Figure 89). We noted that aggregation behaviors are strongly dependent on the concentration of **HCx** and the solvent EtOH/ non-solvent H<sub>2</sub>O volume ratio of the solution. For 0.5 wt% or 1 wt% solutions of **HCx**, a linear increase of the hydrodynamic diameter  $D_h$  of colloidal aggregates was observed after adding amounts of water, without any visible precipitation. Increasing the amount of non-solvent water finally induce the precipitation of **HCx**. These conditions simulate those corresponding to the best results for the aggregate formation used for hybrid polyamide membrane preparation using interfacial polymerization.<sup>92, 96</sup>



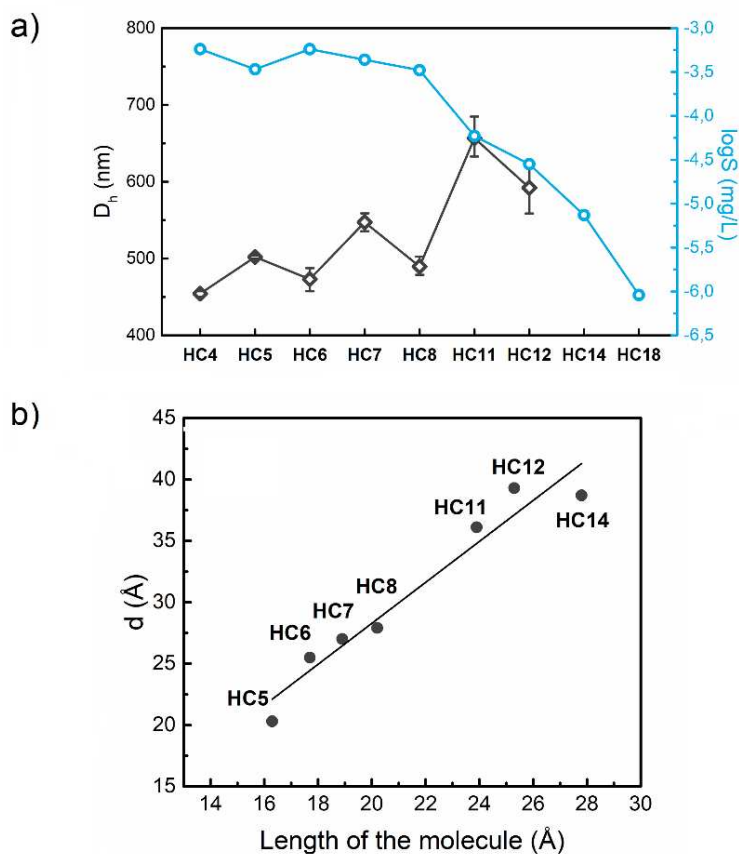


**Figure 75.** (a) DLS experiments using ethanolic aqueous solutions of 0.5 wt% **HC5–HC12** resulting in the formation of the AWC colloidal aggregates with increasing hydrodynamic diameter ( $D_h$ ) and odd–even macroscopic effects on dimensions of formed nanoparticles. Aggregates of 1000–1200 nm were formed for **HC14** and **HC18** (not showed) at lower concentration of 0.125 wt% (Figure 89), while a precipitate is formed at 0.5 wt% and (b) the corresponding distances of the packing distances calculated from powder diffractions patterns plotted against the molecular length of **HC5–HC14**.

Increasing the length of the alkyl tail, in the most concentrated solutions lead to a saturation behavior occurring through the formation of particles with constant maximal  $D_h$  at high  $H_2O/EtOH$  ratios in solution. The  $D_h$  values indicate a progressive increase in the size of particles with the length of the tail, while particles formed with alkyl compounds of  $n_{\text{odd}}$  have a higher size than compounds of  $n_{\text{even}}$ . The constant increase of the dimension of  $D_h$  particles is proportionally inverse to the solubility of the monomers in water, presenting a shift from **HC8** to **HC11** and showing increased aggregation behaviors for longer alkyl tails (Figure 75 a). Moreover, for the series of **HC4** to **HC8**, for which the solubility is almost constant, the  $D_h$  of nanoparticles exhibits

dependencies on both the length ( $n$ ) and parity ( $n_{\text{odd}}$  or  $n_{\text{even}}$ ) of the alkyl chain. The odd–even effect on macroscopic dimensions of formed nanoparticles arises primarily from a difference in the chemical composition at the interfaces and are related to the terminal group orientation as previously described for self-assembled monolayers-SAMs.<sup>114</sup> The surface hydrophobicity originates from changes in the polyethylene chain orientation as  $n_{\text{odd}}$  presents a “methyl-like” surface, exhibiting higher contact angles (greater surface hydrophobicity) than  $n_{\text{even}}$  of comparable chain length exposing an “ethyl-like” surface. The hydrophilic ethyl-like ( $n_{\text{even}}$ ) interfacial termini induces smaller layered particles formation when compared with the bigger particles observed for the more hydrophobic methyl-like ( $n_{\text{odd}}$ ) interfacial termini (Figure 75 a).

The X-ray single-crystal structures of **HC4**, **HC5**, **HC6**, **HC7** and **HC8**<sup>32</sup> reveal the formation of I-quartet superstructures, all (except **HC4**) containing water-wires (Figure 76). The centrosymmetric structures of crystallized columnar arrays of channel-type stacks of I-quartets, **HC4–HC8** showing the formation of successive bundle channels, enclosing dipolar water-wires of opposite orientations (Figure 93).

The **HC5** linear molecules self-assemble via urea ribbons with opposite orientations within the I-quartets. They form strong H-bonds with waters, crystallographically restricted to two orientations within the channel. They are alternatively oriented in opposite directions into neighboring channels, as observed for urea ribbons. **HC6–HC8** are composed of a different packing of both linear (blue circles) and gauche-constrained (red circles) molecules, resulting in the formation of alternative water-filled I-quartets, formed from unidirectional urea ribbons, and separated by free-water I-quartets formed from urea ribbons with opposite orientation (Figure 76 a). The overall structures **HC6–HC8** present an inversion center, so that each water channel of dipolar orientation is present in successive I-quartets of opposite

orientations. The linear alkyl chains are positioned in two conformations that are: a) interdigitated interactions over  $-(\text{CH}_2)_2\text{-CH}_3$  termini, ascribed to the shorter gauche-constricted molecules within the I-quartets and b) face to face interactions, occurring between the I-quartets (Figure 75 c). The successive layers of alternative regions of hydrophilic I-quartets and hydrophobic bilayers of alkyl tails within crystalline structures may be generated in the solid state *via* an evaporation nucleation process of the colloidal alcohol/water suspensions previously detected by DLS.<sup>92</sup>

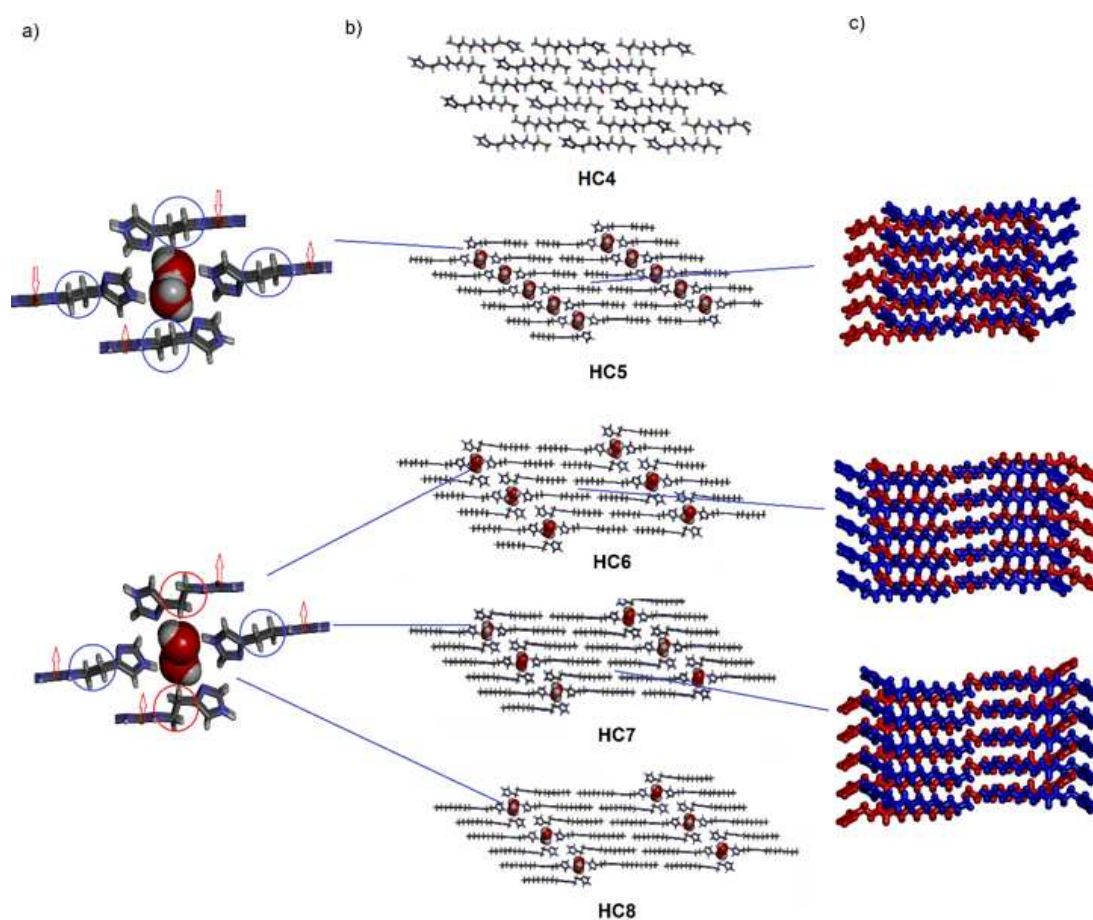


**Figure 76.** X-ray single crystal structures of I-quartet AWCs. (a) Top views in stick representation (N, blue, C, grey, O, red and H-white) of I-quartets self-assembled from linear (blue) molecules *via* urea ribbons with opposite orientations (top) and from linear (blue) and gauche constricted (red) molecules *via* urea ribbons with the same orientation. (b) crystal packing of channels **HC4**, **HC5**, **HC6**, **HC7** and **HC8**, confining dipolar oriented water-wires with an opposite dipolar orientation. lamellar architectures. (c) The successive lamellar layers of alternative hydrophobic bilayers of alkyl tails within crystalline structures (see text for details).

The compatibility between the X-ray fingerprint of bulk crystalline powders of **HC4–HC18**, characterized by X-ray powder diffraction (XPRD) and the packing of the X-ray single crystal structures of **HC4–HC8**, shows that all crystalline structures obtained from colloidal solutions have the same layered arrangement. All PXRD patterns are indicative of the lamellar phases, with the main diffraction peaks (*100*), (*200*) and (*300*), corresponding to interplanar distances of the parallel packing of periodic sheets of the alternative I-quartets/hydrophobic bilayers (Figure 94). Their dimensions are proportionally related to the length of their respective alkyl chain. The first intense diffraction peaks corresponding to the (*100*) reflections are related to the distance *a* of the elementary cell. Over the suite of compounds, the *a* distances are in perfect correlation with the length of the molecules **HC4–HC14** (Figure 75 b), on the basis of the geometry of **HC4–HC8** (Figure 93) in the single-crystal structure or using a linear geometry for the alkyl (C<sub>11</sub>H<sub>23</sub>-, C<sub>12</sub>H<sub>25</sub>-, C<sub>14</sub>H<sub>29</sub>-) substituents. We can assume that the main organization of the lamellar phases is approximately the same for all the compounds having a similar geometrical disposition relative to the plane *ac* of the successive I-quartets, propagated along the main direction *b* to form tubular channels. The size of aggregates in solution may strongly depend on the size of the alkyl chain, surrounding the central I-quartets as a hydrophobic shell with variable dimensions.

The I-quartet channels were reconstituted into lipid vesicles (100 nm in diameter) of phosphatidylcholine/phosphatidylserine/cholesterol (PC/PS/Chl, 4/1/5, molar ratio). The compounds **HC4–HC18** were added from their DMSO solutions to pre-formed vesicles with different compound to lipid molar ratios - mCLRs (see experimental section). Then, the vesicles were exposed to outwardly hypertonic conditions driven by 10 mM PBS buffer solution (pH = 6.4) of 400 mM D(+)-Sucrose osmolyte, to evidence the shrinkage of the liposomes that increased the light-scattering signal. The water transport rates

are strongly dependent on the concentration of the I-quartets, that increase the net water permeability relative to the background lipid permeability in the bilayer membrane (Figures 95–97).

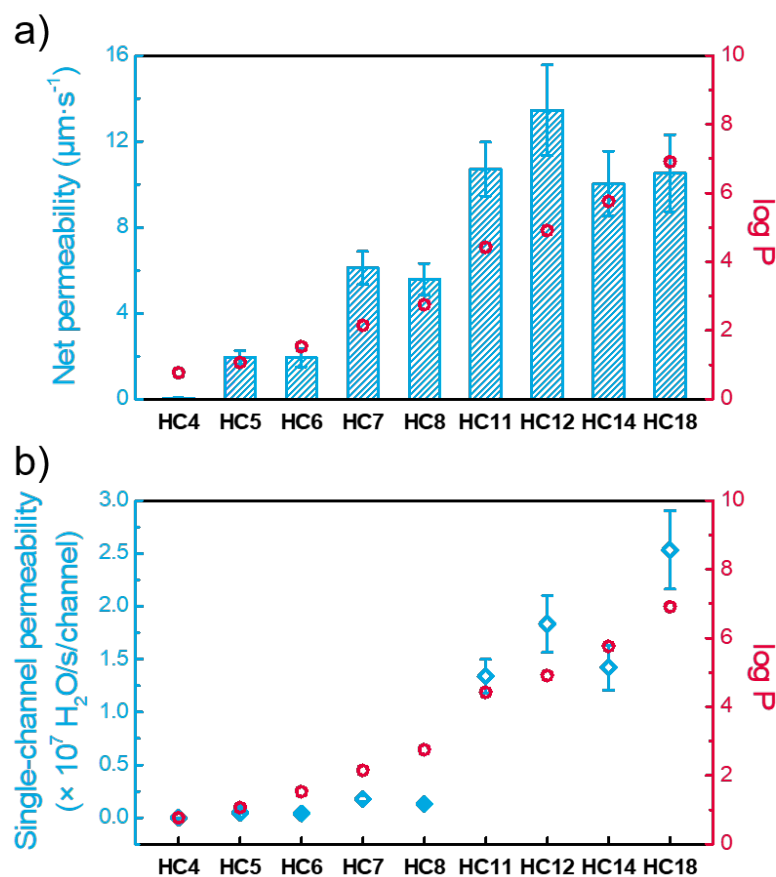


**Figure 77.** (a) Net and (b) single channel water permeabilities of **HC4–HC18** I-quartet channels through lipid bilayer membranes as a function of the lipophilicity (log P) of the former compounds. The net permeabilities are reported as maximal concentration values of **HCx** rendering possible membrane solubilization. Further increase in concentration lead to their precipitation.

The net permeabilities show a continual improvement when the alkyl tail of **HCx** increases. Interestingly, a 92% increase in water net permeability ( $P_n = 10.72 \pm 1.26 \mu\text{m}/\text{s}$ ) has been observed for **HC11** (mCLR = 0.2), when compared with **HC8** ( $P_n = 5.59 \pm 0.74 \mu\text{m}/\text{s}$ ), while a maximal permeability ( $P_n = 13.46 \pm 2.11 \mu\text{m}/\text{s}$ ) can be obtained from **HC12** (mCLR = 0.2), before a further stabilization for longer **HC14** ( $P_n = 10.03 \pm 1.51 \mu\text{m}/\text{s}$ ) and **HC18** ( $P_n = 10.52$

$\pm 1.79 \mu\text{m/s}$ ) compounds (Figure 77 a). The observed overall net permeabilities are most probably related to the increased solubilization in bilayer membranes of I-quartets former monomers with longer alkyl tails and higher hydrophobicity. The single-channel water permeabilities,  $P_s$ , constantly increase with the lipophilicity ( $\log P$ ) of the former compounds, while a sharper raise of the  $P_s$  was recorded for the **HC8–HC18** compared with the **HC4–HC8** (Figure 77 b). In the membranes **HC8–HC18**, the longer alkyl tails with higher lipophilicity are wrapped around I-quartets. Therefore, it generates stabilized and percolated conducting channels, which are not only the simple result of a linear increase of the  $\log P$  values. The  $P_s$  are going beyond the solubility behaviors *via* synergistic self-organization, which in turn results in correspondingly high-water conductivity through more stable channels in the bilayer membrane.

Recent advances in our group<sup>92</sup> and by Zhao et al.<sup>115</sup> have made possible the large-scale fabrication of high density multichannel AWCs-polyamide hybrid materials, for the production of stable and highly performant biomimetic membranes that overcome current industrial RO-membrane performances for desalination. We postulated that one of the most creative strategies for addressing such scale-up challenges was to combine the colloidal AWCs soft aggregates with the PA, known for its easy industrial scalability. This approach has shown that AWCs are functional when embedded in PA layers, aside from lipid bilayers, and upscaling methods at industrial standards are possible but still remain a great challenge as they must be adapted to specific conditions and fabrication methods.<sup>34</sup> Several features need to be achieved to maximize the membrane performances, including high density of percolating functional AWCs with the absence of defects. One effective upscaling approach without creating defects, exploits colloidal AWCs nanoparticles, gently incorporated and *in-situ* generated during a streamlined IP process, within PA layers.<sup>92</sup>

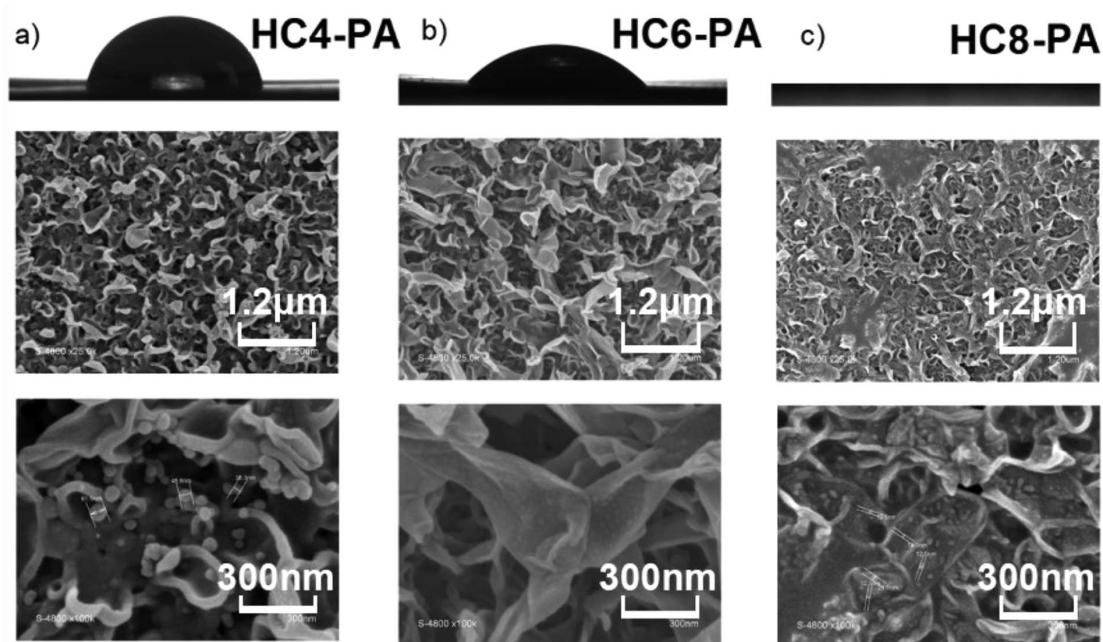


**Figure 78.** Contact angle analysis and SEM micrographs of the surface morphology for (a) **HC4-PA**, (b) **HC6-PA** and (c) **HC8-PA** bioinspired membranes prepared with different **HCx** precursors (1.5 wt%).

The present work considers fabricating reference TFC-PA and hybrid **HCx-PA** membranes *via* the synergetic self-assembly of various recipes, and combining the I-quartets of increased hydrophobicity, **HC4** < **HC6** < **HC8**, with PA components. For the synthesis, the IP procedure started by the incorporation of AWCs by pouring colloidal solutions of **HC4**, **HC6** and **HC8** at the surface of the polysulfone (PSf) support and allowed to sit to induce their partial evaporation. Then, the membranes were immersed in an aqueous m-phenylenediamine (MPD) solution for 2 min. and into a trimesoylchloride (TMC) solution for 1 min. to form the PA layer. The successful integration of AWCs into PA layers is related to a percolation process of colloidal particles of **HCx** formed in water/alcoholic solutions as confirmed by the present or previous DLS studies.<sup>92</sup> Based on this information, different **HCx** were investigated to explore the solubility-dependent formation of aggregated nanoparticles and their effect constitution and morphology of the resulting **HCx-PA** materials, that may control the final membrane transport

performances (Figure 78, Table 7). For the synthesis of TFC-PA layers, the conventional IP procedure was conducted without the addition of **HCx**.

We know that the polymer growth during the PA film formation is determined by the diffusion rate of the MPD in the organic phase. In the present case, the AWCs/MPD colloidal aggregates are formed and migrate together to the organic phase, favoring the IP reaction, resulting in the formation of hybrid AWCs-PA materials. The nano- and micro-structures of PA layers are strongly dependent on the distribution of AWCs aggregates within the PA matrix. Scanning electronic microscopy (SEM) micrographs (Figure 78) suggest that **HC4** and **HC6** can be more finely incorporated than **HC8** during membrane fabrication due to the higher solubility and dispersion degree in the casting solutions. The **HC4**-PA and **HC6**-PA layers appeared continuous and free of microscopic defects, while a visible formation of defects was observed for **HC8**-PA membranes. The addition of **HC4** and **HC6** leads to an increase of membrane thickness, from ~210 nm (reference PA) to 300-450 nm (**HC4**-PA and **HC6**-PA) with alternating thinner/thicker regions, while **HC8**-PA layers have a smaller thickness of 50-100 nm. The “ridge-and-valley” top surfaces of hybrid membranes evolved from a dense (**HC4**-PA) to a highly inhomogeneous (**HC8**-PA) “flake-like” morphology, while a hybrid morphology was observed for (**HC6**-PA). The lower solubility of the **HC8** aggregates, induce a complete change in membrane surface morphology (**HC8**-PA), which presents defective large surface areas. The observed decreasing contact angles of **HC4**-PA (72.0°) > **HC6**-PA (47.6°) >> **HC8**-PA (n. a.) are in accordance with the overall density of the surface morphologies of the layers and not with the appropriate hydrophobicity of **HCx** (Figure 78).

The effect of the diffusion into the organic phase of the increasing size (**HC4** < **HC6** < **HC8**) aggregates observed from DLS studies (Figure 75 a) conducts to the formation of nanoparticles, easily observed on the surfaces and over the



whole thickness of the **HCx**-PA layers, which further leads to the formation of a more complex internal structure than that observed for reference PA membrane. The internal aggregates, corresponding to the brighter spots in SEM micrographs (Figure 78), are homogeneously embedded within the PA matrix for **HC4**-PA and **HC6**-PA, while bigger inhomogeneous particles are present within different regions across the **HC8**-PA layers. Homogeneous and defect-free **HCx**-PA layers are hypothesized to promote faster and selective water passage during membrane filtration.

**Table 7.** BWRO desalination performances at 15.5 bar of reference PA and **HCx**-PA membranes. The SW30HR has been also measured as a commercial reference. Experimental conditions: pure water for the measurement of Water Permeability WP; 100 mM NaCl in the feed solution for the measurement of salt rejection. Please note that all these performances were measured under the same conditions in our laboratory.

Membrane	Water permeability, WP, L m <sup>-2</sup> h <sup>-1</sup> bar <sup>-1</sup>	Observed NaCl rejection, R, %
TFC-PA	1.36	98.98
<b>HC4</b> -PA	2.09	99.25
<b>HC6</b> -PA	3.85	99.51
<b>HC8</b> -PA (defective)	60.0	17.0
SW30HR	2.12	98.52

The filtration performances of **HCx**-PA membranes were measured in brackish water reverse osmosis (BWRO) filtration conditions (Table 7). For the **HC4** to **HC6** loadings, membranes exhibited increasing water permeances from roughly 2.09 to 3.85 L m<sup>-2</sup> h<sup>-1</sup> bar<sup>-1</sup>, with up to 50% to 183% increase with respect to the reference TFC-PA membrane (1.36 L m<sup>-2</sup> h<sup>-1</sup> bar<sup>-1</sup>), while maintaining excellent NaCl rejection (99.25-99.51%) with respect to the reference TFC-PA (98.98%) or commercial SW30HR (98.52%) membranes.

These experiments showed that under BWRO conditions, the **HC6** channels offer an optimal loading and a uniform distribution within PA, that is an essential feature needed to construct the optimally distributed AWCs-PA and to prevent the formation of defects in the selective layer.<sup>33</sup> By changing to the **HC8** loading, a strong increase in permeability and an important drop of selectivity is reminiscent with a defective membrane formation.

Molecular dynamics (MD) simulations were further performed on the **HC6** and PA as a showcase to gain insight into the structural organization of the colloidal aggregates of **HC6** observed by DLS both in an ethanolic aqueous solution and at the interface formed with the PA. In sharp contrast with the scenario encountered in the ethanolic aqueous solution where the structuration of the pristine I-quartet single-crystal aggregate is only mildly affected and still preserve the lamellar organization (Figure 79 a), there is a substantial structural re-organization of **HC6** once embedded in PA (Figure 79 b). This observation is reminiscent with so-called “sponge”-like structure organization previously observed in bilayer membranes.<sup>43</sup> The loosely structures behavior of **HC6** is quantitatively confirmed by the radial distribution functions (RDFs) patent averaged over all **HC6** along the 200 ns MD run for both colloidal aggregates of **HC6** in ethanolic aqueous solution and **HC6**-PA systems with respect to the corresponding data for the **HC6** single-crystal structure (Figure 79 c).

This results from its high structural adaptability/ lability that enables to conform its geometry to the PA scaffold (Figure 79 d) concurrent with a good chemical **HC6**/PA affinity as evidenced with the preferential interactions between the carbonyl oxygen of the urea groups, (and lesser extend the nitrogens of the imidazole) of **HC6** and the amine groups of the PA (see corresponding RDFs in Figure 79 e).

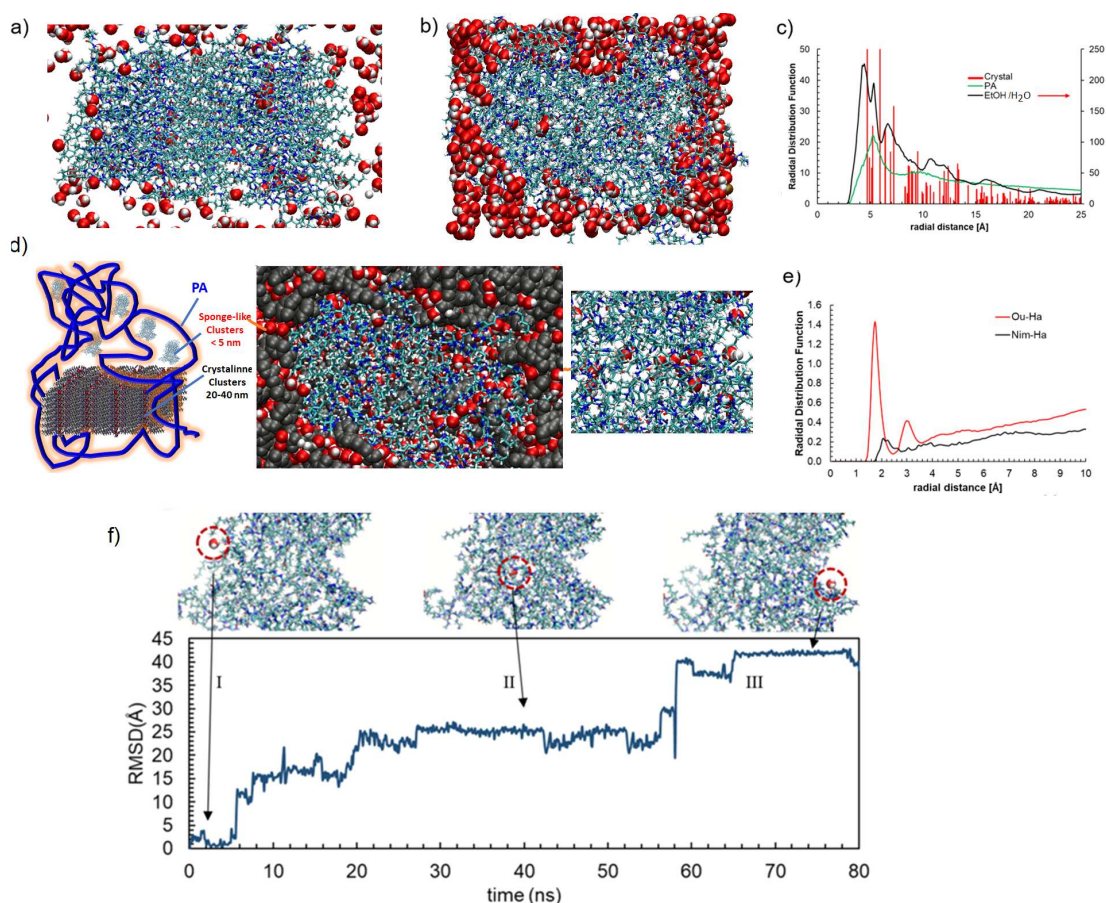


**Figure 79.** Structure organization of **HC6** issued from MD simulations in different media: (a) in ethanolic aqueous solutions and (b) embedded in PA. (Color codes: carbon cyan, nitrogen blue, oxygen red, hydrogen white.) PA atoms are omitted for clarity and water molecules are represented as CPK representation. (c) RDFs calculated for **HC6** in ethanolic aqueous solution and **HC6-PA** systems as compared with the data for the **HC6** crystal structure (d) Crystalline and sponge-like clusters can be sequestered via soft interactions within the PA matrix.<sup>33</sup> Cross-sectional global view of the **HC6-PA** systems of 3 nm thickness alongside the water distribution showing stable water channel within I-quartet and PA regions. Polymer atoms are represented as grey spheres while oxygen and hydrogen of water are represented as red and white spheres, respectively. (e) RDFs between the hydrogen atom of the amine group ( $H_a$ ) of PA and both the oxygen atoms of the urea group ( $O_u$ ) and the nitrogen atoms of the imidazole ring ( $N_{im}$ ), of **HC6**. (f) Mobility of a tagged water molecule throughout the **HC6/PA** system quantified by RMSD averaged over the MD simulations implying consecutive jumps from PA (zone I) to **HC6** (zone II) and back to PA (zone III). PA atoms are omitted for clarity.

Both the structuration of the **HC6/PA** interface and their associated interactions highlight a good compatibility between the two components in line

with the uniform distribution of **HC6** nanoparticles in the PA matrix as well as the formation of continuous defect-free membrane observed experimentally.

Figure 79 d also reveals that some water molecules are present in the **HC6** sponge-like configurations, while the majority of them forms water channel clusters or interact with PA supported by the associated RDFs (Figure 102).

This structural disorganization of the crystalline sponges in PA is however not expected to impede the water transport since a water conductance in sponge like channels embedded in bilayer membranes ( $4.8 \times 10^7$  molecules/s/channel) was previously reported to be one order of magnitude higher than in crystalline lamellar patches of single channels of **HC6** ( $3.8 \times 10^6$  molecules/s/channel)<sup>43</sup>. It should be noted that during the PA synthesis we use colloidal aggregates presenting adaptive soft aggregates as those detected in ethanolic aqueous solutions of **HC6** by DLS. From these soft colloidal self-assemblies, nanoparticles of 20-40 nm size are precipitating in the presence of an excess of water or hexane and are experimentally observed in soft interaction with the PA matrix.<sup>33</sup> They are most probably composed of inner crystalline lamellar phases and outer sponge like nanostructures. The residual still soluble colloidal **HC6** that may form smaller aggregates, which are softly mixed with the PA matrix and cannot be observed by microscopy techniques. The present modelling studies of such **HC6**-PA configurations with a thickness of 3 nm support the sponge-like organization that preserve the cluster like organization of water penetrating the membrane. Notably, MD simulations evidenced that the water molecules (i) maintain hydrogen bonding with the imidazoles of the channel wall as well as with the vicinal waters (see RDF for the corresponding atom pairs in Figure 102) and (ii) are still mobile within the disordered region, following pathway to migrate throughout the **HC6**/PA interface as shown by the RMSD (root-Mean square displacements) profile calculated over the whole MD trajectory (Figure 79 f) which suggests water jump sequences.

The present study leads to the understanding of the key structural parameters contributing to the optimal incorporation of the I-quartets in lipid membrane or to the formation of I-quartet sponge-like particles within the **HCx-PA** membranes. When embedded in bilayer membranes, the **HCx** monomers are self-assembling in tubular I-quartet H-bonding architectures, that are surrounded with hydrophobic alkyls in contact with bilayer membrane lipids. The net permeabilities are continuously increasing from **HC4** to **HC18**, while the single channel permeabilities are slowly increasing for **HC4** to **HC8**, while an important increase in single channel permeability is observed for **HC11**, **HC12** to **HC18**. The tendency for increasing the single channel permeability is not only the results of a linear increase of the solubility of the monomers in the bilayer membranes. A favorable wrapping of the hydrophobic tails around I-quartets at the interface with the bilayers, can be presumed to be much optimal for longer chains. Indeed, the increased tail seemed to be optimal for functional aggregation of I-quartets when mixed with lipids. Oppositely, the strong hydrophobic interactions are less favorable for the *in-situ* adaptive incorporation of colloidal AWCs/PA-sponge like nanostructures into the PA layer. The **HC4** and **HC6** promoted the optimal inclusion of AWCs within PA with formation of a smoother homogeneous membrane layers, while **HC8** counterparts producing a highly porous defective membrane layer. We assume that the optimal membrane performance is achieved thanks to the combined effect of the solubility/colloidal aggregation in water, becoming strongly unfavorable for longer alkyl chains and leading to the formation of defective **HCx-PA** membrane.

The present results show that, using AWCs platforms and a simple restriction mechanism, it becomes possible to control the performances of water translocation. This is a very intriguing system. It is very tempting to equate those different types of aggregates, as single channels in bilayer membranes or

as multichannel crystalline or sponge-like phases in the solid-state present a unifying assumption is that hydrophobicity would be important for an optimal aggregation/stabilization of the channels within membranes.

The key structural features that enable efficient water permeation is hydrophobic stabilization of single channels in bilayer membranes. The modelling studies presented here bring new valuable insights into the re-organization of the channels at the interface with the polymer in the polyamide membranes. The adaptive self-assembly of multichannel architectures, ranging from a strongly organized single file water transport to more dynamic semi-structured sponge-like higher permeation scenarios, would represent the prerequisites for high permeability/ selectivity PA-AWC membranes. Obviously, a matrix induced density and stability of channels is desired to promote high performances of synthesized membranes.

### **4.3. Conclusions**

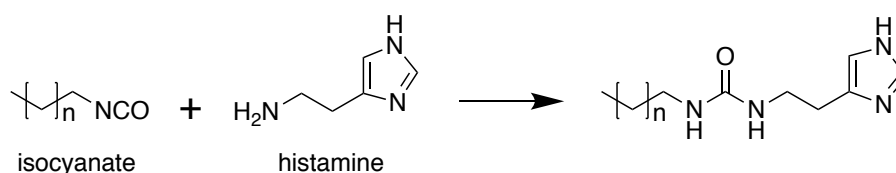
In conclusion, upscaling supramolecular AWC channels used for Å-scale selective separation toward m<sup>2</sup> macroscopic membranes for challenging industrial separations still re-mains a difficult, but possible endeavor.<sup>34</sup> I-quartet channels, hold significant promise for the incipient development of innovative materials based on artificial synthetic scaffolds mimicking the functions of natural water channels. Accordingly, synthetic routes reporting perfect channel alignment from one side to the other side of the active membrane can be reported only for bilayer membrane. Multidomain percolating single channel/sponge-like AWCs that can be “frozen” at the macroscopic level, is representing a straightforward up-scaling approach of high performance next-generation biomimetic membranes for desalination.<sup>96</sup> Future endeavors might precisely trigger the structural features that amount to coupling nano-scaled self-assembly and selective translocation events in

different membrane environments, a feature of tremendous interest for supramolecular construction of high-performance membranes for desalination.

## 4.4. Experimental Section

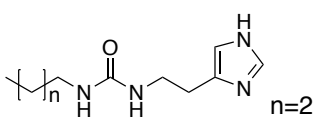
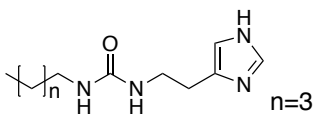
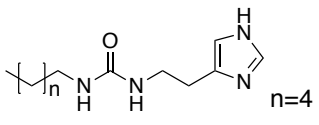
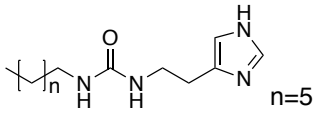
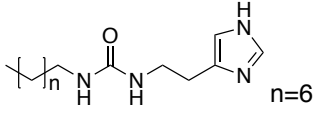
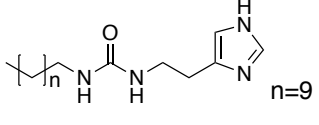
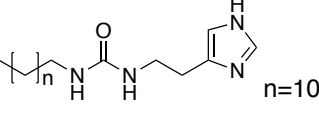
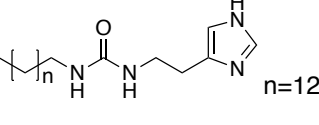
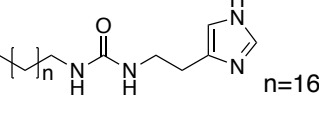
### 4.4.1. Materials and characterization

**Chemical synthesis.** All the compounds were synthesized following the general scheme S1 shown below. The isocyanate (10 mmol) was dissolved in 10 mL of tetrahydrofuran, 5 mL of ethyl acetate and 10 mL of acetonitrile. Then the corresponding equimolar amount of histamine was added. The reaction mixture was stirred and heated to 80°C, under reflux for 3 hours. As the reaction system heated up, the histamine was gradually solubilized. When the reaction was complete, white precipitate (**HCx**) appeared in the flask. After cooling down, solvents were removed as much as possible through conventional rotary evaporation. The products were solubilized in a small amount of ethanol to obtain its saturated solution, then n-hexane was introduced and pure white powder could gradually be produced under stirring. The suspension was separated by rotary centrifuge. The residual solvents were removed by vacuum desiccator to obtain pure compounds.



**Scheme 5.** Synthesis of imidazole compounds.

**Table 8.** Chemical parameters of the compounds.

	Chemical structure	Name	Formula	MS Cal.
HC4	 n=2	1-(2-(1 <i>H</i> -imidazol-4-yl)ethyl)-3-butylurea	C <sub>10</sub> H <sub>18</sub> N <sub>4</sub> O	210.15
HC5	 n=3	1-(2-(1 <i>H</i> -imidazol-4-yl)ethyl)-3-pentylurea	C <sub>11</sub> H <sub>20</sub> N <sub>4</sub> O	224.16
HC6	 n=4	1-(2-(1 <i>H</i> -imidazol-4-yl)ethyl)-3-hexylurea	C <sub>12</sub> H <sub>22</sub> N <sub>4</sub> O	238.18
HC7	 n=5	1-(2-(1 <i>H</i> -imidazol-4-yl)ethyl)-3-heptylurea	C <sub>13</sub> H <sub>24</sub> N <sub>4</sub> O	252.20
HC8	 n=6	1-(2-(1 <i>H</i> -imidazol-4-yl)ethyl)-3-octylurea	C <sub>14</sub> H <sub>26</sub> N <sub>4</sub> O	266.21
HC11	 n=9	1-(2-(1 <i>H</i> -imidazol-4-yl)ethyl)-3-undecylurea	C <sub>17</sub> H <sub>32</sub> N <sub>4</sub> O	308.26
HC12	 n=10	1-(2-(1 <i>H</i> -imidazol-4-yl)ethyl)-3-dodecylurea	C <sub>18</sub> H <sub>34</sub> N <sub>4</sub> O	322.27
HC14	 n=12	1-(2-(1 <i>H</i> -imidazol-4-yl)ethyl)-3-tetradecylurea	C <sub>20</sub> H <sub>38</sub> N <sub>4</sub> O	350.30
HC18	 n=16	1-(2-(1 <i>H</i> -imidazol-4-yl)ethyl)-3-octadecylurea	C <sub>24</sub> H <sub>46</sub> N <sub>4</sub> O	406.37

**Structural characterization.** All reagents were purchased from commercial suppliers and used without further purification. <sup>1</sup>H NMR spectra were recorded on Bruker Avance III 400 MHz NMR spectrometer in DMSO-*d*<sub>6</sub>, with the use of the residual solvent peak (δ = 2.50 ppm) as reference. Mass spectrometric analyses were performed in the positive ion mode using a quadrupole mass spectrometer (Micromass, Platform II).



**1-(2-(1*H*-imidazol-4-yl)ethyl)-3-butylurea, HC4:** <sup>1</sup>H NMR (300 MHz, DMSO-*d*<sub>6</sub>) δ (ppm) = 11.80 (s, 1H), 7.51 (d, *J* = 0.9 Hz, 1H), 6.76 (s, 1H), 5.80 (dt, *J* = 26.0, 5.6 Hz, 2H), 3.20 (q, 2H), 2.96 (q, *J* = 6.5 Hz, 2H), 2.57 (t, *J* = 7.1 Hz, 2H), 1.28 (m, *J* = 14.9, 6.9 Hz, 4H), 0.86 (t, *J* = 7.1 Hz, 3H); MS Cal. = 210.15, ESI-MS found [M+H<sup>+</sup>]<sup>+</sup> = 211.1564.

**1-(2-(1*H*-imidazol-4-yl)ethyl)-3-pentylurea, HC5:** <sup>1</sup>H NMR (300 MHz, DMSO-*d*<sub>6</sub>) δ (ppm) = 11.78 (s, 1H), 7.50 (d, 1H), 6.75 (s, 1H), 5.80 (dt, *J* = 27.7, 5.6 Hz, 2H), 3.21 (q, *J* = 7.0 Hz, 2H), 2.95 (q, *J* = 6.7 Hz, 2H), 2.57 (t, *J* = 7.1 Hz, 2H), 1.37 – 1.19 (m, 6H), 0.86 (t, *J* = 6.9 Hz, 3H); MS Cal. = 224.16, ESI-MS found [M+H<sup>+</sup>]<sup>+</sup> = 225.1872.

**1-(2-(1*H*-imidazol-4-yl)ethyl)-3-hexylurea, HC6:** <sup>1</sup>H NMR (400 MHz, DMSO-*d*<sub>6</sub>) δ (ppm) = 11.80 (s, 1H), 7.51 (d, 1H), 6.75 (s, 1H), 5.80 (dt, *J* = 35.9, 5.6 Hz, 2H), 3.20 (q, *J* = 6.9 Hz, 2H), 2.95 (q, *J* = 6.6 Hz, 2H), 2.57 (t, *J* = 7.1 Hz, 2H), 1.38 – 1.19 (m, 8H), 0.86 (t, *J* = 6.8 Hz, 3H); MS Cal. = 238.18, ESI-MS found [M+H<sup>+</sup>]<sup>+</sup> = 239.1872.

**1-(2-(1*H*-imidazol-4-yl)ethyl)-3-heptylurea, HC7:** <sup>1</sup>H NMR (400 MHz, DMSO-*d*<sub>6</sub>) δ (ppm) = 11.80 (s, 1H), 7.51 (d, *J* = 1.0 Hz, 1H), 6.75 (s, 1H), 5.80 (dt, *J* = 35.3, 5.6 Hz, 2H), 3.20 (q, *J* = 7.1 Hz, 2H), 2.94 (q, *J* = 6.8 Hz, 2H), 2.57 (t, *J* = 7.1 Hz, 2H), 1.37 – 1.19 (d, *J* = 37.2 Hz, 10H), 0.86 (t, 3H); MS Cal. = 252.20, ESI-MS found [M+H<sup>+</sup>]<sup>+</sup> = 253.2034.

**1-(2-(1*H*-imidazol-4-yl)ethyl)-3-octylurea, HC8:** <sup>1</sup>H NMR (400 MHz, DMSO-*d*<sub>6</sub>) δ (ppm) = 11.79 (s, 1H), 7.51 (d, *J* = 1.0 Hz, 1H), 6.75 (s, 1H), 5.80 (dt, *J* = 35.3, 5.6 Hz, 2H), 3.20 (q, *J* = 7.1 Hz, 2H), 2.94 (q, *J* = 6.7 Hz, 2H), 2.57 (t, *J* = 7.1 Hz, 2H), 1.38 – 1.17 (m, 12H), 0.86 (t, 3H); MS Cal. = 266.21, ESI-MS found [M+H<sup>+</sup>]<sup>+</sup> = 267.2189.

**1-(2-(1*H*-imidazol-4-yl)ethyl)-3-undecylurea, HC11:** <sup>1</sup>H NMR (300 MHz, DMSO-*d*<sub>6</sub>) δ (ppm) = 11.80 (s, 1H), 7.51 (d, *J* = 0.9 Hz, 1H), 6.75 (s, 1H), 5.80 (dt, *J* = 25.8, 5.8 Hz, 2H), 3.20 (q, *J* = 7.0 Hz, 2H), 2.94 (q, *J* = 6.5 Hz, 2H), 2.57 (t, *J* = 7.1 Hz, 2H), 1.24 (m, 18H), 0.85 (t, 3H); MS Cal. = 308.26, ESI-MS found [M+H]<sup>+</sup> = 309.2656.

**1-(2-(1*H*-imidazol-4-yl)ethyl)-3-dodecylurea, HC12:** <sup>1</sup>H NMR (300 MHz, DMSO-*d*<sub>6</sub>) δ (ppm) = 11.79 (s, 1H), 7.51 (d, *J* = 0.9 Hz, 1H), 6.75 (s, 1H), 5.79 (dt, *J* = 26.0, 5.8 Hz, 2H), 3.20 (q, *J* = 7.0 Hz, 2H), 2.94 (q, *J* = 6.5 Hz, 2H), 2.57 (t, *J* = 7.1 Hz, 2H), 1.24 (m, 20H), 0.85 (t, 3H); MS Cal. = 322.27, ESI-MS found [M+H]<sup>+</sup> = 323.2812.

**1-(2-(1*H*-imidazol-4-yl)ethyl)-3-tetradecylurea, HC14:** <sup>1</sup>H NMR (300 MHz, DMSO-*d*<sub>6</sub>) δ (ppm) = 11.77 (s, 1H), 7.50 (d, *J* = 0.9 Hz, 1H), 6.72 (s, 1H), 5.79 (dt, *J* = 26.1, 5.8 Hz, 2H), 3.20 (q, *J* = 7.0 Hz, 2H), 2.94 (q, *J* = 6.5 Hz, 2H), 2.59 (t, *J* = 7.0 Hz, 2H), 1.24 (m, 24H), 0.85 (t, 3H).; MS Cal. = 350.30, ESI-MS found [M+H]<sup>+</sup> = 351.3127.

**1-(2-(1*H*-imidazol-4-yl)ethyl)-3-octadecylurea, HC18:** <sup>1</sup>H NMR (300 MHz, Chloroform-*d*) δ (ppm) = 7.57 (d, 1H), 6.82 (s, 1H), 4.93 (t, 1H), 4.31 (t, 1H), 3.50 (q, *J* = 6.3 Hz, 2H), 3.12 (q, 2H), 2.82 (q, 2H), 1.47 (m, 2H), 1.25 (m, 30H), 0.87 (t, 3H).; MS Cal. = 406.37, ESI-MS found [M+H]<sup>+</sup> = 407.3754.

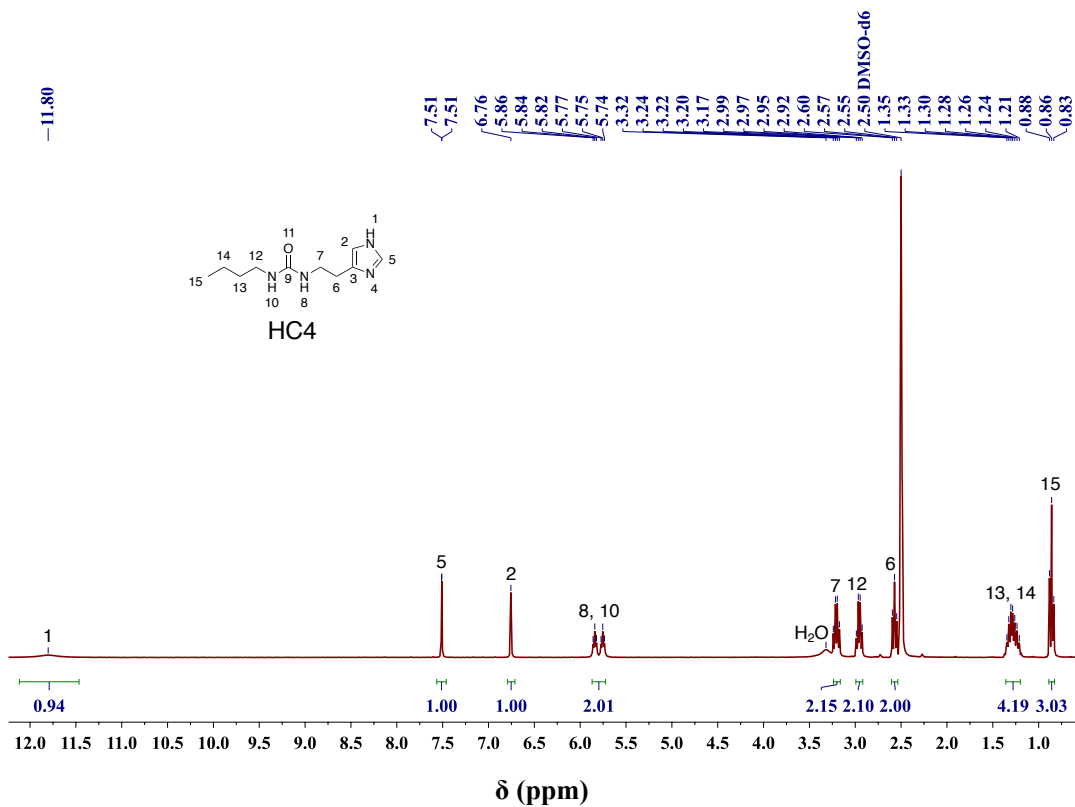


**Figure 80.**  $^1\text{H}$  NMR spectrum of **HC4**.

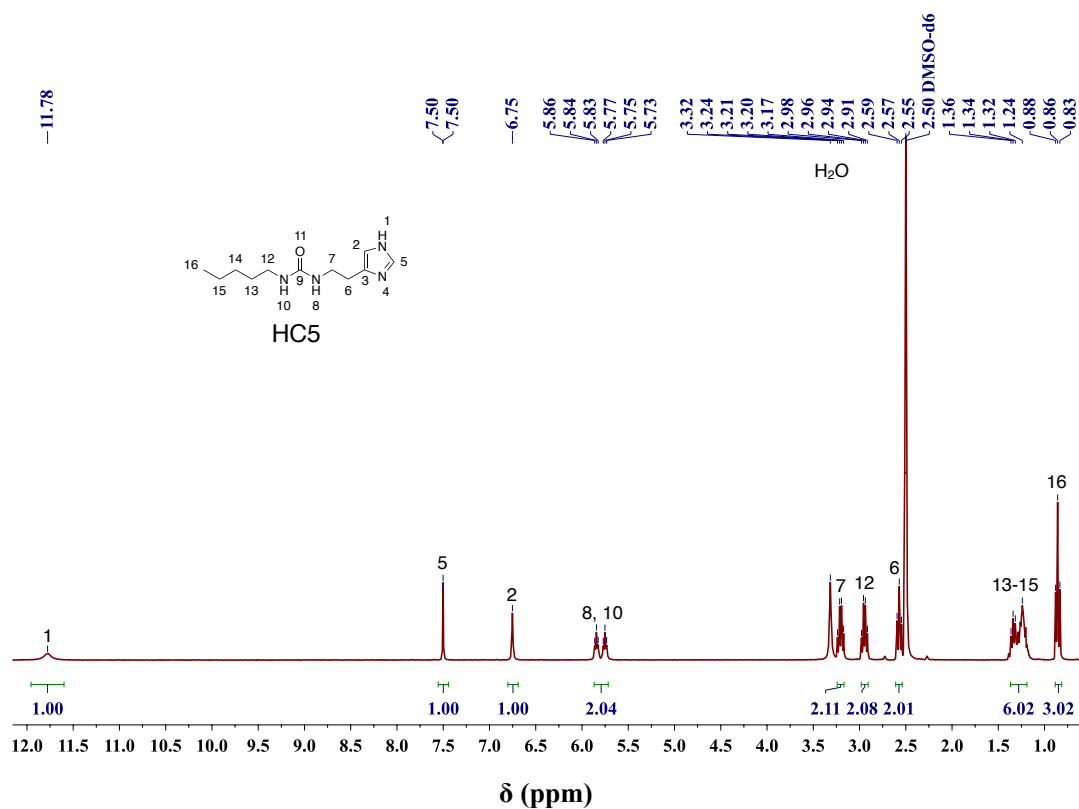


**Figure 81.**  $^1\text{H}$  NMR spectrum of **HC5**.

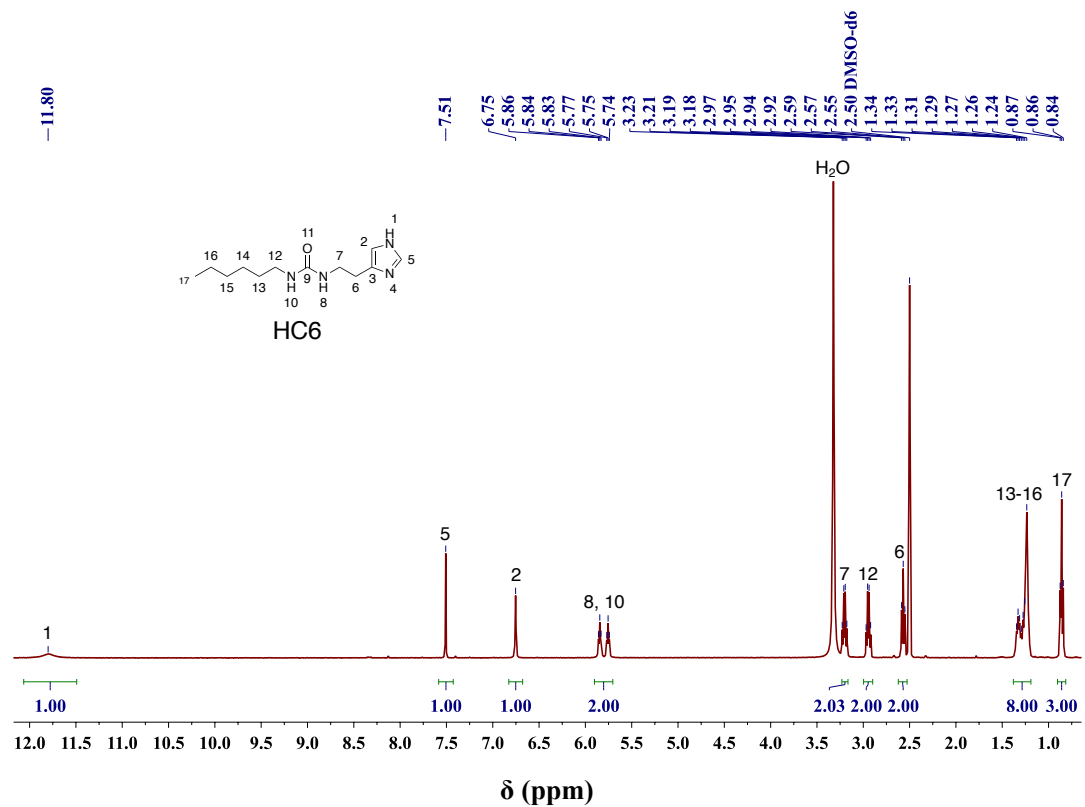


**Figure 82.**  $^1\text{H}$  NMR spectrum of **HC6**.

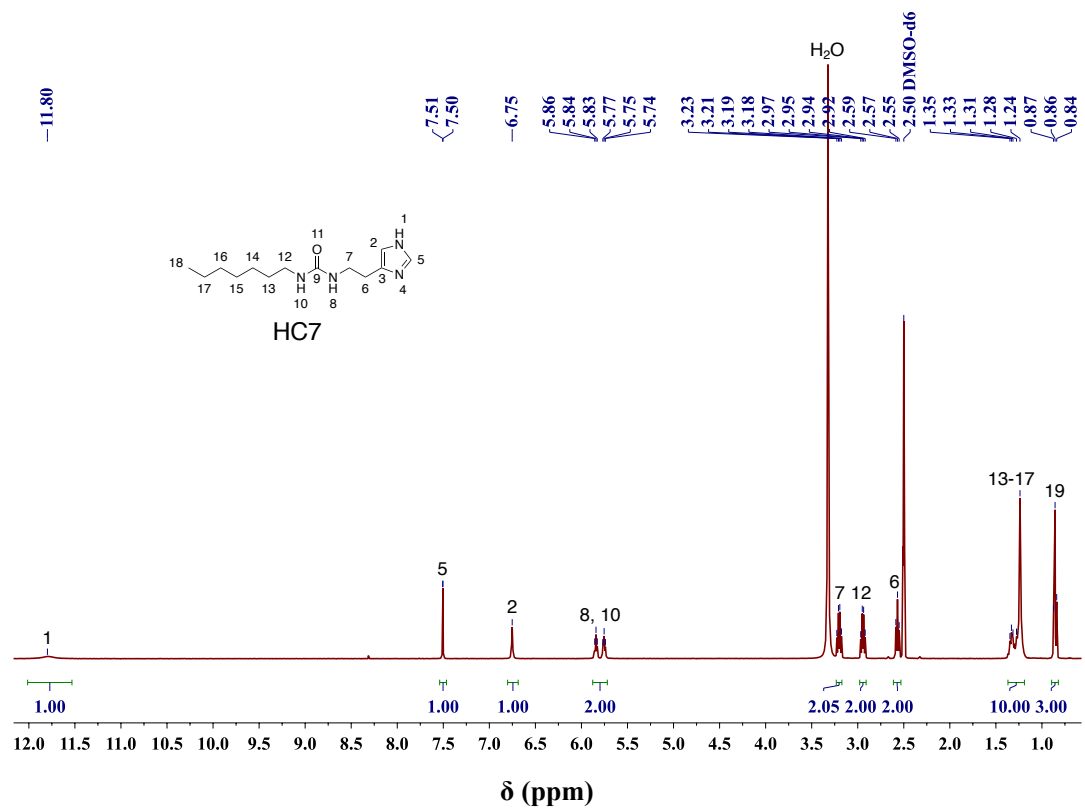


**Figure 83.**  $^1\text{H}$  NMR spectrum of **HC7**.

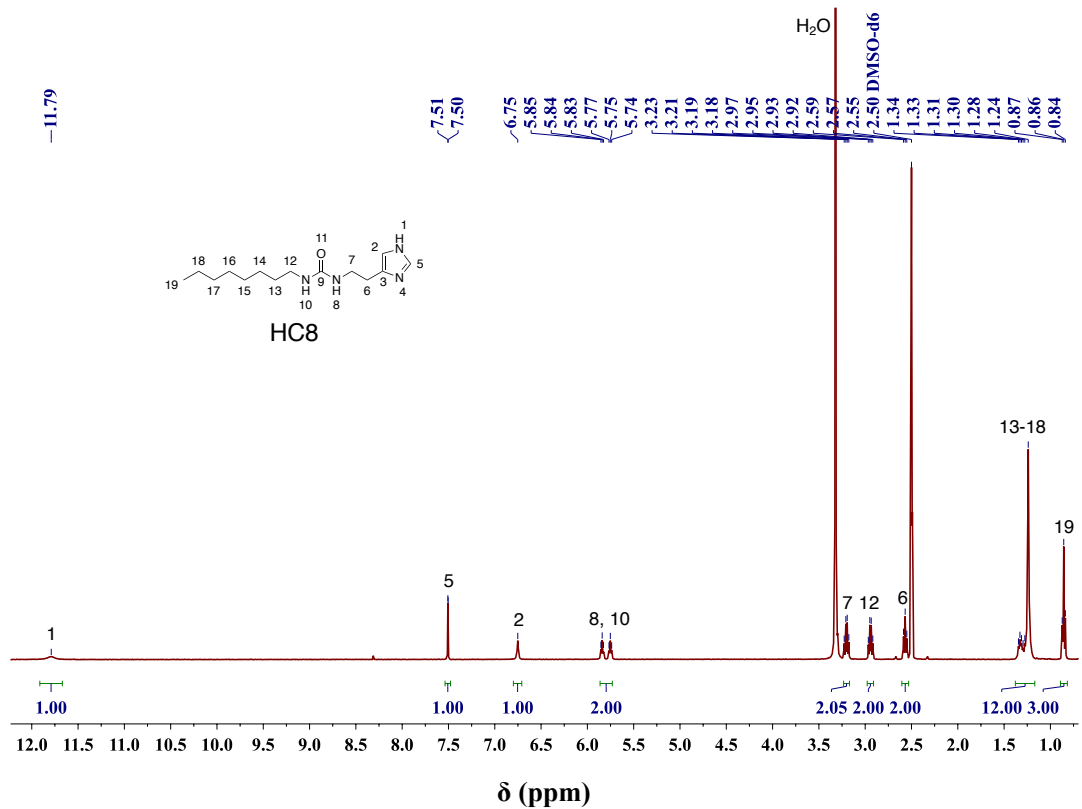


Figure 84. <sup>1</sup>H NMR spectrum of HC8.

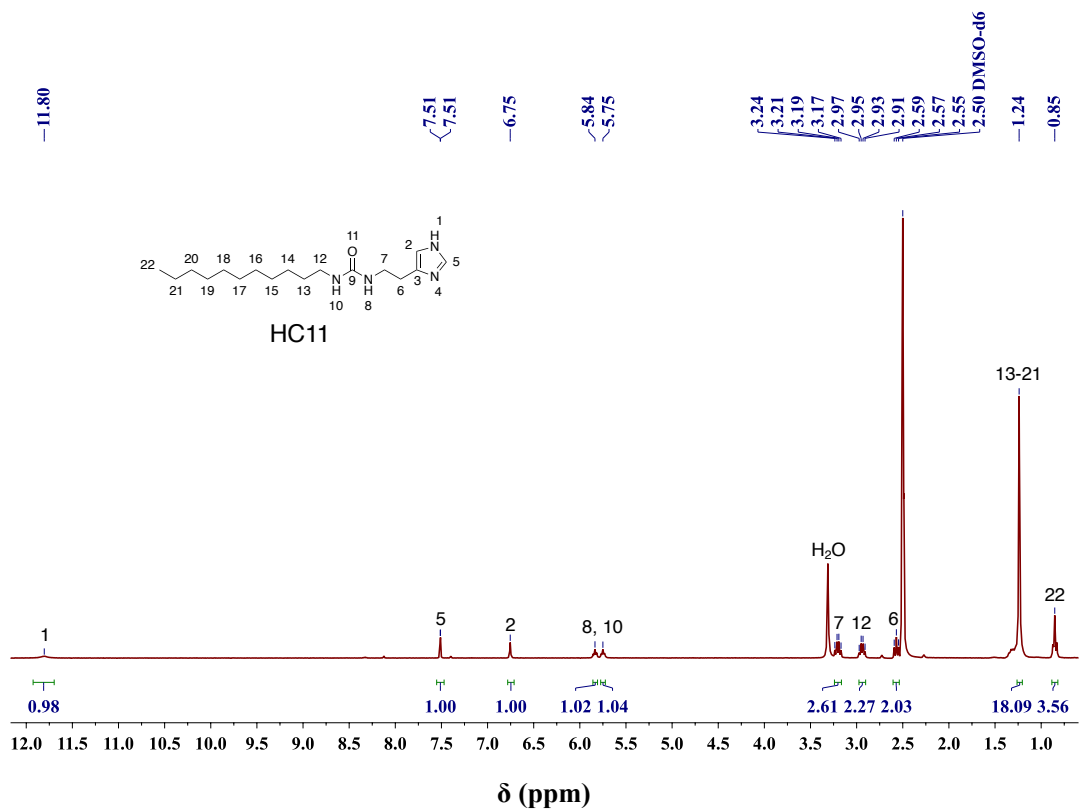
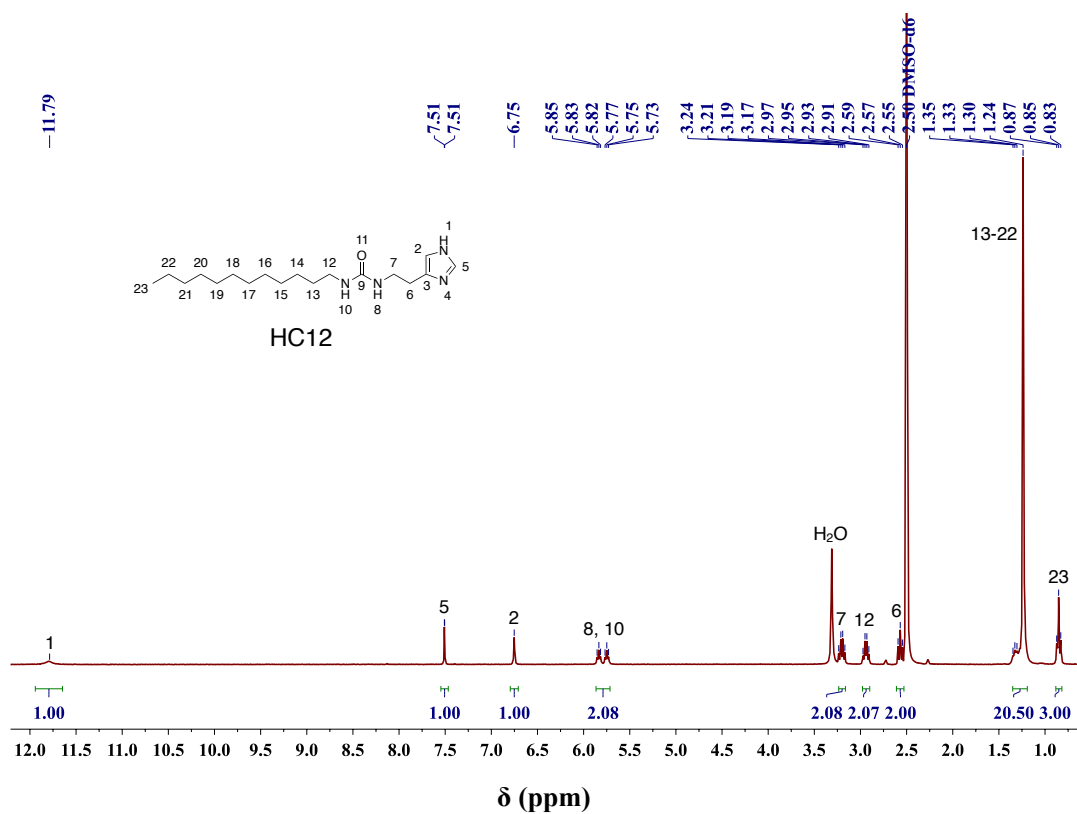
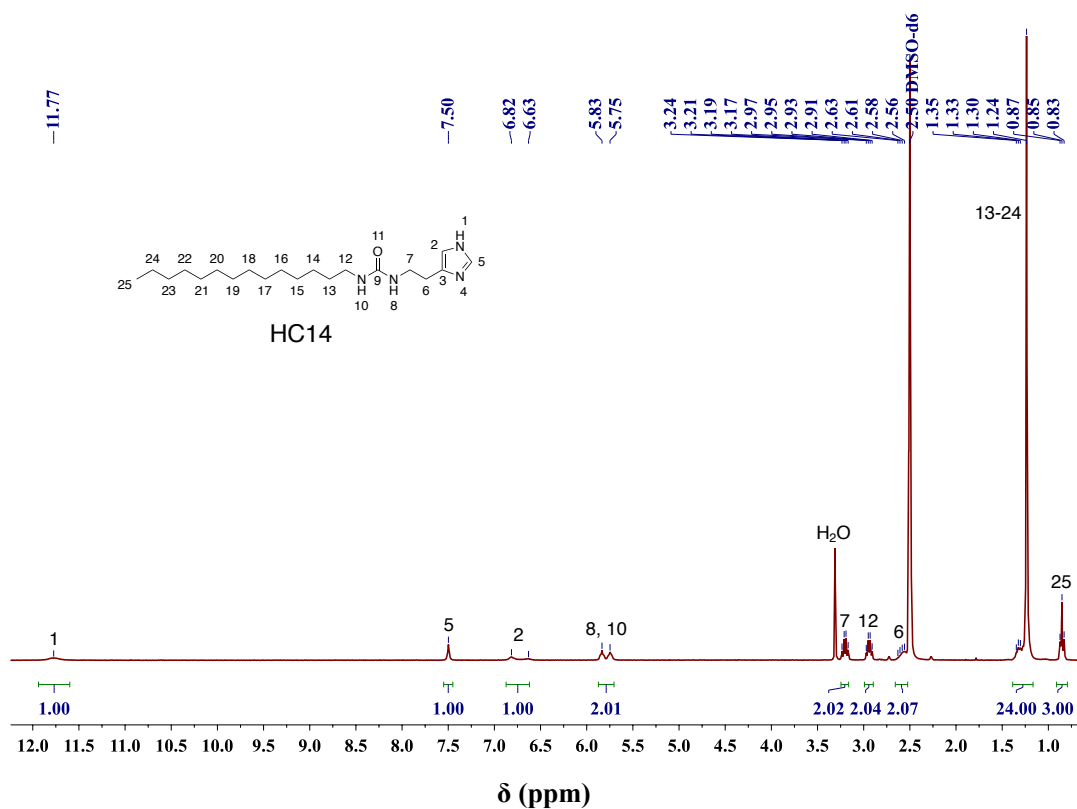


Figure 85. <sup>1</sup>H NMR spectrum of HC11.



**Figure 86.** <sup>1</sup>H NMR spectrum of HC12.



**Figure 87.** <sup>1</sup>H NMR spectrum of HC14.

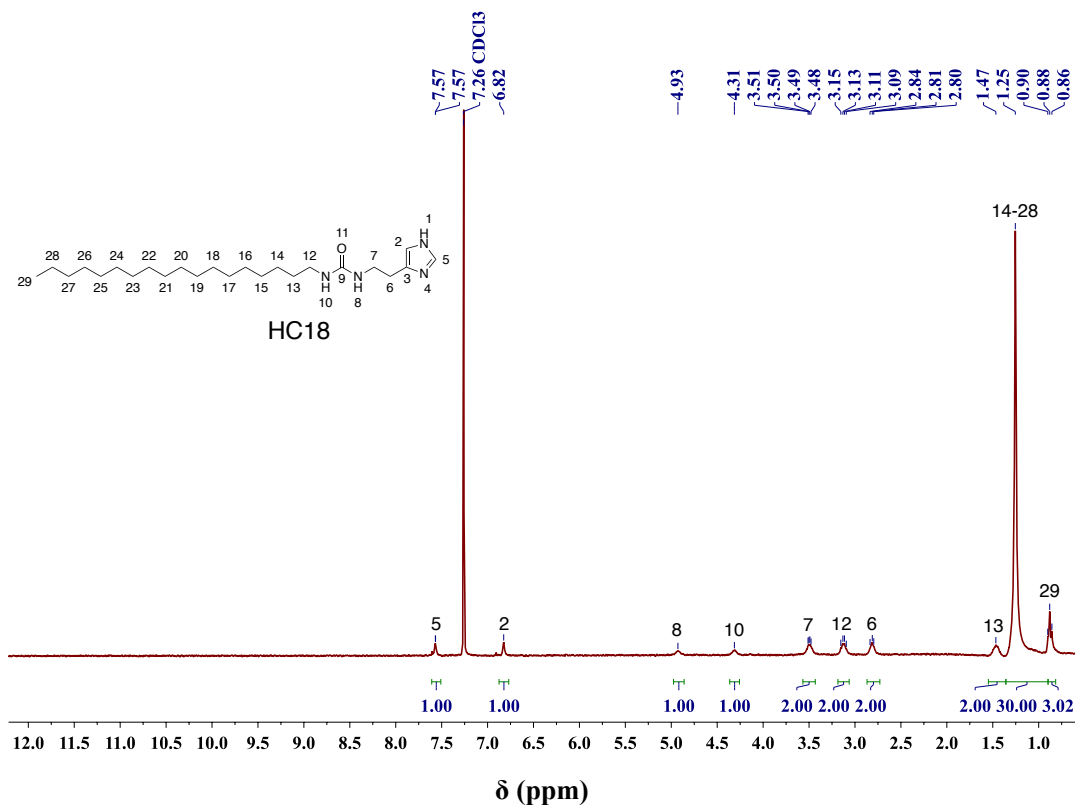


**Figure 88.** <sup>1</sup>H NMR spectrum of **HC18**.

#### 4.4.2. Dynamic light scattering

The dynamic light scattering (DLS) experiments were performed using a Malvern Zetasizer Nano-S ZEN1600 with a 173° backscatter measurement angle and a quartz cuvette with a square aperture. The average size was calculated by using the hydrodynamic diameter values ( $D_h$ ) obtained from at least three different measurements with good quality reports.

**Sample preparation.** 5 mg or 10 mg of corresponding compounds were dissolved in 1 mL ethanol to prepare 0.5 wt% or 1.0 wt% **HC4**, **HC5**, **HC6**, **HC7** and **HC8** I-quartet channel solutions. Due to the limitation of solubility, 2.5 mg or 1.25 mg of corresponding compounds were dissolved in 1 mL ethanol to prepare 0.25 wt% **HC11** and **HC12** or 0.125 wt% **HC14** and **HC18** I-quartet AWC solutions. In order to investigate the formation of AWC colloidal aggregates, we injected 0.2 mL water each time to obtain the mixtures with

different H<sub>2</sub>O/EtOH ratios, then the mixture was thermostated at 20°C for 5 minutes before the DLS experiments.

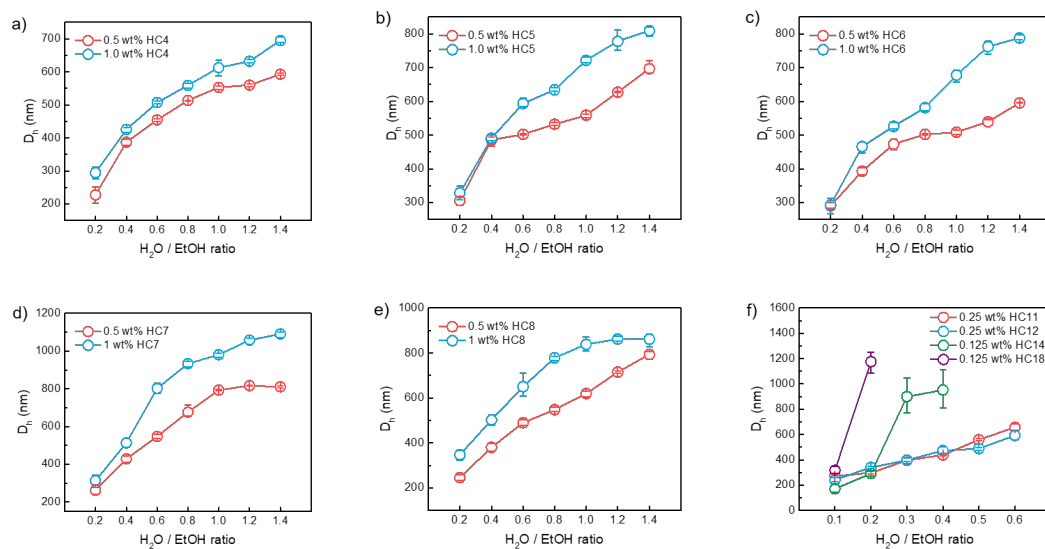


**Figure 89.** Average diameters of 0.5 wt% and 1.0 wt% (a) **HC4**, (b) **HC5**, (c) **HC6**, (d) **HC7**, (e) **HC8**, and (f) 0.25 wt% **HC11** and **HC12**, together with 0.125 wt% **HC14** and **HC18** colloidal aggregates with different H<sub>2</sub>O / EtOH ratios.

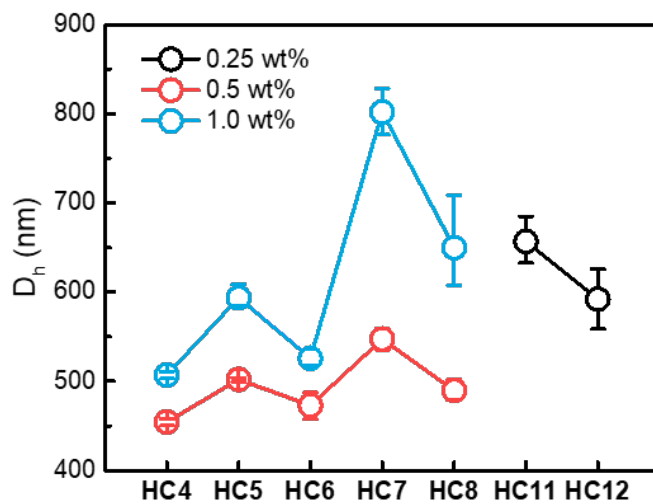


**Figure 90.** Average diameters of **HC6-HC12** aggregates 0.6 H<sub>2</sub>O/EtOH v:v ratio.



### 4.4.3. Log P and log S

Log P values<sup>[S1,S2]</sup>, which are often used for evaluating the lipophilicity of the compounds, are increasing gradually, thus their partition within the lipid bilayer is increasing as their alkyl tails chains become longer (Table 9). Within this context, the alkyl chains might have a positive impact on the formation of the channels inside the membranes at lower concentrations via aggregation, which allows **HC11**, **HC12**, **HC14** and **HC18** to exceed the maximum permeability of **HC8** at low concentration (wCLR = 0.2).

Log S values are related to the aqueous solubility of the compounds. Unexpectedly, the aqueous solubility of I quartet compounds is almost constant for **HC4-HC8** while is abruptly decreasing for **HC11-HC18**, with increasing alkyl chain tails (Figure 75 a). Furthermore, their alternant descends aqueous solubility of AWC fit their alternately raising sizes of colloidal aggregates well (Figure 75 a or 90).

**Table 9.** Calculated log P and log S values obtained by VCCLAB online calculator ALOGPS 2.1 to assess the lipophilicity and aqueous solubility of the compounds<sup>[1, 2]</sup>.

Compounds	log P	log S (aqueous solubility)
<b>HC4</b>	0.77	-3.24 (0.12 g/L)
<b>HC5</b>	1.07	-3.47 (76.88 mg/L)
<b>HC6</b>	1.53	-3.24 (0.14 g/L)
<b>HC7</b>	2.15	-3.36 (0.11 g/L)
<b>HC8</b>	2.75	-3.48 (88.64 mg/L)
<b>HC11</b>	4.42	-4.23 (18.17 mg/L)
<b>HC12</b>	4.91	-4.55 (9.15 mg/L)
<b>HC14</b>	5.76	-5.13 (2.58 mg/L)
<b>HC18</b>	6.91	-6.04 (0.38 mg/L)

#### 4.4.4. X-ray crystallography

**X-ray data collection, structure solution and refinement.** Data for **HC5** were collected on a Rigaku-Oxford Diffraction Gemini-S diffractometer ( $\lambda=0.7107 \text{ \AA}$ ), for **HC7** on a Bruker Venture diffractometer ( $\lambda=1.5418 \text{ \AA}$ ). The CrysAlis-Pro<sup>[S3]</sup> was used for the data collection and reduction for **HC5** and APEX3 (Bruker, 2016)<sup>[S4]</sup> for that for **HC7**. The Superflip program<sup>[S5]</sup> was used to solve the structures with parameters described by Van der Lee<sup>[S6]</sup> and the CRYSTALS program<sup>[S7]</sup> was used to refine the structures. Both crystals were very weak scatterers, which resulted especially for **HC7** in rather mediocre values for  $R_{\text{int}}$  and  $\langle \sigma(I)/I \rangle$ . The structural refinements proceeded, however, without any particular problem without the need to apply geometrical restraints (Table S2). All atomic displacement ellipsoids appeared to behave well. One of the hydrogen positions of the water molecule in the structure of **HC5** appeared to be disordered over two equal-occupancy positions (Figures 91, 92).

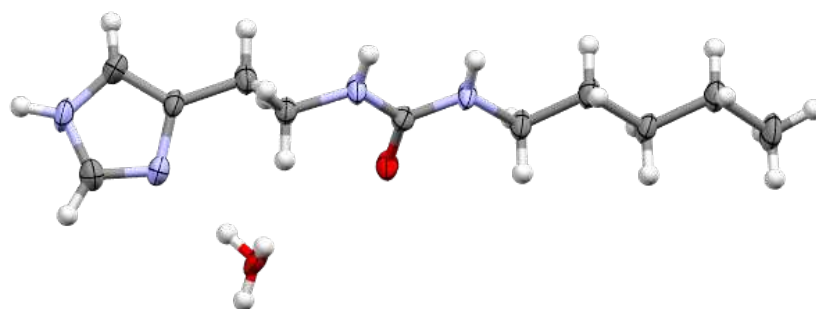


**Figure 91.** Atomic displacement parameter representation of the structure of **HC5** ('Ortep plot'). The ellipsoids are at the 50% probability level.

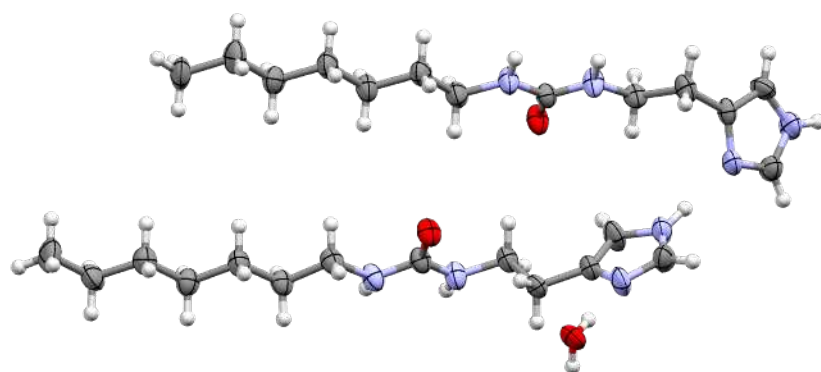


**Figure 92.** Atomic displacement parameter representation of the structure of **HC7** ('Ortep plot'). The ellipsoids are at the 50% probability level.

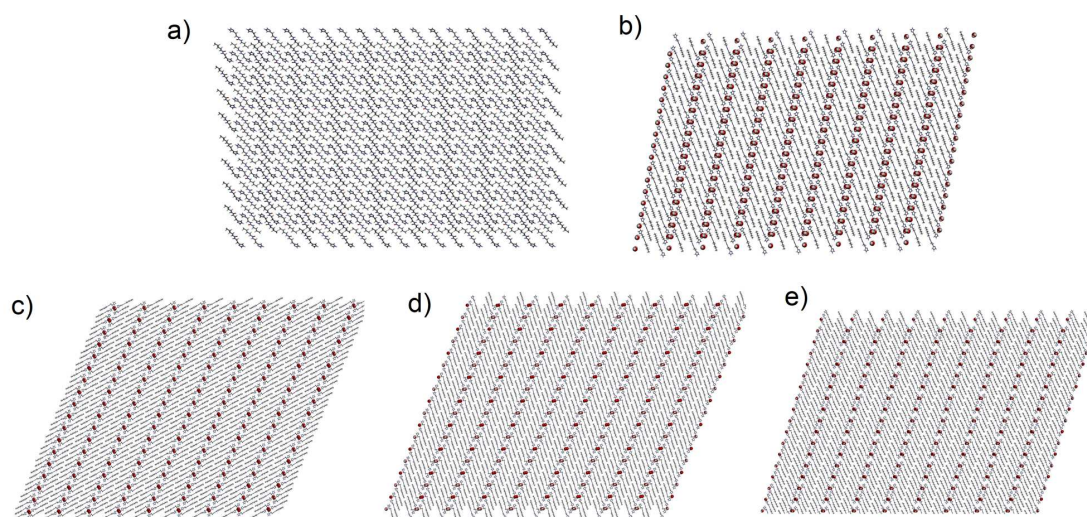


**Figure 93.** The single crystal structure packing of a) **HC4**, b) **HC5**, c) **HC6**, d) **HC7**, e) **HC8**.

**Table 10.** Crystal structure data.

	<b>HC5</b>	<b>HC7</b>
<b>formula</b>	C <sub>11</sub> H <sub>22</sub> N <sub>4</sub> O <sub>2</sub>	C <sub>26</sub> H <sub>50</sub> N <sub>8</sub> O <sub>3</sub>
<b>moiety</b>	C <sub>11</sub> H <sub>20</sub> N <sub>4</sub> O,H <sub>2</sub> O	2(C <sub>13</sub> H <sub>24</sub> N <sub>4</sub> O),H <sub>2</sub> O
<b>T (K)</b>	175	173
<b>Space group</b>	<i>P</i> 2 <sub>1</sub> / <i>c</i>	<i>P</i> 2 <sub>1</sub> / <i>a</i>
<b>crystal system</b>	monoclinic	monoclinic
<b>a (Å)</b>	20.7063(19)	23.94660(4)
<b>b (Å)</b>	4.5994(3)	4.58700(2)
<b>c (Å)</b>	14.4235(9)	29.16260(5)
<b>α (°)</b>	90	90
<b>β (°)</b>	101.488(8)	111.908(4)
<b>γ (°)</b>	90	90
<b>V (Å<sup>3</sup>)</b>	1346.13(9)	2971.98(9)
<b>Z</b>	4	4
<b>ρ (gcm<sup>-3</sup>)</b>	1.196	1.168
<b>M<sub>r</sub> (gmol<sup>-1</sup>)</b>	242.33	522.74
<b>μ (mm<sup>-1</sup>)</b>	0.084	0.628
<b>R<sub>int</sub></b>	0.070	0.264
<b>θ<sub>max</sub> (°)</b>	29.274	63.960
<b>resolution (Å)</b>	0.82	1.05
<b>N<sub>tot</sub> (measured)</b>	9684	32932
<b>N<sub>ref</sub> (unique)</b>	3233	4911
<b>N<sub>ref</sub> (I &gt; 2σ(I))</b>	1979	2022
<b>N<sub>ref</sub> (least-squares)</b>	1979	2022
<b>N<sub>par</sub></b>	172	334
<b>&lt;σ(I)/I&gt;</b>	0.0890	0.369
<b>R<sub>1</sub> (I &gt; 2σ(I))</b>	0.0724	0.0852
<b>wR<sub>2</sub> (I &gt; 2σ(I))</b>	0.0692	0.0793
<b>R<sub>1</sub> (all)</b>	0.1307	0.1945
<b>wR<sub>2</sub> (all)</b>	0.0692	0.0958
<b>GOF</b>	1.1053	1.0646
<b>Δρ (eÅ<sup>-3</sup>)</b>	-0.36/0.30	-0.37/0.34
<b>crystal size (mm<sup>3</sup>)</b>	0.05x0.15x0.19	0.02x0.04x0.10

#### 4.4.5. X-ray powder diffraction

The powder samples were measured as filtrated from the reactional mixture, while the nanocrystal AWC samples were prepared from the AWC solutions in water and ethanol as the DLS samples. To obtain the nanocrystal AWC, the solvents in AWC solution were evaporated naturally on the evaporating dish, in which fibrous nanocrystal was formed. The X-ray powder diffraction patterns were recorded using a PanAnalytical X'pert-Pro diffractometer.

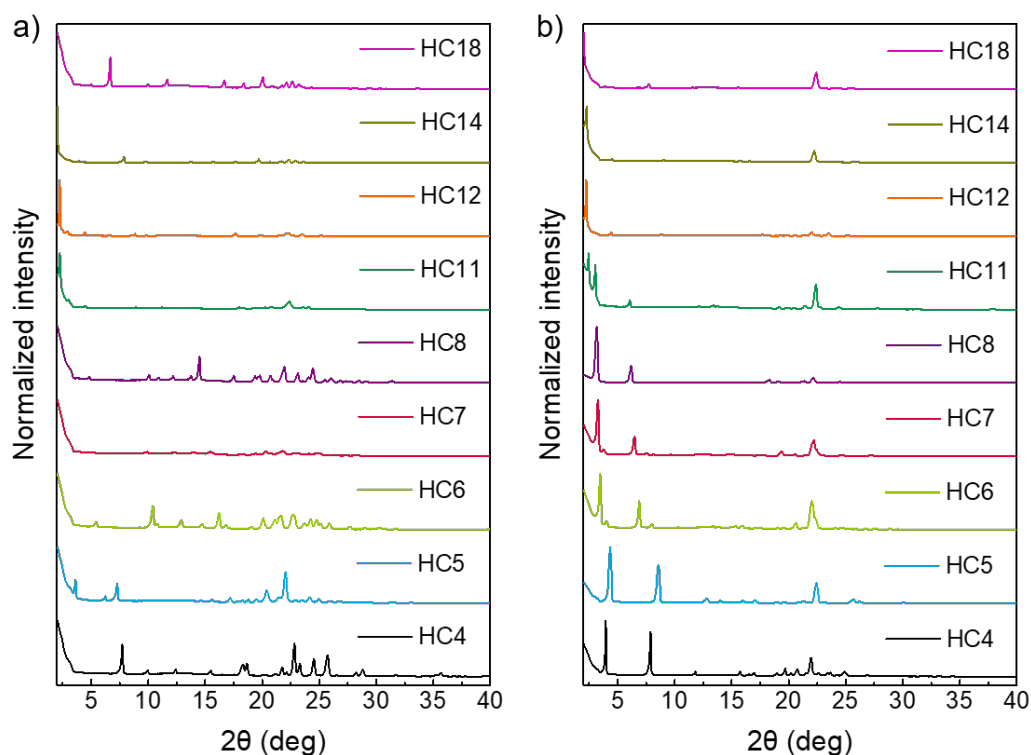


**Figure 94.** Comparisons for X-ray powder diffraction patterns of (a) powder and (b) nanocrystal AWC from different imidazole compounds.

#### 4.4.6. Transmembrane transport experiments

**Sample preparation.** The concentration for **HC4**, **HC6** and **HC8** were 25 mg/mL (wCLR = 1) and we set the concentration gradients to 5, 10, 15, 20 and 25 mg/mL (wCLR = 0.2, 0.4, 0.6 0.8 and 1, respectively) of **HC5** and **HC7** solutions in DMSO for water transport experiments. Simultaneously, the concentrations for **HC11**, **HC12**, **HC14** and **HC18** were 1.25, 2.5, 3.75 and 5 mg/mL, equivalent to channel to lipid ratio at weight (wCLR) = 0.05, 0.1, 0.15 and 0.2.

**Water transport.** Liposomes were prepared using the film rehydration method. A phosphatidylcholine/phosphatidylserine/cholesterol PC/PS/Chl mixture with a molar ratio of 4/1/5 was dissolved in chloroform/methanol mixture (CHCl<sub>3</sub>/MeOH, v/v: 1/1). The solution was dried on a rotary evaporator and subsequently in a vacuum desiccator to remove residual solvent. After rehydration with 1 mL buffer solution containing 200 mM sucrose and 10 mM PBS (pH = 6.4), the suspension was extruded through 0.1 μm track-etched filters for 21 times (Whatman, UK) to obtain monodisperse unilamellar vesicles, the size of which was characterized by dynamic light scattering (Zetasizer Nano-S ZEN1600, Malvern Instruments Ltd., UK). The aliquots of the compounds dissolved in DMSO have been added to the liposomes. The water permeability tests were conducted on a stopped-flow instrument (SFM3000 + MOS450, Bio-Logic SAS, Claix, France). Exposure of vesicles to hypertonic osmolyte (400 mM sucrose) in the same buffer resulted in the shrinkage of the vesicles due to an outwardly directed osmotic gradient. The changes of light scattering were recorded at a wavelength of 345 nm.

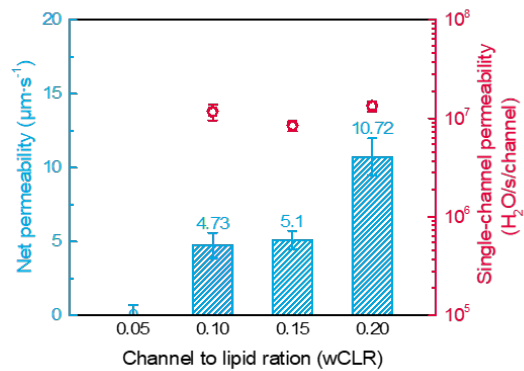
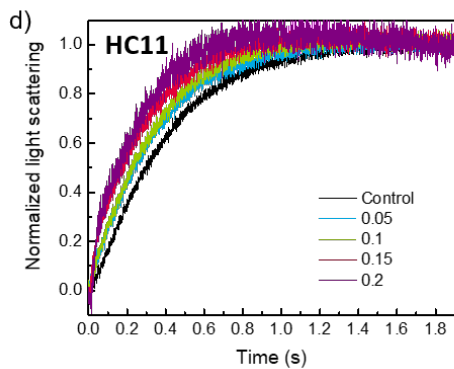
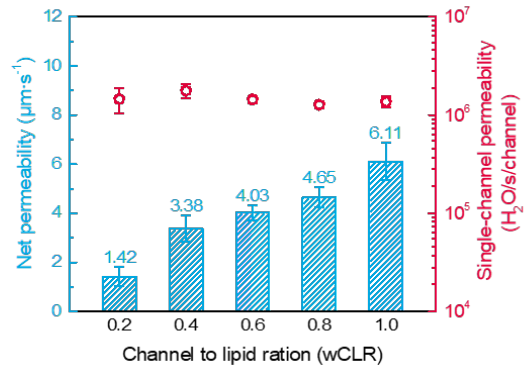
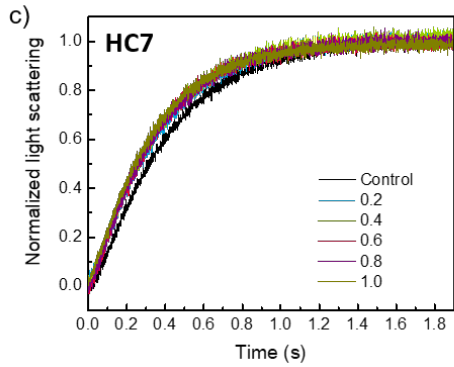
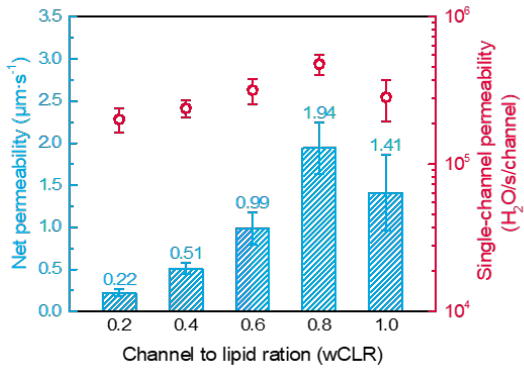
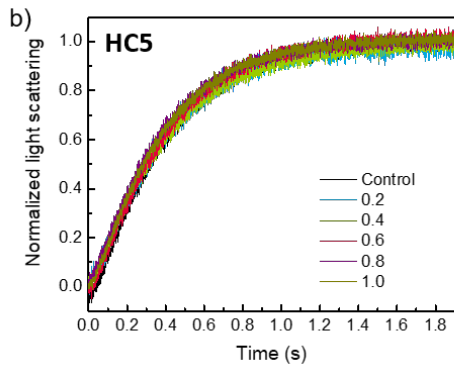
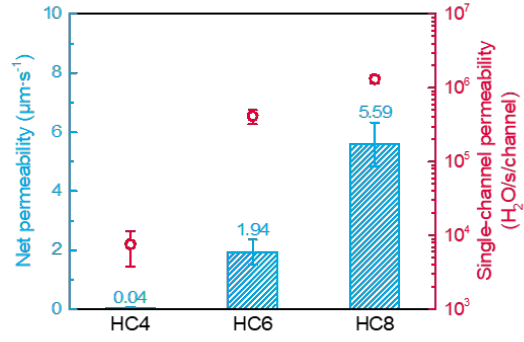
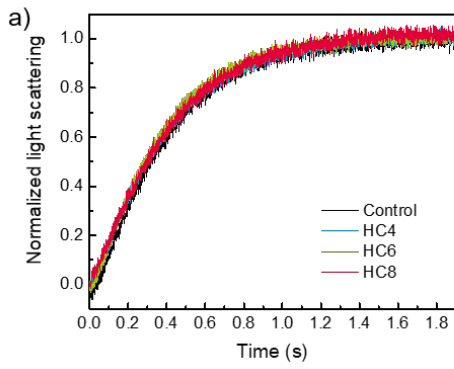
The abrupt change of the vesicle size lead to variation in the light scattering at 90° according to the Rayleigh-Gans theory applied to this system and could be

fitted in the form of the sum of two exponential functions. The osmotic permeability ( $P_f$ ) was calculated as following:

$$P_f = \frac{k}{\frac{S}{V_0} \times V_w \times \Delta_{osm}}$$

where  $k$  is the exponential coefficient of the change in the light scattering;  $S$  and  $V_0$  are the initial surface area and volume of the vesicles, respectively;  $V_w$  is the molar volume of water, and  $\Delta_{osm}$  is the osmolarity difference.

In an average experiment, 100  $\mu$ L stock lipid solution containing 0.524 mg of lipids was diluted with 1880  $\mu$ L of 200 mM sucrose in 10 mM PBS buffer solution. The compounds were injected in 20  $\mu$ L aliquots in DMSO. The solution mix was thermostated at 20°C for 30 minutes before exposure to the 400 mM sucrose solution. Experiments have been conducted at different concentrations of the injected compounds, in which the concentrations of **HC4**, **HC6** and **HC8** I-quartet channels solutions in DMSO were channel to lipid ratio at weight (wCLR) = 1. And the concentrations of **HC5** and **HC7** were 0.2, 0.4, 0.6, 0.8 and 1. Due to the limitation of solubility, the concentrations of **HC11**, **HC12**, **HC14** and **HC18** channels were wCLR = 0.05, 0.1, 0.15 and 0.2. The average permeability was calculated by using the permeability values obtained from at least three different batches of vesicles.





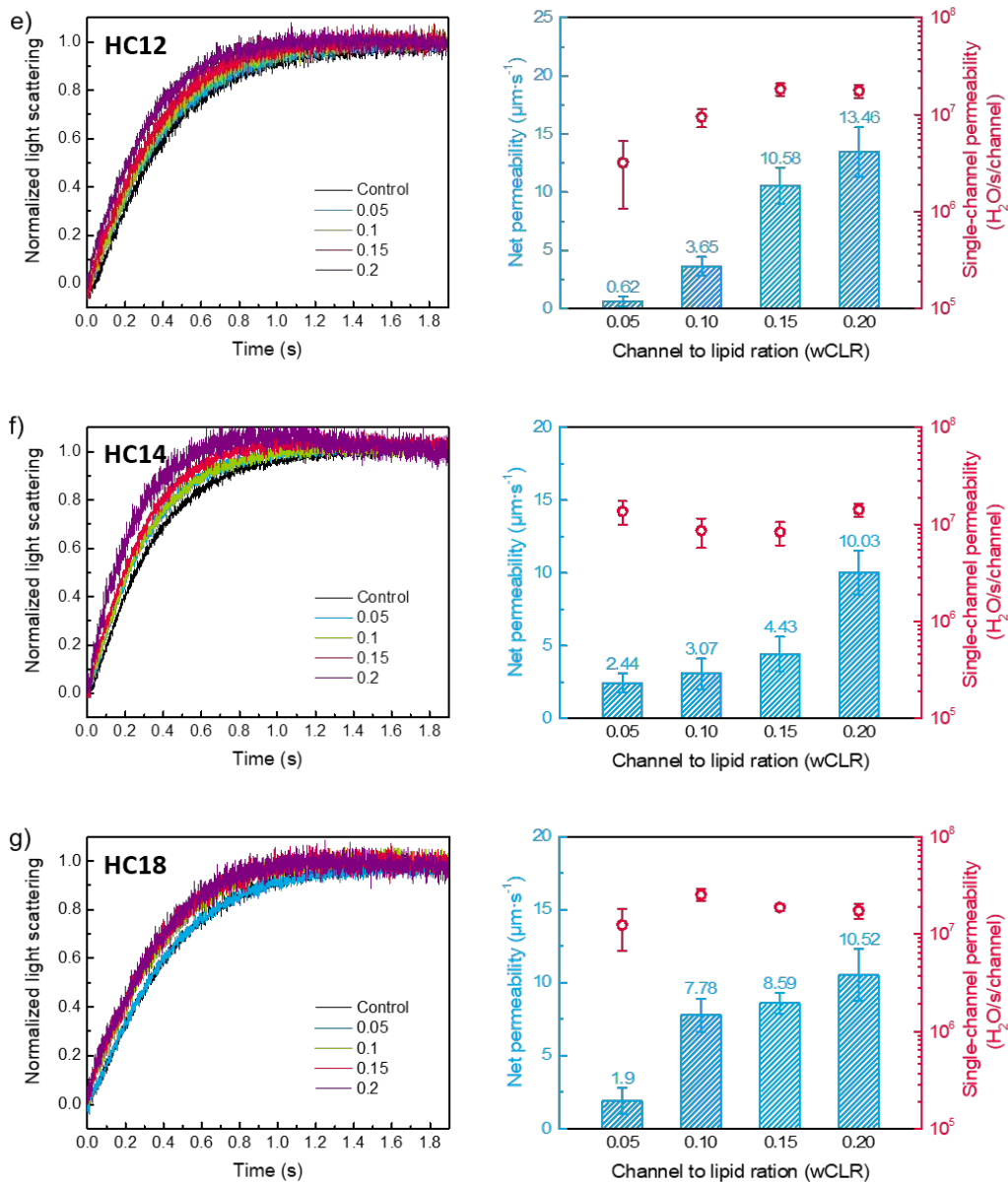


**Figure 95.** Water permeabilities expressed as normalized light scattering of the channels assembled by (a) **HC4**, **HC6** and **HC8**, (b) **HC5**, (c) **HC7**, (d) **HC11**, (e) **HC12**, (f) **HC14** and (g) **HC18** were determined by stopped-flow light scattering experiments. The stopped-flow traces of liposomes containing different concentrations of I-quartet channels (left). And the comparison of net permeability and single-channel permeability values with different channel to lipid ratios of I-quartet channels (right).

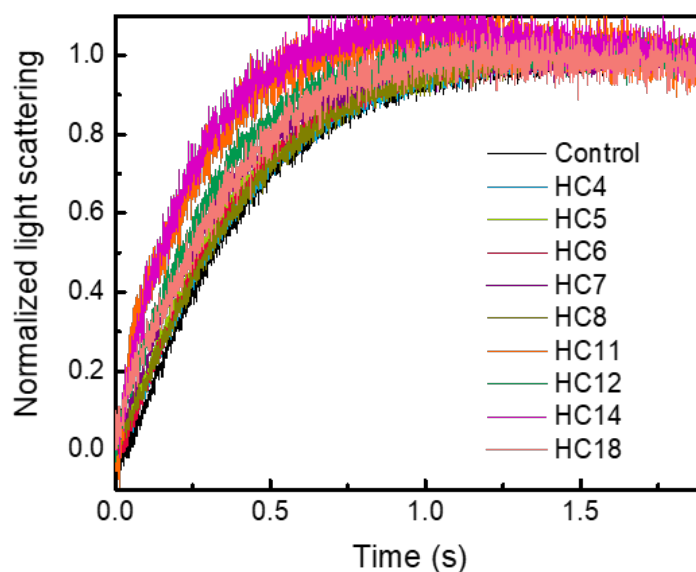


**Figure 96.** Stopped-flow light scattering traces of liposomes containing different I-quartet channels with highest net permeability.

**Table 11.** Single-channel permeability values of I-quartet channels.

I-quartet channels	wCLR	Single-channel permeability (water molecules/s)
<b>HC4</b>	1.0	$(7.63 \pm 3.81) \times 10^3$
<b>HC5</b>	1.0	$(4.78 \pm 0.76) \times 10^5$
<b>HC6</b>	0.8	$(4.13 \pm 0.92) \times 10^5$
<b>HC7</b>	0.4	$(1.77 \pm 0.28) \times 10^6$
<b>HC8</b>	1.0	$(1.32 \pm 0.17) \times 10^6$
<b>HC11</b>	0.2	$(1.33 \pm 0.16) \times 10^7$
<b>HC12</b>	0.15	$(1.83 \pm 0.27) \times 10^7$
<b>HC14</b>	0.2	$(1.42 \pm 0.21) \times 10^7$
<b>HC18</b>	0.1	$(2.53 \pm 0.29) \times 10^7$

Note: 48 molecules self-assembled into an I-quartet channel within a transmembrane length of 5 nm based on MD simulation. Taking the sample of **HC8** at wCLR = 1 as an example, the molar channel to lipid ratio is 0.045. The average radius of the liposome was 72.5 nm determined by DLS experiments. Hence, the sum of outer and inner surface areas

was  $4\pi \times R^2 + 4\pi \times (R - 5)^2 = 123,308 \text{ nm}^2$ . The average cross-sectional area of a lipid in average was  $0.287 \text{ nm}^2$  (PC/PS/Chl lipids with a molar ratio of 4/1/5: the cross-sectional areas of PC and PS were  $\sim 0.35 \text{ nm}^2$  and that of cholesterol was  $0.223 \text{ nm}^2$ ), and that of the I-quartet channel (not including the alkyl chain) was estimated as  $0.7 \text{ nm}^2$ . So, the insertion number of the channel was  $\sim 8,768$  per vesicle. If the overall net permeability by channels in liposomes was  $(5.59 \pm 0.74) \mu\text{m/s}$ , the single-channel permeability was  $(3.93 \pm 0.52) \times 10^{-17} \text{ cm}^3/\text{s}$  and  $(1.32 \pm 0.17) \times 10^6$  water molecules/s. According to the same algorithm, the highest single-channel permeability for each I-quartet channel and their corresponding wCLR as shown in Figure 95. The single channel permeability values varied obviously, covering the range of  $7.63 \times 10^3$  to  $2.53 \times 10^7 \text{ H}_2\text{O/s/channel}$ , which are only one order of magnitude lower than that of AQPs ( $\sim 10^8$ - $10^9$  water /s/channel).

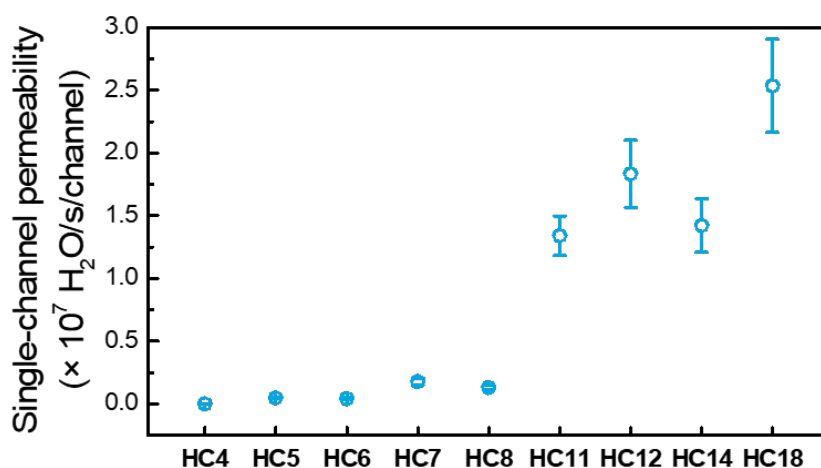


**Figure 97.** The comparison of single-channel permeability for different I-quartets.

#### 4.4.7. Simultaneous TGA/DSC thermal analysis

The thermogravimetric analysis (TGA) and differential scanning calorimetry (DSC) unveiled good thermal stability for I-quartet channels (Figures 98-100), of which TGA curves indicated thermal decomposition of the compounds were at  $\sim 200 \text{ }^\circ\text{C}$ . Several phase-transition events can be detected around  $\sim 100 \text{ }^\circ\text{C}$  and  $\sim 125 \text{ }^\circ\text{C}$  reminiscent with progressive H-bonding rupture in the highly cross-linked crystalline matrices.

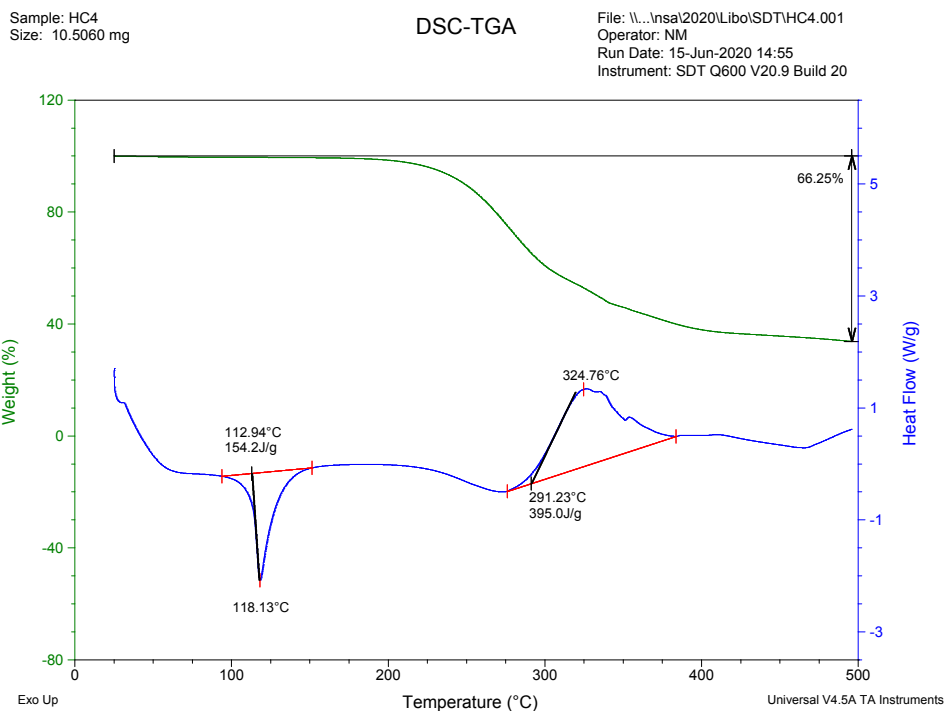


**Figure 98.** Thermogravimetric analysis TGA (green) and differential scanning calorimetry DSC (blue) curves for **HC4**.

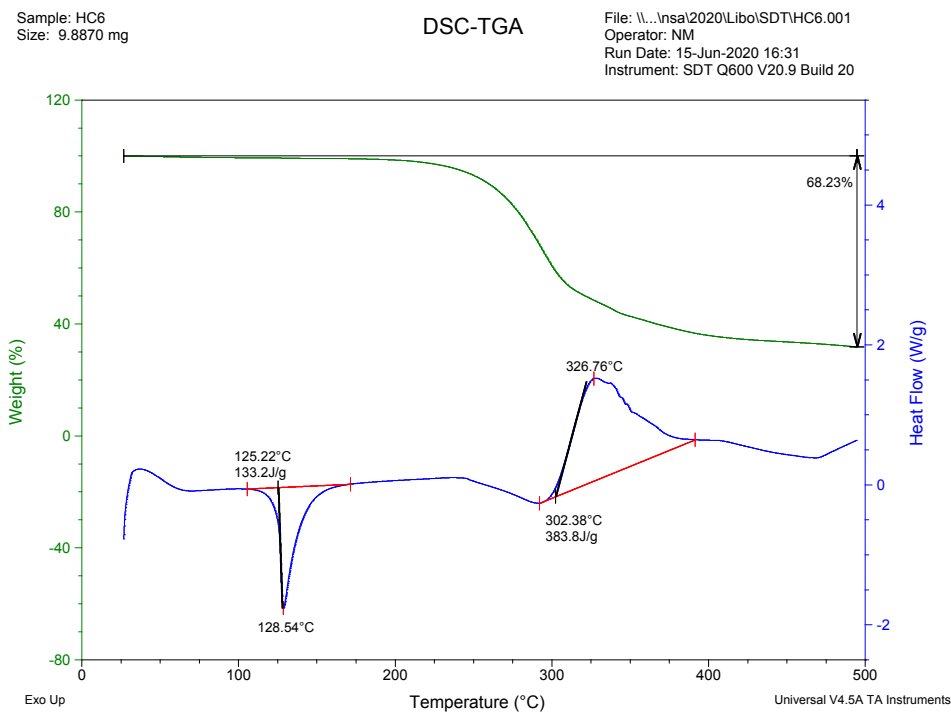


**Figure 99.** Thermogravimetric analysis TGA (green) and differential scanning calorimetry DSC (blue) curves for **HC6**.

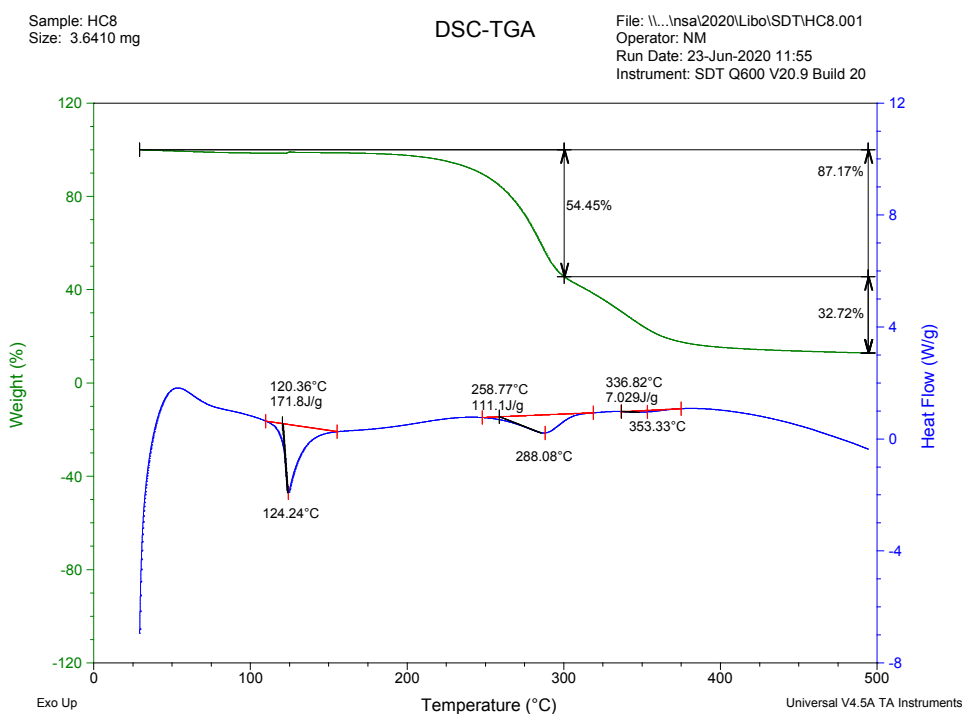


**Figure 100.** Thermogravimetric analysis TGA (green) and differential scanning calorimetry DSC (blue) curves for **HC8**.

#### 4.4.8. Membrane preparation

Commercial flat-sheet Polysulfone (PSf) ultrafiltration membranes, PS35-GPP (Solecta, USA), were used as support layers for the fabrication of all the PA-based membranes. Trimesoyl chloride (TMC, 98%), m-phenylenediamine (MPD, flakes 99%), histamine ( $\geq 97\%$ ), hexyl isocyanate (97%), sodium chloride (NaCl) ( $\geq 99.5\%$ ), sodium metabisulfite ( $\text{Na}_2\text{S}_2\text{O}_5$ , 98%) were purchased from Sigma-Aldrich, France. All solvents used in this study were HPLC grade. Methanol (MeOH), ethanol (EtOH), tetrahydrofuran (THF), ethyl acetate (EtOAc), dimethylacetamide (DMA), acetonitrile (ACN), and hexane were purchased from VWR International Ltd. Unless specified, all chemicals were dissolved in deionized (DI) water obtained from a Milli-Q ultrapure water purification system (Millipore, France). All the reagents and solvents were used without any further purification.

**Fabrication of reference TFC membranes.** Traditional polyamide active layers were cast on top of the commercial PSf ultrafiltration support. This support was taped onto a stainless-steel plate to leave only the topmost surface available for reaction. It was then placed in an amine aqueous solution (MPD: 2.0 wt%) for 120 s. An air gun was used to remove the excess solution from the membrane surface. The membrane was then immersed in a hexane solution of TMC (0.1 wt%) for 60 s. During this step, the ultrathin polyamide layer was formed. The composite membrane was then cured in DI water at 95°C for 120 s, rinsed with a 200 ppm NaOCl aqueous solution for 120 s, followed by soaking in a 1000 ppm Na<sub>2</sub>S<sub>2</sub>O<sub>5</sub> aqueous solution for 30 s and a final wet curing step at 95°C for 120 s in DI water. The TFC membranes were stored in DI water at 4°C until use as a comparison with our membranes.

**Fabrication of biomimetic TFC-HC6 membranes incorporating artificial water channels.** The conventional procedure described above was adjusted to embed I-quartets within the polyamide environment. **HC4**, **HC6** and **HC8** monomers were dissolved (1.5 wt%) in a mixed ethanol/water solution, followed by sonication to obtain a homogeneous solution. This solution was poured onto the commercial PSf support and allowed to sit for a time before starting the traditional IP procedure, as described above. During IP, the I-quartets self-assemble, aggregate, and diffuse through the film. The morphology and performance of the final layer depend on the density of the self-assembled imidazole structures and on their interaction with the surrounding polyamide matrix. The membranes referred to as “**HCx-PA**” were fabricated using the same monomer concentrations and contact times relative to the synthesis of the control TFC membranes.

**Membrane morphological characterization.** The incorporation of artificial water channels in polyamide (PA) layers was verified by a high-resolution scanning electron microscope (SEM, HITACHI S-4800), at an

accelerating voltage of 2 kV. For cross-sectional studies, membrane coupons were prepared by freeze-fracturing in liquid nitrogen and then dried in dry air for at least 24 h. A 5-nm thick coating of chromium was sputtered (SC7620 Mini Sputter Coater, Quorum Technologies Ltd.) under Ar atmosphere ( $10^{-1}$  mbar) to achieve a minimum conductivity for reliable SEM information.

**Membrane performance evaluation.** Intrinsic transport properties of control TFC and bioinspired membranes were evaluated using a laboratory-scale cross-flow unit, comprising a high-pressure pump, a feed vessel, and a flat membrane housing cell. The effective membrane active area was 28.9 cm<sup>2</sup>, the crossflow velocity was fixed at 0.9 m/s, and the temperature was constant at  $25 \pm 0.5^\circ\text{C}$ . Prior to each experiment, the membrane was immersed in water overnight. The filtration tests were conducted, referred to as “brackish water” BWRO tests. The membranes were compacted with DI water as feed at 18 bar (261 psi) of applied pressure,  $\Delta P$ , until the permeate flux reached a steady-state. The pressure was then lowered to 15.5 bar (217 psi) or 6 bar (87 psi) for brackish water tests, respectively. The pure water flux,  $J_{w,0}$ , was calculated by dividing the volumetric permeate rate, obtained at steady-state, by the membrane active area. The pure water permeability coefficient,  $WP$ , was determined by dividing the water flux,  $J_{w,0}$ , by the applied pressure,  $WP = J_{w,0}/\Delta P$ . Subsequently, for brackish water tests, NaCl was added from a 5 M stock solution to reach a final concentration of 100 mM, and salt concentrations in the feed and permeate streams were measured using a calibrated conductivity meter (pHenomenal® CO 3100 H, VWR Instruments). Upon reaching steady-state, the permeate flux,  $J_w$ , was calculated by dividing the volumetric permeate rate by the membrane area. Observed rejection,  $R$ , was then computed from the concentrations determined in bulk feed,  $c_f$ , and in the permeate stream,  $c_p$ , for each ionic species or for global salinity (using conductivity as a proxy for salinity):  $R =$

$1 - c_p/c_f$ . The rejection values reported for each sample are the average of three different measurements.

#### 4.4.9. Molecular simulations

Molecular Dynamics (MD) simulations were carried out in order to gain understanding of the interactions between **HC6** and two distinct media corresponding to the different stages of the membrane fabrication procedure: (i) an ethanolic aqueous solution with 1:3 (vol/vol) ethanol/water content and (ii) a crosslinked polyamide (PA) matrix.

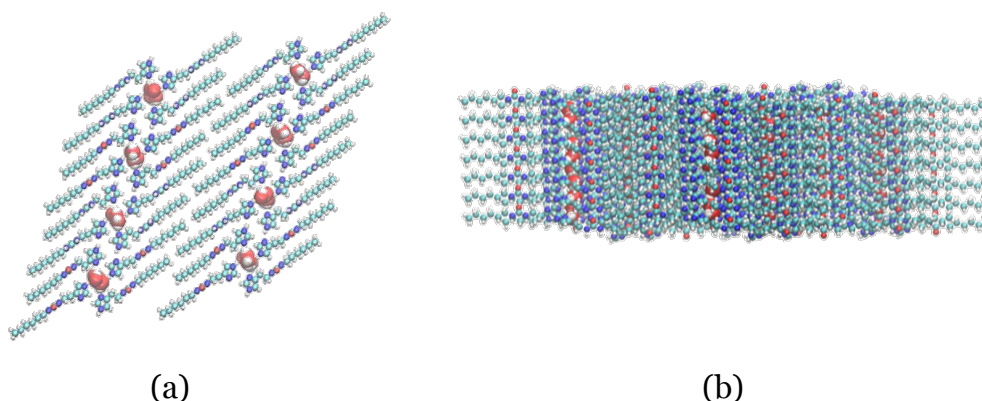


**Figure 101.** Initial structure model considered for HC6 where the channels run along the y-axis: (a) view through the I-quartets and (b) side view, with water molecules illustrated inside the channels.

Starting with the crystal structure reported previously<sup>[S8]</sup>, a model for HC6 was first constructed with dimensions along the 3 directions of  $5.5 \text{ nm} \times 3 \text{ nm} \times 4.8 \text{ nm}$ , containing 2 sets of 4 parallel channels in 7 layers as shown in Figure 101. All atoms were treated as charged Lennard-Jones (LJ) sites with LJ parameters taken from the GAFF force field<sup>[S9]</sup> while their associated Density functional theory (DFT)-derived ESP charges<sup>[S10]</sup> were calculated for a cluster of I-quartet (4 chains of HC6) using the Perdew–Burke–Ernzerhof (PBE) functional<sup>[S11]</sup> and 6-31G\*\* basis set<sup>[S12,S13]</sup> as implemented in Gaussian09<sup>[S14]</sup> software. The



corresponding charges are available in the structure files provided as supplementary files.

The **HC6**/ethanolic aqueous solution model was built as follows. The **HC6** model was initially placed at the center of a cubic box of 120 Å dimension and the corresponding box was solvated with a 1:3 (vol/vol) mixture of ethanol and water in the *Amorphous Cell* module of the Materials Studio 5.5 (Accelrys Inc., USA) simulation package to pack the solvent molecules with an arbitrary target density of 0.850 g/cm<sup>3</sup> at 298 K. Water molecule was represented by the flexible TIP3P model<sup>[S15]</sup> and ethanol molecule was treated using the well-established TraPPE force field<sup>[S16]</sup>. The interactions were modeled by the sum of a van der Waals contribution (Lennar-Jones-LJ) and a Coulombic term. A 14-Å cut-off was applied for the LJ interactions accompanied by tail corrections and Ewald method was considered for the calculations of the electrostatic terms. The resulting **HC6**/ethanolic aqueous solution model containing 90 272 atoms was further equilibrated using NPT-MD simulations at 1 bar and 298 K for 10 ns in LAMMPS molecular simulation package<sup>[S17]</sup> leading to a density of 0.905(3) g/cm<sup>3</sup>. An integration step of 1 fs was adopted for these simulations and the Velocity-Verlet algorithm was applied to integrate the equations of motions, combined with Nose-Hoover thermostat and barostat using relaxation times of 0.5 ps and 0.1 ps respectively.

For the generation of the **HC6**/PA interface model, the model of **HC6** was placed at the center of a rectangular box with dimensions of 140 Å × 85 Å × 140 Å and packed with a crossed-linked polyamide (PA). PA was modeled as a linear chain of 12 repeated units, where each repeated unit was formed of alternating MPD and TMC monomeric units. Considering subsequent crosslinking process, 300 of these chains were packed together with 1000 MPD molecules to ensure a high crosslinking ratio using the *Amorphous Cell* module of Material Studio, following the work of Kotelyanskii *et al*<sup>[S18]</sup> with a target density of 1.1 g/cm<sup>3</sup> for

the polymer phase at 298 K. The resulting polymer matrix was then subjected to a progressive crosslinking procedure using the script developed by DeJoannis *et al*.<sup>[S19]</sup>. This script connects gradually the carboxylic acid groups of TMC units separated by  $<5 \text{ \AA}$  with the MPD molecules. This procedure yielded a crosslinking ratio of 78% for PA. In these calculations all atoms of the polymers were treated as charged Lennard-Jones (LJ) sites with LJ parameters taken from the GAFF force field<sup>[S9]</sup> while their associated DFT-derived ESP charges were derived from a dimer using the same methodology applied for HC6. The corresponding charges are available in the structure files provided as supplementary files. Since the non-crosslinked carboxylic acid groups in the polymer would exist primarily in the ionized form (-R-COO-), Na<sup>+</sup> ions were added to maintain the neutrality of the system.<sup>[S20]</sup> The interactions were also modeled by the sum of a LJ contribution and a Coulombic term as applied for the HC6/ethanolic aqueous solution system. The resulting PA/HC6 system was then relaxed and equilibrated with a series of NVT and NPT-MD runs (T = 298 K, P = 1 bar) (using the same set-up defined above) using the LAMMPS software.<sup>[S17]</sup> Next, extra water molecules (25 wt%) were introduced in the polymeric matrix to mimic the experimental hydration using the *Sorption* module of the Materials Studio software package. The final HC6/PA system contains 120,032 atoms and associated with a density of 1.393(2) g/cm<sup>3</sup> at 298 K.

The structural evolution of both HC6/ethanolic aqueous solution and HC6/PA systems was further followed by longer NPT-MD simulations at 1 bar and 298 K using LAMMPS. The HC6/ethanolic aqueous solution and HC6/PA systems were simulated for 60 ns and 200 ns respectively. Further analysis of the MD trajectories including the calculations of radial distribution functions (RDF) and root-mean-square displacements (RMSD) was further performed and discussed in the manuscript.

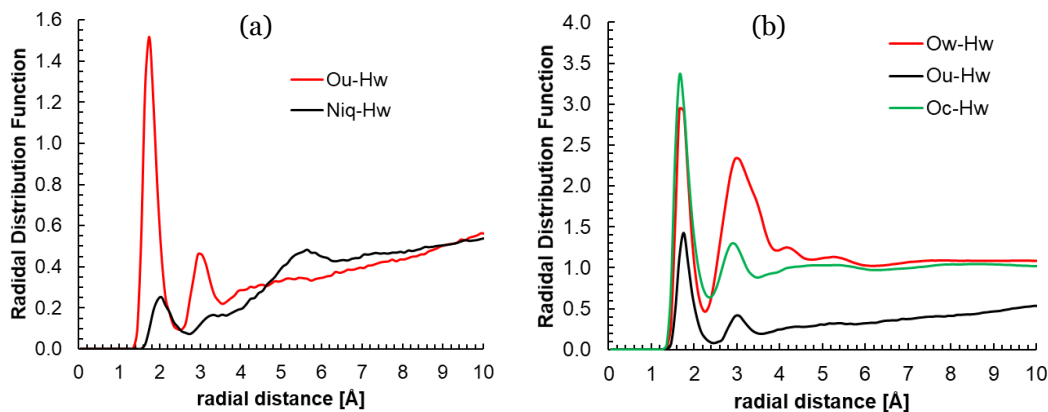


**Figure 102.** Radial distribution function plots (RDFs) for the **HC6/PA** system (a) between the hydrogen atoms of water ( $H_w$ ) and both the oxygen atoms in the urea group ( $O_u$ ) and the nitrogen atoms in the imidazole ring ( $N_{im}$ ) of **HC6** and (b) between the hydrogen atoms of water ( $H_w$ ) and both the oxygen atoms in the urea group ( $O_u$ ) of **HC6** ( $O_u$ ), and the oxygen of the carboxylate of the PA ( $O_c$ ) as well as between the hydrogen atoms of water ( $H_w$ ) and the oxygen atom of water ( $O_w$ ).

## References

- [S1] Mannhold, R.; Poda, G. I.; Ostermann, C.; Tetko, I. V. *J. Pharm. Sci.* **2009**, *98* (3), 861–93.
- [S2] VCCLAB, Virtual Computational Chemistry Laboratory, <http://www.vcclab.org>, **2005**
- [S3] CrysAlisPro Agilent Technologies, England 2012.
- [S4] Bruker (2016). *APEX3*. Bruker AXS Inc., Madison, Wisconsin, USA.
- [S5] Palatinus, L.; Chapuis, G. *J. Appl. Crystallogr.* **2007**, *40*, 786–790.
- [S6] van der Lee, A. *J. Appl. Crystallogr.* **2013**, *46*, 1306–1315.
- [S7] Betteridge, P. W.; Carruthers, J. R.; Cooper, R. I. Prout, K.; Watkin, D. J. *J. Appl. Crystallogr.* **2003**, *36*, 1487–1487.
- [S8] Licsandru, E.; Kocsis, I.; Shen, Y. X.; Murail, S.; Legrand, Y. M.; van der Lee, A.; Tsai, D.; Baaden, M.; Kumar M.; Barboiu, M. *J. Am. Chem. Soc.* **2016**, *138*, 5403–5409.
- [S9] Wang, J.; Wolf, R. M.; Caldwell, J. W.; Kollman, P. A.; Case, D. A. *J. Comp. Chem.* **2004**, *25* (9), 1157–1174.

- [S10] Heinz, H.; Suter, U. W. Atomic Charges for Classical Simulations of Polar Systems. *J. Phys. Chem. B* **2004**, 108 (47), 18341–18352.
- [S11] Perdew, J. P.; Burke, K.; Ernzerhof, M. Generalized Gradient Approximation Made Simple. *Phys. Rev. Lett.* **1996**, 77 (18), 3865–3868.
- [S12] Becke, A. D. Density-functional Thermochemistry. III. The Role of Exact Exchange. *J. Chem. Phys.* **1993**, 98, 5648–5652.
- [S13] Lee, C.; Yang, W.; Parr, R. G. Development of the Colle-Salvetti Correlation-energy Formula into a Functional of the Electron-density. *Phys. Rev. B: Condens. Matter Mater. Phys.* **1988**, 37, 785–789.
- [S14] Frisch, M. J.; Trucks, G. W.; Schlegel, H. B.; Scuseria, G. E.; Robb, M. A.; Cheeseman, J. R.; Scalmani, G.; Barone, V.; Petersson, G. A.; Nakatsuji, H.; Li, X.; Caricato, M.; Marenich, A. V.; Bloino, J.; Janesko, B. G.; Gomperts, R.; Mennucci, B.; Hratchian, H. P.; Ortiz, J. V.; Izmaylov, A. F.; Sonnenberg, J. L.; Williams; Ding, F.; Lipparini, F.; Egidi, F.; Goings, J.; Peng, B.; Petrone, A.; Henderson, T.; Ranasinghe, D.; Zakrzewski, V. G.; Gao, J.; Rega, N.; Zheng, G.; Liang, W.; Hada, M.; Ehara, M.; Toyota, K.; Fukuda, R.; Hasegawa, J.; Ishida, M.; Nakajima, T.; Honda, Y.; Kitao, O.; Nakai, H.; Vreven, T.; Throssell, K.; Montgomery Jr., J. A.; Peralta, J. E.; Ogliaro, F.; Bearpark, M. J.; Heyd, J. J.; Brothers, E. N.; Kudin, K. N.; Staroverov, V. N.; Keith, T. A.; Kobayashi, R.; Normand, J.; Raghavachari, K.; Rendell, A. P.; Burant, J. C.; Iyengar, S. S.; Tomasi, J.; Cossi, M.; Millam, J. M.; Klene, M.; Adamo, C.; Cammi, R.; Ochterski, J. W.; Martin, R. L.; Morokuma, K.; Farkas, O.; Foresman, J. B.; Fox, D. J. Gaussian 16 Rev. C.01; Wallingford, CT, **2016**.
- [S15] Jorgensen, Chandrasekhar, Madura, Impey, Klein, *J. Chem. Phys.* **1983**, 79, 926.
- [S16] Chen, B.; Potoff, J.J.; Siepmann, J.I. *J. Phys. Chem. B* **2001**, 105, 3093–3104.
- [S17] Plimpton, S. *J. Comp. Phys.* **1995**, 117, 1–19.
- [S18] Kotelyanskii, M.J.; Wagner, N. J.; Paulaitis, M. E. *J. Membr. Sci.* **1998**, 139, 1–16.
- [S19] DeJoannis, J.; Todd, S.; Wescott, J. <https://bioviacommunity.force.com>, **2017**.
- [S20] Ridgway, H. F.; Orbell, J.; Gray, S. *J. Membr. Sci.*, **2017**, 524, 436–448.



## Conclusions and Outlook

Water plays a crucial role in all living cells and organisms, and efficient regulation of transmembrane water dynamic homeostasis is essential for most biological processes. Aquaporins, as naturally occurring proteins, are able to facilitate the transport of water across cell membranes with high permeability and exceptional selectivity. However, the structural complexity and poor stability of aquaporins in artificial media other than cellular membranes have prompted researchers to mimic aquaporins and develop artificial water channels combining high permeability and selectivity with chemical stability. In this thesis, we have designed and synthesized a series of small amphiphilic molecules with specific structures used to construct artificial water channels with hydrophilic cavities, urea scaffolding backbone and hydrophobic lateral chains in interaction with external membranes. Moreover, we focused on the water transport performances of artificial water channels in bilayer and polymeric membrane environments, and mainly obtained three parts of research results. This thesis hopes to tackle the above issues through developing new synthetic water channel to leverage their versatility, rich chemistry, tunable structures, and solution-processability.

In chapter II, a class of octyl-ureido-polyol compounds **H1–H6** are designed and synthesized, capable of self-assembly into hydrophilic hydroxy channels. Variants of ethanol, propanediol, and trimethanol are used as head groups to modulate the water transport permeabilities, with rejection of ions. As a result, the new class of water channels, the hydroxy channels achieve a highest single-channel permeability of  $2.33 \times 10^8$  water molecules per second which is within the same order of magnitude as the transport rates for aquaporins. Depending on their concentration in the membrane, adaptive channels are observed in the membrane. Over increased concentrations, a significant shift occurs, initiating unexpected higher water permeation. Molecular simulations probe that

spongelike or cylindrical aggregates can form to generate transient water-cluster pathways through the bilayer. Altogether, the adaptive self-assembly is a key feature influencing water permeability. The adaptive behaviors of the channels described in this work may be considered an important milestone contributing to the systematic discovery of artificial water channels for water desalination.

Water-wire/water-clusters widely exist as well-established mechanisms for water permeation through artificial water channels. In chapter III, to get deeper insight into the differences of these two water permeation approaches, we design and synthesize a class of pyridine bis(formamide-ethyl-imidazole) derivatives **U1-U6**, capable of self-assembly into U-shaped diimidazole water channels. The crystal structures reveal that two types of channel superstructures are formed, one with a hydrophilic cavity with a diameter of  $\sim 9$  Å, accommodating water clusters. In the other type of channel, the hydrophobic methyl formate side chain shields the hydrophilic sites, leading to the H-bonds of water molecules to the carbonyl groups and the formation of water-wires. As a result, a single-channel permeability of  $1.22 \times 10^7 \text{ H}_2\text{O s}^{-1} \text{ channel}^{-1}$  have been achieved by the U-shape diimidazole water channels, which is only one order of magnitude lower than that of aquaporins. Moreover, U-channels completely rejects anions and are expected to be applied in desalination after slight structural modifications. The results suggest that water-clusters transporting behavior present a higher water permeability compared to the water-wire transport. However, the selectivity of artificial water channels for ions and protons is independent of the water-wire/clusters transport behaviors, but depends on the interaction between the water molecules and the inner motifs of the channels. To the best of our knowledge, this work is the first to realize both water-wires/clusters transport through an individual class of channels at the single-crystal structure level, providing a clever prototype for the structural design of artificial water channels.

Chapter IV of the thesis critically discuss the structural details that can impact on performances of biomimetic I-quartets, obtained *via* adaptive self-assembly of alkylureido-ethylimidazoles **HC4–HC18** in bilayer or polyamide membranes. We first explore the performances in bilayer membranes, identifying that hydrophobicity is an essential key parameter to increase water permeability. We compare various I-quartets with different hydrophobic tails (from **HC4** to **HC18**) and we reveal that a huge increase in single channel water permeability, from  $10^4$  to  $10^7$  water molecules/s/channel, is obtained by increasing the size of the alkyl tail. Quantitative assessment of AWC-polyamide-PA membranes shows that water permeability increases roughly from 2.09 to 3.85 L m<sup>-2</sup> h<sup>-1</sup> bar<sup>-1</sup>, for **HC4** and **HC6** reverse osmosis membranes respectively, while maintaining excellent NaCl rejection (99.25–99.51%). Meanwhile, comparable **HC8** loading induces a drop of performance reminiscent with a defective membrane formation. We show that the production of nanoscale sponge-like water channels can be obtained with insoluble low soluble and low dispersed AWCs, explaining observed subpar performance. We conclude that optimal solubility enabling breakthrough performance must be considered to not only maximize the inclusion and the stability in the bilayer membranes but also to achieve an effective homogeneous distribution of percolated particles that minimizes the defects in hybrid polyamide membranes.

Overall, a variety of self-assembled artificial water channels have been constructed, and comprehensive analyses toward the structures of AWCs in relation to their water transport mechanism provide theoretical basis for the structural design of novel AWCs. Besides, by embedding I-quartet water channels into bilayer and polymeric membranes, as well as modulating their compatibility and membrane morphology to achieve excellent water selective permeability, the foundation for the applications of biomimetic AWC



membranes in desalination has been laid. In conjunction with the discoveries of this thesis, several research directions remain to be explored.

- i) At present, in order to control variables as well as increase the credibility and reproducibility of experiments, the study on the transport properties of AWCs is mostly based on the phospholipid bilayer vesicles made in our laboratory. However, the performance of AWCs in the real cell membrane environment is unknown. It is well known that cellular water uptake and loss are related to cellular differentiation, proliferation and apoptosis in living organisms. If we can rely on biological research tools to conduct experiments observing the behavior of cells under the regulation of artificial water channels, it will help us to gain a deeper understanding of the mechanism of cellular activities with AWCs, and expand the applications of AWCs in the field of medical treatment for AQP-related diseases.
- ii) Since self-assembled AWCs generally have a small channel size (3–9 Å), the formation, transport and disassembly processes of water channels cannot be directly observed by conventional electron microscopy. In the future, it is expected that the structure of AWCs can be directly observed with the ultra-high resolution of cryogenic electron microscopy. In combination with other relevant characterizations, the real-time transport of water molecules in bilayer and polymeric membranes can be studied, providing targeted improving methods for the structural design and performance of AWCs.
- iii) Only I-quartet water channels have been successfully embedded in polymeric membranes for desalination, achieving high water permeability and NaCl rejection compared to conventional RO membranes. However, the applications of hydroxy channels and U-shaped channels are still limited in bilayer membranes. These two new classes of AWCs are expected to be embedded in polyamide or other polymeric membranes in a similar way and

potentially to be applied in desalination with water-clusters transport behavior, thereby significantly increasing the water permeability of polymeric membranes while maintaining a high salt rejection.

iv) Finally, a fundamental understanding of AWC-membrane interaction is highly important. Explaining such interactions is necessary to explain the water permeability patterns. Unlike AWCs are nanoscale supramolecular entities that can agglomerate differently under different membrane fabrication environments to form structures such as amorphous or crystalline aggregates, colloids or even as single molecules. Therefore, the microscopic understanding of AWCs in membranes is crucial for the understanding of the favorable structure through which water tends to permeate the fastest. Further studies are highly recommended to investigate the AWC-membrane interaction mechanisms, AWCs self-assembly distribution tendency and water permeation patterns.



## List of Publications

1. **Li-Bo Huang**, Maria Di Vincenzo, M. Göktuğ Ahunbay, Arie van der Lee, Didier Cot, Sophie Cerneaux, Guillaume Maurin, Mihail Barboiu, Bilayer versus polymeric artificial water channel membranes: structural determinants for enhanced filtration performances. *J. Am. Chem. Soc.* **2021**, *143*, 35, 14386–14393.
2. **Li-Bo Huang**, Arthur Hardiagon, Istvan Kocsis, Cristina-Alexandra Jegu, Mihai Deleanu, Arnaud Gilles, Arie van der Lee, Fabio Sterpone, Marc Baaden, Mihail Barboiu, Hydroxy channels–adaptive pathways for selective water cluster permeation. *J. Am. Chem. Soc.* **2021**, *143*, 11, 4224–4233. (Supplementary cover)
3. Maria Di Vincenzo, Alberto Tiraferri, Valentina-Elena Musteata, Stefan Chisca, Rachid Sougrat, **Li-Bo Huang**, Suzana P. Nunes, Mihail Barboiu, Biomimetic artificial water channel membranes for enhanced desalination. *Nat. Nanotechnol.* **2021**, *16*, 190–196.
4. Wen-Zhi Wang, **Li-Bo Huang**, Shao-Ping Zheng, Emilie Moulin, Odile Gavot, Mihail Barboiu, Nicolas Giuseppone, Light-driven molecular motors boost the selective transport of alkali metal ions through phospholipid bilayers. *J. Am. Chem. Soc.* **2021**, *143*, 38, 15653–15660.
5. Arthur Hardiagon, Samuel Murail, **Li-Bo Huang**, Arie van der Lee, Fabio Sterpone, Mihail Barboiu, Marc Baaden, Molecular dynamics simulations reveal statistics and microscopic mechanisms of water permeation in a membrane-embedded artificial water channel nanoconstructs. *J. Chem. Phys.* **2021**, *154*, 184102.
6. **Li-Bo Huang**, Maria Di Vincenzo, Yuhao Li, Mihail Barboiu, Artificial water channels: towards biomimetic membranes for desalination. *Chem. Eur. J.* **2020**, *27*, 2224–2239.
7. Shao-Ping Zheng, **Li-Bo Huang**, Zhanhu Sun, Mihail Barboiu, Self-assembled artificial ion-channels toward natural selection of functions. *Angew. Chem. Int. Ed.* **2020**, *60*, 566–597.
8. Yangyang Mao, Mengchen Zhang, Long Cheng, Jianwei Yuan, Gongping Liu, **Libo Huang**, Mihail Barboiu, Wanqin Jin, Bola-amphiphile-imidazole embedded GO membrane with enhanced solvent dehydration properties. *J. Membrane Sci.* **2020**, *595*, 117545.



## References

1. Agre, P., Aquaporin water channels (Nobel Lecture). *Angew. Chem. Int. Ed. Engl.* **2004**, *43* (33), 4278-90.
2. Lehn, J.-M., Supramolecular Chemistry—Scope and Perspectives Molecules, Supramolecules, and Molecular Devices (Nobel Lecture). *Angewandte Chemie International Edition in English* **1988**, *27* (1), 89-112.
3. Lehn, J.-M., Towards Complex Matter: Supramolecular Chemistry and Self-organization. *European Review* **2009**, *17* (2), 263-280.
4. Eliasson, J., The rising pressure of global water shortages. *Nature* **2015**, *517* (7532), 6.
5. Mekonnen, M. M.; Hoekstra, A. Y., Four billion people facing severe water scarcity. *Sci Adv* **2016**, *2* (2), e1500323.
6. Barboiu, M.; Gilles, A., From natural to bioassisted and biomimetic artificial water channel systems. *Acc. Chem. Res.* **2013**, *46* (12), 2814-23.
7. Ball, P., Water as an active constituent in cell biology. *Chem. Rev.* **2008**, *108* (1), 74-108.
8. Ball, P., Water is an active matrix of life for cell and molecular biology. *Proc. Natl. Acad. Sci. U. S. A.* **2017**, *114* (51), 13327-13335.
9. Murata, K.; Mitsuoka, K.; Hirai, T.; Walz, T.; Agre, P.; Heymann, J. B.; Engel, A.; Fujiyoshi, Y., Structural determinants of water permeation through aquaporin-1. *Nature* **2000**, *407* (6804), 599-605.
10. Pohl, P.; Saparov, S. M.; Borgnia, M. J.; Agre, P., Highly selective water channel activity measured by voltage clamp: analysis of planar lipid bilayers reconstituted with purified AqpZ. *Proc. Natl. Acad. Sci. U. S. A.* **2001**, *98* (17), 9624-9.
11. de Groot, B. L.; Grubmuller, H., The dynamics and energetics of water permeation and proton exclusion in aquaporins. *Curr. Opin. Struct. Biol.* **2005**, *15* (2), 176-83.
12. Tajkhorshid, E.; Nollert, P.; Jensen, M. O.; Miercke, L. J.; O'Connell, J.; Stroud, R. M.; Schulten, K., Control of the selectivity of the aquaporin water channel family by global orientational tuning. *Science* **2002**, *296* (5567), 525-30.

13. Horner, A.; Siligan, C.; Cornean, A.; Pohl, P., Positively charged residues at the channel mouth boost single-file water flow. *Faraday Discuss.* **2018**, *209* (0), 55-65.
14. Eriksson, U. K.; Fischer, G.; Friemann, R.; Enkavi, G.; Tajkhorshid, E.; Neutze, R., Subangstrom resolution X-ray structure details aquaporin-water interactions. *Science* **2013**, *340* (6138), 1346-1349.
15. Zachariae, U.; Kluhspies, T.; De, S.; Engelhardt, H.; Zeth, K., High resolution crystal structures and molecular dynamics studies reveal substrate binding in the porin Omp32. *J. Biol. Chem.* **2006**, *281* (11), 7413-20.
16. Lynch, C. I.; Rao, S.; Sansom, M. S. P., Water in Nanopores and Biological Channels: A Molecular Simulation Perspective. *Chem. Rev.* **2020**, *120* (18), 10298-10335.
17. Yan, Z. J.; Wang, D.; Ye, Z.; Fan, T.; Wu, G.; Deng, L.; Yang, L.; Li, B.; Liu, J.; Ma, T.; Dong, C.; Li, Z. T.; Xiao, L.; Wang, Y.; Wang, W.; Hou, J. L., Artificial Aquaporin That Restores Wound Healing of Impaired Cells. *J. Am. Chem. Soc.* **2020**, *142* (37), 15638-15643.
18. Tang, C. Y.; Zhao, Y.; Wang, R.; Helix-Nielsen, C.; Fane, A. G., Desalination by biomimetic aquaporin membranes: Review of status and prospects. *Desalination* **2013**, *308*, 34-40.
19. Tang, C.; Wang, Z.; Petrinić, I.; Fane, A. G.; Hélix-Nielsen, C., Biomimetic aquaporin membranes coming of age. *Desalination* **2015**, *368*, 89-105.
20. Yang, Z.; Ma, X.-H.; Tang, C. Y., Recent development of novel membranes for desalination. *Desalination* **2018**, *434*, 37-59.
21. Yang, Z.; Guo, H.; Tang, C. Y., The upper bound of thin-film composite (TFC) polyamide membranes for desalination. *J. Membr. Sci.* **2019**, *590*.
22. Kumar, M.; Grzelakowski, M.; Zilles, J.; Clark, M.; Meier, W., Highly permeable polymeric membranes based on the incorporation of the functional water channel protein Aquaporin Z. *Proc. Natl. Acad. Sci. U. S. A.* **2007**, *104* (52), 20719-24.
23. Helix-Nielsen, C., Biomimetic Membranes as a Technology Platform: Challenges and Opportunities. *Membranes (Basel)* **2018**, *8* (3).
24. Li, Y.; Qi, S.; Tian, M.; Widjajanti, W.; Wang, R., Fabrication of aquaporin-based biomimetic membrane for seawater desalination. *Desalination* **2019**, *467*, 103-112.

25. Zhao, Y.; Qiu, C.; Li, X.; Vararattanavech, A.; Shen, W.; Torres, J.; Hélix-Nielsen, C.; Wang, R.; Hu, X.; Fane, A. G.; Tang, C. Y., Synthesis of robust and high-performance aquaporin-based biomimetic membranes by interfacial polymerization-membrane preparation and RO performance characterization. *J. Membr. Sci.* **2012**, *423-424*, 422-428.
26. He, Y.; Hoi, H.; Abraham, S.; Montemagno, C. D., Highly permeable biomimetic reverse osmosis membrane with amphiphilic peptide stabilized aquaporin as water filtering agent. *J. Appl. Polym. Sci.* **2018**, *135* (15).
27. Li, X.; Chou, S.; Wang, R.; Shi, L.; Fang, W.; Chaitra, G.; Tang, C. Y.; Torres, J.; Hu, X.; Fane, A. G., Nature gives the best solution for desalination: Aquaporin-based hollow fiber composite membrane with superior performance. *J. Membr. Sci.* **2015**, *494*, 68-77.
28. Li, Z.; Valladares Linares, R.; Bucs, S.; Fortunato, L.; Hélix-Nielsen, C.; Vrouwenvelder, J. S.; Ghaffour, N.; Leiknes, T.; Amy, G., Aquaporin based biomimetic membrane in forward osmosis: Chemical cleaning resistance and practical operation. *Desalination* **2017**, *420*, 208-215.
29. Hernandez, S.; Porter, C.; Zhang, X.; Wei, Y.; Bhattacharyya, D., Layer-by-layer Assembled Membranes with Immobilized Porins. *RSC Adv* **2017**, *7* (88), 56123-56136.
30. Tu, Y. M.; Song, W.; Ren, T.; Shen, Y. X.; Chowdhury, R.; Rajapaksha, P.; Culp, T. E.; Samineni, L.; Lang, C.; Thokkadam, A.; Carson, D.; Dai, Y.; Mukthar, A.; Zhang, M.; Parshin, A.; Sloand, J. N.; Medina, S. H.; Grzelakowski, M.; Bhattacharya, D.; Phillip, W. A.; Gomez, E. D.; Hickey, R. J.; Wei, Y.; Kumar, M., Rapid fabrication of precise high-throughput filters from membrane protein nanosheets. *Nat. Mater.* **2020**, *19* (3), 347-354.
31. Livingston, A. G.; Jiang, Z., Proteins tailor pore geometry. *Nat. Mater.* **2020**, *19* (3), 257-258.
32. Le Duc, Y.; Michau, M.; Gilles, A.; Gence, V.; Legrand, Y. M.; van der Lee, A.; Tingry, S.; Barboiu, M., Imidazole-quartet water and proton dipolar channels. *Angew. Chem. Int. Ed. Engl.* **2011**, *50* (48), 11366-72.
33. Barboiu, M., Artificial water channels. *Angew. Chem. Int. Ed. Engl.* **2012**, *51* (47), 11674-6.
34. Hu, X. B.; Chen, Z.; Tang, G.; Hou, J. L.; Li, Z. T., Single-molecular artificial transmembrane water channels. *J. Am. Chem. Soc.* **2012**, *134* (20), 8384-7.



35. Barboiu, M., Artificial water channels--incipient innovative developments. *Chem. Commun. (Camb.)* **2016**, 52 (33), 5657-65.
36. Licsandru, E.; Kocsis, I.; Shen, Y. X.; Murail, S.; Legrand, Y. M.; van der Lee, A.; Tsai, D.; Baaden, M.; Kumar, M.; Barboiu, M., Salt-Excluding Artificial Water Channels Exhibiting Enhanced Dipolar Water and Proton Translocation. *J. Am. Chem. Soc.* **2016**, 138 (16), 5403-9.
37. Barboiu, M.; Le Duc, Y.; Gilles, A.; Cazade, P. A.; Michau, M.; Marie Legrand, Y.; van der Lee, A.; Coasne, B.; Parvizi, P.; Post, J.; Fyles, T., An artificial primitive mimic of the Gramicidin-A channel. *Nat. Commun.* **2014**, 5, 4142.
38. Werber, J. R.; Osuji, C. O.; Elimelech, M., Materials for next-generation desalination and water purification membranes. *Nature Reviews Materials* **2016**, 1 (5).
39. Sengur-Tasdemir, R.; Tutuncu, H. E.; Gul-Karaguler, N.; Ates-Genceli, E.; Koyuncu, I., Biomimetic Membranes as an Emerging Water Filtration Technology. In *Biomimetic Lipid Membranes: Fundamentals, Applications, and Commercialization*, Kök, F. N.; Arslan Yildiz, A.; Inci, F., Eds. Springer International Publishing: Cham, 2019; pp 249-283.
40. Werber, J. R.; Elimelech, M., Permselectivity limits of biomimetic desalination membranes. *Sci Adv* **2018**, 4 (6), eaar8266.
41. Wagh, P.; Escobar, I. C., Biomimetic and bioinspired membranes for water purification: A critical review and future directions. *Environmental Progress & Sustainable Energy* **2019**, 38 (3).
42. Artificial Water Channels. *Faraday Discuss.* **2018**, 209 (0), 3-8.
43. Murail, S.; Vasiliu, T.; Neamtu, A.; Barboiu, M.; Sterpone, F.; Baaden, M., Water permeation across artificial I-quartet membrane channels: from structure to disorder. *Faraday Discuss.* **2018**, 209 (0), 125-148.
44. Kocsis, I.; Sorci, M.; Vanselous, H.; Murail, S.; Sanders, S. E.; Licsandru, E.; Legrand, Y. M.; van der Lee, A.; Baaden, M.; Petersen, P. B.; Belfort, G.; Barboiu, M., Oriented chiral water wires in artificial transmembrane channels. *Sci Adv* **2018**, 4 (3), eaa05603.
45. Kocsis, I.; Sun, Z. H.; Legrand, Y. M.; Barboiu, M., Artificial water channels-deconvolution of natural Aquaporins through synthetic design. *Npj Clean Water* **2018**, 1 (1).
46. Baaden, M.; Barboiu, M.; Bill, R. M.; Chen, C. L.; Davis, J.; Di Vincenzo, M.; Freger, V.; Froba, M.; Gale, P. A.; Gong, B.; Helix-

Nielsen, C.; Hickey, R.; Hinds, B.; Hou, J. L.; Hummer, G.; Kumar, M.; Legrand, Y. M.; Lokesh, M.; Mi, B.; Murail, S.; Pohl, P.; Sansom, M.; Song, Q.; Song, W.; Tornroth-Horsefield, S.; Vashisth, H.; Voegelé, M., Biomimetic water channels: general discussion. *Faraday Discuss.* **2018**, *209* (0), 205-229.

47. Zhao, H.; Ong, W. Q.; Zhou, F.; Fang, X.; Chen, X.; Li, S. F. Y.; Su, H.; Cho, N.-J.; Zeng, H., Chiral crystallization of aromatic helical foldamers via complementarities in shape and end functionalities. *Chemical Science* **2012**, *3* (6).

48. Zhao, H.; Sheng, S.; Hong, Y.; Zeng, H., Proton gradient-induced water transport mediated by water wires inside narrow aquapores of aquafoldamer molecules. *J. Am. Chem. Soc.* **2014**, *136* (40), 14270-6.

49. Ma, W.; Wang, C.; Li, J.; Zhang, K.; Lu, Y. J.; Huo, Y.; Zeng, H., The Dynamics, energetics and selectivity of water chain-containing aquapores created by the self-assembly of aquafoldamer molecules. *Org Biomol Chem* **2015**, *13* (43), 10613-9.

50. Shen, J.; Ye, R.; Romanies, A.; Roy, A.; Chen, F.; Ren, C.; Liu, Z.; Zeng, H., Aquafoldmer-Based Aquaporin-like Synthetic Water Channel. *J. Am. Chem. Soc.* **2020**, *142* (22), 10050-10058.

51. Kruse, E.; Uehlein, N.; Kaldenhoff, R., The aquaporins. *Genome Biol.* **2006**, *7* (2), 206.

52. Siwy, Z.; Fornasiero, F., Improving on aquaporins. *Science* **2017**, *357* (6353), 753.

53. Agrawal, K. V.; Shimizu, S.; Draushuk, L. W.; Kilcoyne, D.; Strano, M. S., Observation of extreme phase transition temperatures of water confined inside isolated carbon nanotubes. *Nat. Nanotechnol.* **2017**, *12* (3), 267-273.

54. Kolesnikov, A. I.; Zanotti, J. M.; Loong, C. K.; Thiyagarajan, P.; Moravsky, A. P.; Loutfy, R. O.; Burnham, C. J., Anomalously soft dynamics of water in a nanotube: a revelation of nanoscale confinement. *Phys. Rev. Lett.* **2004**, *93* (3), 035503.

55. Maniwa, Y.; Matsuda, K.; Kyakuno, H.; Ogasawara, S.; Hibi, T.; Kadowaki, H.; Suzuki, S.; Achiba, Y.; Kataura, H., Water-filled single-wall carbon nanotubes as molecular nanovalves. *Nat. Mater.* **2007**, *6* (2), 135-41.

56. Majumder, M.; Chopra, N.; Andrews, R.; Hinds, B. J., Nanoscale hydrodynamics: enhanced flow in carbon nanotubes. *Nature* **2005**, *438* (7064), 44.

57. Holt, J. K.; Park, H. G.; Wang, Y.; Stadermann, M.; Artyukhin, A. B.; Grigoropoulos, C. P.; Noy, A.; Bakajin, O., Fast mass transport through sub-2-nanometer carbon nanotubes. *Science* **2006**, *312* (5776), 1034-7.
58. Secchi, E.; Marbach, S.; Nigues, A.; Stein, D.; Siria, A.; Bocquet, L., Massive radius-dependent flow slippage in carbon nanotubes. *Nature* **2016**, *537* (7619), 210-3.
59. Yang, Y.; Hillmann, R.; Qi, Y.; Korzetz, R.; Biere, N.; Emmrich, D.; Westphal, M.; Buker, B.; Hutten, A.; Beyer, A.; Anselmetti, D.; Golzhauser, A., Ultrahigh Ionic Exclusion through Carbon Nanomembranes. *Adv. Mater.* **2020**, *32* (8), e1907850.
60. Hummer, G.; Rasaiah, J. C.; Noworyta, J. P., Water conduction through the hydrophobic channel of a carbon nanotube. *Nature* **2001**, *414* (6860), 188-90.
61. Noy, A.; Park, H. G.; Fornasiero, F.; Holt, J. K.; Grigoropoulos, C. P.; Bakajin, O., Nanofluidics in carbon nanotubes. *Nano Today* **2007**, *2* (6), 22-29.
62. Geng, J.; Kim, K.; Zhang, J.; Escalada, A.; Tunuguntla, R.; Comolli, L. R.; Allen, F. I.; Shnyrova, A. V.; Cho, K. R.; Munoz, D.; Wang, Y. M.; Grigoropoulos, C. P.; Ajo-Franklin, C. M.; Frolov, V. A.; Noy, A., Stochastic transport through carbon nanotubes in lipid bilayers and live cell membranes. *Nature* **2014**, *514* (7524), 612-5.
63. Tunuguntla, R. H.; Allen, F. I.; Kim, K.; Belliveau, A.; Noy, A., Ultrafast proton transport in sub-1-nm diameter carbon nanotube porins. *Nat. Nanotechnol.* **2016**, *11* (7), 639-44.
64. Tunuguntla, R. H.; Henley, R. Y.; Yao, Y. C.; Pham, T. A.; Wanunu, M.; Noy, A., Enhanced water permeability and tunable ion selectivity in subnanometer carbon nanotube porins. *Science* **2017**, *357* (6353), 792-796.
65. Freger, V., Selectivity and polarization in water channel membranes: lessons learned from polymeric membranes and CNTs. *Faraday Discuss.* **2018**, *209* (0), 371-388.
66. Kaucher, M. S.; Peterca, M.; Dulcey, A. E.; Kim, A. J.; Vinogradov, S. A.; Hammer, D. A.; Heiney, P. A.; Percec, V., Selective transport of water mediated by porous dendritic dipeptides. *J. Am. Chem. Soc.* **2007**, *129* (38), 11698-9.
67. Percec, V.; Dulcey, A. E.; Balagurusamy, V. S. K.; Miura, Y.; Smidrkal, J.; Peterca, M.; Nummelin, S.; Edlund, U.; Hudson, S. D.; Heiney, P. A.; Duan, H.; Magonov, S. N.; Vinogradov, S. A., Self-assembly

of amphiphilic dendritic dipeptides into helical pores. *Nature* **2004**, *430* (7001), 764-768.

68. de Groot, B. L.; Tieleman, D. P.; Pohl, P.; Grubmüller, H., Water Permeation through Gramicidin A: Desformylation and the Double Helix: A Molecular Dynamics Study. *Biophys. J.* **2002**, *82* (6), 2934-2942.

69. Zhou, X.; Liu, G.; Yamato, K.; Shen, Y.; Cheng, R.; Wei, X.; Bai, W.; Gao, Y.; Li, H.; Liu, Y.; Liu, F.; Czajkowsky, D. M.; Wang, J.; Dabney, M. J.; Cai, Z.; Hu, J.; Bright, F. V.; He, L.; Zeng, X. C.; Shao, Z.; Gong, B., Self-assembling subnanometer pores with unusual mass-transport properties. *Nat. Commun.* **2012**, *3* (1), 949.

70. Gong, B., Artificial water channels: inspiration, progress, and challenges. *Faraday Discuss.* **2018**, *209* (0), 415-427.

71. Ogoshi, T.; Kanai, S.; Fujinami, S.; Yamagishi, T.-a.; Nakamoto, Y., para-Bridged Symmetrical Pillar[5]arenes: Their Lewis Acid Catalyzed Synthesis and Host–Guest Property. *J. Am. Chem. Soc.* **2008**, *130* (15), 5022-5023.

72. Ogoshi, T.; Yamagishi, T. A.; Nakamoto, Y., Pillar-Shaped Macrocyclic Hosts Pillar[n]arenes: New Key Players for Supramolecular Chemistry. *Chem. Rev.* **2016**, *116* (14), 7937-8002.

73. Si, W.; Hu, X. B.; Liu, X. H.; Fan, R. H.; Chen, Z. X.; Weng, L. H.; Hou, J. L., Self-assembly and proton conductance of organic nanotubes from pillar[5]arenes. *Tetrahedron Lett.* **2011**, *52* (19), 2484-2487.

74. Si, W.; Xin, P.; Li, Z. T.; Hou, J. L., Tubular Unimolecular Transmembrane Channels: Construction Strategy and Transport Activities. *Acc. Chem. Res.* **2015**, *48* (6), 1612-9.

75. Chen, L.; Si, W.; Zhang, L.; Tang, G.; Li, Z. T.; Hou, J. L., Chiral selective transmembrane transport of amino acids through artificial channels. *J. Am. Chem. Soc.* **2013**, *135* (6), 2152-5.

76. Shen, Y. X.; Si, W.; Erbakan, M.; Decker, K.; De Zorzi, R.; Saboe, P. O.; Kang, Y. J.; Majd, S.; Butler, P. J.; Walz, T.; Aksimentiev, A.; Hou, J. L.; Kumar, M., Highly permeable artificial water channels that can self-assemble into two-dimensional arrays. *Proc. Natl. Acad. Sci. U. S. A.* **2015**, *112* (32), 9810-5.

77. Li, Q.; Li, X.; Ning, L.; Tan, C. H.; Mu, Y.; Wang, R., Hyperfast Water Transport through Biomimetic Nanochannels from Peptide-Attached (pR)-pillar[5]arene. *Small* **2019**, *15* (6), e1804678.

78. Shen, Y. X.; Song, W.; Barden, D. R.; Ren, T.; Lang, C.; Feroz, H.; Henderson, C. B.; Saboe, P. O.; Tsai, D.; Yan, H.; Butler, P. J.; Bazan, G. C.; Phillip, W. A.; Hickey, R. J.; Cremer, P. S.; Vashisth, H.; Kumar, M., Achieving high permeability and enhanced selectivity for Angstrom-scale separations using artificial water channel membranes. *Nat. Commun.* **2018**, *9* (1), 2294.
79. Lang, C.; Ye, D.; Song, W.; Yao, C.; Tu, Y. M.; Capparelli, C.; LaNasa, J. A.; Hickner, M. A.; Gomez, E. W.; Gomez, E. D.; Hickey, R. J.; Kumar, M., Biomimetic Separation of Transport and Matrix Functions in Lamellar Block Copolymer Channel-Based Membranes. *ACS Nano* **2019**, *13* (7), 8292-8302.
80. Song, W.; Joshi, H.; Chowdhury, R.; Najem, J. S.; Shen, Y. X.; Lang, C.; Henderson, C. B.; Tu, Y. M.; Farrell, M.; Pitz, M. E.; Maranas, C. D.; Cremer, P. S.; Hickey, R. J.; Sarles, S. A.; Hou, J. L.; Aksimentiev, A.; Kumar, M., Artificial water channels enable fast and selective water permeation through water-wire networks. *Nat. Nanotechnol.* **2020**, *15* (1), 73-79.
81. Zhao, D.; Liu, J.; Jiang, J., Porous organic cages embedded in a lipid membrane for water desalination: A molecular simulation study. *J. Membr. Sci.* **2019**, *573*, 177-183.
82. Noy, A.; Wanunu, M., A new type of artificial water channels. *Nat. Nanotechnol.* **2020**, *15* (1), 9-10.
83. Strilets, D.; Fa, S.; Hardiagon, A.; Baaden, M.; Ogoshi, T.; Barboiu, M., Biomimetic Approach for Highly Selective Artificial Water Channels Based on Tubular Pillar[5]arene Dimers. *Angew. Chem. Int. Ed. Engl.* **2020**, *59* (51), 23213-23219.
84. Barboiu, M.; Cerneaux, S.; van der Lee, A.; Vaughan, G., Ion-driven ATP pump by self-organized hybrid membrane materials. *J. Am. Chem. Soc.* **2004**, *126* (11), 3545-50.
85. Barboiu, M. D.; Hovnanian, N. D.; Luca, C.; Cot, L., Functionalized derivatives of benzocrown-ethers, V multiple molecular recognition of zwitterionic phenylalanine. *Tetrahedron* **1999**, *55* (30), 9221-9232.
86. Michau, M.; Barboiu, M., Self-organized proton conductive layers in hybrid proton exchange membranes, exhibiting high ionic conductivity. *J. Mater. Chem.* **2009**, *19* (34), 6124-6131.

87. Barboiu, M., Facilitated transport of organics of biological interest I. A new alternative for the separation of amino acids by fixed-site crown-ether polysiloxane membranes. *J. Membr. Sci.* **2000**, *172* (1-2), 91-103.
88. Barboiu, M., Facilitated transport of organics of biological interest II. Selective transport of organic acids by macrocyclic fixed site complexant membranes. *J. Membr. Sci.* **2000**, *174* (2), 277-286.
89. Legrand, Y. M.; Barboiu, M., Self-assembled supramolecular channels: toward biomimetic materials for directional translocation. *Chem. Rec.* **2013**, *13* (6), 524-38.
90. Barboiu, M., Constitutional Hybrid Materials - Toward Selection of Functions. *Eur. J. Inorg. Chem.* **2015**, *2015* (7), 1112-1125.
91. Petersen, R. J., Composite reverse osmosis and nanofiltration membranes. *J. Membr. Sci.* **1993**, *83* (1), 81-150.
92. Di Vincenzo, M.; Tiraferri, A.; Musteata, V. E.; Chisca, S.; Sougrat, R.; Huang, L. B.; Nunes, S. P.; Barboiu, M., Biomimetic artificial water channel membranes for enhanced desalination. *Nat. Nanotechnol.* **2021**, *16* (2), 190-196.
93. Roy, A.; Shen, J.; Joshi, H.; Song, W.; Tu, Y. M.; Chowdhury, R.; Ye, R.; Li, N.; Ren, C.; Kumar, M.; Aksimentiev, A.; Zeng, H., Foldamer-based ultrapermeable and highly selective artificial water channels that exclude protons. *Nat. Nanotechnol.* **2021**.
94. Yuan, Y. D.; Dong, J.; Liu, J.; Zhao, D.; Wu, H.; Zhou, W.; Gan, H. X.; Tong, Y. W.; Jiang, J.; Zhao, D., Porous organic cages as synthetic water channels. *Nat. Commun.* **2020**, *11* (1), 4927.
95. Li, Y.; Li, Z.; Aydin, F.; Quan, J.; Chen, X.; Yao, Y. C.; Zhan, C.; Chen, Y.; Pham, T. A.; Noy, A., Water-ion permselectivity of narrow-diameter carbon nanotubes. *Sci Adv* **2020**, *6* (38).
96. Huang, L. B.; Di Vincenzo, M.; Li, Y.; Barboiu, M., Artificial Water Channels: Towards Biomimetic Membranes for Desalination. *Chemistry* **2021**, *27* (7), 2224-2239.
97. Wiegandt, H., Glycosphingolipids<sup>1</sup> <sup>1</sup>The survey of the literature pertaining to this review was essentially concluded in May 1970. The nomenclature is mostly in accordance with the tentative rules of the IUPAC-IUB commission. In *Adv. Lipid Res.*, Paoletti, R.; Kritchevsky, D., Eds. Elsevier: 1971; Vol. 9, pp 249-289.
98. Kanfer, J. N.; Hakomori, S., *Sphingolipid Biochemistry*. Springer US: 2012.

99. Siskind, L. J.; Colombini, M., The lipids C2- and C16-ceramide form large stable channels. Implications for apoptosis. *J. Biol. Chem.* **2000**, *275* (49), 38640-4.
100. Ferdani, R.; Li, R.; Pajewski, R.; Pajewska, J.; Winter, R. K.; Gokel, G. W., Transport of chloride and carboxyfluorescein through phospholipid vesicle membranes by heptapeptide amphiphiles. *Org Biomol Chem* **2007**, *5* (15), 2423-32.
101. Schalley, C. A., *Analytical Methods in Supramolecular Chemistry*. Wiley: 2007.
102. Li, Y.; Zheng, S.; Legrand, Y. M.; Gilles, A.; van der Lee, A.; Barboiu, M., Structure-driven selection of adaptive transmembrane Na<sup>+</sup> carriers or K<sup>+</sup> channels. *Angew. Chem. Int. Ed. Engl.* **2018**.
103. Saha, T.; Dasari, S.; Tewari, D.; Prathap, A.; Sureshan, K. M.; Bera, A. K.; Mukherjee, A.; Talukdar, P., Hopping-mediated anion transport through a mannitol-based rosette ion channel. *J. Am. Chem. Soc.* **2014**, *136* (40), 14128-35.
104. Saha, T.; Gautam, A.; Mukherjee, A.; Lahiri, M.; Talukdar, P., Chloride Transport through Supramolecular Barrel-Rosette Ion Channels: Lipophilic Control and Apoptosis-Inducing Activity. *J. Am. Chem. Soc.* **2016**, *138* (50), 16443-16451.
105. Decoursey, T. E., Voltage-gated proton channels and other proton transfer pathways. *Physiol. Rev.* **2003**, *83* (2), 475-579.
106. Hoekstra, A. Y.; Wiedmann, T. O., Humanity's unsustainable environmental footprint. *Science* **2014**, *344* (6188), 1114-7.
107. Jung, J. S.; Preston, G. M.; Smith, B. L.; Guggino, W. B.; Agre, P., Molecular structure of the water channel through aquaporin CHIP. The hourglass model. *J. Biol. Chem.* **1994**, *269* (20), 14648-14654.
108. Agre, P.; King, L. S.; Yasui, M.; Guggino, W. B.; Ottersen, O. P.; Fujiyoshi, Y.; Engel, A.; Nielsen, S., Aquaporin water channels--from atomic structure to clinical medicine. *J. Physiol.* **2002**, *542* (Pt 1), 3-16.
109. Verkman, A. S.; Anderson, M. O.; Papadopoulos, M. C., Aquaporins: important but elusive drug targets. *Nat. Rev. Drug Discovery* **2014**, *13* (4), 259-277.
110. Huang, L. B.; Hardiagon, A.; Kocsis, I.; Jegu, C. A.; Deleanu, M.; Gilles, A.; van der Lee, A.; Sterpone, F.; Baaden, M.; Barboiu, M., Hydroxy

Channels-Adaptive Pathways for Selective Water Cluster Permeation. *J. Am. Chem. Soc.* **2021**, *143* (11), 4224-4233.

111. Kyakuno, H.; Matsuda, K.; Yahiro, H.; Inami, Y.; Fukuoka, T.; Miyata, Y.; Yanagi, K.; Maniwa, Y.; Kataura, H.; Saito, T.; Yumura, M.; Iijima, S., Confined water inside single-walled carbon nanotubes: global phase diagram and effect of finite length. *J. Chem. Phys.* **2011**, *134* (24), 244501.

112. Otake, K. I.; Otsubo, K.; Komatsu, T.; Dekura, S.; Taylor, J. M.; Ikeda, R.; Sugimoto, K.; Fujiwara, A.; Chou, C. P.; Sakti, A. W.; Nishimura, Y.; Nakai, H.; Kitagawa, H., Confined water-mediated high proton conduction in hydrophobic channel of a synthetic nanotube. *Nat. Commun.* **2020**, *11* (1), 843.

113. Si, W.; Chen, L.; Hu, X. B.; Tang, G.; Chen, Z.; Hou, J. L.; Li, Z. T., Selective artificial transmembrane channels for protons by formation of water wires. *Angew. Chem. Int. Ed. Engl.* **2011**, *50* (52), 12564-8.

114. Ben Amara, F.; Dionne, E. R.; Kassir, S.; Pellerin, C.; Badia, A., Molecular Origin of the Odd-Even Effect of Macroscopic Properties of n-Alkanethiolate Self-Assembled Monolayers: Bulk or Interface? *J. Am. Chem. Soc.* **2020**, *142* (30), 13051-13061.

115. Liu, G.; Zhang, X.; Di Yuan, Y.; Yuan, H.; Li, N.; Ying, Y.; Peh, S. B.; Wang, Y.; Cheng, Y.; Cai, Y.; Gu, Z.; Cai, H.; Zhao, D., Thin-Film Nanocomposite Membranes Containing Water-Stable Zirconium Metal–Organic Cages for Desalination. *ACS Materials Letters* **2021**, *3* (3), 268-274.





## **Résumé de la thèse**

L'eau joue un rôle crucial dans toutes les cellules et organismes vivants. Les aquaporines, canaux d'eau naturels, sont capables de faciliter le transport de l'eau à travers les membranes cellulaires. Cependant, la complexité et la faible stabilité des aquaporines ont incité les chercheurs à les imiter et à développer des canaux d'eau artificiels combinant une perméabilité et une sélectivité élevées avec une stabilité chimique. Dans ce document, nous avons élaboré et synthétisé une série de petites molécules amphiphiles ayant des structures spécifiques utilisées pour construire des canaux d'eau artificiels. Ces molécules sont formées de cavités hydrophiles, un assemblage d'urée et des chaînes latérales hydrophobes en interaction avec des membranes externes. De plus, nous nous sommes concentrés sur les performances de transport d'eau à travers les canaux d'eau artificiels situés dans des membranes en bicouches et des membranes polymériques. Cette thèse présente de nouveaux canaux d'eau synthétiques et développe l'analyse structure-performance qui peut être utilisée pour rationaliser la conception de canaux d'eau artificiels en vue de la fabrication de membranes hautement permselectives pour le dessalement.

## **Abstract**

Water plays a crucial role in all living cells and organisms. Aquaporins, as natural water channels, are able to facilitate the transport of water across cell membranes. However, the complexity and poor stability of aquaporins have prompted researchers to mimic them and develop artificial water channels combining high permeability and selectivity with chemical stability. Herein, we have designed and synthesized a series of small amphiphilic molecules with specific structures used to construct artificial water channels with hydrophilic cavities, urea scaffold and hydrophobic lateral chains in interaction with external membranes. Moreover, we focused on their water transport performances in bilayer and polymeric membrane environments. This thesis introduces new synthetic water channels, and elaborate on the structure-performance analysis that can be used to rationalize artificial water channels design toward the fabrication highly permselective membranes for desalination.

**Mots clés :** canaux d'eau artificiels, auto-assemblage, biomimétique, membranes, dessalement